CRANFIELD UNIVERSITY

COLLEGE OF DEFENCE MANAGEMENT AND TECHNOLOGY

DEPARTMENT OF ENGINEERING SYSTEMS AND MANAGEMENT

FOR THE DEFENCE AND SECURITY SECTORS

PhD THESIS

Academic Year 2007 - 2008

Adisak Showichen

Numerical analysis of vehicle bottom structures subjected to anti-tank mine explosions

Supervisor: Dr A Hameed

May 2008

ABSTRACT

It is important to estimate the damage caused to a vehicle and its occupants so that necessary measure to enhance the protection can be considered. Real life tests or experiments are expensive. In addition the nature of loading is such that it is not easy to measure the deflections or damage caused to the vehicle due to many uncertainties and factors. Thus numerical simulation based analysis has steadily grown to estimate the damage experienced by the vehicle subjected to mine blast.

This research estimated the damage to the vehicle floor panels against a mine blast using both LS-DYNA and AUTODYN software. To begin with, a review of the available anti-tank (AT) mines was made to establish the magnitude of the threat. In addition, these mines were classified into different categories, using the criteria set up by the researcher. Thereafter numerical models of a single and a double plate, representing vehicle floor, with a space in between subjected to simulated mine blasts using both LS-DYNA and AUTODYN were developed. Comparison of the numerical results with that of experiments has shown a satisfactory agreement. The simulation was then extended to the full-scale vehicle. It is recommended that the vehicle should be modelled as a 'single-floor hull' and a 'double-floor hull' instead of a single plate and a 'plain' box in order captured the impact between both floor panels. The thesis then investigated the effects of changing different parameters, such as stand off distance, panel thickness, amount of explosive charge, and gap distance. In addition, the effects of vehicle having single-floor, double-floor, and 'V' bottom setting were also compared. Finally, this thesis has shown the implementation of soil parameters into a numerical simulation of a vehicle structure subjected to a buried charge under soil. Based on this method, the structural response from the blast load using an hemispherical charge on a reflected surface is comparable to the blast load from a buried spherical charge at 30 mm below the cohesive soil having 7.7% moisture content.

ACKNOWLEDGEMENTS

The author would like to acknowledge and thank,

- Firstly, to my supervisor, Dr A Hameed for all the fantastic things he has done and given to me. Without him, I would not be like I am today.
- Dr Iremonger, for his magnificent supports and generosity.
- Prof Hetherington, for his wonderful kindness, who always give and give.
- Engineering System Department, Cranfield University and all the staffs (for example, Mr Chris Prowting, Mr Alan Peare, Dr Hugh Goyder, and Dr Darina Fiserova) for all the helps and supports, especially in financial support throughout this work.
- Mrs Ross Gibson and Mr Michael Gibson, who have kindly read parts of the thesis.
- The Royal Thai Army, which has also provided financial support to me from March 1997 to November 2006.
- Dr Jon Glenville, Dr Chris Maslin, Mr Alex Pett, and all the staffs at Century Dynamics, who have given advices on AUTODYN.
- Last but not least, my parents, my family and my wife, for all the loves they have always given.

CONTENTS

List of Tables

List of figures

CHAPTER 1 Introduction

This chapter will give an overview of the research works in this thesis. Its background, aim, and thesis outline are presented.

1.1 Background to the research

It is commonly known that a landmine is one of the most dangerous weapons. Upon encounter, it can cause damage to the vehicle and injury or death to its occupants. Thus peacekeeping forces and other humanitarian agencies working in the vicinity of anti-vehicle landmines are under serious threat. The devastating effects of it not only demoralises the operators but it also hinders the tempo of the operation. Thus efforts are being invested to design vehicles with greater protection against these mines. A naive solution to the problem is to have vehicles with thicker wall section to dissipate the energy; however this approach will reasonably affect the vehicle performance. Alternatively, using new materials with optimised vehicle structural geometry can enhance protection. However this approach would also require significant amount of tests and experiments to develop a suitable structural geometry. This would consume both time and money. Numerical analyses are being introduced to reduce the number of experimental tests required and hence it could provide a more economical method of development. Unlike experimental tests, numerical simulations, once validated, can be designed to create different scenarios with parametric studies of different physical parameters.

This thesis is restricted to study to anti-tank (AT) mines, as they pose a much greater threat to vehicles than anti-personnel (AP) mines, although a few AP mines may be included in the analysis because of their destruction ability. According to the Ottawa Mine Ban Treaty in1997, 147 countries support the ban of AP mines, Landmine Monitor Editorial Board (2005). This accounts for over three-quarters of the world's nations. The ban prohibits the use of, stockpiling, production and transfer of anti-personnel mines. Therefore, the chances of encountering anti-personnel mines are reducing.

The vehicle structure used in mine-blast experiments and numerical simulations may range from a simple plate structure to a real vehicle. Results from the experiments are normally classified or held back due to commercial reasons and subsequently there is limited literature available in this area. Moreover, experiments are cost-prohibitive and limited available experimental results are difficult to correlate because some of the parameters affecting the results have not been well defined. Often a simple structure such as a flat plate is used for testing and validation of numerical simulation.

1.2 General research areas

In general, the research in mine protected vehicles may be divided into the following categories:

a. Threat evaluation: Research may be undertaken to gather information on different types of mines currently available that can cause damage to vehicles and their occupants. The level of damage or threat, in terms of lethality or amount of explosive content they pose is analysed. The threat in different countries or areas may be different. Study in this topic provides specific threats that particular vehicles may face.

b. Blast load evaluation: This area covers all activities prior to the blast loading interacting with the vehicle structure. Upon initiation, detonation wave builds up an overpressure, along with the soil ejecta, which acts on the vehicle structure to cause damage. Blast loading may arise from a mine laid above the ground surface, or laid flush with the ground level or buried under ground (soil). The magnitude of the blast loading may change due to the soil and its condition.

c. Vehicle response: Damage or deformation to vehicle structure as a result of blast loading is analysed. Possible approach to mitigate the effect of the blast either using appropriate material or geometric configuration of the vehicle's bottom plate are considered.

d. Effects on occupants: This may be performed together with the vehicle response. Vehicle occupants are affected upon blast interaction with the vehicle.

Study in this area may cover possibilities of likely injuries or in the extreme cases, the death. Using a synthetic human body may assist the analysis.

It is noticed that the general research area is very broad, thus demanding high resources, in terms of time and finances to analyse all aspects of the study. This thesis will therefore focus on the threat evaluation and vehicle response against mine blast.

1.3 Aim and objectives

The aim of this research is to develop a numerical model of a vehicle bottom structure subjected to an anti-tank (AT) mine blast in order to assess the effects without the need of conducting full-scale experiments.

In order to achieve the above aim, several objectives are set.

a. To evaluate the nature and magnitude of the threat by reviewing the available AT mines.
b. To develop a numerical model using different methodologies, compare and validate with the available experimental or test results with the view to access the full-scale model without undertaking full-scale destructive test.
c. To assess the effects of using different full-scale vehicle bottom geometries and configurations against mine blasts.

1.4 Thesis outline

To meet the above objectives, the thesis has been outlined in the following manner:

Chapter 2, Anti-tank mines

An assessment of expected threat has been made by undertaking a detailed review of available AT mines. Mines are then classified into different categories so that each category will indicate type of risks to vehicle and hence will indicate the characteristic of AT mines that will be used in numerical simulations.

Chapter 3, Literature reviews and theory

This chapter briefly describes the previous work undertaken in this area. The fundamentals of the blast theory, the numerical simulation methodologies adopted both in AUTODYN and LS-DYNA, and the material models used in this thesis are explained.

Chapter 4, Single and double plate numerical simulations

Numerical simulations of single and double plates subjected to exploding charge in the air using different methodologies in LS-DYNA and AUTODYN are developed, compared and validated with the available experimental results.

Chapter 5, Development of vehicle hull numerical simulations

In this chapter validated models are extended to represent the actual vehicle models. The vehicle bottom in single floor configuration is represented by a single plate model while the vehicle bottom in double (spaced) floor configuration is represented by a plain box panel. These vehicle bottom models are developed further to include the crew compartment sections. A comparison is made between a single plate and a single-floor vehicle hull model, and a plain box model and a double-floor vehicle hull model.

Chapter 6, Comparison on different vehicle hull models

This chapter focuses on the comparison between single-floor vehicle hull model, and double-floor vehicle hull model in reducing the blast effects. The effects of having single and double floor configurations, different stand off distances, thicknesses, and amount of charges are compared. The bottom part of the double-floor vehicle is changed to a 'V' shape and a further comparison between single, double, and 'V' vehicle hull models are made.

Chapter 7, Vehicle bottom subjected to a buried charge under soil numerical simulations

The work reported in this chapter is the extension to the recent study performed by Fiserova (2006), which formulated a soil model that take into account of the different soil moisture content. The effect of a spherical charge buried 30 mm below the soil surface with 7.7%

moisture content is compared with an hemispherical charge on a reflected surface, which is used in Chapter 4, 5, and 6. A single plate and a double-floor vehicle hull models are used in the comparison. The results indicate the validity of using an hemispherical charge on a reflected surface in the thesis instead of a spherical charge buried 30 mm under the soil surface with 7.7% moisture content.

Chapter 8 Further discussion

This chapter discusses important points, which have not been discussed in the previous chapters.

Chapter 9, Conclusions and recommendations for future works

The thesis concludes with contribution to the knowledge and suggest for future works.

1.5 Supporting works

During the course of study, the following supporting tasks were undertaken to report the findings of this study. These are listed in chronological order:

- Presentation to Alvis Vickers Ltd. in March 2004 (a single plate model)
- Journal paper: SHOWICHEN, A., *et al*., 2005. Simulation of plate structures subjected to Anti-tank mines. *Journal of Battlefield Technology*. 8, 1 (March 2005), 1-7.
- Poster presentation in 3rd Research Student Symposium at College of Defence Management and Technology on 17 May 2005 (single and double plate models)
- Presentation to DSTL and Qinetic in October 2005 (single and double plate models)
- Article: SHOWICHEN, A., HAMEED, A., and IREMONGER, M.J. Anti-tank mines. *ARMOR magazine*. Accepted to be published in the future issue. Kentucky: U.S. Army Armor Center.

CHAPTER 2 Anti-tank mines

This chapter gives an introduction and a historical overview of AT mines. For simplification, these mines have been categorised to help understanding their mode of initiation, mode of attack, mode of deployment, magnitude of threat level, etc. This summary of classification provides the basis on which the author has chosen the most likely mine that a vehicle may come across during its operation. The amount of TNT explosive charge from this mine is selected to use in the simulation studies to understand its effects on the vehicle bottom. This chapter also gives literature reviews on the effects of mine blasts and suggested means to prevent its threats.

2.1 Introduction

It is believed that a landmine is one of the most dangerous weapons to human life in the world. In 1994, a report by the U.S. Department of State (1998), estimated that there were around 60 million mines buried around the world. Since 1975, landmines have killed or injured more than 1 million people, Kevin (2006). The estimated number of landmines and unexploded ordnance (UXO) casualties of both military and civilian personnel is between 15,000 and 20,000 per year, Landmine Monitor Editorial Board (2005). It was estimated by Sloan (1986) that 20 percent of tank losses in the Second World War were from mines, rising to 70% during the Vietnam War, Ashcroft (1999). A single mine costs as little as £2 but could cost hundreds to remove and thousands to overcome the injuries and damage caused by it to the occupant and vehicle respectively, United Nations Association of the USA (2006).

King (2002, 2003, 2004) has defined a mine, with reference to the North Atlantic Treaty Organisation (NATO) definition, as ‘an explosive or other material, normally encased, designed to destroy or damage vehicles, boats or aircraft, or designed to wound, kill, or otherwise incapacitate personnel. It may be detonated by the action of its target, the passage of time or by controlled means.’ To be more specific, with respect to land application, a mine is then described as an explosive, normally encased, designed to destroy, damage or disable ground vehicles, or to wound, kill, or otherwise incapacitate personnel.

Mines are generally divided into anti-tank (AT) mines and anti-personnel (AP) mines due to their main targets. In this research, AT mines include all mines that are capable of attacking vehicles, whether they are soft-skin vehicles or tanks. Because AT mines are comparatively larger and contain several times more explosive material than AP mines-the typical amount of explosive contained in AP blast mines is 0.003–0.25 kg, while in AT blast mines it is 1.5–10 kg, King (2001). Therefore AT mine poses a much greater threat to vehicle and its crews. Ultimately, it is very important for the blast-protected-vehicle designers to have an accurate estimate of mine threats, especially AT mines, which are the main danger. Hence there is a real need to tabulate all the important data of available mines that are a threat to vehicles and occupants, and are believed to be currently employed, in production and under development in terms of their means of initiation, deployment, modes of attack, amount of charge, types of fuze and laying options available in each mine. This chapter will give a better picture of these mines, which pose the most likely threat, so that analysis on their effects can be performed more accurately.

It is noted that, in recent military conflicts, such as in Iraq, Improvised Explosive Devices (IED) have become one of the main threats to vehicles and personnel. Knights (2005) states that the Washington Institute for Near East Policy statistics has reported that 84% of attacks on multinational forces in Iraq involved roadside IEDs. In addition, the average number of IED-related US fatalities has jumped from 19 per month in 2003 – 2004 to 38 per month in 2005. Pike (2005) defines IED as a 'homemade' device that is designed to cause death or injury by using explosive alone or in combination with toxic chemicals, biological toxins, or radiological material, which can be produced in varying sizes, functioning methods, containers, and delivery methods. This thesis focuses on AT mines because of several reasons. Firstly, IED is relatively new subject and in a way is similar to mine. Secondly, there are many variations in IEDs, but limited information is available to the public domain. Dosquet *et al* (2004) stated that IED without primary fragments is often used due to the simplicity of assembly and their effectiveness. The analyses in this thesis, which involve a bare explosive charge without its casing and fuze representing an AT mine, may be related to IED by using the same amount of explosive charge. Explosive charge contained within an IED is not fixed and usually more than a typical mine. Likewise,

several mines may be stacked together to achieve maximum destruction. The classification of AT mines in this chapter is based on a single AT mine being deployed. Multiple mines stacked together can be modelled as a single mine where explosive content is equal to the sum of explosive contents of multiple mines.

2.2 History of AT mines

A brief history of AT mines was summarised based on King (2002), Landmine Monitor Editorial Board (2002), Sloan (1986), and United Nations Association of the USA (2002). AT mines were first used by German combat engineers to counter the British and French tanks during the First World War. At the beginning, they used artillery and mortar shells with sensitive fuses and also started to use command-detonated mines. In 1929, they launched the pressure fuzed AT mines, the Tellermine 29. During the Second World War, full-width AT mines with tilt-rod fuses, and side attack AT mines, based on anti-tank rockets, were first used. Early on AT mines could be easily neutralised and re-laid by the enemy. Smaller AP mines were then introduced and deployed around AT mines to avoid AT mines being removed. Initially, AT mines were used as defensive weapons but in the 1960s scatterable mines were invented and deployed by the United States during the Vietnam War as offensive weapons. Since then, new technologies in design and manufacture have made a variety of mines available: self-destructing (can automatically explode after a pre-set time), self-neutralising mechanisms (can defuse themselves after a period of time without exploding), low metal content (can be extremely durable and difficult to detect), remote delivery systems (capable of deploying in a long distance), wide area mines (can remotely attack over a big area with accuracy), and sophisticated sensors (can detect targets and detonate at the best possible time to maximise the damage).

2.3 General mechanism of a buried AT blast mine

Figure 2.1 TM-62M AT blast mine with pressure fuze, King (2002).

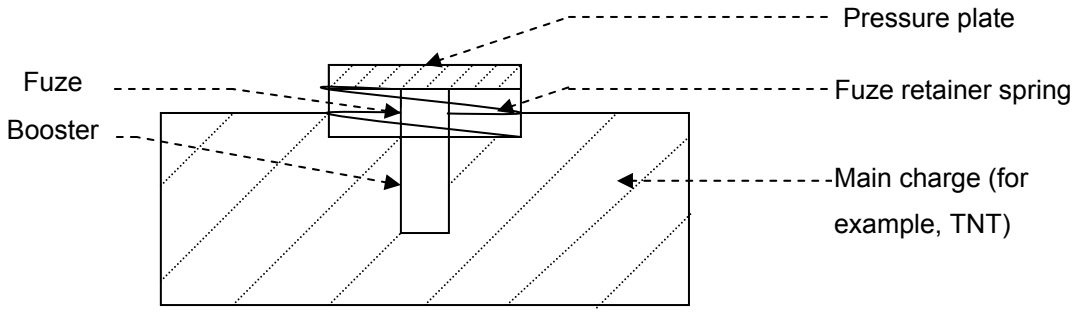

Figure 2.2 General diagrammatic view of a typical AT blast mine

A general mechanism of a typical pressure-operated AT blast mine is shown in Figure 2.2. It is activated when a vehicle rolls over an AT mine; its pressure causes the pressure plate to push down. Below the pressure plate is the fuze retainer spring (usually a Belleville spring type) and the firing pin that moves into the pressure fuze, which usually consists of a detonator. The firing pin then detonates the detonator, and subsequently the booster charge. This will detonate the main charge and hence cause explosion. Upon initiation of the main charge, the detonation wave propagates through the explosive material, generating high pressures and temperature in the detonation products. These products expand violently, pushing the surrounding soil and air out of the occupied volume and creates a pressure shock-wave propagating through the surrounding material in all directions from the charge. As soil is forced out, the detonation products break through the surface. Soil then gains

kinetic energy and hence moves upwards. After impinging on the target, soil falls back and forms the apparent crater surface.

2.4 Classifications of AT mines

Various authors [Held (1984), King (2002), Landmine Monitor Editorial Board (2005), Sloan (1986), Smith (1996), and Williams (2000)] have described AT mines in different ways. In this work, mine classification has been simplified by categorising the mines based on modes of initiation, modes of deployment and modes of attack. Most of the raw data in this research work is referenced from King (2002, 2003, and 2004). Table A.1 in Appendix A displays mines that were used to determine their classification. These mines are currently available for use and have been considered to cause damage to vehicles. Mines were not considered where their production has been stopped and which are now believed to be obsolete.

2.4.1 Mines that are a threat to vehicles

From the available information, based on their written characteristics, there are 168 mines that are currently a threat to vehicles. Figure 2.3 shows that the majority of AT mines can cause damage to heavy armoured vehicles, hence they are also certain to damage soft-skin and lightly armoured vehicles. All 168 AT mines are capable of defeating soft-skin and lightly armoured vehicles. However, some AP mines, especially directional fragmentation mines, can also attack lightly armoured vehicles because of their charge weight and the energy possessed by their fragments. The ‘attack capability’ in Figure 2.3 is defined using the following criteria. Mines which are deemed to penetrate 100 mm of armour either by blast pressure or fragmentation or by shape charge effect have been considered a threat to heavy armour, while penetrability of less than 50 mm is considered to be a threat to light armoured vehicles. There are some mines that can certainly penetrate light armoured vehicles but may or may not penetrate heavy armoured vehicles depending on the armour thickness. Their penetrability is between 50 to 100 mm. They are considered as the ‘possibly heavy armoured vehicle’ group. The very few mines, about which there is very

little information, have been placed into a category based upon the author's knowledge and experience. Note that the armour penetration data is from the published data in King (2002, 2003, 2004).

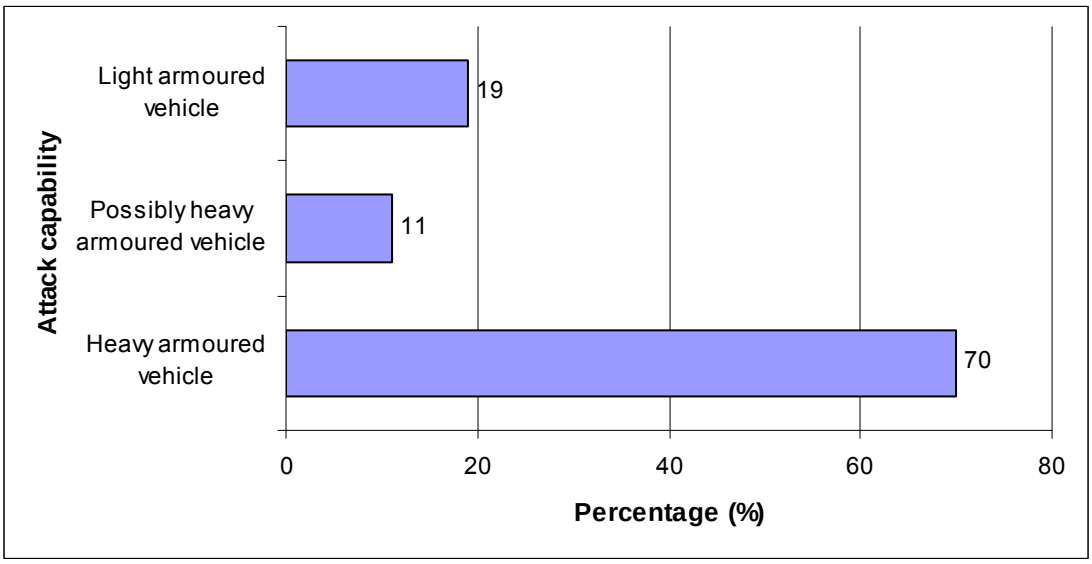

Figure 2.3 Mines that are a threat to vehicle

2.4.2 Classification in terms of countries used

If a mine is either under development or under possession but is believed to have never been laid in any country or its production has ceased and has never been laid, it is classified as 'low' threat category. 'Medium' threat includes mines that are believed to be laid and are active between 1 to 5 countries, while 'high' threat corresponds to more than 5 countries. Figure 2.4 shows this classification, whereas Figure 2.5 highlights that only 4 mines or about 2% of the available mines have been laid in more than 12 countries. The Russian TM-46 and TM-57, which are AT blast mines with charge weight of 5.7 and 6.34 kg TNT respectively, have been found in 23 countries.

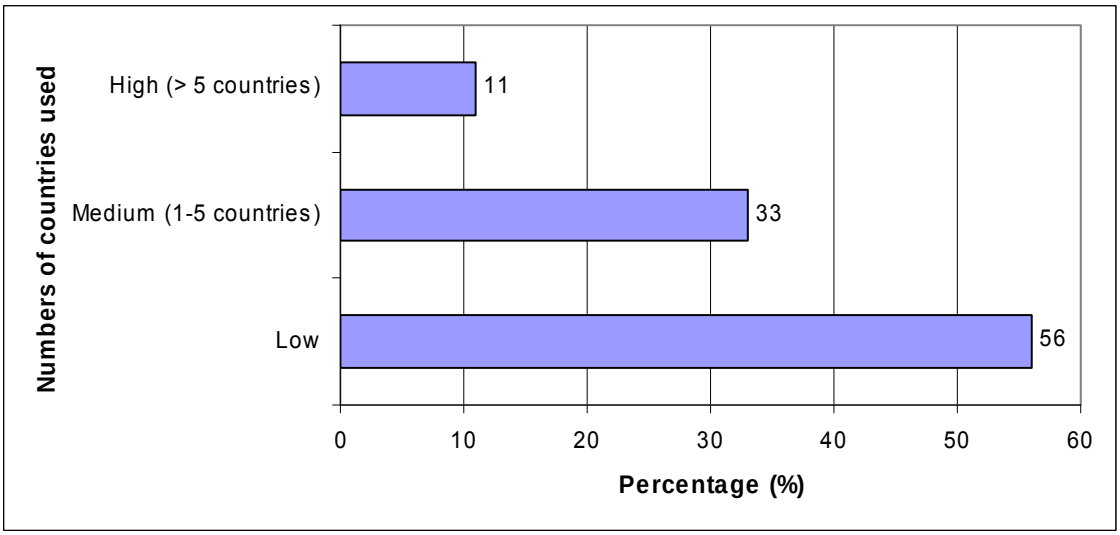

Figure 2.4 Percentage of active mines in countries (1)

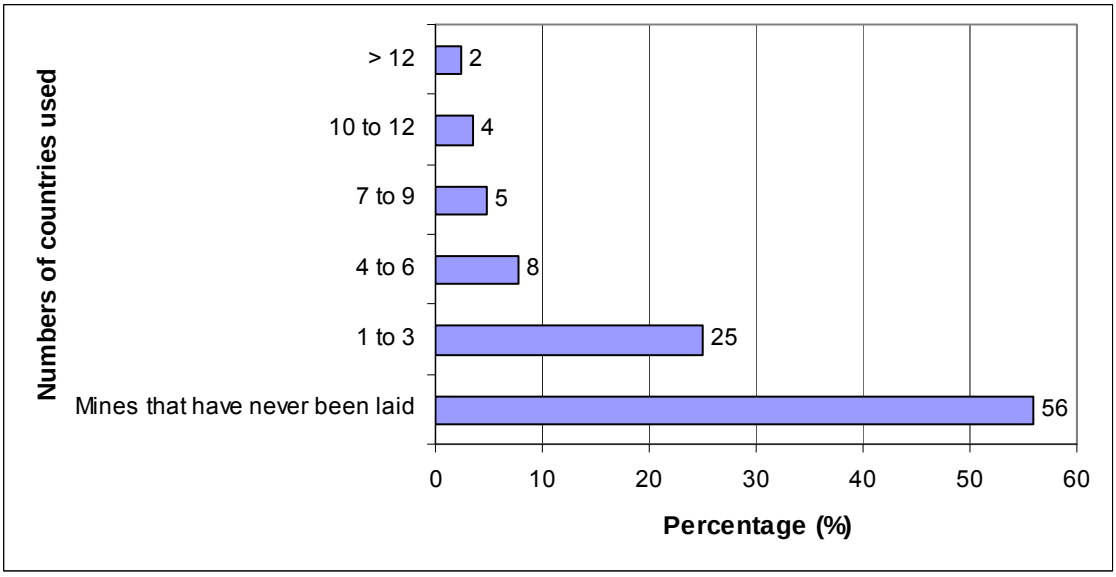

Figure 2.5 Percentage of active mines in countries (2)

2.4.3 Classification based on modes of initiation (Fuze)

First generation mines (historical threat) covers mines that are initiated by a pressure-activated or tilt rod fuze for full width attack, such as TMRP-6 and TM-62M. It normally operates when a tank rolls over the mine and hence pushes down on the pressure plate, and subsequently causes explosion in the main charge. Second generation mines (current technology threat) such as the Russian TM-72 with MVN-72 fuze, Indian Adrushy, etc, use

a magnetic influence fuze to increase lethality in a full-width attack. Some use more advanced fuzes, such as a standard electronic fuze rather than a mechanical pressure-operated fuze, as was used in the first generation mines. Third generation mines operate on high-technology sensors and fuzes. These are high-technology electronic fuze mines, off-route mines and wide area mines. Examples are the US XM-93 wide area mines and the European venture ARGES off-route mines. The classification in this category can be seen in Figure 2.6.

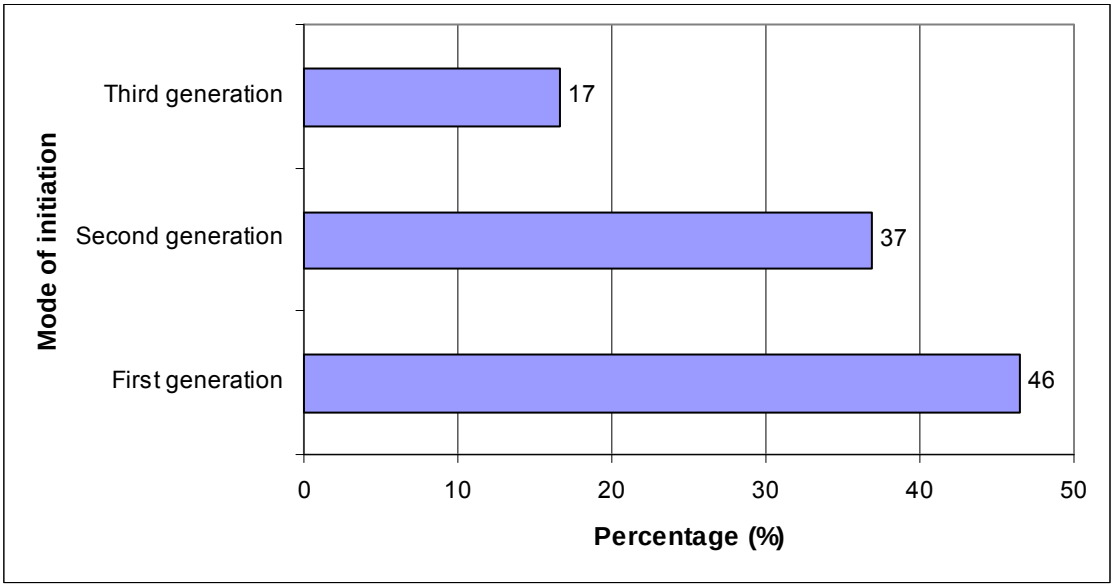

Figure 2.6 Mines indicating their mode of initiation

Figure 2.7 TMK-2 anti-tank shaped charge mine with MVK-2 fuze (tilt-rod fuze), King (2002)

2.4.4 Classification based on modes of deployment

Mines can be deployed as well-defined (planned pattern), remotely delivered, off-route, and wide area. Well-defined mines can be laid according to a definite plan of deployment either by hand, minelayers, or by means of a mine dispensing system using mechanical ejection such as remote anti-armour mine, or by means of propellant charges with the mine dispenser. Scatterable mines are short-range munitions which may be laid manually by hand and/or using remotely delivered means. Remotely delivered mines are usually longer-range weapons whose target area may be completely out of sight of the person dispensing them. They may be deployed by rocket launching such as a 155 mm rocket launched projectile, by using aircraft dispensers, or stand-off-missile dispensers. Examples are AT I, AT II, and M-718.

Off-route mines were originally based upon anti-tank rockets fired in the side attack mode. They can all defeat light armour and are normally used in ambush. However, they are more complex, more expensive and tend to achieve less consistent results; although using high-tech sensors can improve their accuracy. In general, two types of technology warheads are used to improve their lethality: High Explosive Anti Tank (HEAT) using Munroe shape charge principle and Misznay Schardin (MS) using a plate or dish to produce a self-forging fragment. Examples are the German PARM DM-12, and US M-24.

Wide area mines are designed to be an improved counter-mobility weapon. They can attack the enemy over a wide area from a long distance, with accuracy. For example, the US XM-93, which has just entered the service, can be used to attack within 100m radius. Most mines are currently still under development. Figure 2.8 indicates their breakdown in terms of percentage.

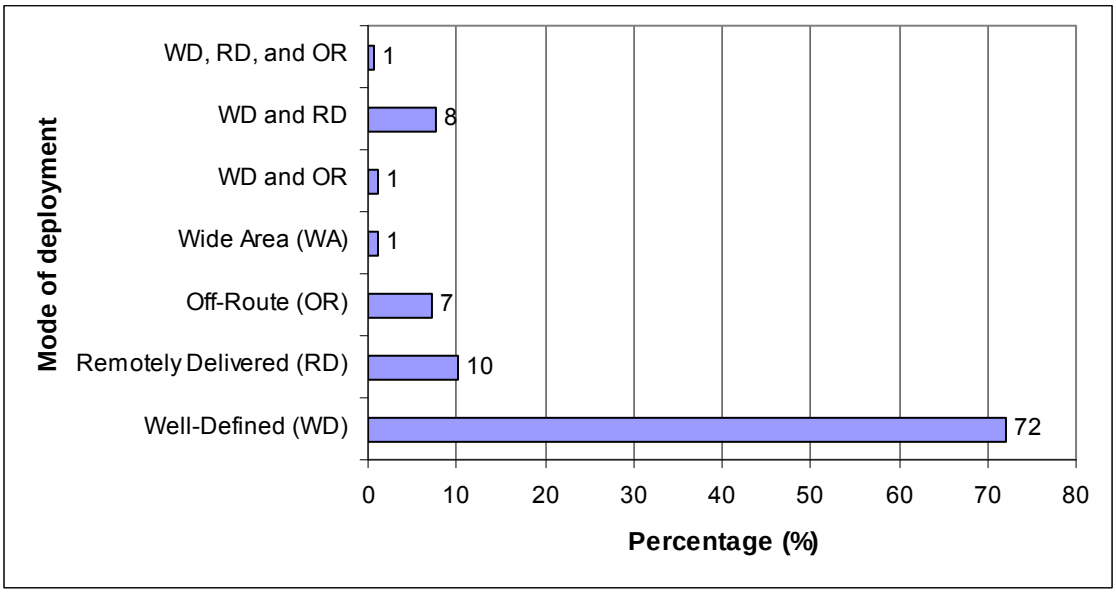

Figure 2.8 Mines and their modes of deployment

Figure 2.9 The ARGES/MACPED off-route mine, King (2002)

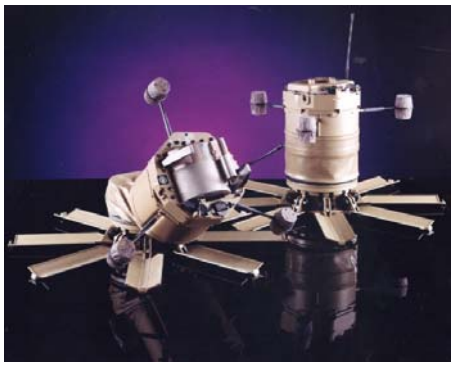

Figure 2.10 The US XM-93 wide area mines, King (2002)

2.4.5 Classification based on modes of attack

Modes of attack are divided into 5 types, track attack, belly attack, full width attack, side attack, and top attack which can be clearly seen in Figure 2.11. Track attack mines (see W) are normally pressure activated. They will explode when the vehicle track passes over it. Belly attack mines (see X) may use standard tilt–rod fuzes to detonate under the vehicle's belly. Although some use pressure operated fuzes, they are classified as belly attack because of their large charge weight which can also damage the vehicle's belly. Off-route mines are usually classified as side attack mode (see V). However, some may be able to achieve full-width attack or top attack and hence are grouped as full-width attack and top attack mode respectively. Full-width attack mines (see Y) incorporate 2nd generation fuzes to delay their detonation and are able to differentiate between main battle tanks and armour personnel carriers. Some use tilt-rod fuzes to achieve full-width attack capability. Fragmentation mines are considered to be in this mode because of their characteristics. Very few mines, such as Russian TEMP 30, are able to attack from the top (see Z). Figure 2.12 represents the percentage of different modes of attack on this classification.

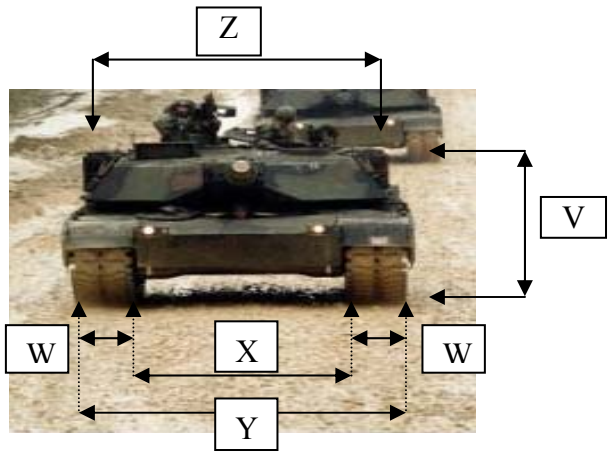

Figure 2.11 Mode of attack on a tank.

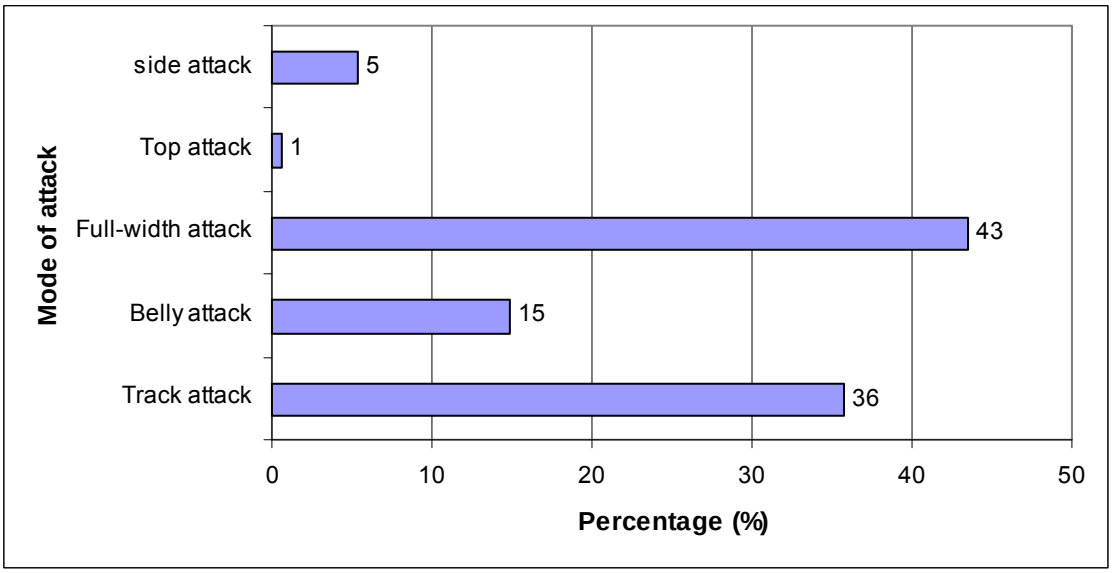

Figure 2.12 Mines and their mode of attack

2.4.6 Classification based on their main destruction effects

Mines may be classified based on their main destruction effects as blast mine, shape charge mine, and fragmentation mine. Blast mines rely on their high pressure effects to cause damage to vehicles and occupants, while shape charge mines use a warhead in which the explosive is specially shaped to achieve a directional penetration onto the armour. Shape charge mines may include High Explosive Anti-Tank (HEAT) or Misznay Schardin (MS) warhead. Fragmentation mines, as its name suggested, can create lots of fragments to destroy targets in a wide area. Figure 2.13 breaks down mines into different types in this category.

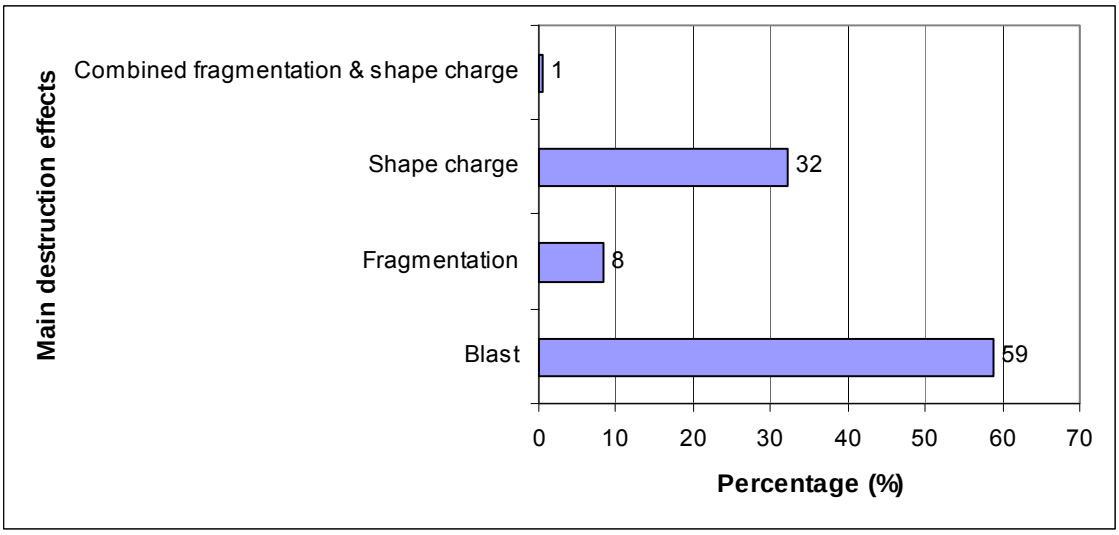

Figure 2.13 Mines and their main destruction effects

2.4.7 Classification based on the amount of charge

Different mines usually contain a different amount of explosive. Their charge may also be different. Some may use TNT (Trinitrotoluene) or RDX (Cyclonite), or Composite B. Some specific mines may even have a choice of charges. Figure 2.14 classifies mines into groups of different amounts of TNT charge or the equivalent charge each mine possesses. Where their charge is not TNT, this has been converted to TNT equivalent, based on mass specific energy taken from Baker *et al* (1983) as shown in Table 2.1 or based on explosive strength (magnitude of its explosion relative to that from the same quantity of reference TNT) taken from Kinney & Graham (1985) as shown in Table 2.2. Some of them cannot be converted because the lack of information on TNT equivalent on their charges, so similar explosive charge types were used to calculate TNT equivalent. In addition, information on some of them may also not be available and hence a TNT equivalent value cannot be given. In cases where either TNT or other charges may be used in the mine, TNT equivalent will be based on TNT charge.

This research has found out the average charge weight to be 6.13 kg TNT, taking into account all 168 mines and excluding the ones where the information is unavailable. In addition, considering only blast mines, the average charge weight is 6.66 kg TNT, while for

shape charge mines only, the average charge weight is 3.75 kg TNT. There are only 12 mines or 7% of all available mines where their charges weigh more than 10 kg.

Explosive charge	TNT conversion factor (specific energy)
TNT (Trinitrotoluene)	1.000
Composition B (60% RDX, 40 % TNT)	1.148
Pentolite (50% PETN, 50% TNT)	1.129
PETN	1.282
Picric acid	0.926
RDX (Cyclonite)	1.185
Tetryl	1.000
Torpex (42% RDX/40% TNT/18% Al)	1.667

Table 2.1 TNT conversion factor based on mass specific energy from Baker et al (1983)

Charge type	TNT conversion factor (explosive strength)
Composite H-6 (45% RDX / 30% Al / 21% wax)	1.28

Table 2.2 TNT conversion factor based on explosive strength from Kinney & Graham (1985)

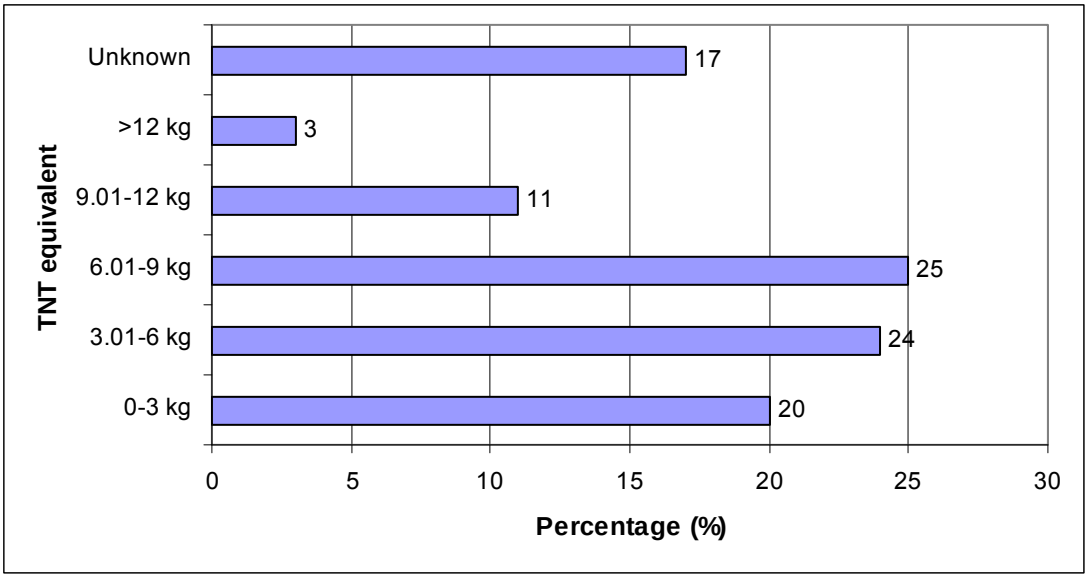

Figure 2.14 Mines and their TNT equivalent (kg)

2.5 Effects of mine blasts on vehicle structures and their occupants

Figure 2.13 indicates that 59% of mines are blast mines, therefore only the effects of mine blasts will be explained here. Impact of mine blasts on a target such as a vehicle generates stress waves in its hull with a peak acceleration in the floor plates as high as 2,400,000 m/s^2. It can also cause considerable dynamic deformation of the hull floor plate, which can bow inwards up to 150 mm or more, at high velocity and then spring back, Ogorkiewicz (2003). Overpressure associated with the blast could cause serious damage to vehicles and injury to vehicle occupants. The vehicle movement could cause injuries if the occupants are not restrained. Moreover, the loss of vehicle control with reasonable forward momentum is highly likely to cause a rollover accident. Soil ejecta, generated by buried mines, augments the impact of blast wave and blast wind. Fragmented material and any loose parts can also be propelled by mine blasts. For example, when landmines are detonated under tyres, lethal fragments from steel-belted tyres could occur.

Occupants within a vehicle subjected to mine blast may be killed or injured depending upon the type and amount of explosive charge, internal and external vehicle protection, individual health condition, or the occupant's position during the blast. The most important effect which may cause death or injury to the occupants comes from the crew compartment floor transferring its high deformation and acceleration through the occupants' feet and body. If the vehicle hull is breached, the blast pressure may affect the occupants. Smith and Hetherington (1994) have classified three blast-induced injury categories: primary, secondary, and tertiary. Based on Smith and Hetherington (1994), Primary injury is directly due to the blast wave overpressure and duration, which can be combined to form specific impulse. Overpressures are induced in the body following the arrival of the blast and the level of injury sustained depends on a person's size, sex and (possibly) age. The likely damage areas are lungs (which are prone to haemorrhage and oedema), the ears (especially the middle ear, which can rupture), the larynx, trachea, and the abdominal cavity. Pressure-impulse diagrams can be used to evaluate the possibility of injury levels. Secondary injury is due to the impact of fragments or other debris picked up and carried by the blast wave. The iso-casualty curves may be used to assess the probability level of damage from different debris weights impacting at different velocities. Tertiary injury occurs when the

body suffers high decelerations, particularly on landing. Example of the worse scenario is when the head impacts against a hard floor or the wall surface in the vehicle. The level of injury can be correlated with the velocity of impact. Pressure-impulse graphs may be used to assess the level of likely injury.

2.6 Prevention and/or reduction the effects from mine blasts

Obviously, the best possible solution is to avoid contact with blast explosion by staying away from the high-risk areas. However, in reality this is not really possible. Smith and Hetherington (1994), Bird (2001) and Ogorkiewicz (2003), have described methods to reduce blast mine effects which are as follows: To avoid the transmitted high acceleration from the crew compartment floor, the crew should not stand directly on the hull floor, their seats should be attached to the hull sides or, preferably, to the hull roof, and low impedance cushioning material should be incorporated to their seats. Further reduction can be achieved by using double, separate floor plates (but this will reduce ground clearance or space within the hull and also will increase the vehicle weight considerably). To avoid primary injury to occupants, there must be no air path and therefore no openings in the hull bottom and no cracks in welded joints or floor plates. The floor plates should be softer with more ductile armour than the front and side hull plates to lower the risk of floor plates cracking. The use of thicker floor plates could reduce blast damage but will increase the overall weight. Blast waves can be deflected or floor plates can be stiffened by being V-shaped, or convex. Secondary injury may be reduced by not having loose equipment, which might hit the crew. Using deflector plates installed under the wheels or the installation of armour plate to interior floors may also reduce the risk of secondary injury. Tertiary injury may be minimised by using low drag coefficient hulls, for example, using V-bottoms. Occupants should wear seat belts and crash helmets. If possible, there should be restraints on side head movement. Speed reduction when entering the mine affected area may reduce the injuries associated with vehicle rollover. Vehicle shock acceleration and deformation, which could cause substantial lower leg injuries to occupants, may be reduced by using false floors (an internal floor with an air cavity of ~100mm), energy absorbing systems.

Apart from specially designed armoured-blast-protected vehicles, for example, as in Figure 2.15 and Figure 2.16, occupants would likely to be killed if AT mines were encountered. For example, in Bird (2001), Land Rovers Series III and 110 models have been tested against an explosive charge weighing 1 kg to 4 kg plastic explosive (PE4). The results have shown that, following blast effects, fragments may penetrate the aluminium floor and kill occupants. Land Rovers with steel deflector plates or armoured protection can stop these fragments but cannot avoid the lethal translation shock loading from a landmine charge of more than 3 kg.

Figure 2.15 Mamba armoured personnel carrier, King (2002)

Figure 2.16 Cougar Mine resistant vehicle, King (2002)

Note that there is a standard protection levels for logistic and light armoured vehicle occupants from NATO (North Atlantic Treaty Organization), called STANAG 4569 (NATO STANDARDISATION AGREEMENT 4569). It states 4 standard levels of floor protection to the occupants against grenade and blast mine threats. For example, level 4b means there is 90% probability of providing protection to the occupants against 10 kg

(explosive mass) blast AT mine under the centre, while level 4a is the same except AT mine explodes under any wheel or track location. More details are in North Atlantic Organization (2004), while the procedures for evaluating the protection level of logistic and light armoured vehicles (mine threats) is in AEP-55 Volume 2, North Atlantic Organization (2006).

2.7 Discussion

Figure 2.3 indicates that the majority of AT mines (at least 70%) can cause damage to heavy armoured vehicles. The average charge weight based on all mines available in this research is 6.13 kg TNT, with the average charge for blast mines and shape charge mines only, are 6.66 and 3.75 kg TNT respectively. Moreover Figure 2.14 shows that there are only 20% of all mines that weigh below 3 kg. Most of them are shape charge mines which have a different kill mechanism than blast mines and can penetrate targets using a little amount of charge. By taking into account the results from Bird (2001) which has been mentioned in section 2.6 that soft-skin vehicle like Land Rover 110 with steel-deflector plates, are more likely to be fatal to occupants when encountering blast mines having charges more than 3 kg, it is therefore concluded that there is indeed a high chance that an AT mine will kill occupants within the soft-skin vehicle.

Figure 2.4 demonstrates that the majority of mines (56%) have not been used before. 89% of mines have never been laid or have been laid in 5 countries or below. Figure 2.5 shows that only 6% of mines were used in 10 countries or more. This illustrates that AT mines are comparatively low in threat, considering that a large number of them have rarely been used. However, it does not mean that there are fewer chances to encounter mines, because most countries still stock them and they are available for their use.

AT mines are mainly first generation mines which can be seen in Figure 2.6. The first generation mines account for 46% of all mines, while second and third generation account for 37% and 17% respectively. The proportion of first generation mines has been decreasing because technological advances in mines have more and more influenced on their design and manufacture. Commanders and military vehicle designers must take this

threat into account and realise that second and third generation mines are increasing in number.

Figure 2.8 indicates that mines are usually deployed in a definite pattern, either by hand or by mechanical means. This may help in de-mining operations. By classifying mines, it can be seen that modern technology in mines is moving into remotely delivered and wide area deployment, so that maximum damage of a large area and surprise against the enemy can be achieved.

Full-width attack (43%), as shown in Figure 2.12, is the main mode of attack in mines. Old traditional mines, which attack mainly at the vehicle's tracks, are ranked second, at 36%. It shows that the majority of mines are capable of attacking all areas under the vehicle, which is very dangerous.

Ogorkiewicz (2003) has estimated that around 80% of the mines likely to be encountered are blast mines. Figure 2.13 confirms that blast mines still remain the most important threat to armoured vehicles, which have accounted for 59% of all mines. However, the number of shape charged mines is increasing because of their effectiveness in penetrating armoured vehicles; while fragmentation mines are more dangerous to soft-skin and light armoured vehicles.

As mentioned in section 2.4.7, there are only 7% of all mines which weigh more than 10 kg TNT. These minority mines are heavy and difficult to transport and deploy. Hence 10 kg may represent one of the worst case scenarios that a vehicle may encounter a single mine. The results in section 2.4.7 indicates that the overall average charge weight is 6.13 kg TNT, the blast mines' average charge weight is 6.66 kg TNT and the shape charge mines' average charge weight is 3.75 kg TNT. The charge weights of interest are 6.13 kg TNT and 6.66 kg TNT. However, it is virtually impossible that a mine with a charge of 6.13 kg TNT or 6.66 kg TNT will attack a vehicle because each mine has its own pre-designed charge weight which is not the same as the average weight. Furthermore, the results in section 2.4.2 indicate that TM-46 and TM-57, having their charge weight of 5.7 kg TNT and 6.34 kg TNT correspondingly, have been used by 23 countries. The charge weight of 6.34 kg

TNT may represent one of the likely threat scenarios that may attack a vehicle. Therefore in order to perform numerical simulations on realistic scenarios later in this research, it is proposed that the charge weights that should be used are 10 kg TNT and 6.34 kg TNT as extreme and most likely cases respectively.

2.8 Conclusions

Extensive research on AT mines has been undertaken in this chapter, with the emphasis on classifications of AT mines. Each individual mine has been put into a different category where the type and the criteria on each type was formulated by the author based on different literatures. The number of mines in each group within each classification was converted into a percentage and compared with the others. This has given an indication on the types of mines which vehicles are likely to encounter. It shows that a first generation blast mine, having full width attack capability with a definite deployment pattern and a charge weight up to 10 kg TNT is a typical AT mine that a vehicle is likely to come across at present. Advanced technologies in mines, such as using sophisticated sensors and a remote delivery with low metal content, are making AT mines even more dangerous, versatile and cost-effective. Consequently this guarantees that AT mines remain one of the most dangerous weapons. Not only can they cause damage to the vehicles and injury or death to the occupants, but they can also cause significant impact on the medical, psychological, economical, environmental and political aspects.

CHAPTER 3 Literature reviews and theory

This chapter describes relevant information to this thesis. Literature reviews related to this thesis are also presented.

1D, 2D, and 3D	one, two, and three dimensions
a, b	geometry notations
A, B, C, n	user-defined constants in Johnson and Cook material model
A, B, R_1, R_2, ω	empirically derived constants in the Jones-Wilkins-Lee (JWL) equation of state
c	speed of sound
$C_0, C_1, C_2, C_3, C_4, C_5, C_6$	user-defined constants
c_v	specific heat at constant volume
D	damage
e	specific internal energy
E	internal energy per volume
E_p	plastic strain hardening modulus
E_y	Young's modulus
f_i	external body force per unit mass
H	a variable function
I_a	second moment of area
i_s	specific impulse of the positive phase duration
J_2	second stress invariant
K_f	stiffness of the structure
K_{LM}	load mass factor
l	the smallest cell dimension
M_s	mass of the structure
N	safety factor
p	pressure
p_{shift}	pressure shift

P_0	initial pressure
P_a	atmospheric pressure
P_{min}	maximum negative pressure
P_s	peak overpressure
q	viscous term
s_{ij}	deviatoric stress
t	time
t_a	arrival time
t_d	positive phase duration
T^*	homologous temperature
T	temperature
T_{melt}	melting temperature
T_n	natural period of the system
T_{room}	room temperature
V	relative volume
v_i	velocity
σ_{ij}	stress tensor
σ_y	yield stress
ε_{ij}	strain tensor
ε_p	effective plastic strain
$\dot{\varepsilon}_{ij}$	strain rate tensor
$\dot{\varepsilon}^*$	normalised plastic strain rate
γ	adiabatic constant
μ	a parameter in the linear polynomial equation of state
ρ	material density

Table 3.1 symbols

3.1 General blast theory

3.1.1 General

Based on literature in Elliott, Mays, and Smith (1992), and Smith and Hetherington (1994), there are generally two main categories of explosives; low and high. Low explosives are those in which an explosion propagates away from its initiation site thermally (surrounding material is heated sufficiently to cause it to explode). High explosives are those in which the energy is transferred from the exploded to the unexploded material through shock pressure; this effect is much more rapid than the thermal propagation. High explosives are used in anti-tank or anti-personnel mines because of their lethal effects at low charge weight. It is estimated by Ngo *et al* (2007) that the detonation of a condensed high explosive generates hot gases under pressure up to 3 x 10^5 N/m^2 and a temperature of about 3000-4000° C.

In a free-air blast, once high explosive material is detonated, it releases a highly pressurised volume of very hot gases, which expands violently. The air, the medium surrounding the charge, is forced out of the volume that it occupies and becomes highly compressed. The air then forms a blast wave which is shown in Figure 3.1. It consists of an instantaneous rise in pressure followed by decay over a period, called positive phase duration, t_d. As the energy of the expanding gases dissipates, their momentum falls. The blast wave is in rarefaction which can be seen as the negative phase where the pressure is below atmospheric pressure, P_a. The maximum negative pressure is P_{min}, and the peak overpressure is P_s.

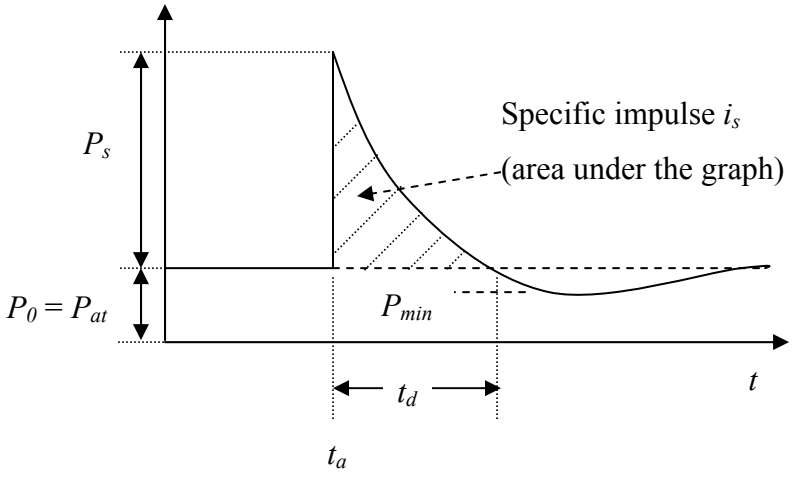

Figure 3.1 A pressure-time curve of idealised blast wave, redrawn from Smith and Hetherington (1994)

3.1.2 Explosion under soil

Normally, mines are placed under soil. Fiserova (2006) has explained that the soil structure is complex. It comprises of a skeleton of solid particles and interconnected spaces (void), which are filled by water and gases (usually air). There are two forces in the contact areas between the particles. The surface force, which arises from electro-chemical activity, make the soil cohesive, while the gravitational (frictional) force, which exists from the mass of the particles, makes the soil less cohesive. Soil theory is fully described in various literatures such as Fiserova (2006), and will not be discussed in this thesis, unless it is relevant. If one considers a bare charge, upon initiation, the detonation wave propagates through the explosive material, and high pressures and temperatures are generated in the detonation products. These products expand violently, force the soil and air out of the occupied volume and create a pressure wave propagating in all directions from the charge. As soil is forced out forming ejecta, the detonation products break through the surface. Soil gains kinetic energy and moves upwards. After impinging on the target or reaching the maximum height, soil falls back and forms the apparent crater surface.

US Department of the Army, (1985), described a crater as a hole in the ground formed by an explosion, as shown in Figure 3.2. A crater is normally referred to as the 'apparent

crater', which is the visible hole left after the explosion. The true crater is the hole which has been excavated by the explosion, but normally masked by the dirt or debris that falls back into the true crater. The true crater radius will generally be about 10% to 15% greater than the apparent crater radius for all depth of burst (DOB) which are less than 'optimum' in soil. 'Optimum' DOB is the depth where the crater volume is at maximum. At higher DOB, the weight of the soil above tends to suppress the crater formation. On the surface, the rupture (a region immediately surrounding the true crater in which the earth material remains in place, but has been severely disturbed by the force of the explosion) and plastic zones (a larger region of lesser disturbance) form a region of surface displacement, or upthrust. This is normally covered by ejecta, i.e., earth material thrown out of the crater by the explosion. The greater the crater is, the more the ejecta is, which if at a sufficient weight, size, and height, may cause damage to structures and personnel. This is different to the blast loading produced by a charge exploding in the air or on a rigid surface, where there are no ejecta. Craters formed in sandy soils are smaller than in clay, while wet soils will usually produce a larger crater than dry soils. US Department of the Army, (1985) also mentioned that water contents in soil can have a profound influence on ground shock propagation in cohesive soil, particularly if the degree of soil saturation is 95% or greater. Hlady (2004) stated that the moisture content, which creates cohesion in soil, contributes to the formation of clumps in the ejecta. Hence the higher moisture content in soil, the larger clumps, which carry significant energy and transfer to the target. Hlady (2004) also stated that there is an optimum overburden (or DOB), where if there is little or no overburden, the ejecta, and thus the energy transfer to the target, is decreased, while for large overburden, the soil is able to absorb a large amount of the explosive energy, and thus the amount of ejecta is reduced (in an extreme case, an explosive buried deep underground does not produce any ejecta at all).

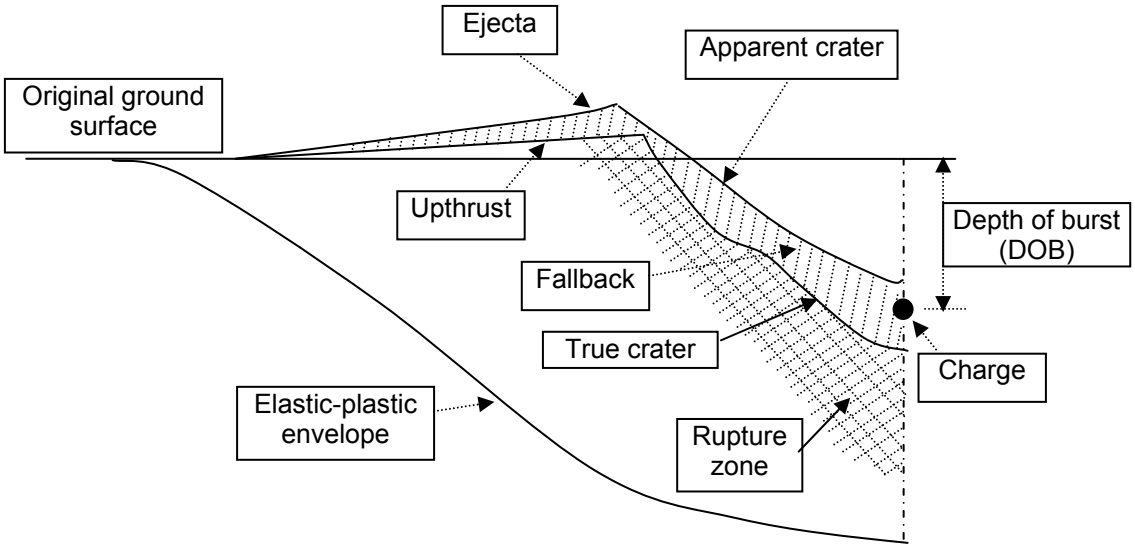

Figure 3.2 Half-crater profile, reproduced from US Department of the Army, (1985).

3.1.3 Structure response to blast loading

Elliott, May, and Smith (1992) described two ways, external and internal loading, in which the blast wave interacts with the structure. This depends upon whether the blast wave is originated inside or outside the target structure.

When a blast wave initiates outside the structure, it propagates to the surface of a structure, the pressurised fast-moving air is first brought to rest and is then reflected, applying a pressure on the surface. US Department of the Army (1985) states that, as the blast wave impinges on a rigid surface (structure) oriented at an angle to the direction of wave propagation, a reflected pressure is instantly developed on the structure, and the pressure is raised to the value more than the incident pressure. The high reflected pressure then propagates to the low pressure region to relieve the high pressure. The reflected pressure varies from a maximum, where the structure is perpendicular (0° angle of incidence), to a minimum pressure where the structure is parallel (90° angle of incidence), to the direction of wave propagation. This minimum pressure will be the same as the incident pressure. The variation of the pressure and impulse patterns on a reflecting surface is a function of the angle of incidence and the magnitude of the incident pressure. For example, the plot between reflection coefficient can be seen in page 49 in Smith and Hetherington (1994) or

in US Department of the Army (1991). It indicates that the reflection coefficient (reflected pressure divided by the incidence pressure) at 10° angle of incidence is less than the reflection coefficient at 0° angle of incidence. This means that the reflected pressure at 10° angle of incidence is always less than the one at 0° angle of incidence. Smith and Hetherington (1994) also noted that at a very close range, the experimental measurements of reflection coefficient up to 20 have been observed.

Apart from reflection, a blast wave of sufficient size could also diffract around a structure, and hence create compressive pressure on all exposed surfaces. The structure would also be subject to drag forces produced by the dynamic pressure component (the pressure generated by the high velocity propagation of the air and explosive particles) of the blast wave which also depend on its size and shape. Small targets, such as vehicle and people, would react more to the drag loading component than large structures.

When a charge is detonated within a structure, the loading is much more complex. Firstly, the structure will encounter a series of reflected shockwaves (supersonic blast wave) from the confinement of the initial pulse. Secondly, there will also be loading from the built-up pressure from detonation products. This loading varies upon the shape of the structure which allows venting of detonation products.

As a structure, such as a plate, interacts with the blast load (external loads), it will be deformed and internal forces, which resist the structure deformation, will be set up in its members. If the external loads are increased, the deformation will also be increased. US Department of the Army (1985) states that the maximum deflection and stress in its members will be affected by plate geometry and the type of support provided at the plate edges. The large deflection of a simple flat plate can be reduced by the use of supported beams or stiffeners. In most plate structures, the boundary conditions are neither simply supported nor fixed supported. Fixed boundary conditions should only be used in the analysis, as a conservative assumption, if there is no evidence that the structure is really simply supported. It is estimated by Ogorkiewicz (2003) that the impact of mine blast on a target such as a vehicle can cause considerable dynamic deformation of the hull floor, which can bow inwards up to 150 mm or more at high velocity and then spring back, with a

peak acceleration in the floor plates as high as 2,400,000 m/s^2. Ngo *et al* (2007) estimated that blast loading typically produces very high strain rates in the range of $10^2 – 10^4$ s^{-1} rather than the ordinary static strain rates of $10^{-6} – 10^{-5}$ s^{-1}. At this strain rate, the dynamic mechanical properties of the structure may be different from the mechanical properties under static loading. It is reported that the yield strength of a mild steel could be doubled when the strain rate was changed from $10^{-3} – 2 \times 10^3$ s^{-1}. Therefore, when modelling the structure blast loading, a suitable material model, which accounts for high strain rate variations, should be used.

Smith and Hetherington (1994) described 3 cases which relate the blast loading and the structure response. Figure 3.3 displays these 3 cases graphically, where R (t) is a structure resistance with time and F(t) is a blast load with time. The first case is called a quasi-static (pressure) loading, where the blast load duration is much larger than the natural period of vibration of the structure, for example, a blast wave from a nuclear device at medium to long range propagates to the structure. The maximum displacement in this case is solely a function of the peak blast load and the stiffness, and does not involve either the positive phase duration or the mass of the structure. The second case is referred to as an impulsive loading where the positive phase duration of the blast is much shorter than the natural response period of the target. In this case, the blast load rises to its maximum and drops to its minimum before the structure has had time to respond significantly. The final case is a dynamic loading where the blast loading duration and the structure response time is similar.

The principal approach to solve the response of the structure was described in Mays and Smith (1995) by equating the work done on the structure (quasi-static loading) or the total kinetic energy (impulsive loading) to the strain energy acquired by the structure as it deforms. This analysis can be time-consuming if the structure and load configuration is complex. Another approach is to assess the response of the structure by assuming that the structure behaves as a single degree of freedom (SDOF) system, where the equation of motion is solved analytically or numerically to obtain a deformation-time history for the structure. Smith and Hetherington (1994) and in particular, US Department of the Army, (1991), presented this approach in more detail. However, this approach is based on numerous assumptions and if the structure and load configuration is complex, the

discrepancies compared with the experiments may be large. The fast development in computer hardware and software technology has now made numerical simulation method an attractive alternative because the designer can obtain various results from complex problems in reasonable time and accuracy.

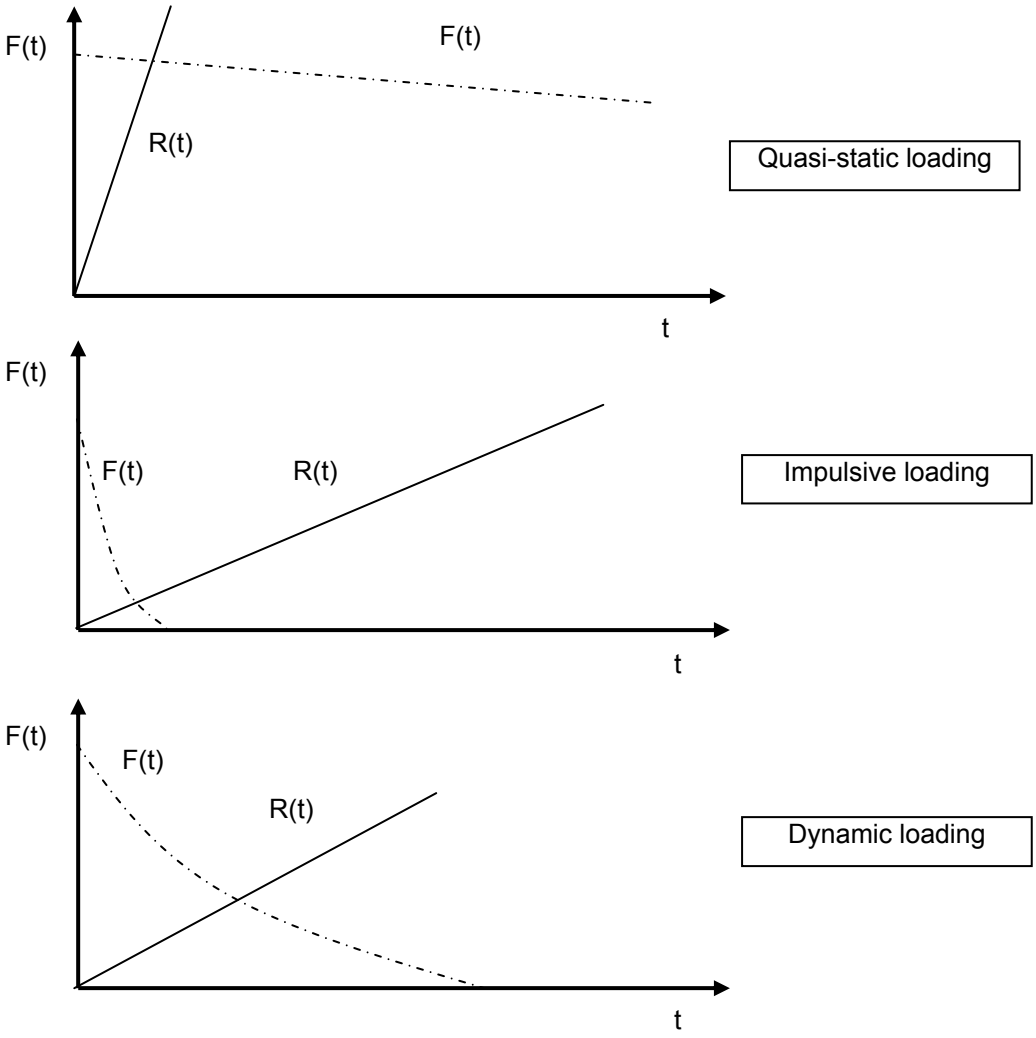

Figure 3.3 Types of blast loading and structure response.

3.1.4 TNT equivalent

The use of TNT as the reference explosive is universal. In LS-DYNA, the keyword *LOAD_BLAST will need an input of the amount of TNT explosive charge. If the charge

used is not TNT then a method to convert this charge to TNT equivalent mass is applied. Smith and Hetherington (1994) described two methods. One is to use Baker *et al* (1983) method by using conversion factors for different explosives based on their specific energy and that of TNT. For example, Pentolite has its TNT equivalent of 1.282. The other method is to use the two conversion factors from US Department of the Army, (1985), where the choice depends on whether the peak overpressure or the impulse delivered is to be matched for the actual explosive and the TNT equivalent. For example, at pressure range of 5-600 PSI (0.0344 – 4.1368 MPa) Pentolite has TNT equivalent weight pressure factor of 1.38 and TNT equivalent weight impulse of 1.14.

US Department of the Army, (1985), states that for the load to be impulsive,

$$\frac{t_d}{T_n} \leq 0.1 \qquad \textbf{(3.1)}$$

Where T_n is the natural period of the system and t_d is the positive phase duration

The period of any structural system may be calculated using:

$$T_n = 2\pi \sqrt{\frac{K_{LM}.M_S}{K_f}} \qquad \textbf{(3.2)}$$

Where K_{LM} is the load mass factor, M_s is the mass of the structure, and K_f is the stiffness of the structure

Depending on the structure's configuration, these parameters (K_{LM}, M_s, and K_f) can be found from table 10-1, 10-2, and 10-3 in the US Department of the Army, (1985).

For example, a mild steel plate (1.0 x 1.0 x 0.005 m, so $a/b = 1$) with fully fixed boundary condition, subjected to an explosive (Pentolite weighing 0.250 kg) blast centrally above the plate at 0.25 m stand off in the air, has $K_{LM} = 0.63$ and $K_f = 810E_yI_a/a^2$.

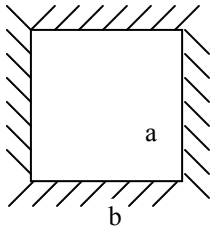

Figure 3.4 Plate geometry

M_s (mass of the plate) = 7850 x 0.005 = 39.25 kg

I_a = 1 x $(0.005)^3$ /12 = 1.0417 x 10-8 m^4

$K_f = 810EI_a/a^2 = (810)(203 \times 10^9)(1.0417 \times 10^{-8})/(1)^2 = 1.713 \times 106$

Therefore $T_n = 2\pi\sqrt{\frac{(0.63)(39.25)}{1.713x10^6}} = 0.02387 \sec ond / cycle$

t_d can be found, by using Hyde (1991) = 0.142 x 10^{-3} seconds

So t_d/T_n = (0.142 x 10^{-3})/(23.87 x 10^{-3}) = 0.006 which is less than 0.1

Therefore, the load acting on the steel plate structure is impulsive in nature and hence a TNT equivalent weight impulse factor of 1.14 from the US Department of the Army (1985) will be used to convert Pentolite to TNT in this case.

It should be noted that each explosive contains unique chemical compositions, and hence produces unique blast wave. Muzychuk (2005) mentioned that oxygen rich explosives such as nitroglycerin or PETN are considered as 'point energy source', which is different from highly oxygen deficient explosives such as TNT or HNS. Following the initial detonation in the latter, its products continue to react with atmospheric oxygen because of the lack of oxygen in its chemical structure. This increases the release of chemical energy, the gas pressure, impulse and the duration of the blast. Therefore relating different explosives to TNT may not be 100% matched because of the variation in blast wave parameters. The measurement of the energy released from the explosive is also very difficult to measure because of its highly violent energy release. It is often conducted in the laboratory, rather than in the field because of its convenience. Kinney and Graham (1985) gave examples of

these tests such as Trauzl block test, ballistic mortar test, etc, and commented that these testing methods are strictly empirical and may give different results.

3.2 Numerical simulations

In a complex problem, such as a mine blast underneath the vehicle, analytical solution is extremely difficult to obtain without numerous assumptions. For such complex problem, numerical methods, such as LS-DYNA from Hallquist (1998), and AUTODYN from Century Dynamics, Inc. (2003), are the suitable alternative choice.

Colins (2002) describes that numerical simulations are generally based on the Newtonian laws of motion, the equation of state, and the constitutive model. Incompressible inviscid fluid flow may be described by the Newtonian laws of motion in the form of the conservation of mass, momentum and energy equations, which can be mathematically expressed as;
Conservation of mass:

$$\frac{d\rho}{dt} + \rho \frac{\partial v_i}{\partial x_i} = 0 \qquad \textbf{(3.3)}$$

Conservation of momentum:

$$\frac{dv_i}{dt} = f_i + \frac{1}{\rho} \frac{\partial \sigma_{ij}}{\partial x_i} \qquad \textbf{(3.4)}$$

Conservation of Energy:

$$\frac{de}{dt} = -\frac{p}{\rho} \frac{\partial v_i}{\partial x_i} + \frac{1}{\rho} s_{ij} \dot{\varepsilon}_{ij} \qquad \textbf{(3.5)}$$

Where ρ is the material density, v_i is the velocity, e is the specific internal energy, σ_{ij} is the stress tensor, which is composed of a hydrostatic part, the pressure p , and a deviatoric

part s_{ij}. f_i is the external body force per unit mass, and $\dot{\varepsilon}_{ij}$ is the deviatoric strain rate. The subscript is the standard tensor notation.

The equation of state expresses the relationship between pressure, density, and specific internal energy. It accounts for the effects of compressibility in fluid.

Equation of state:

$$p = p(\rho, e) \tag{3.6}$$

The constitutive model, which accounts for the material strength, relates the stress to deformation in terms of strain ε_{ij} and strain rate effects $\dot{\varepsilon}_{ij}$, internal energy *e*, and damage *D*.

Constitutive model:

$$\sigma_{ij} = g(\varepsilon_{ij}, \dot{\varepsilon}_{ij}, e, D) \tag{3.7}$$

Additional equations might be used to further describe the variables and to facilitate equation solving. For example, the stress tensor equation, which expands stress into the hydrostatic and deviatoric components, together with the viscous term *q*, used to treat shock. Initial and boundary conditions also contribute to the equation solving process by defining the variables.

Stress tensor:

$$\sigma_{ij} = -(p + q) + s_{ij} \tag{3.8}$$

The numerical method is a suitable approach to solve these equations, especially in a complex problem where there are so many variables. There are many equations of state and constitutive models, which describe different materials. The most appropriate choice should be made so that the material can be sufficiently represented in the numerical simulation.

Numerical simulations break the problem of interest into finite smaller problems, a process called discretisation. The problem is discretised in time (temporal) and space (spatial). Temporal discretisation in numerical simulation usually uses the explicit method, which calculates function values at the new time step from known function values at the previous time step. The time step should satisfy the Courant-Friedrich-Levy (CFL) condition that it should be less than the time taken for sound to cross the smallest cell. This enables the simulation to capture the necessary activity within all the cells. Normally, a safety factor needs to be included, which might be different for each computer software. The general condition can be seen below:

$$0 < \Delta t \leq N.\frac{l}{c} \qquad \textbf{(3.9)}$$

Where N is the safety factor (default value is 0.9 (LS-DYNA) and 0.66 (AUTODYN)), l is the smallest cell dimension, c is the speed of sound through the material in the cell.

The classic discretisation methods are based on the finite difference or finite element methods. Finite difference represents a geometry with a grid of nodes. The differential equations are replaced by the difference equations. For example, both AUTODYN and LS-DYNA, use the central difference method in temporal discretisation. They may change $\partial H / \partial t$ to $\Delta H / \Delta t$, where H represents a variable function. It can be shown as:

$$\frac{\partial H}{\partial t}\Big|t_n = \frac{H_{n+1} - H_{n-1}}{2(\Delta t)} \qquad \textbf{(3.10)}$$

Finite element analysis represents a geometry into a set of interconnected elements, which is not necessarily in a rectilinear shape. It uses interpolation functions to give the variation of variables (for example, displacement, stress, and strain) over the elements, though constant stress within the element is usually used. Each element consists of nodes, the number and distribution of which varies according to the element formulation. In structural analysis, the stiffness of the element is calculated as the relationship of any forces acting on these nodes to the resulting displacements at the nodes. This results in a large matrix

equation relating the forces and displacements for the whole geometry. Solution of this equation for the applied loads then gives the displacements at all of the nodes. Finally, the strains and stresses anywhere in each element can be found from its nodal displacements.

In this thesis, there are two spatial discretisation schemes, which are used to solve problems: the Lagrangian scheme, which is based on the finite element method and the Eulerian scheme which is based on the finite difference method and/or the finite volume method. The finite volume discretises the problem into a smaller finite volume. The variables are averaged across the volume. In the Lagrangian scheme, the elements (and hence the nodes) move with the material, while in the Eulerian scheme, the nodes are fixed in space but the material is allowed to flow. The Lagrangian scheme is most suitable for modelling solid materials, while Eulerian scheme is most suitable for modelling fluid materials. The main disadvantage of the Lagrangian scheme is the severe element distortion, which may cause very small time steps and grid tangling. The main disadvantage of the Eulerian scheme is the longer computational time and that the materials cannot flow into a non Eulerian element.

In the Lagrangian scheme, at the start of the cycle, the nodal forces, which are the sum of all the internal forces and external forces, such as from the boundary conditions, are integrated to find the new nodal accelerations and, subsequently the new nodal velocities and displacements can be found from further integration. At the new nodal positions, the new densities and strain rates can be calculated from the conservation of mass and direct calculation. From the strains rate, the new pressure, internal energy and stress can be found from the conservation of energy and material model. The internal force at each node can be calculated from the new internal stress of the element using the conservation of momentum. The internal forces and external forces are summed again to calculate the new computational cycle.

In the Eulerian scheme, the calculation follows the Lagrangian scheme but with the added advection step. After the new node position is found, like in the Lagrangian scheme, the deformed element is mapped back onto the original element which is fixed in space. The new mass, momentum, and energy from this advection step are then used to calculate the new element density and strain rates, hence the usual Lagrange calculation can follow.

It is widely known that using shell elements would be a cheaper alternative than using solid elements in the Lagrangian computational scheme because it can use a larger time step in explicit transient dynamic analyses. Shell elements would be efficient when the thickness of the structure is much smaller than the in-plane dimensions because it assumes the nodes to be on the mid-plane. Belytschko-Lin-Tsay shell element, which uses the Mindlin theory of plates and shells to partition the velocity of any point in the shell, was selected to use in LS-DYNA and AUTODYN 3D. This element has a transverse shear stress. More details on this theory are given in the LS-DYNA theory manual, Hallquist (1998), and the AUTODYN theory manual, Century Dynamics, Inc. (2003). Note that, apart from the reason that the thickness of the structure is much smaller than the in-plane dimensions, the other reasons to use Belytschko-Lin-Tsay shell element instead of solid elements are; Firstly, it is likely that the steel structure used in this thesis will response predominantly in bending with significant deformation because of the size and support of the structure. Secondly the location of the explosive charge is not directly in contact or adjacent to the structure. Smith and Hetherington (1994) mentioned that if a detonating explosive is in contact with a structure, it will create a 'brisance' effect, by generating intense stress waves in the material, producing crushing, and shattering disintegration of the material. Thirdly, computational time of shell element is normally less than solid elements. Finally, a comparison between using Belytschko-Lin-Tsay shell elements and 8-nodes solid elements was done in Appendix B, and the results between the two are very similar. Therefore shell elements are chosen to use in this thesis. To model a fluid, 8-noded brick elements with one integration point are used in LS-DYNA, while the default brick elements are used in AUTODYN.

3.3 LS-DYNA

LS-DYNA, Hallquist (1998), is a general purpose finite element code for analysing the large deformation dynamic response of structures including structures coupled to fluids. It is generally based on an explicit time integration method. The FEMB pre-processor by Engineering Technology Associates Inc (2001) was used to develop preliminary models ready to run in LS-DYNA.

In this thesis, some of the numerical models were developed in LS-DYNA software, Hallquist (1998). The modelling of the blast was implemented using blast-modelling software CONWEP, Hyde (1991), which is an empirically based loading model within LS-DYNA. The CONWEP blast model was developed based on Kingery and Bulmash (1984) and US Department of the Army (1985). The blast loading model implemented in LS-DYNA is based on the report by Randers-Pehrson and Bannister (1997). It helps to reduce the process of explicitly simulating the progress of the shock wave from the high explosive through the air and its interaction with the structure. Randers-Pehrson and Bannister (1997) indicated that the model has been tested and is adequate for use in engineering studies of vehicle response to the blast from land mines. The CONWEP code in LS-DYNA can be used in two cases, free air detonation of a spherical charge and surface detonation of an hemispherical charge. Surface detonation is the preferred option in the case of a mine buried at the depth of 5 – 20 cm. However, it should be noted that the depth of burial has a significant effect on the energy released from the explosive, through the soil and onto the target. Other variables determined by the composition of the ground, such as soil moisture content and soil types can also have some effects on the energy released. These below ground effects are not included in the CONWEP blast model. The CONWEP blast model does not take into account any confinement or tunnel effects, the shape of the explosive charge, effect of shadowing objects, and requires explosive contents to be expressed in TNT equivalent mass. The keyword *LOAD_BLAST, which needs an input of TNT explosive charge, is required to utilise the CONWEP blast model.

There are many options to allow fluid-structure interaction in LS-DYNA. The penalty coupling method is used in this thesis, where the Eulerian part is called the master and the Lagrangian part is called the slave. During the interaction, the relative displacement

between fluid and the structure is tracked. The nodal forces, which are proportional to the magnitude of the relative displacements, are applied, forcing the fluid and structure to follow each other. The normal vector of the slave part should point toward the Eulerian part being coupled.

3.4 AUTODYN

AUTODYN, Century Dynamics, Inc. (2003), is a hydrocode program which is especially suited to the solution of interaction problems of different systems of structure, liquid and gas together, as found in blast and ballistics applications. It has integrated pre-processor, post processor and analysis execution code together, which make it easy to use. AUTODYN allows different solvers (or processors), such as Lagrange and Euler to be used together in the same model.

There are 3 Eulerian solvers in AUTODYN: Euler, Euler Godunov, and Euler Flux Corrected Transport (Euler FCT). Euler, which is used in AUTODYN 2D, is based on the first-order approach. It allows multi-materials to be modelled. Euler Godunov, which can also model multi-materials, is a second order scheme and only available in AUTODYN 3D. Euler FCT is a second order single material Eulerian processor used in AUTODYN 2D and 3D.

In AUTODYN, Eulerian and Lagrangian grids may interact with each other. The Euler-Lagrange coupling allows the Lagrangian interface to cut through the Eulerian mesh, which will define a stress profile for the Lagrangian mesh. The Lagrangian interface will also provide the flow boundary to the Eulerian mesh. Lagrange and Lagrange can also interact to each other.

The remap capability in AUTODYN allows the solution of one analysis to map onto another so that the computation costs can be reduced. A remap data-file can only be created in AUTODYN 2D and can be mapped into AUTODYN 2D or 3D. For example, a 1D wedge model in AUTODYN multi-materials (Euler), consisting of air and an explosive charge, can be used to generate a blast load, which can then remapped onto an AUTODYN

2D or AUTODYN 3D single material (Euler FCT). The 1D wedge model is run until the expansion is large enough for the mixture of explosive and air to behave like an ideal gas (say, 10 times from the original volume) in order to avoid the numerical errors due to the density value being too small. This can be seen from Jones-Wilkins-Lee (JWL) equation of state, which will be shown later, that at large expansion, the first and second terms on the right of the equation become negligible and hence it is equivalent to the ideal gas equation of state. The next step is to change the JWL equation of state to the ideal gas equation of state and change the value of adiabatic constant and reference density to 1.35 and $1x10^{-4}\,g/cm^3$. The 1D wedge is run again until the pressure front is very close to the distance of the intended target. This 1D wedge model is then saved as a file ready to be mapped onto another model.

3.5 Material models

Equations of state and strength models were used to describe the materials in the numerical simulations. They are:

3.5.1 Air

For the blast to travel in air in LS-DYNA, Halquist (1998), defines air using a linear polynomial equation of state and is defined as:

$$p = \left[C_0 + C_1\mu + C_2\mu^2 + C_3\mu^3\right] + \left[C_4 + C_5\mu + C_6\mu^2\right]E \qquad \textbf{(3.11)}$$

Where E is the internal energy per initial volume, $C_0, C_1, C_2, C_3, C_4, C_5, C_6$ are user-defined constants

$$\mu = \frac{1}{V} - 1 \qquad \textbf{(3.12)}$$

Where V is the relative volume

To model air, $C_0 = C_1 = C_2 = C_3 = C_6 = 0$ and

$$C_4 = C_5 = \gamma - 1 \qquad \textbf{(3.13)}$$

Where γ is the ratio of specific heat at constant pressure per specific heat at constant volume (for example γ = 1.4)

The pressure is then given by:

$$p = (\gamma - 1)\frac{\rho}{\rho_0} E \qquad \textbf{(3.14)}$$

Where:

$$E(air) = \rho_0 c_V * T \qquad \textbf{(3.15)}$$

In AUTODYN, Century Dynamics Inc. (2003), an ideal gas equation of state (EOS) is used to describe air, which is in the form of:

$$p = (\gamma - 1)\rho e + p_{shift} \qquad \textbf{(3.16)}$$

Where p is the pressure, γ is the adiabatic constant, for air behaving as an ideal gas γ is estimated to be 1.4, ρ is the density, p_{shift} is a small pressure defined to give a zero starting pressure in order to avoid complications in problems with multiple materials where initial small pressures in the gas would generate small unwanted velocities.

e is the specific internal energy:

$$e = c_v T \qquad \textbf{(3.17)}$$

Where the constant c_v is the specific heat at constant volume.

3.5.2 Explosive

In this thesis, CONWEP is used to provide LS-DYNA with blast loading while avoiding the need to use an explosive model. In AUTODYN, Hallquist (1998), the Jones-Wilkins-Lee (JWL) equation of state is used to describe the explosive, which is in the form:

$$p = A\left(1-\frac{\omega}{R_1 V}\right)e^{-R_1 V} + B\left(1-\frac{\omega}{R_2 V}\right)e^{-R_2 V} + \frac{\omega E}{V} \quad \textbf{(3.18)}$$

Where *A, B, R_1, R_2, ω* are empirically derived constants which are different in each explosive, *V* is the relative volume or the expansion of the explosive product, and *E* is the detonation energy per initial unit volume.

In AUTODYN, the parameters were derived from Dobratz and Crawford (1985), which are based on the cylinder experiments. It involved monitoring the axial expansion of a hollow copper tube subjected to an internal detonation of the explosive. There are a wide range of different high explosive parameters available to use.

3.5.3 Mild steel and rolled homogenous armour (RHA) steel

Boyds (2000) used an isotropic elastic-plastic material model to represent a mild steel. According to Hallquist (1998), it uses the Von Mises yield condition, which is given by:

$$\phi = J_2 - \frac{\sigma_y^2}{3} \quad \textbf{(3.19)}$$

Where J_2 is the second stress invariant which is equal to:

$$J_2 = \frac{1}{2} s_{ij} s_{IJ} \quad \textbf{(3.20)}$$

σ_y is the instantaneous yield stress, which is a function of the yield stress, σ_0, the effective plastic strain, ε_p and the plastic strain hardening modulus, E_p giving:

$$\sigma_y = \sigma_o + E_p \varepsilon_p \quad \textbf{(3.21)}$$

It is probably the most cost-effective plasticity model (only one history variable is stored with this model). However, this model may lead to inaccurate updating of shell thickness and stress after yield.

An alternative material model, namely the Johnson and Cook material model, Johnson and Cook (1983), may be used. It is used in AUTODYN and LS-DYNA, and expresses the flow stress as a function of plastic strain, plastic strain rate and temperature as follow:

$$\sigma_y = \left[A + B * \left(\varepsilon_p\right)^n\right] * \left[1 + C * \ln\left(\dot{\varepsilon}^*\right)\right] * \left[1 - \left(T^*\right)^m\right] \quad \textbf{(3.22)}$$

Where *A, B, C,* and *n* are user-defined constants, ε_p is the effective plastic strain, $\dot{\varepsilon}^*$ = normalised plastic strain rate, and T^* is the homologous temperature

$$\dot{\varepsilon}^* = \frac{\dot{\varepsilon}_p}{\dot{\varepsilon}_0} \text{ for } \dot{\varepsilon}_0 = 1/\text{s} \quad \textbf{(3.23)}$$

$$T^* = \frac{T - T_{room}}{T_{melt} - T_{room}} \quad \textbf{(3.24)}$$

This material model is widely used to represent materials in applications subjected to large strains, high strain rates and high temperature, such as experienced in high-velocity impact and explosive detonation. In this thesis, apart from the isotropic elastic-plastic material model, mild steel and RHA steel will be represented by the Johnson and Cook material model. The principal stress and strain failure model, which defines the maximum value of principal stress and strain in tensile and shear modes, will also be used.

3.6 Previous works on numerical simulations

The numerical simulations within mine-blast related research were developed using various techniques in order to be comparable with the experimental results, which can later be used to reduce the numbers of experiments required. This thesis will only provide the literature reviews, which are deemed to be important to this work.

In Williams and Mcclennan (2003), the surface blast loading option in LS-DYNA, which is based on the CONWEP code, has been used to simplify blast loading from buried mines less than 20 cm depth (mines were buried to a 5 cm depth and the target plate was around 40 cm above the ground). The FEMAP CAD/CAE software package was used as a pre-processor to build the solid model and finite-element mesh of the experimental set-up. The numerical model was developed in accordance with the experiment. Results from this paper have shown that a scaling factor of 2.2 would be needed to achieve the same maximum displacement as the experimental results. In the same paper, another method, which used LS-DYNA was developed. The empirical relationship developed by Westine *et al* (1985) at the Southwest Research Institute under contract from the US Army TACOM predicts the impulse applied by a buried mine to a plate at a given offset from the mine. The model is based on a series of tests that were conducted to measure the impulse at various locations above a land mine explosion. These results were then used to develop an empirical model, which accounts for effects such as mine depth of burial, charge size, target height, and soil density. A pre-processor then has been developed in LS-DYNA code by Dumas and Williams (2002). Results have shown that a scaling factor of 66% would give a good agreement on maximum displacement with the experimental results. It shows that the latter method has given results closer to the experiment than the former because below ground effects are not included in the blast loading as in the former method. Blast loading from CONWEP simply used an hemispherical charge detonated on a reflected surface to represent a blast loading from a buried charge. It does not account for the soil properties. In addition, CONWEP was formulated from empirical relationship derived from experiments. Therefore in some cases, the blast loading was estimated from interpolations. The differences in soil properties between the experiments and the simulations may have contributed to the discrepancies in the latter method. For example, the soil used to produce

the empirical blast loading may have contained higher moisture content than the soil used during the experiment day, therefore blast loading was higher and hence the deformation results factor of 66% was needed.

Vulitsky and Karni (2002) developed a numerical simulation using LS-DYNA to predict the effect of the detonation of high explosives on steel structures. This method was aimed at the explosive blast in the air to the structure. The simulation used the Jones-Wilkins-Lee (JWL) equation of state to describe the explosive. A linear polynomial equation of state was used to simulate the proper behaviour of air. The mix of the air and explosion reaction products is modelled using LS-DYNA multi-materials capabilities. The blast pressure wave travelling through the air interacts with the structure by means of a gas-structure interface algorithm. Numerical results were compared with those from the experiment and they gave a maximum under-prediction of permanent deformation around 20 – 40 %.

Williams and Fillion-Gourdeau (2002) developed a simplified vehicle model of a Cougar 6 x 6 LAV (without turret, hatches, interior bulkheads, wheels, drive shafts, engine and transmission were modelled as blocks etc.) to investigate the effect of mine blasts on vehicle occupants using Hybrid III ATD (Anthropomorphic test devices) to assess their injuries. Blast loading was based on the work done by Westine *et al* (1985) and Dumas and Williams (2002). Results regarding the occupants were presented but the results of vehicle structure were not shown. The same empirical relationship blast loading developed by Westine *et al* (1985) was previously used in Williams and Poon (2000) to assess the floor deformation of M113 armoured personnel carriers subjected to a buried 7.5 kg C-4 mine. The model was developed in LS-DYNA3D and compared with experimental maximum permanent deformation results. The engine, tracks, wheels, and suspension systems were not included. The numerical simulation result was 50% higher than the experimental result. Further work on this blast loading was conducted in LS-DYNA to try to incorporate the welding of the structure by Gaudreault, *et al.* (2005). The numerical results were not shown because further developments were required to incorporate more sophisticated constitutive models in order to represent the material property in the welded area correctly. Note that the blast load model from Westine *et al* (1985) only accounted for soil variations in terms of soil density. It did not take into account other variations in soil, such as the soil type and

moisture content, which can influence blast loading. It is thought that the impulse from the simulations by Williams and Poon (2000) may have been lower than the corresponding experiments, which make the simulation results 50% higher than the experiment results. The differences in impulse may have come from the differences in soil properties, such as moisture content, which can give different results. The experiment itself may have also contributed the differences, for example, the charge may have been buried at different depth or stand off distances, the position of the charge with respect to the target may have been different, etc. These may have contributed to the discrepancies.

From these literatures it seems that the discrepancies between the simulations and the experiments are normally high. Vulitsky and Karni (2002) mentioned that explosion prediction in many literatures may give discrepancies up to 100% and even higher with respect to the test data.

Fairlie and Bergeron (2002) and Fairlie (2003) developed numerical simulations in AUTODYN 2D to compare the target momentum of a steel plate between the AUTODYN 2D multi-materials (Euler) and AUTODYN 2D single material (Euler FCT) methods. The AUTODYN 2D single material method remapped the explosive products pressure onto the model. Both methods seemed to give very similar results. This paper then progressed to model a pendulum target subjected to the explosive charge buried in soil. The explosive charge was modelled as a high pressure gas in AUTODYN 3D single material, and the soil was modelled using a Lagrangian model. This paper mentioned further work by Patria Vehicles Oy of Finland, which simulated the vehicle model subjected to mine blasts but results were restricted.

There were some mine-related works using CTH hydrocode, McGlaun, Thompson, and Elrick (1990), which is suitable for explosive problems, by various authors. The interesting work by Gupta (2003) was done in 2D planar symmetry models to assess the effects of flat, ‘curved’, ‘V’, and ‘double V’ lower hull bottoms subjected to a cylindrical 8-kg TNT charge on a fully-reflected hard ground surface. All simplified hull models were modelled as completely-solid-block steel structures (719.12 mm wide and around 600 mm high depending on the bottom shapes) with the same equivalent mass of 8,172 kg. The curve

geometry was constructed from 4 curves to achieve a smooth curve geometry on an axi-symmetric model. The 'V' geometry was at 9 degree angle from the base while the tip of the double 'V' geometry was at the same distance as the 'V' geometry. The results indicated that the V-shaped hull bottom shapes trapped the lowest vertical integrated momentum than the 'double V', 'curved' and the flat hull bottom shapes respectively. However, this work was performed on 2D (X and Y axis) models, which assumed the geometry in z-direction is infinite. It did not account for the actual vehicle hull accurately. The whole structure was solid so the deformation of the hull bottom was very small and cannot be assessed. The parametric study of different properties, such as the stand off, was not included. The previous work by Gupta (2001) was performed in 3D but used a plain steel RHA plate (2440 x 2440 x 15 and 20 mm thick) subjected to a cylindrical buried charge of 9.05 kg TNT under dry sand and wet sand.

Cheng *et al* (2002) used AUTODYN and DYTRAN to investigate the response of box-like structures to near-by explosion. A plain box structure (1.5 x 4 x 1 m) with two compartments separated by two plain steel plates, with the opening on the top plate represented by shell elements with an isotropic elastic plastic material model in DYTRAN. The blast loading was calculated from AUTODYN 2D multi-materials Eulerian meshes, in which the ideal gas and the JWL equation of state were used to represent air and TNT. Neither the validation of the methodology nor the comparison with the experimental results was discussed, though the mesh sensitivity was analysed. It concluded that the response of the box-like structure is mainly due to the blast wave that hits the bottom of the structure.

The limitation on the amount of charge that can be used on the range has limited the availability of the experimental results at full scale. Experiments may need to be done at small scale. For example, there were experiments on different scaled single-solid plates with v shape, and pyramid shape subjected to very small charges of 0.636 grams by Genson (2006).

3.7 Conclusions

The relevant theories on blast loading and methods of numerical simulation were explained. LS-DYNA and AUTODYN commercial software packages, which are widely used in the mine blast application, were chosen for use in this thesis, and their abilities and features were summarised. Material models used in both simulations, describing air, explosive, and steel, were presented in terms of equations of state or material strength models.

Literature reviews indicated there were works in the general area of structures subjected to mine blasts, which related to the work in this thesis. However, there is no particular work in numerical simulation on vehicle bottoms of single floor and double floor settings subjected to mine blasts, accounting for variations in bottom shapes, stand off distances, and thicknesses.

CHAPTER 4 Single and double plate numerical simulations

In this chapter, numerical simulations of a single and double plates subjected to an exploding charge in the air were developed and validated with the experimental results. For validation, deformation was used as a criterion. Various numerical simulation techniques from LS-DYNA and AUTODYN were considered and compared.

4.1 Introduction

In general, it is very expensive to conduct mine blast experiments for research and vehicle development purposes. It consumes high resources in terms of time and finances. Highly experienced technicians are needed to achieve the best possible results. Numerical simulation analyses are generally used to reduce the project cost by reducing the required number of experimental tests and hence this leads to more economical methods of development. It also offers economical means to conduct sensitivity studies.

The vehicle structure used in mine-blast experiments and numerical simulations may range from a simple plate structure to a real vehicle. Results from the experiments are normally classified and subsequently there is little literature available in the public domain. Moreover, experiments are cost-prohibitive and previous experimental results are difficult to find and correlate because some of the parameters affecting the results might not have been well defined. Frequently a simple structure such as a mild steel plate is used for testing and validation of numerical simulation.

The main aim of this chapter is to develop numerical simulations of single and double plate structures subjected to an exploding charge in the air using both LS-DYNA and AUTODYN. These models are validated with the experimental results and are also compared with each other to assess their suitability. In addition, this work will lead to better understanding and confidence building in structural analysis against the mine blast. Both LS-DYNA and AUTODYN are commercial software that are widely used to model this type of problem.

The preliminary model was based on a simple plate subjected to an exploding charge in the air. It is assumed that in the numerical simulations within this research, AT mines will be represented as pure explosive charges without the fuze, casing, and casing fragments. The effects of these fragments are not included. Note that in reality, the detonation of an

explosive charge is normally not perfect, which may give uneven blast wave propagation due to the lack of oxygen in the detonation process. This difference in the blast wave may lead to the difference in the structural responses.

4.2 Single plate simulations

4.2.1 Experiments and simulations from Boyd (2000)

Boyd (2000) has performed experiments on a plate, which was subjected to an explosive blast. A mild steel plate (1,200 x 1,200 x 5 mm) bolted around its perimeter to a frame was subjected to a mine blast as shown in Figure 4.1. There was around 1,000 mm x 1,000 mm area free to move under the blast load (This dimension was then used in the subsequent simulations). The frame was positioned on four Pendine blocks. A spherical explosive charge of Pentolite weighing 0.250 kg was detonated centrally above the plate. The experiments were series of trials intended to measure the acceleration and displacement of the plate by varying the distances between the plate and the explosive to 250, 400, and 500 mm. The experiments were performed once at 250 and 400 mm and twice at 500 mm stand-off distance. The average experimental results from 500 mm stand off distance were used for validation and comparison. Five gauges were pasted on each plate as shown in Figure 4.2. There were two Endevco 7255A piezoelectric accelerometers (referred as gauge G1 at 100 mm and G2 at 200 mm from gauge G5), two PCB Piezotronic 109A piezoelectric pressure gauges (referred as gauge G4 at 100 mm and G3 at 200 mm from gauge G5), and a Novotechnik TI50 LVDT (Linear Variable Displacement Transducer) resistive displacement gauge (referred as gauge G5 and located at the centre point on the plate).

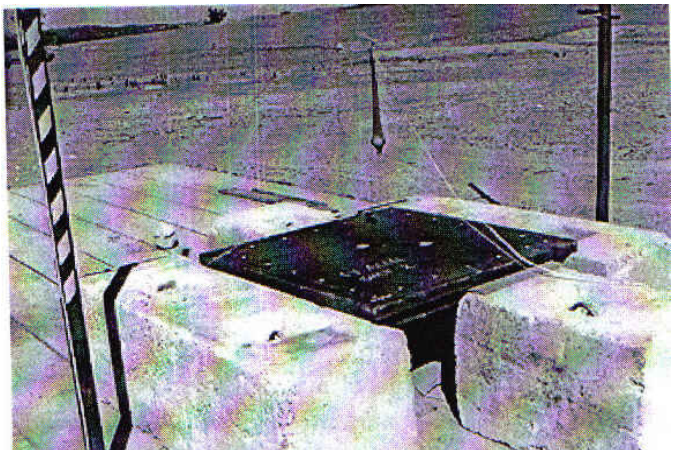

Figure 4.1 Boyd's experiment set-up, from Boyd (2000)

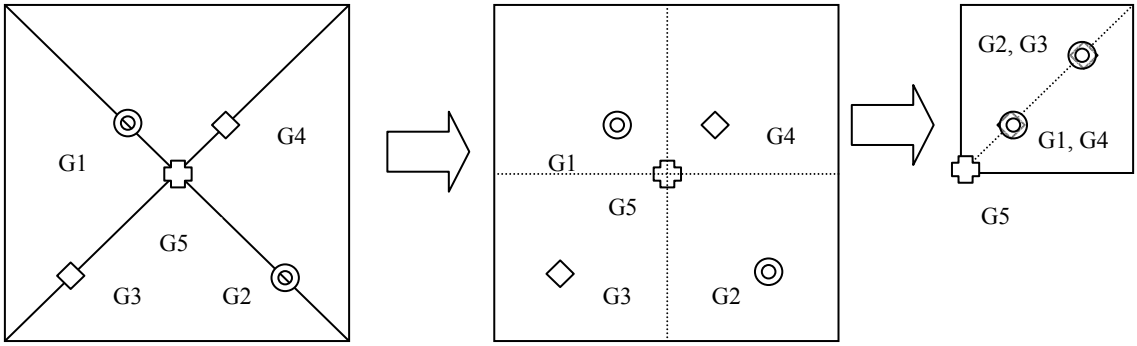

Figure 4.2 Boyd's experiment's schematic drawing showing gauge positions

Boyd (2000) developed a numerical simulation using LS-DYNA3D version 940. The relevant parameters (peak overpressure, positive impulse and time of arrival) applied to the model was derived from Hyde (1991). The pressure was applied equally over the plate. The plate was modelled using isotropic elastic/plastic shell elements. The relevant material properties of the target plate are given in Table 4.1. Results were obtained directly from the nodes. No accelerometer options were used in the numerical simulation.

Material properties	Parameter value
Density, ρ	7850 kg/ m^3
Hardening parameter, β	1.0
Poisson's ratio, ν	0.3
Tangent modulus, E_T	470 MPa
Yield stress, σ_y	270 MPa
Young's modulus, E	203 GPa

Table 4.1 Material properties of mild steel used in Boyd (2000)

4.2.2 LS-DYNA with CONWEP

Based on the available information from Boyd's experiments and numerical simulation, a similar model was created using LS-DYNA (version 960 & 970), for validation and familiarisation with the software. ETA/FEMB-PC version 27 was used as a pre- and post-processor, Engineering Technology Associates, Inc. (2001). For verification, the initial model was developed using isotropic elastic plastic material model and thin shell elements. The results seemed comparable with the experiment and Boyd's simulation; see Showichen *et al* (2005) for more details. However, in this study, a more realistic material model proposed by Johnson and Cook (1983), was used. It is difficult to find the exact Johnson and Cook parameters for the mild steel plate used in Boyd (2000), therefore very similar parameters of 1006 steel from Johnson and Cook (1983) as shown in Table 4.2, were used with the adjustment being made to the yield stress equalling to 270 kPa. An equivalent weight impulse factor of 1.14 was used to convert Pentolite to TNT equivalent weight. The LOAD_BLAST card in LS-DYNA was used to generate blast loading from CONWEP. During model build up and initial analysis for fine tuning, it was ascertained that 900 shell elements gave good accuracy, see Figure 4.4. Based on the configuration of the plate symmetry, a quarter model (0.5×0.5×0.005m) was created as shown in Figure 4.3. Note that the centre of symmetry of the plate is at (0,0,0). All edges of the outer plate were fixed in all degrees of freedom. *ELEMENT_SEATBELT_ACCELEROMETER cards were used to represent Endevco 7255A piezoelectric accelerometers placed at 0.0943m and 0.1886m from the centre (0,0,0), each accelerometer weighed 0.005 kg, Endevco Corporation (2006). This weight was added to the node representing the accelerometer in the numerical simulation accordingly, however it did not take into account the mounting plates. There was no information on the weight of a PCB Piezotronic 109A piezoelectric pressure gauge from PCB Piezotronics, Inc. (2006). A lumped mass of 0.025 kg was added to represent it. Simulations were initially run by modelling the explosive both above and below the target plate for a given stand-off distance; results obtained were exactly the same. The former simulations were then used to compare with the experimental results.

Parameter	Parameter value
A	270 MPa
B	275 MPa
n	0.36
C	0.22
m	1.00

Table 4.2 Material property of 1006 steel used in Johnson and Cook material model to represent steel in Boyd's experiment, based from Johnson and Cook (1983)

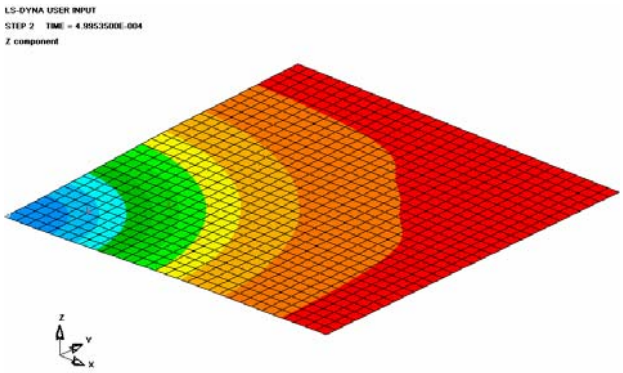

Figure 4.3 Contour plot of deformation in z-direction result from LS-DYNA using CONWEP at a stand-off distance 0.25m at 0.5 ms

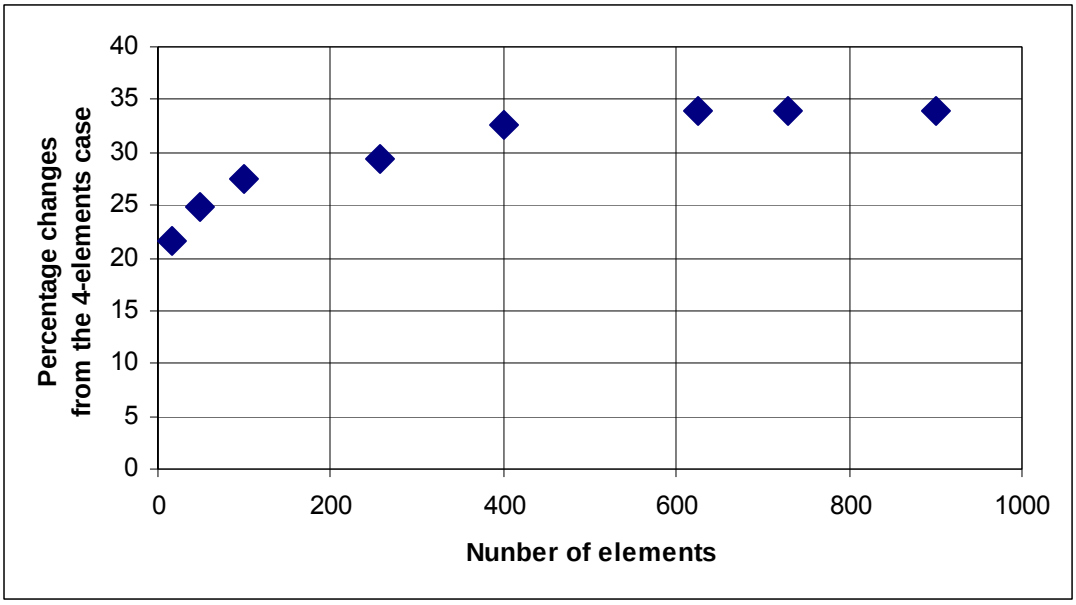

Figure 4.4 Percentage changes of maximum deformation (%) from 4-elements case: mesh sensitivity analysis in LS-DYNA with CONWEP methodology

4.2.3 AUTODYN 2D to solve 3D problems (AUTODYN 2D)

This option used AUTODYN 2D to solve a 3D numerical simulation of a plate subjected to mine-blast. A 2D axis-symmetric model was developed using Lagrange and multi-materials Euler solvers with 0.25, 0.4 and 0.5 m stand-off distances. Eulerian elements were used to represent air and explosive charge. Note that shell elements are not allowed to be used in the axis-symmetric AUTODYN 2D model. Material data from Table 4.2 was applied to the model. Ideal gas equation of state was chosen to describe air, while Jones-Wilkins-Lee (JWL) equation of state described Pentolite explosive charge. The plate was fixed in all degrees of freedom by constraining its edges while the Eulerian materials were allowed to flow out of the boundary, as shown in Figure 4.5. This allows explosive products (gases) to expand outside and away from the plate. In AUTODYN 2D, it is not possible to get acceleration as an output therefore velocities are obtained and differentiated with respect to time to evaluate the acceleration.

Note that the charge was in spherical shape, so 250g of Pentolite having the density of 1.7 g/cm^3 (from Dobratz and Crawford (1985)), had a radius of 36.040 mm. Eulerian element sizes of 5, 4, 3, 2, 1, 0.75, and 0.5 mm were used to perform mesh sensitivity analysis at 0.25 m stand-off and their results are in Figure 4.6 – 4.8, while Lagrangian element size of the plate will be based on the shell element size which was previously done in LS-DYNA. The Lagrangian elements will consist of two layers of elements through the plate's thickness in order to speed up the computation process.

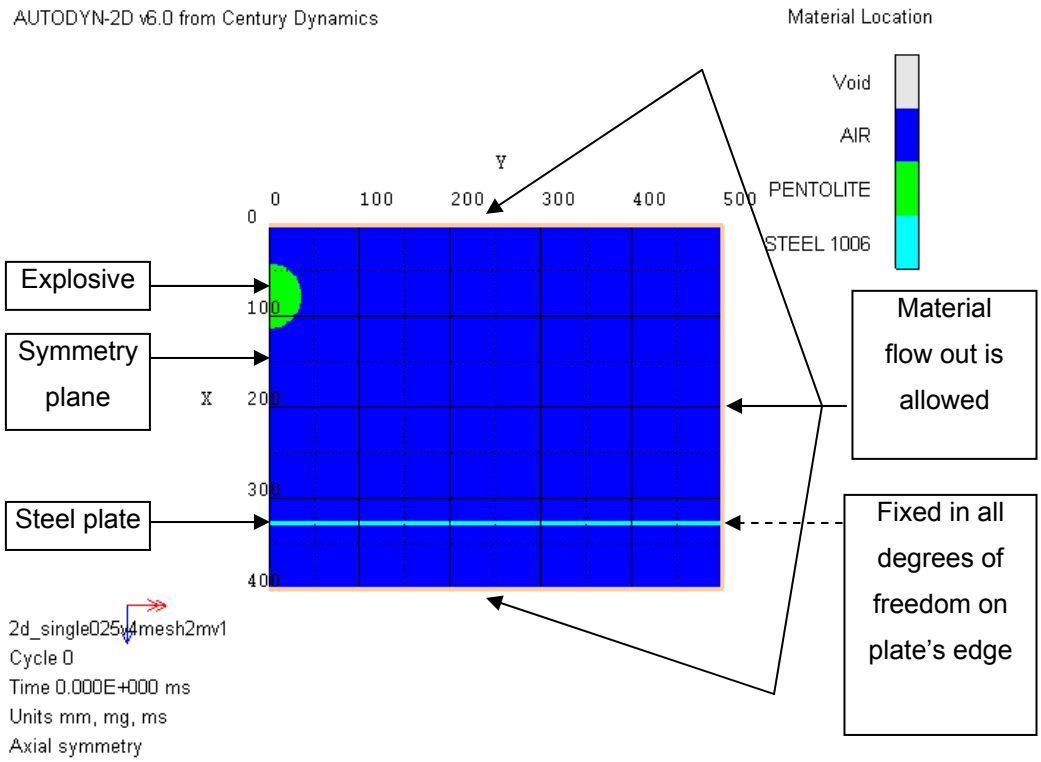

Figure 4.5 AUTODYN 2D axis-symmetric multi-materials simulation model based on Boyd's simulation

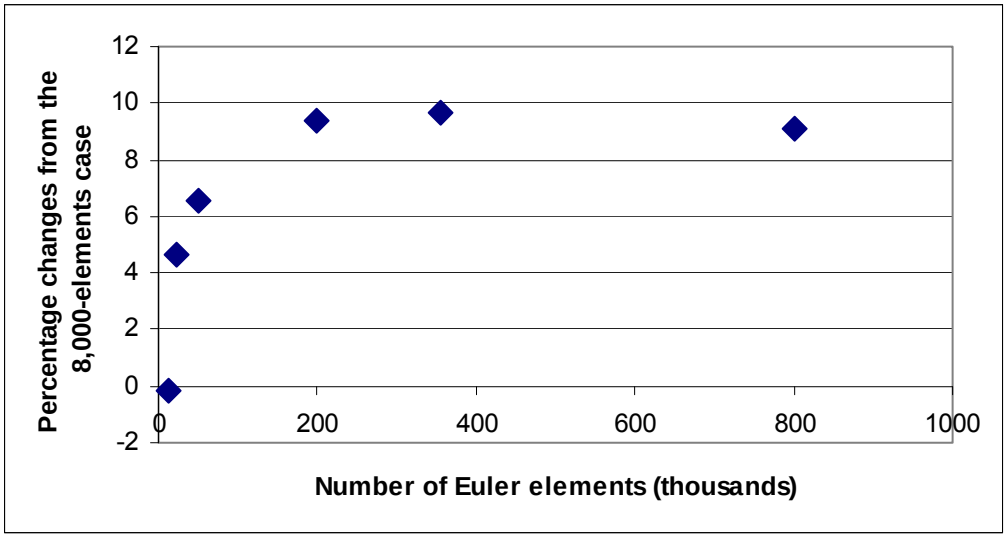

Figure 4.6 Percentage changes of maximum deformation (%) from the 8,000-Eulerian-elements case: mesh sensitivity analysis in AUTODYN 2D to solve 3D problems methodology

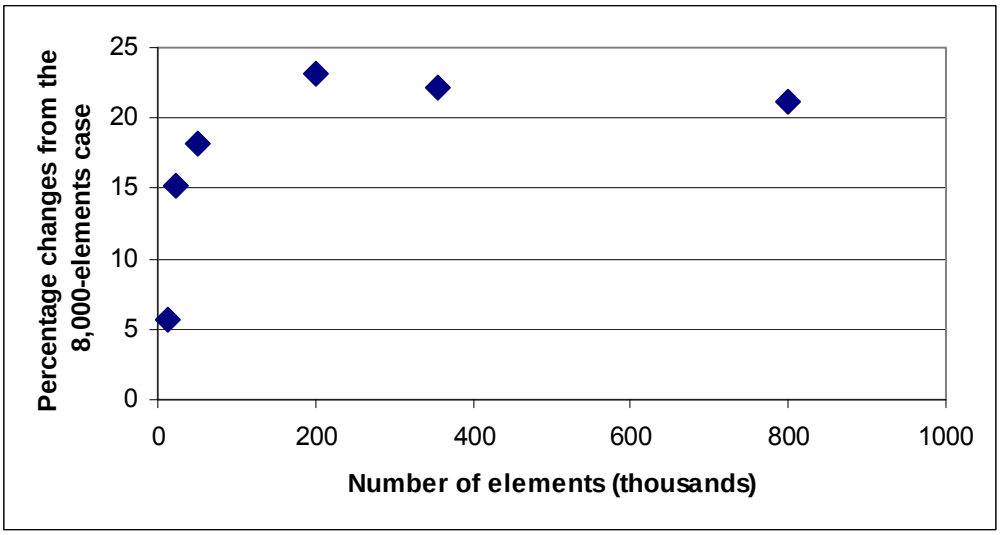

Figure 4.7 Percentage changes of maximum acceleration (%) at gauge G2 and G3 (200 mm from the centre) from the 8,000-Eulerian-elements case: mesh sensitivity analysis in AUTODYN 2D to solve 3D problems methodology

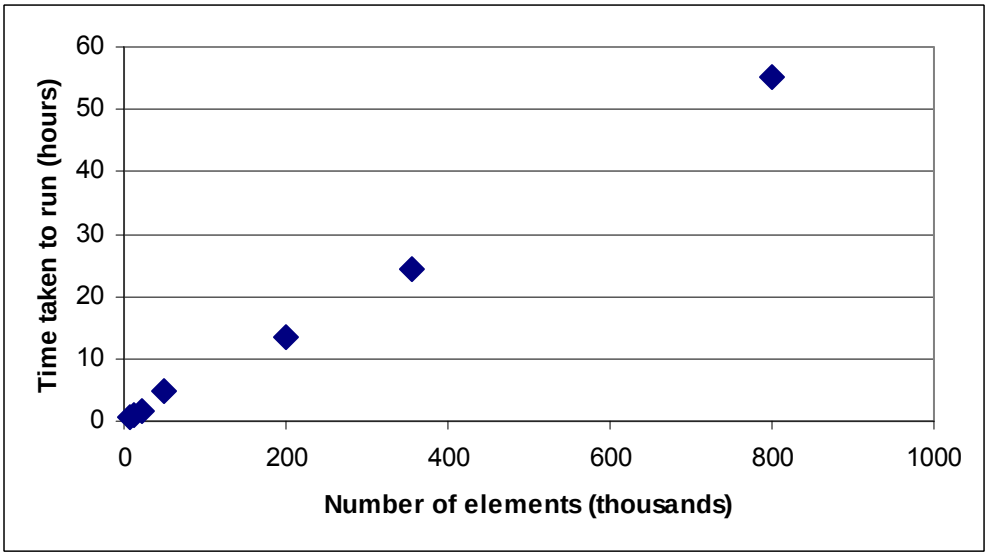

Figure 4.8 Time taken to run the same model of different number of elements (hours): mesh sensitivity analysis in AUTODYN 2D to solve 3D problems methodology

From the mesh sensitivity results shown in Figure 4.6 – 4.8, it is clear that the change (percentage) in output parameters such as maximum deformation and acceleration reaches diminishing returns at a mesh size of 0.75 mm (356 thousands elements). In addition, with

the increase in mesh size, computation time approaches to non-practical limits. Thus it was decided to use 0.75 mm as an Eulerian element size for further analysis.

4.2.4 AUTODYN 2D using the same equivalent mass (AUTODYN 2D (AREAL))

Axis-symmetric model in AUTODYN 2D means that it is a circular plate instead of a rectangular shape. The total mass of the plate will thus be different from the actual experiment model. Therefore the model was modified to account for the mass difference by changing the geometry accordingly as shown in Figure 4.9. Other parameters, such as element size and types were similar to the previous analysis in section 4.2.3.

Both plates were made from the same steel therefore if the total mass were equal, the total volumes were also equal.

Volume of the full actual plate (rectangular shape) = 1.0 x 1.0 x 0.005 = 5 x 10^{-3} m^3

Volume of the full new plate (circular shape) = $\pi r^2 \times 0.005$

So, $\pi r^2 \times 0.005 = 5 \times 10^{-3}$

$r = 0.564190m$

Thus a 1 m square plate having a thickness of 5 mm can be represented by a circular plate of radius 564.19 mm, as shown in Figure 4.9. Note that by changing the shape from square to circular shape, the length along the fixed support edge is reduced from 4 m to 3.545 m. In terms of flexural rigidity, which is a measure of rigidity of the plate and is defined as $E_y t^3/12(1-\upsilon^2)$, where E_y is the young's modulus, t is the plate thickness, and υ is the poisson's ratio, both the circular plate and the square plate have the same flexural rigidity because they are made from the same material having the same thickness.

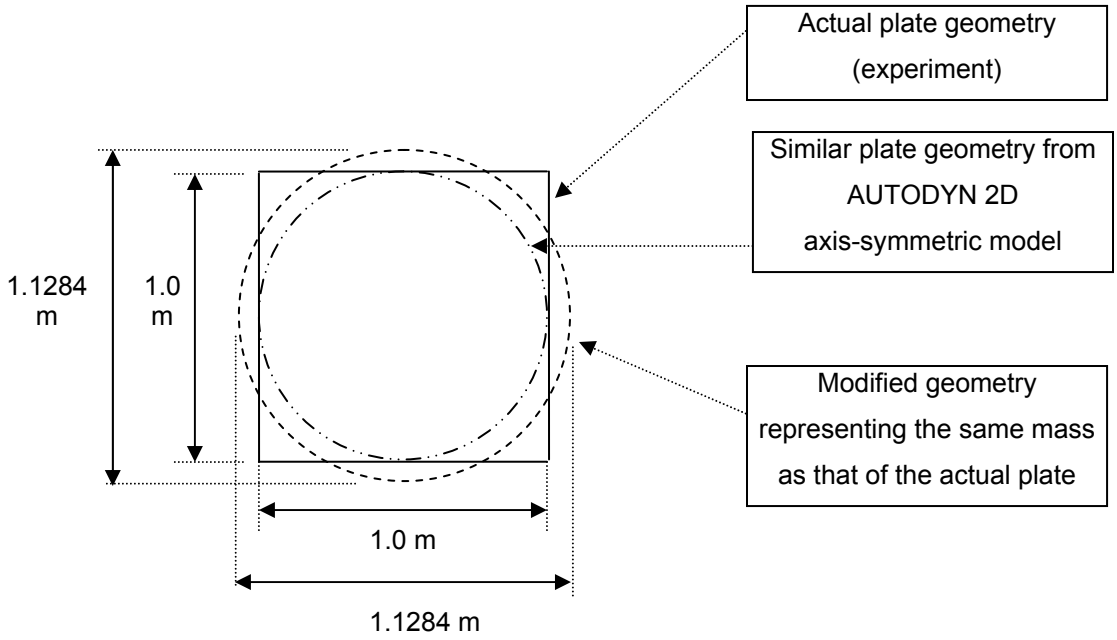

Figure 4.9 Comparing the full plate geometry from Boyd's experiment and from AUTODYN 2D axis-symmetric models

4.2.5 AUTODYN 3D using multi-materials method (AUTODYN 3D)

An alternative model may be developed as a 3D model, however a 3D model is computationally more expensive than a 2D model. In this section, a similar approach was used to develop a 3D model in AUTODYN 3D. A rectangular plate having shell elements was developed, while a mine was modelled using Eulerian brick elements in the form of a sphere. For shell and Eulerian elements to interact effectively, it is important for Eulerian elements to be equal or smaller than the shell elements, otherwise blast pressure will numerically leak through the shell elements. Hence plate thickness dictated the element size. This resulted in a model whose size was beyond the capacity of the computer in use. The problem was resolved and the model was fixed by using variable mesh density (bias technique). This meant that a denser mesh of 5 mm was used in the region between the blast origin and the plate, and the area where the plate (shell elements) could deform and interact with the air (Eulerian elements), while for all other regions a mesh size of up to10 mm was used.

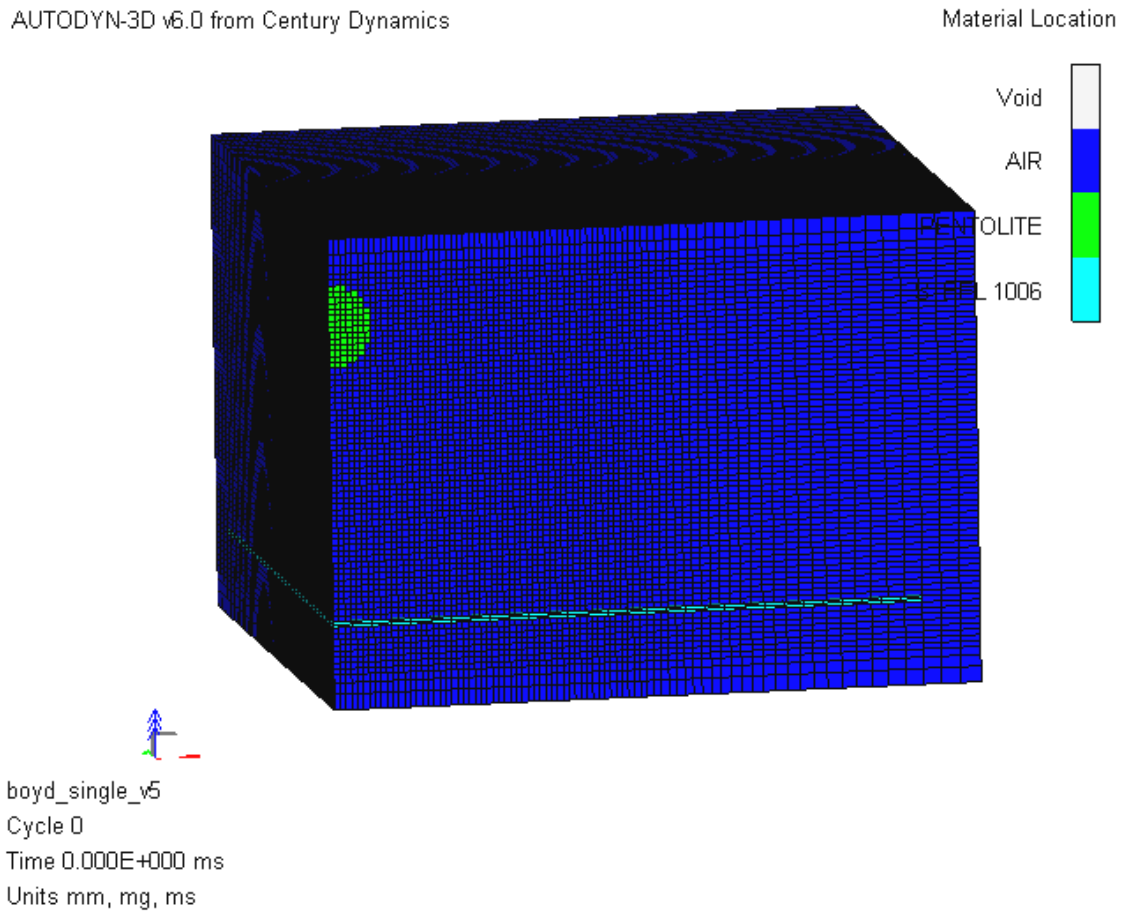

Figure 4.10 AUTODYN 3D model representing Boyd's experiment (initial model)

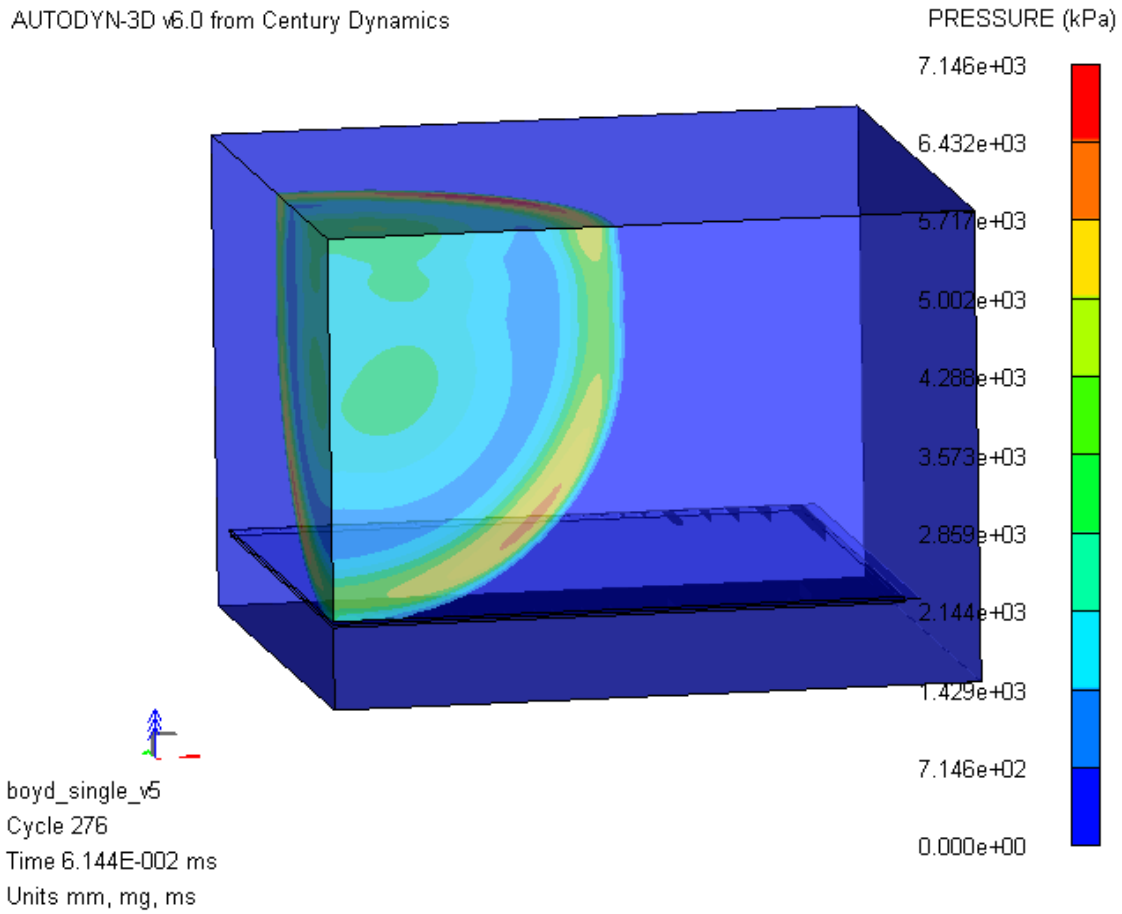

Figure 4.11 AUTODYN 3D model representing Boyd's experiment showing pressure contour (at 0.06 ms)

4.2.6 AUTODYN 3D using remapping method (AUTODYN 3D remap)

With remapping, the model is developed in two stages. The first stage involves acquiring blast loading from AUTODYN 1D or 2D which is then remapped into AUTODYN 3D model during the second stage. In that, air is modelled using single material Euler elements in which the pressure from the first stage travels and acts upon the target plate to cause deformation.

In this application, it was a spherical charge blast in the air, where there was nothing obstructing the blast propagation between the explosive charge and the plate. Blast loading will come from a 1D wedge model, which took little time to run even at a very fine mesh size. Mesh sensitivity analysis is not necessary as long as the mesh size is smaller than 10

mm and there are at least 10 elements of explosive charge within the model in order to allow the blast to propagate effectively, Century Dynamics Inc. (2003).

In the first stage, a spherical explosive charge as shown in Figure 4.12 was developed using AUTODYN 1D wedge shape model. The radius of the wedge represented the stand off distance between the explosive charge and the target plate. Upon initiation, detonation products travel through the air, which was modelled using Ideal gas equation of state, while the explosive charge was modelled using JWL equation of state. Once the detonation products reached the far end of the model, the simulation was stopped. The remapped file was saved in a file ready to use in AUTODYN 3D.

In the second stage, due to symmetry, a quarter model of the target plate was developed, which consisted of air and target plate elements. Air and target plate was modelled using Eulerian and shell elements respectively. Ideal gas equation of state described the air Eulerian elements, while Johnson and Cook material model was used to describe the behaviour of RHA target plate. Blast loading from the remap file in the first stage was applied into the model at the intended position. To ensure accuracy and effective interaction, the Eulerian mesh size was set to be compatible with the target plate thickness. Suitable gauges were built to record results at the appropriate location.

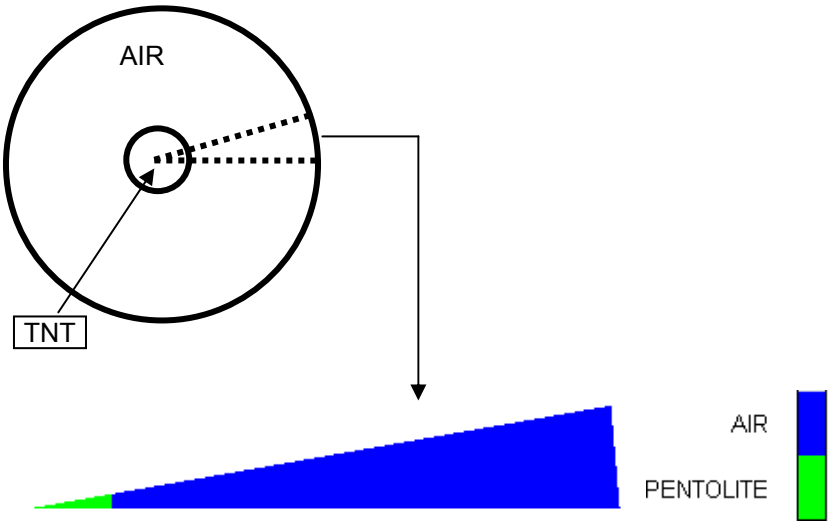

Figure 4.12 1D wedge model used in AUTODYN 2D to provide blast loading in AUTODYN 3D

4.2.7 Single plate results

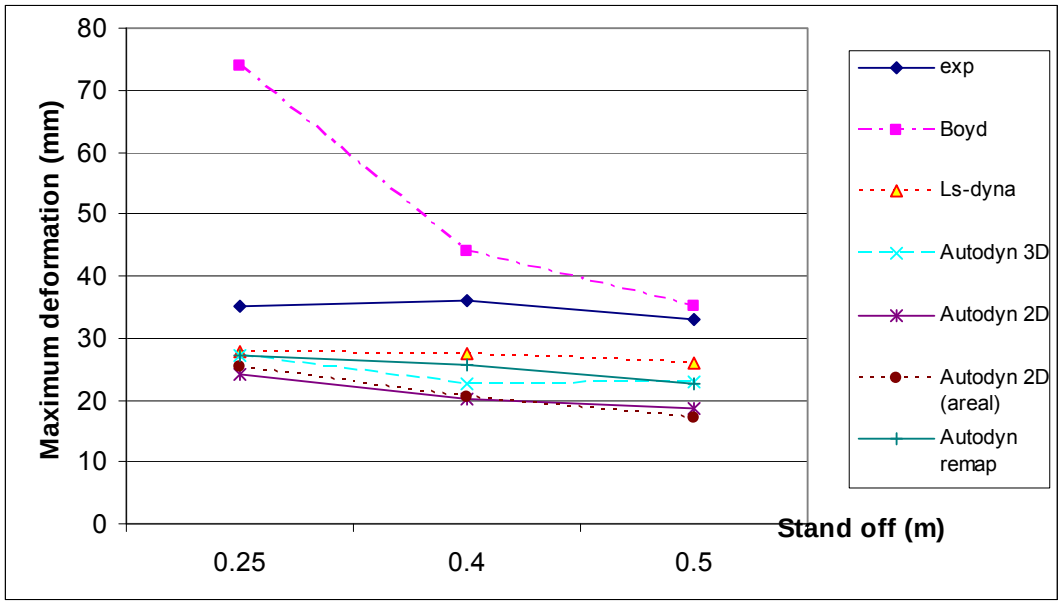

Figure 4.13 Comparing maximum dynamics deformation results from various methodologies with experimental results from Boyd (2000). (Note that exp = experimental result, Boyd = Boyd's numerical simulation, Ls-dyna = LS-DYNA with CONWEP method, Autodyn 3D = AUTODYN 3D multi-materials method, Autodyn 2D = AUTODYN 2D method, Autodyn 2D (areal) = AUTODYN 2D (areal) method, and Autodyn remap = AUTODYN 3D remap method.)

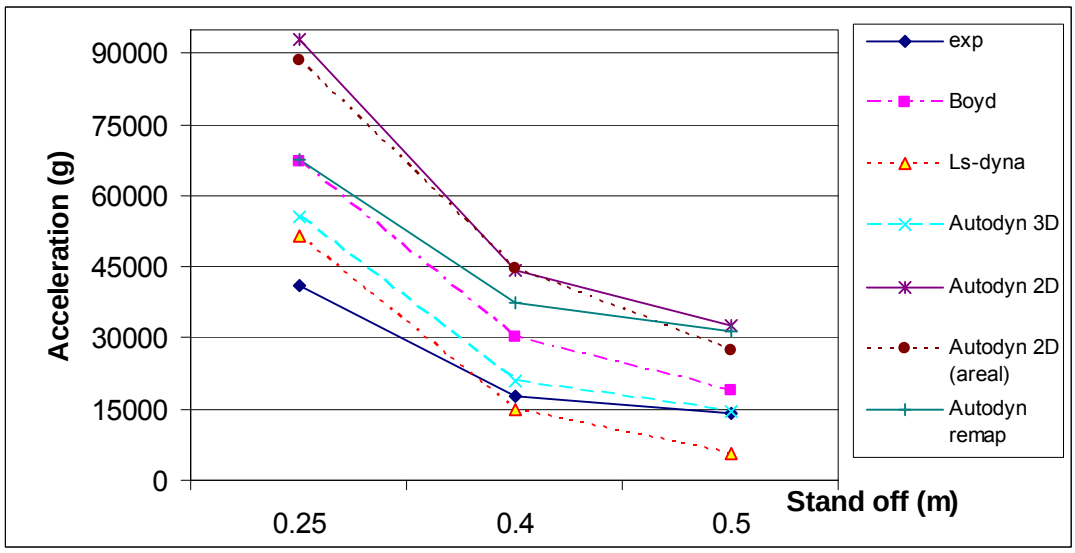

Figure 4.14 Comparing maximum acceleration results at point G1 and G4 (100 mm from the centre) from various methodologies with experimental results from Boyd (2000). (Note that exp = experimental result, Boyd = Boyd's numerical simulation, Ls-dyna = LS-DYNA with CONWEP method, Autodyn 3D = AUTODYN 3D multi-materials method, Autodyn 2D = AUTODYN 2D method, Autodyn 2D (areal) = AUTODYN 2D (areal) method, and Autodyn remap = AUTODYN 3D remap method.)

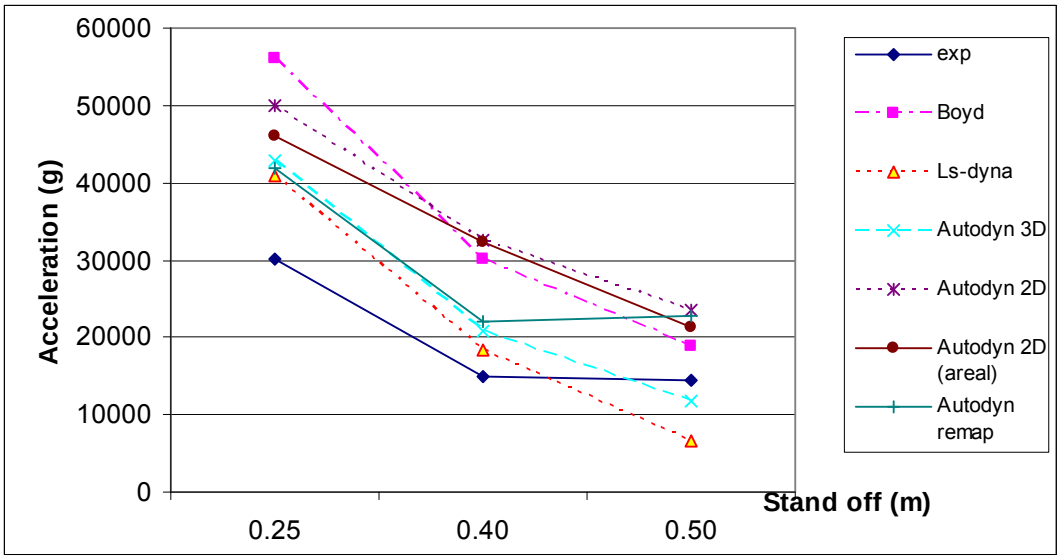

Figure 4.15 Comparing maximum acceleration results at point G2 and G3 (200 mm from the centre) from various methodologies with experimental results from Boyd (2000). (Note that exp = experimental result, Boyd = Boyd's numerical simulation, Ls-dyna = LS-DYNA with CONWEP method, Autodyn 3D = AUTODYN 3D multi-materials method, Autodyn 2D = AUTODYN 2D method, Autodyn 2D (areal) = AUTODYN 2D (areal) method, and Autodyn remap = AUTODYN 3D remap method.)

4.2.8 Single plate discussion

Results of single plate models analysed using different approaches indicate that all methodologies give comparable results as shown in Figure 4.13 – 4.15. It is clear that as the stand-off distance increases, the plate deflection and acceleration reduces. This is as expected because it is logical that the further away you are from the blast, the less effect you will get. Mays and Smith (1995) stated that, Brode (1955) estimated the peak blast overpressure, P_s, from a spherical charge as:

In the near field ($P_s > 1 \times 10^6$ N/m^2):

$$P_S = \left(\frac{6.7}{Z^3} + 1\right) \times 10^5 \frac{N}{m^2} \quad \textbf{(4.1)}$$

In the medium to far field (1×10^4 N/m^2 < P_s < 1×10^6 N/m^2):

$$P_S = \left(\frac{0.975}{Z} + \frac{1.455}{Z^2} + \frac{5.85}{Z^3} - 0.019\right) \times 10^5 \frac{N}{m^2} \quad \textbf{(4.2)}$$

Where Z is scaled distance given by:

$$Z = \frac{R}{W^{1/3}} \quad \textbf{(4.3)}$$

Where R is the distance from the centre of a spherical charge (m) and W is the charge mass (kg TNT).

Equations 4.1 – 4.3 show that as the stand off distance, R, is increased, the scale distance is also increased, which results in the reduction in the peak blast overpressure. This supports that the further away you are from the blast, the less effect you will get.

With the exception of Boyd's simulation (over estimated by 47%), maximum dynamics deformation was under estimated by 22%, 27%, 30%, 40%, and 40% using LS-DYNA with CONWEP, AUTODYN 3D remap, AUTODYN 3D multi-materials, AUTODYN 2D (areal), and AUTODYN 2D respectively.

In terms of acceleration, with the exception of LS-DYNA with CONWEP model and AUTODYN 3D multi-materials, all models gave over estimated results with 65%, 74%, 97%, and 110% from Boyd's simulation, AUTODYN 3D remap, AUTODYN 2D (areal), and AUTODYN 2D respectively. AUTODYN 3D multi-materials gave over predicted results of 26% in all cases except at gauge G2 and G3 (200 mm from the centre) recorded at 0.5 m stand off distance (under predicted by 19%). LS-DYNA with CONWEP gave an over estimated results of 28% at 0.25 m and 0.4 m (gauge G2 and G3 only) stand off distances, while at 0.4 m (gauge G1 and G4 only), and 0.5 m stand off distances gave an under estimated results of 43%.

It seems that the acceleration from numerical simulation results are not in as good agreement as the deformation to the experimental results. Considering the experimental results, the recorded acceleration even from the same gauge position was different. At 0.5 m stand off, two identical experiments were performed. The recorded peak displacement results are the same; however, two different acceleration values were recorded at the same gauge point. The differences between both experimental results at point G1 (and G4) and

point G2 (and G3) are 10% and 11% respectively. Therefore the sensitivity of the gauge point position in the experiment is likely to give significantly different acceleration results. Considering the modelling, the sensitivity of the gauge position in numerical simulation can also give significant different results. For example, using the same configuration as before, when considering the position of the gauge point on the model, at point 'a', 'b', and 'c' as shown in Figure 4.16 which are 23.6 mm apart, the results using LS-DYNA with CONWEP are different as shown in Table 4.3 and Table 4.4, while the results using AUTODYN remap at point 'd', 'e', and 'f' as shown in Figure 4.17, are shown in Table 4.5 and Table 4.6.

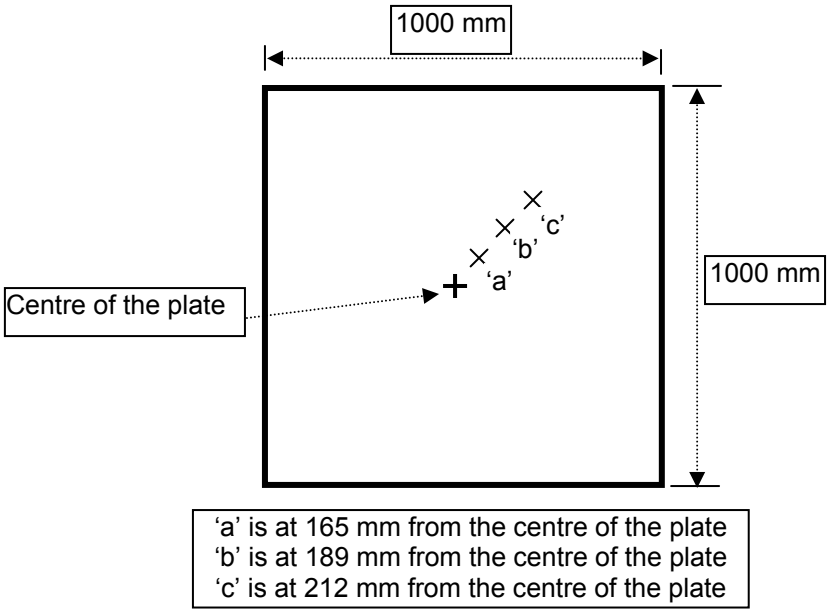

Figure 4.16 Schematic diagram showing different positions ('a', 'b', and 'c') of the gauge used in LS-DYNA

Stand off (m)	Maximum acceleration at point 'a' (g)	Maximum acceleration at point 'b' (g)	Maximum acceleration at point 'c' (g)
0.25	50767	40980	17800
0.4	15730	18428	14481
0.5	7233	6640	7084

Table 4.3 Sensitivity of maximum acceleration results from different gauge positions ('a', 'b', and 'c') using LS-DYNA with CONWEP

Stand off (m)	Maximum dynamics deformation at point 'a' (mm)	Maximum dynamics deformation at point 'b' (mm)	Maximum dynamics deformation at point 'c' (mm)
0.25	25.38	24.87	24.07
0.4	23.03	22.41	21.60
0.5	20.65	20.17	19.44

Table 4.4 Sensitivity of maximum dynamics deformation results from different gauge positions ('a', 'b', and 'c') using LS-DYNA with CONWEP

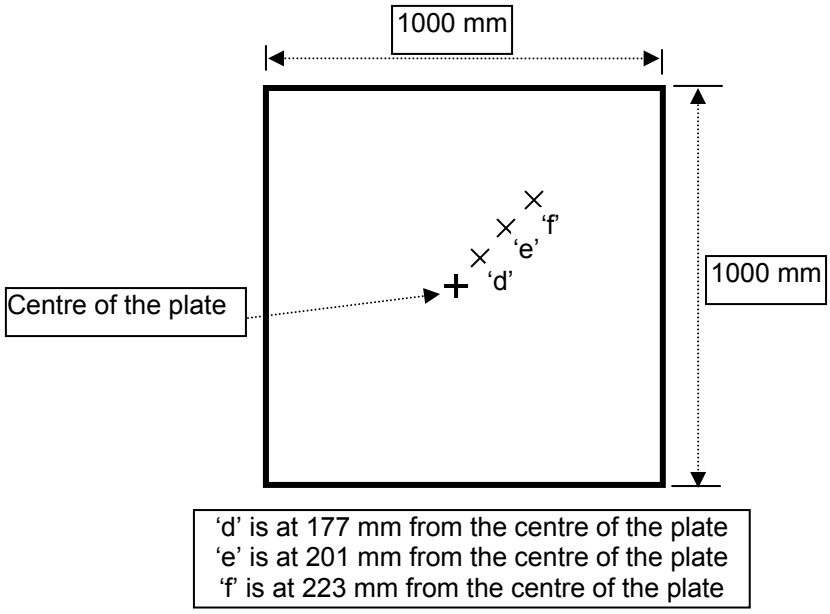

Figure 4.17 Schematic diagram showing different positions ('d', 'e', and 'f') of the gauge used in AUTODYN

Stand off (m)	Maximum Acceleration at point 'd' (g)	Maximum Acceleration at point 'e' (g)	Maximum Acceleration at point 'f' (g)
0.25	44903	41803	34842
0.4	33109	30298	26126
0.5	19892	19473	18495

Table 4.5 Comparing maximum acceleration results from different gauge positions ('d', 'e', and 'f') using AUTODYN remap

Stand off (m)	Maximum dynamics deformation at point 'd' (mm)	Maximum dynamics deformation at point 'e' (mm)	Maximum dynamics deformation at point 'f' (mm)
0.25	26.45	24.20	23.06
0.4	25.41	24.02	22.59
0.5	23.27	22.13	20.95

Table 4.6 Sensitivity of maximum dynamics deformation results from different gauge positions ('d', 'e', and 'f') using AUTODYN remap.

The results in Table 4.3 – 4.6 show that acceleration results from adjacent nodes in LS-DYNA and AUTODYN remap are more sensitive to the position of the gauge than

deformation results. The averaged percentage differences from adjacent nodes in acceleration and dynamics deformation using LS-DYNA are 35% and 3% respectively. When using AUTODYN remap, the averaged percentage differences in acceleration and deformation are 10% and 6% respectively. Based on these findings, it is possible that the discrepancies in term of acceleration between the simulation results and the experimental results are more than in terms of deformation.

Results in section 4.2.7 indicate that overall, AUTODYN 3D (multi-materials), LS-DYNA with CONWEP, and AUTODYN remap models gave comparable results to the experiment, on average, approximately 28%, 31%, and 59% relative difference was observed respectively.

AUTODYN 2D model gave an averaged relative difference of 86% due to geometric dissimilarity. It assumed the target plate to be in circular instead of square shape, which caused different resistance to the blast. AUTODYN 2D (areal) model having equivalent mass yielded 78% relative difference from the experimental results, which was better than the former 2D model but was not as good as the 3D models. Boyd's simulation gave an averaged 59% difference when compared with the experiments. This was as a result of uniform loading being applied to the plate which was different from the experiment, in that the pressure impacting on the plate varies, with the maximum expected at the nearest point to the explosive. Accelerations were recorded directly at the nodes instead of the recommended acceleration card method from the later version of LS-DYNA. The material was assumed to be isotropic elastic plastic that ignored strain rate effects, which often occurs in the ductile materials.

There are many parameters that may have influenced the results. The experiment itself might have some errors such as exact location of the charge with respect to the target plate, the position and the condition of the plate, (how bent and rusty), the movement of the rig due to the blast and the accuracy with which measurements were taken. These can all have significant effects on the results. In addition, the simulation assumed that the plate edge was fully constrained in all degrees of freedom, which was not quite happening in the experiment. The gauge position in LS-DYNA and AUTODYN were not at the exact

location, though very near, because it depended on the grid position on the plate. Parameters in Johnson and Cook material model should have come from the laboratory test of the actual steel plate used in Boyd's experiment. In addition, the nature of the blast produces very high pressure. Because of these many variables, Vulitsky and Karni (2002) mentioned that in explosion predictions, discrepancies of up to 100% or even higher with respect to the experiment data was found in many literatures.

Because of the nature of mine blast experiments which consume high resources, it is very rare to conduct experiments as much as the researcher wanted to. In terms of Boyd's experiment, it seemed that only one test on each stand-off distance was performed, except for 0.25m, which was done twice. As a result it is difficult, in scientific terms, to say how reproducible the results are.

4.3 Double plate structures simulations

In order to further confirm the validity of the numerical simulations and to extend the work to double plate structure case, the following numerical simulation involved a double plate structure subjected to mine blast. The results and discussions from single plate simulations will be reported later on in this chapter. The methodology from AUTODYN 2D axis-symmetric model will not be used in double plate structure because it did not really account for the shape of the plate. The plate in the simulation was a circular shape instead of a square (rectangular) shape because of the way it was modelled as a 2D axial symmetric model. Both circular plates from AUTODYN 2D were also of a different size from the square plate used in AUTODYN 3D. In reality, considering the plate is fixed in all degrees of freedom, a circular plate and a rectangular plate may behave differently when encountering the blast. In double plate simulation, where two plates are used, it may behave even more differently and hence both cases were not included.

4.3.1 Experiments from Sharples (2002)

Following experiments on single-plate structure from Boyd (2000), Sharples (2002) has performed experiments to evaluate the resistive performance against a mine blast for four different configurations, namely homogeneous single steel plate, spaced steel, bonded and unbonded honeycomb core sandwich configurations (an aluminium honeycomb core surrounded by steel plates). The experimental results of the spaced steel target plates with 93 mm gap in between the plates were used to compare and validate the numerical simulations. It involved detonation of 0.5 kg of PE4 in the air at stand-off distances of 0.1, 0.2, 0.3, 0.4, and 0.5 m from the first (top) plate as shown in Figure 4.18. 500×500×6-mm target plates (BS EN 10025: S275JR) were constrained on a rigid rig by means of bolts. The final dimensions of each plate were reduced to 495×495 mm to allow for any misalignment of the rig during assembly. During experiments, only maximum permanent deformation was recorded, which is used for comparison with the numerical simulation.

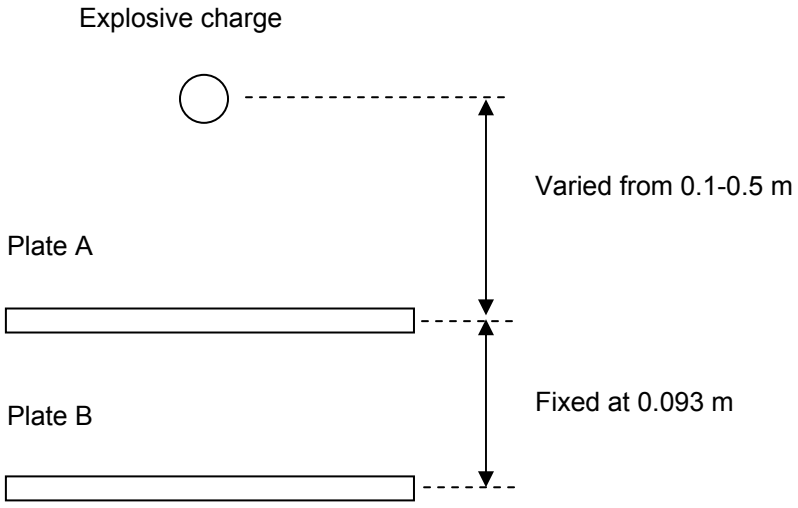

Figure 4.18 Schematic drawing of Sharples's experiment

4.3.2 LS-DYNA with CONWEP

Numerical simulation was created in the same way as of the single plate simulation as discussed in section 4.2.2. The method to find permanent deformation was not explained within LS-DYNA manual, Hallquist (1998). It is thought that permanent deformation can be obtained by finding the average value from the deformation curve. Alternatively a dynamic relaxation method is used to obtain permanent deformation. For trial purposes, firstly, single plate numerical simulations using both methods in finding the maximum permanent deformation were developed and compared together. A quarter symmetric model having shell elements representing target plate A was developed. Johnson and Cook material model was used to represent target plate material, as shown in Table 4.7. Figure 4.19 and Figure 4.20 were used to obtain permanent deformation using average deformation and dynamic relaxation approaches respectively. Results of single plate simulation, using average and dynamic relaxation methods are in Table 4.8.

Parameter	Parameter value
A	350 MPa
B	275 MPa
n	0.36
C	0.22
m	1.00

Table 4.7 Material property of 1006 steel used in Johnson and Cook material model to represent steel in Sharples's experiment, from Johnson and Cook (1983)

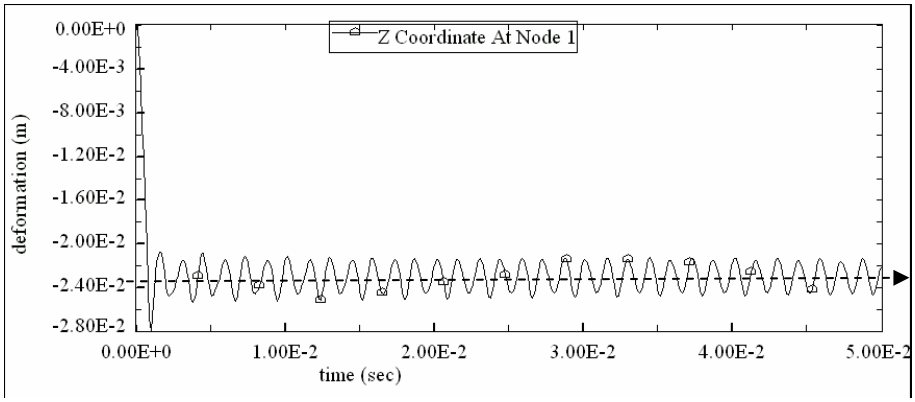

Figure 4.19 Method to find permanent deformation by finding the average value without dynamic relaxation (normal) at 0.4 m stand-off

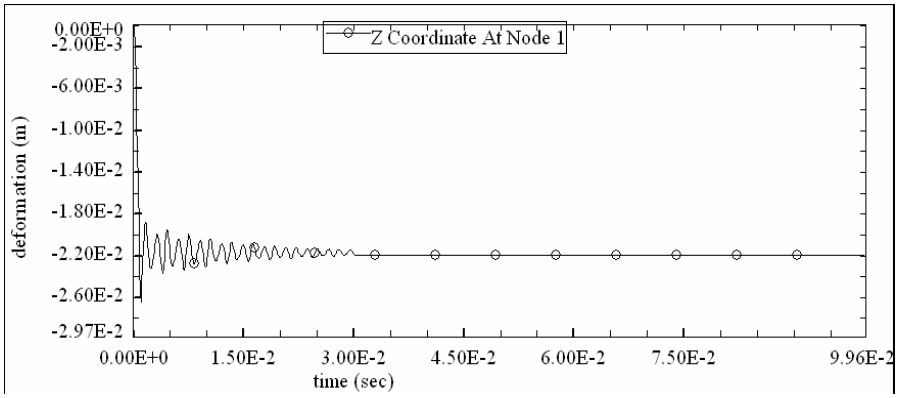

Figure 4.20 Method to find permanent deformation using dynamic relaxation at 0.4 m stand-off

Stand-off (m)	Maximum permanent deformation using average value from the curve (mm)	Maximum permanent deformation using dynamic relaxation method (mm)
0.5	–17.5	–16.0
0.4	–23.0	–22.0
0.3	–31.5	–31.0
0.2	–42.0	–42.0

Table 4.8 Maximum permanent deformation of Plate A (single plate configuration) using averaged value and dynamic relaxation methods.

From the initial results in Table 4.8, it is observed that as the stand-off distance increases, the permanent deformation reduces. This is in line with our expectation. The maximum permanent deformation for all other stand off distances using 'average value' and 'dynamic

relaxation' methods are very close to each other. The difference between them is no more than 1.5 mm. Therefore using either method will provide similar results. The model is progressed further by including plate B. In order to model both plate A and B accurately, air must be included as a medium between the two plates in order to transmit the blast load from the first plate (plate A) to the second plate (plate B), as shown in Figure 4.21. Air was represented by solid elements with Eulerian formulation and using a linear polynomial equation of state. Both plates were modelled using shell elements with Lagrangian formulation. For stability and effective transmission of the load, the nodes at the boundary between the plates and air were merged together. LS-DYNA with CONWEP (without air) simulations were also developed to compare the effect of modelling with air and without air. The procedures were exactly the same but the air elements were deleted. The results are in Table 4.9. LS-DYNA with CONWEP (without air) simulations were developed further to investigate the effects at stand off distances between 0.1 – 0.2 m. The results are in Table 4.10.

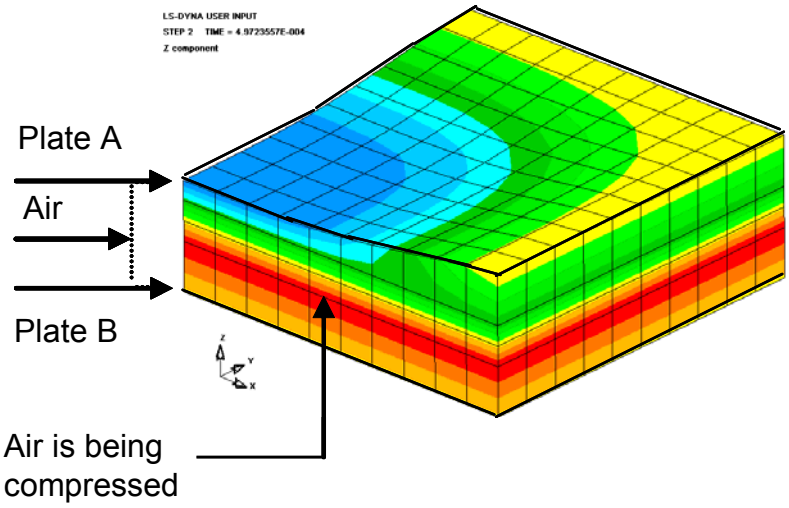

Figure 4.21 Contour of z-deformation results of deformed double plate with air in-between at 0.3m stand-off at ~0.001s using LS-DYNA with CONWEP methodology

4.3.3 AUTODYN 3D using multi-materials method

A 3D double plate model was set up using the procedure explained earlier in section 4.2.5. A quarter symmetric model of explosive charge, air, and two plates was developed. Both plates were fixed in all degrees of freedom around their edges. Mesh sensitivity analysis using 5, 4, and 3 mm mesh size at 0.1m stand-off distance were performed. The results have showed little change in maximum permanent deformation on plate A with only 6% difference in 5 mm and 3 mm mesh size and there was virtually no deformation on plate B in all cases. However, by using 0.2 – 0.5 m stand-off, the simulation did not work because of lack of sufficient computational resources. It was then decided to use Eulerian element size of 5 mm while the size of the plate element was 10 x 10 x 6 mm. Note that the maximum permanent deformation was obtained using the average deformation approach.

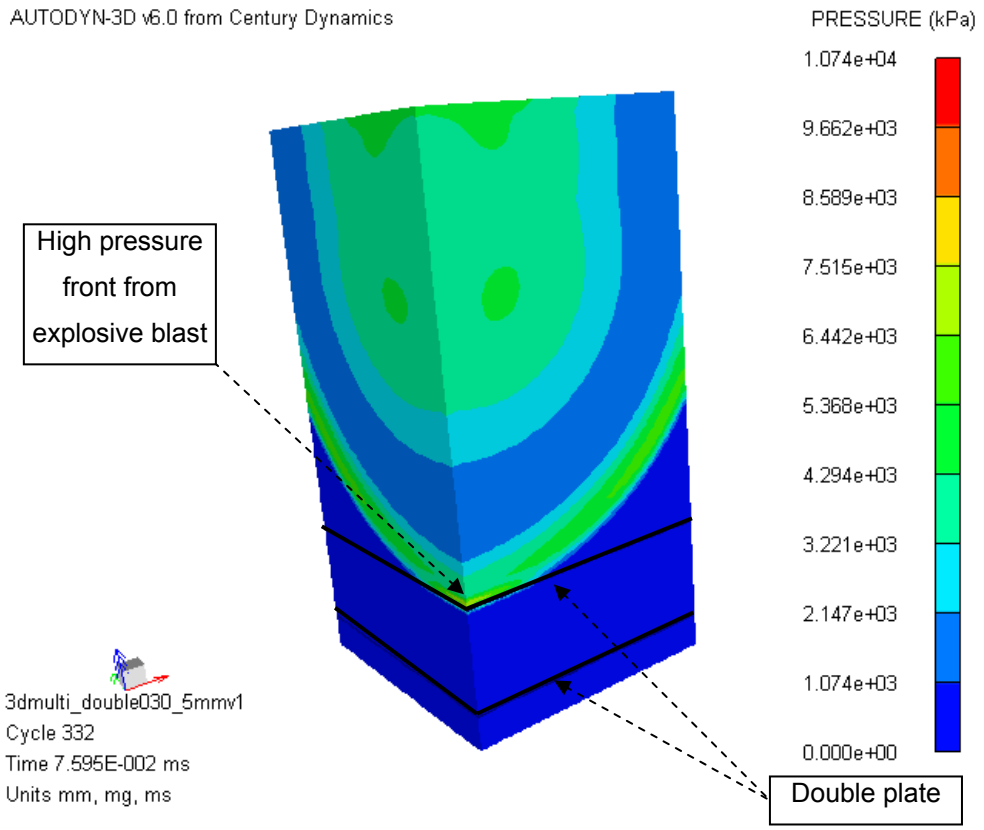

Figure 4.22 Example pressure gradient plot of double plate simulation using AUTODYN 3D multi-materials methodology

4.3.4 AUTODYN 3D using remapping method

The methodology reported in section 4.2.6 was used to develop a 3D model. A similar wedge was developed to simulate mine explosive initiation and expansion of explosive products. Upon reaching stand-off distance under consideration, the simulation was stopped to save the remapped file. In the second stage, a 3D double plate model having an air gap between them was developed using Eulerian and shell elements. Mesh density for both the air and plate model was the same as in section 4.3.3 while mesh density for the wedge model was the same as of earlier model discussed in section 4.2.6.

4.3.5 Double plate results

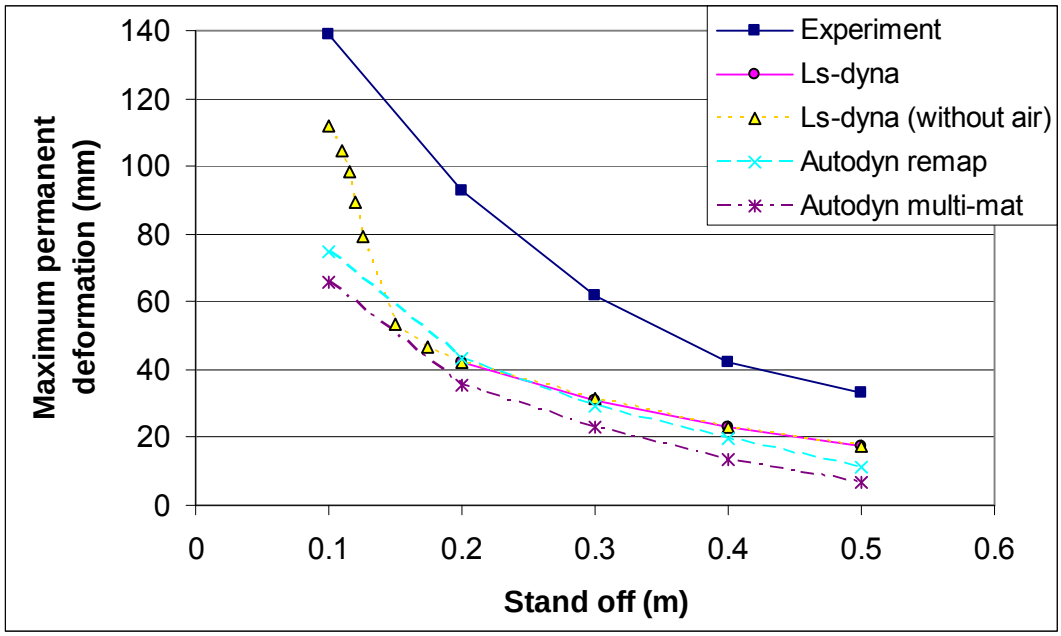

Figure 4.23 Comparing maximum permanent deformation results on plate A from different methodologies with experimental results from Sharples (2002)

Stand off distances(m)	Maximum permanent deformation (mm)				
	0.1	0.2	0.3	0.4	0.5
Experiment	37.00	1.00	0	0	0
LS-DYNA with CONWEP	n/a	1.03	0.99	0.96	0.95
LS-DYNA with CONWEP (without air)	41.00	0	0	0	0
AUTODYN remap	0	0	0	0	0
AUTODYN multi-mat	0	0	0	0	0

Table 4.9 Comparing maximum permanent deformation results on plate B from different methodologies with experimental results from Sharples (2002)

Stand off distances(m)	Maximum permanent deformation (mm)							
	0.1	0.110	0.115	0.120	0.125	0.150	0.175	0.2
LS-DYNA with CONWEP (without air)	41.00	21.50	12.25	2.30	0	0	0	0

Table 4.10 Maximum permanent deformation results on plate B at stand off distances between 0.1 – 0.2 m using LS-DYNA with CONWEP (without air)

4.3.6 Double plate discussion

It is observed that the maximum permanent deformation in plate 'A' is comparable with the experiments as shown in Figure 4.23. LS-DYNA with CONWEP, AUTODYN 3D remap, and AUTODYN 3D (multi-materials) gave an averaged under estimate of 49%, 54%, and 65% when compared with the experiments respectively. These discrepancies were in line with the single plate analysis, though they are higher. The deformation discrepancies in the single plate analysis are based on the maximum dynamic deformation, while in the double plate analysis, they are based on the permanent deformation. Discussions on these discrepancies are similar to single plate simulation, which have already been discussed in section 4.2.8. It should be noted again that discrepancies from experiments in mine blast

simulations of up to 100% or even higher have been reported in various literatures as mentioned in Vulitsky and Karni (2002). Smith and Hetherington (1994) commented that the accuracy of prediction and measurements in the near field is lower than in the far field because of the complexity of the flow processes involved in forming the blast wave close to the charge where the influence of the explosive gases is difficult to quantify. Note that the near field is defined as the scale distance (the ratio of the distance from the charge centre (m) to the cube root of the charge weight (kg TNT)) of less than 0.3. Note that the scale distances used in the double plate analysis are 0.095 (0.1 m stand off), 0.190 (0.2 m stand off), 0.285 (0.3 m stand off), 0.380 (0.4 m stand off), and 0.475 (0.5 m stand off), while in the single plate analysis are 0.165 (0.25 m stand off), 0.263 (0.4 m stand off), and 0.329 (0.5 m stand off).

In addition to the discussion of discrepancies as in section 4.2.8, LS-DYNA with CONWEP method, whose blast loading is applied using empirically derived method (CONWEP), is based on some assumptions and estimations. It can only apply blast load on geometrically simple structure using *LOAD_BLAST card. It cannot apply blast load on a more complex structure. For example, if one considers a simulation of a vertical plate subjected to a mine blast situated on the same vertical plane as of the plate using LS-DYNA with CONWEP. The blast load will be applied directly on the plate as if the blast is at right angle to the plate, which is wrong. The same problem applies to angle plate and other complex structures. Other assumptions such as the charge is assumed to be spherical in shape and needs to be converted to TNT equivalent, in addition it extrapolates the load curve in order give the blast load at certain distance (for example, it has only six sets of data results from the centre of the charge up to 100 mm for 1 kg of TNT spherical burst). These assumptions render LS-DYNA with CONWEP unsuitable for further analysis in this thesis. Note that LS-DYNA with CONWEP can still be useful in simple simulations, such as a horizontal plate structure model. It can give acceptable results with a much shorter run time compared with the AUTODYN because the blast load has already been formulated prior to running the analysis. It took only a few minutes to run the problem of single plate structure. When modelling LS-DYNA with CONWEP in double plate structure, the run time can be reduced. Showichen *et al* (2005) suggested that, in this simulation configuration where air between the two plates can easily escape, modelling with air or

without air gave virtually exactly the same permanent deformation of the plate. Hence modelling without air and applying the load only on the top plate in LS-DYNA with CONWEP model can be used instead to simplify the cases where only permanent deformation result is required. However, there are some dynamic deformations on plate B, which can be seen in Figure 4.24.

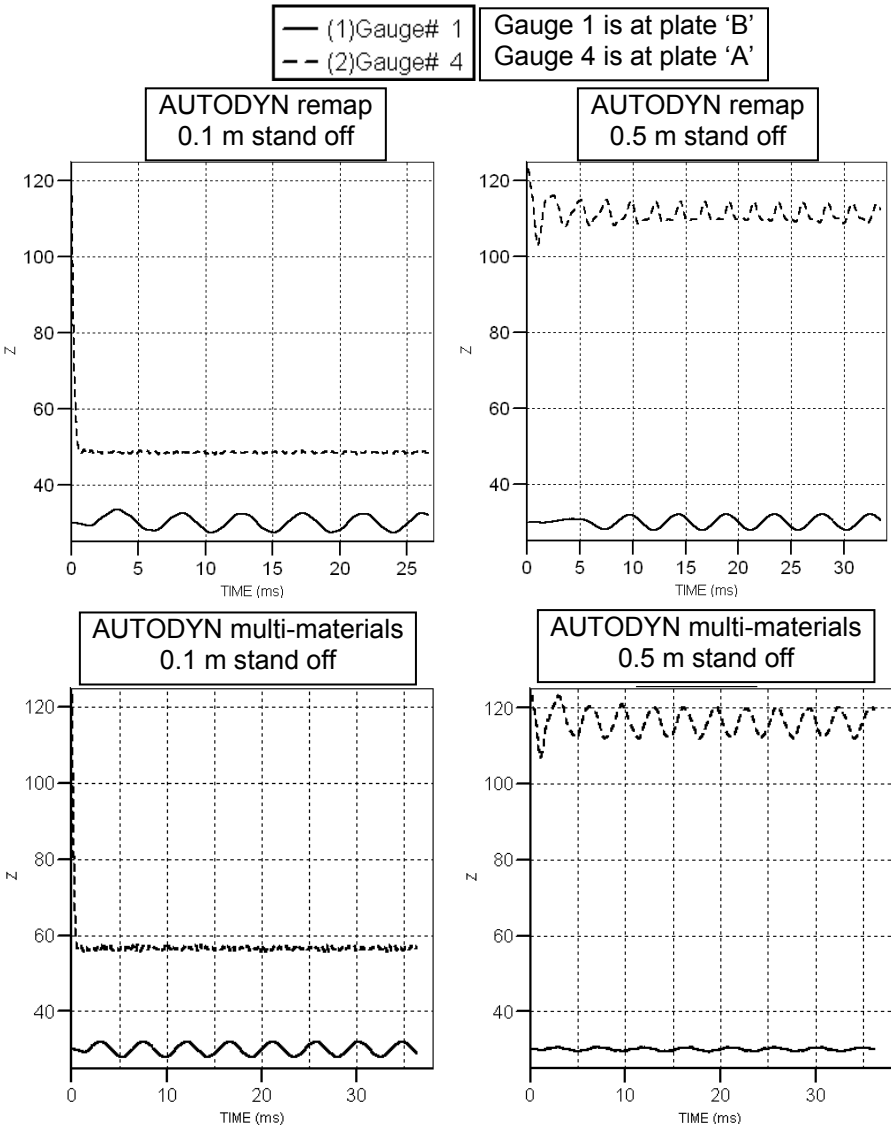

Figure 4.24 Deformation plots of AUTODYN remap and AUTODYN multi-materials method at 0.1 m and 0.5 m.

Note that LS-DYNA with CONWEP (without air) simulations were included in the results to compare modelling with air and without air. The results showed that modelling with air

or without air gave virtually the same permanent deformation results. This is due to the configuration of Sharple's experiments which allowed air to escape and hence did little to influence the permanent deformation results. LS-DYNA with CONWEP (without air) simulations were also used to investigate the collision between plate 'A' and plate 'B' between 0.1 m to 0.2 m stand off distances. The results showed that plate 'A' impacted plate 'B' and forced plate 'B' to deform at 0.100 m, 0.110 m, 0.115 m, and 0.120 m stand off distances, the example of which can be shown in Figure 4.25. Plate 'B' was fixed in all degrees of freedom and there were no air elements to transfer the load, Hence, plate 'B' deformed purely due to the deformation in plate 'A'. Apart from the results of LS-DYNA with CONWEP (without air) at 0.1 m – 0.12 m stand off distances, all other results showed that plate 'A' did not touch plate 'B'. Maximum permanent deformations at plate 'B' from LS-DYNA were comparable with the experimental results while in 'AUTODYN 3D remap' and 'multi-materials' methods were very small and were quoted as zero. Figure 4.24 shows the deformation plots from AUTODYN remap and AUTODYN multi-materials methods at 0.1 and 0.5 m stand off distances. It is evident from the plot that plate 'A' did not touch plate 'B'.

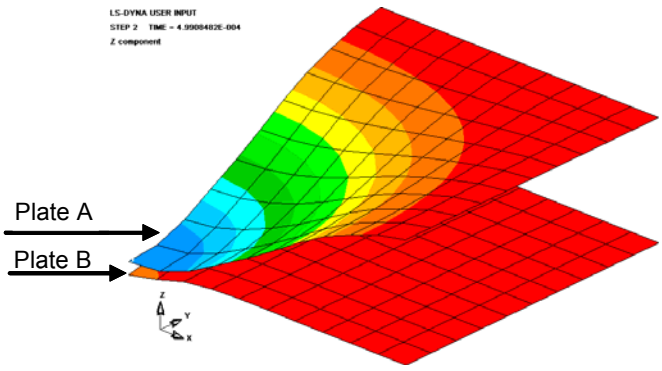

Figure 4.25 Contour z-deformation of double plate structure using LS-DYNA with CONWEP (without air) at 0.110 m stand off, at ~ 0.5 ms.

Figure 4.23 indicates that as the stand-off increases the maximum permanent deformation in plate 'A' decreases. It is also noticed that in AUTODYN 3D and AUTODYN remap, the closer the double plate structure to the explosive, the more the simulation results deviates

away from the experimental results. In AUTODYN 3D (multi-materials) and AUTODYN 3D remap analyses, due to the small stand-off distance the explosive products may not have completely expanded and transferred its energy to the plate. In AUTODYN 3D remap method, during blast load creation in AUTODYN 2D, one needs to estimate that at a certain point the explosive expands and behaves like ideal gas so that it is ready to remap into AUTODYN 3D single material. This is done by looking at the compressibility plot during the simulation running if it is less than -0.99. All other stand-off distances were within this criterion except at 0.1 m stand-off distance. At 0.1 m stand-off, its compressibility was still slightly more than -0.99, however the pressure front had just arrived at 0.1 m distance which forced the simulation to stop and remapped into AUTODYN 3D. This has made 0.1 m stand-off results to be more different from the experimental results than other distances. In LS-DYNA (without air), the maximum permanent deformation was increased significantly at stand off distance of 0.125, 0.120, 0.115, 0.110, and 0.100 m compared with the trend at other stand off distances. By using the actual CONWEP software (not LS-DYNA), Hyde (1991) to find out the blast parameters at these stand off distances using the same amount of charge, the software has given out a warning message. The message was 'scaled distance is out of range for duration calculation, waveform may not be accurate'. Using other stand off distances, such as 0.150 m, did not get this message. It is likely that at very close range (0.125 – 0.100 m or in scale distance terms, 0.095 - 0.119 m/kg$^{1/3}$), the blast parameters generated in LS-DYNA were based heavily on extrapolation. Interestingly, the maximum permanent deformations at these close range stand off distances were much closer to the experiments than the other stand off distances. However, it should be noted that the results acquired using these close range stand off distances may not be accurate.

It was observed that the double-plate configuration significantly reduces the damage to the bottom plate (plate B) in comparison to the plate in the single plate configuration. For example, the gap between the two plates is estimated to be 0.1 m (instead of 0.093 m) and the top plate (plate 'A') of the double plate configuration is equivalent to the plate in the single plate configuration. So by considering the effect on the plate at the same stand off distance (as in Figure 4.18 configuration), plate 'A' at a stand-off distance of 0.3 m can be compared with plate 'B' at a stand off distance of 0.2 m. Considering the LS-DYNA with

CONWEP method, the deformation of plate 'A' at 0.3 m stand off distance in Figure 4.16 is 31.5 mm, while the deformation of plate 'B' at 0.2 m stand off distance in Table 4.3 is 1 mm. This confirms that the double-plate configuration significantly reduces the damage in comparison to the single plate configuration, though with the weight penalty.

In order to clarify the above discussion, more works were performed. In Figure 4.26, it is assumed that the blast origin is at the ground (below the plates) and also the top plate or the single plate is assumed to be the occupant's floor. The numerical simulations in all 4 cases were developed using LS-DYNA with CONWEP method and their maximum permanent deformation results are compared. By having 2 x plates of 6 mm thickness (as in case II), it will double the mass in comparison of just 1 x plate of 6 mm thickness (as in case I) and reduce the ground clearance of the vehicle. However, it will add protection to the crew as the plate near the crew only deformed about 1 mm (case II) in comparison to 31.5 mm (case I). Although case II and case III have the same mass, case III, which use a single 12 mm thick plate gave maximum permanent deformation of 11.5 mm. Case IV, which use a single 12 mm thick plate gave maximum permanent deformation of 19.5 mm. Although case II may intrude crew compartment more case IV but it has offered more protection to the crew inside, especially at the plate near the crew.

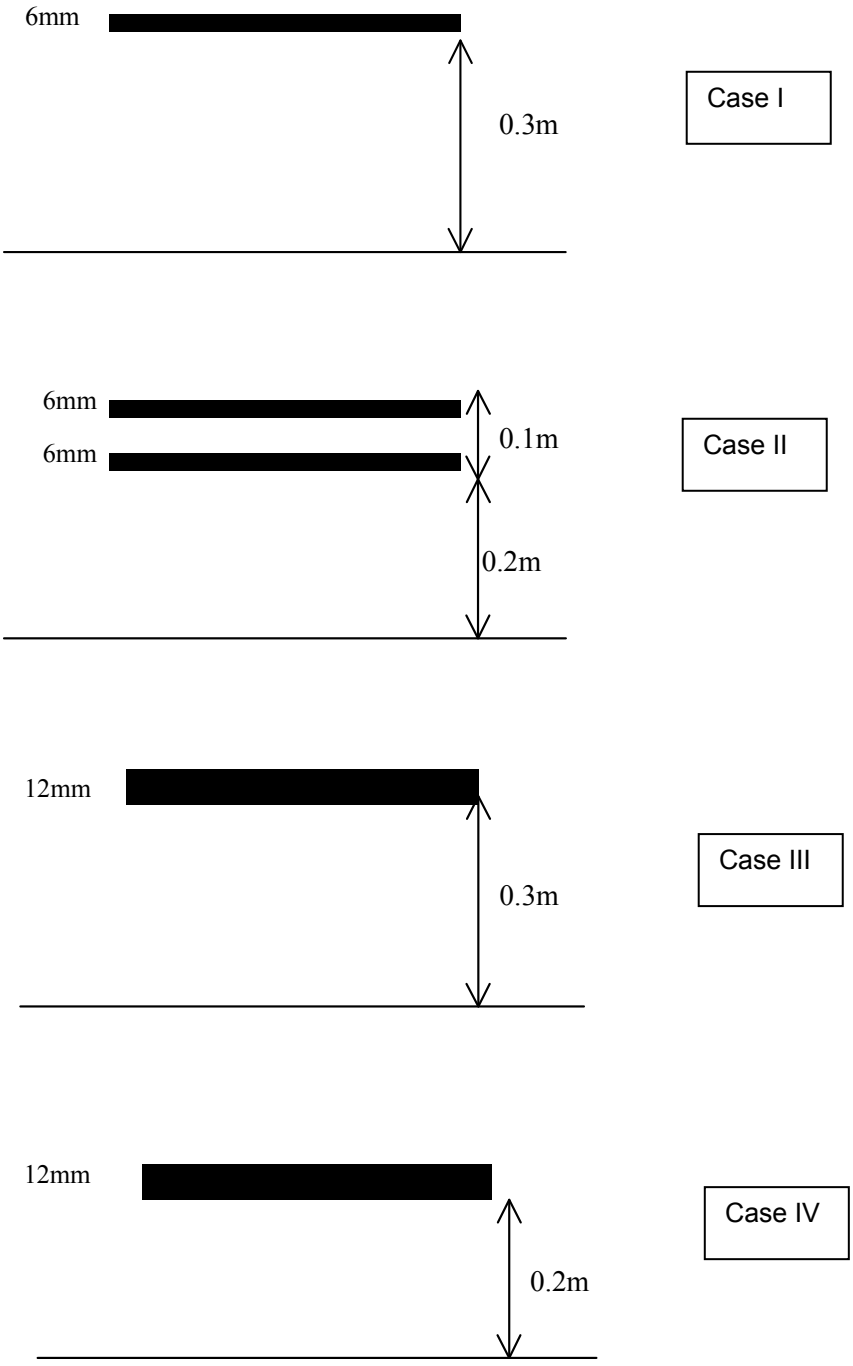

Figure 4.26 comparison on different scenarios of single and double plate configurations subjected to a mine blast

Overall, results from single and double plates using LS-DYNA with CONWEP, AUTODYN 3D remap, and AUTODYN 3D multi-materials methods seemed comparable with experimental results. As has been discussed, LS-DYNA with CONWEP is limited to

simple structural problems because it can only apply the blast load at the structure face directly, making it unrealistic in more complex shape such as 'V' plate. Computation time is short because the blast load has been formulated and ready to use. However, the blast load is from CONWEP which sometimes may be based on estimations and assumptions, and hence may not be suitable in some cases.

Computational time in AUTODYN 3D multi-materials is longer comparing to single-material model because there are at least two Eulerian materials, which AUTODYN needs to analyse their interaction with each other, in addition to the interaction to the structure models. It consumes high computer resources and hence needs advanced computer equipment in order to cope with the scale of the simulation and provide acceptable results. This has made it unsuitable for larger problems.

AUTODYN 3D remap relies on the blast load from AUTODYN 2D multi-materials model which unlike AUTODYN 3D multi-materials model, can have finer meshes with less time penalty. The blast load is then remapped onto AUTODYN 3D single material which does not need to calculate the interaction process between Eulerian materials. This speeds up the running time enormously. However, it assumes that the mixture of explosive and air just before it is remapped behaves like an ideal gas in order to be able to remap into AUTODYN 3D single material. If the stand-off distance is too short, the mixture of explosive and air may not have expanded enough to be like an ideal gas. It is therefore not suitable for very small stand-off distances.

Note that generally, the permanent deflections become small compared to the maximum deflections. In Figure 4.20, the dynamic deflections are only slightly larger than the permanent deflection, this is unusual but possible because the size of plate is relatively small (0.5 x 0.5 x 0.006 m). By increasing the plate size to 2.5 x 2.5 x 0.006 m, as in Figure 4.27, a different deflection time history plot occurs. Figure 4.28 – 4.34 show the comparison results between the two different size plates, 0.5 x 0.5 x 0.006 m and 2.5 x 2.5 x 0.006 m at 0.05 and 0.5 seconds durations, keeping all other configurations the same as previously used in Figure 4.20. Results indicate that using different plate geometries gave different deflection time history results. Having a larger plate size allows the plate to

deform dynamically more but gives less permanent deflection; in this example, the permanent deflection is virtually zero. The blast load (force) applied on the big plate (2.5 x 2.5 x 0.006 m) contain the same blast load applied on the same area as the small plate (0.5 x 0.5 x 0.006 m) plus the blast load applied on the rest of the plate. Because the charge is in spherical shape, the blast load varies according to the distance from the centre of the charge. Therefore the total blast pressure (blast load (force) per unit area) applied on the small plate is higher than the total blast pressure on the big plate and hence creates more permanent deformation. However, because the blast load applied mainly at the centre, the size of the plate allows the plate more freedom to move under load. This can be seen that the maximum dynamic deformation of the big plate is more than the dynamic deformation of the small plate.

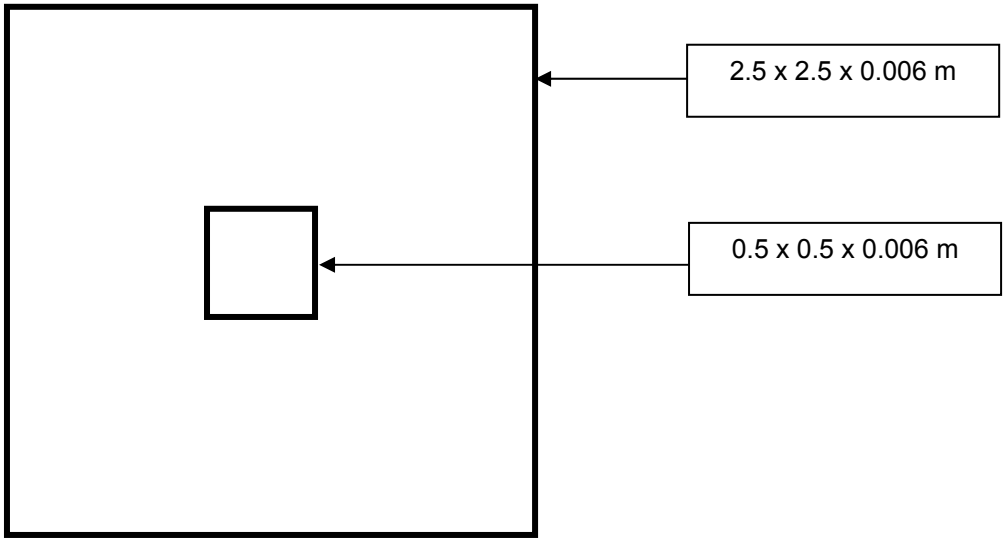

Figure 4.27 Two different plate sizes, 0.5 x 0.5 x 0.006 m and 2.5 x 2.5 x 0.006 m, were used in the simulations. The sizes of the plates were scaled down relative to each other.

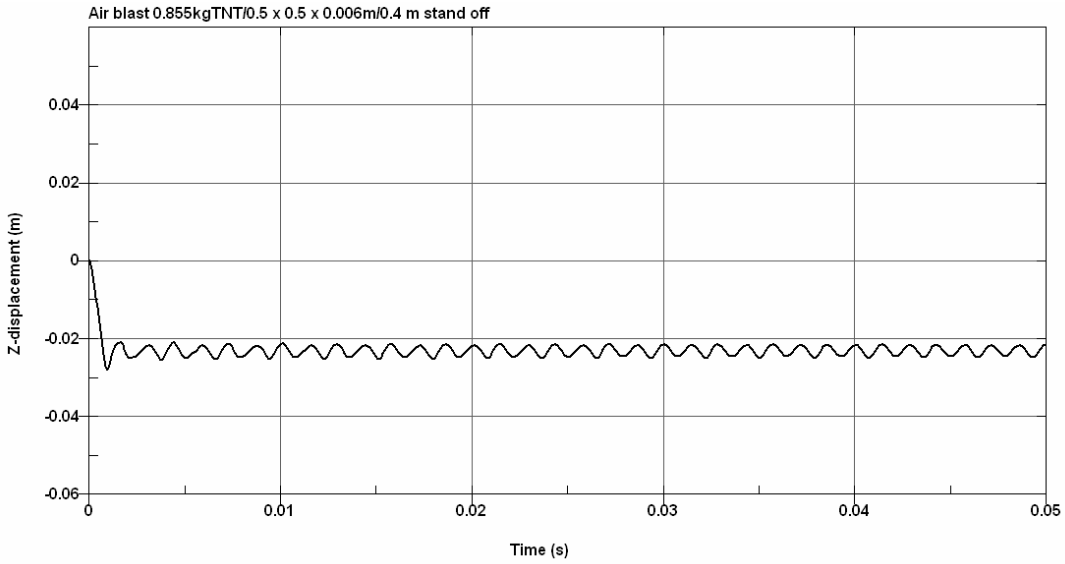

Figure 4.28 Deflection time history results for 0.05 seconds duration of a single 0.5 x 0.5 x 0.006m mild steel plate (measured at the centre of the plate) subjected to 0.855 kg TNT blast in the air at 0.4 m stand off

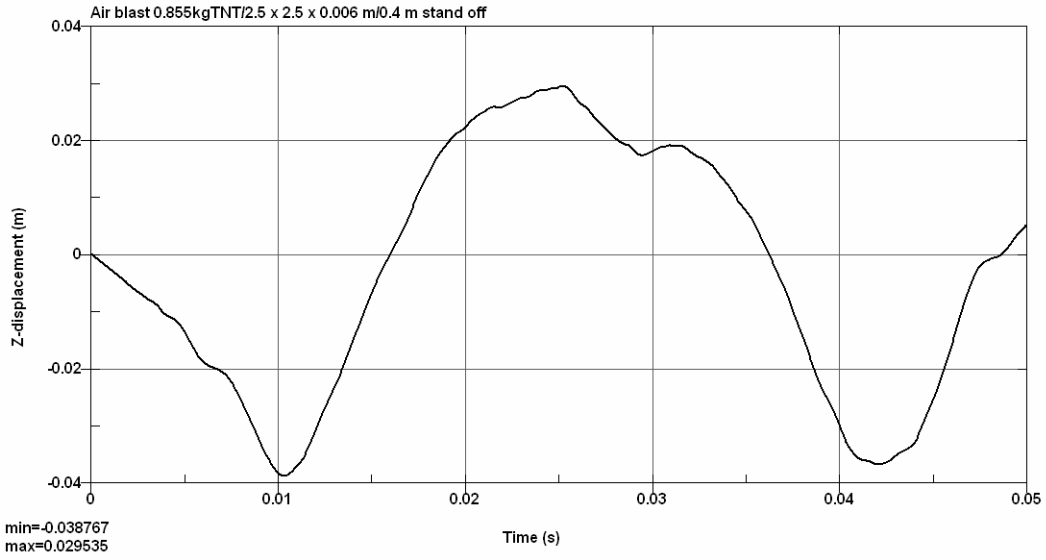

Figure 4.29 Deflection time history results for 0.05 seconds duration of a single 2.5 x 2.5 x 0.006m mild steel plate (measured at the centre of the plate) subjected to 0.855 kg TNT blast in the air at 0.4 m stand off

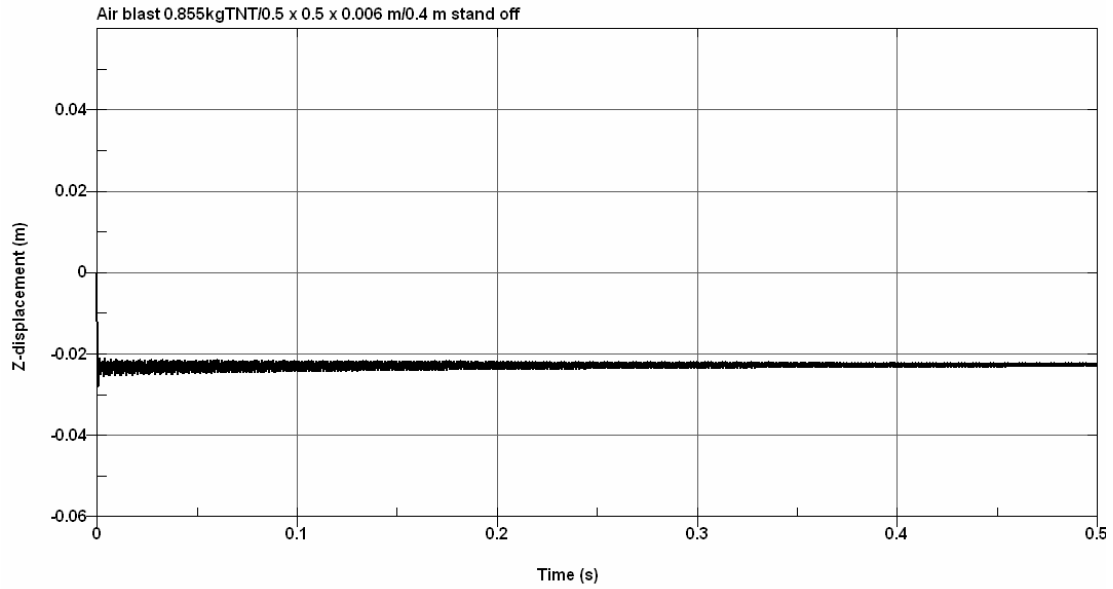

Figure 4.30 Deflection time history results for 0.5 seconds duration of a single 0.5 x 0.5 x 0.006m mild steel plate (measured at the centre of the plate) subjected to 0.855 kg TNT blast in the air at 0.4 m stand off

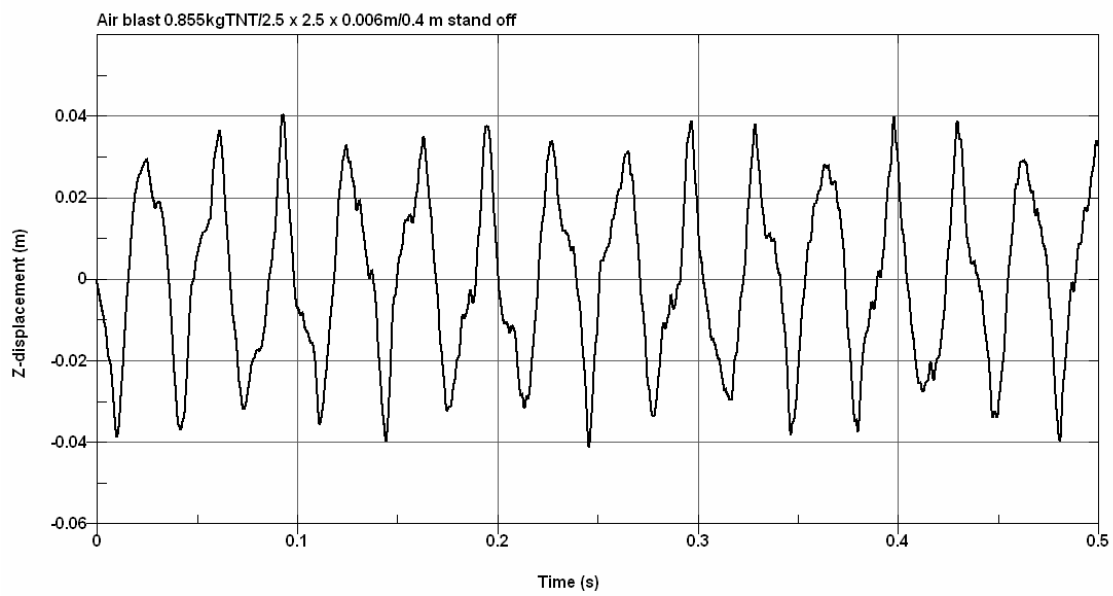

Figure 4.31 Deflection time history results for 0.5 seconds duration of a single 2.5 x 2.5 x 0.006m mild steel plate (measured at the centre of the plate) subjected to 0.855 kg TNT blast in the air at 0.4 m stand off

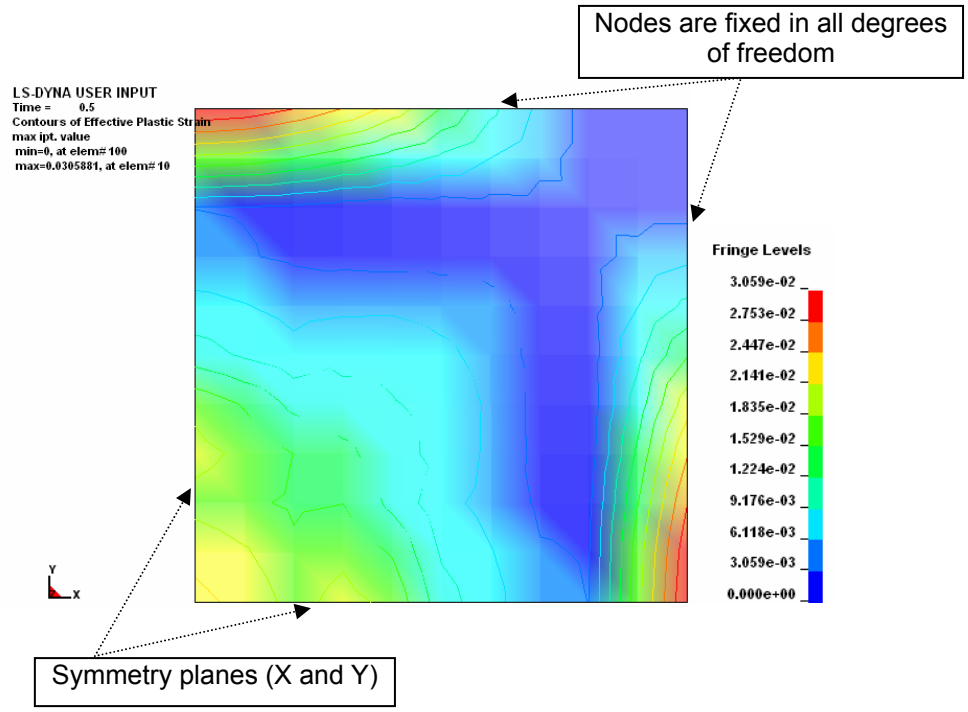

Figure 4.32 Plastic strain contour plot of a quarter model (0.5 x 0.5 x 0.006 m in full plate dimension) after 0.5 seconds

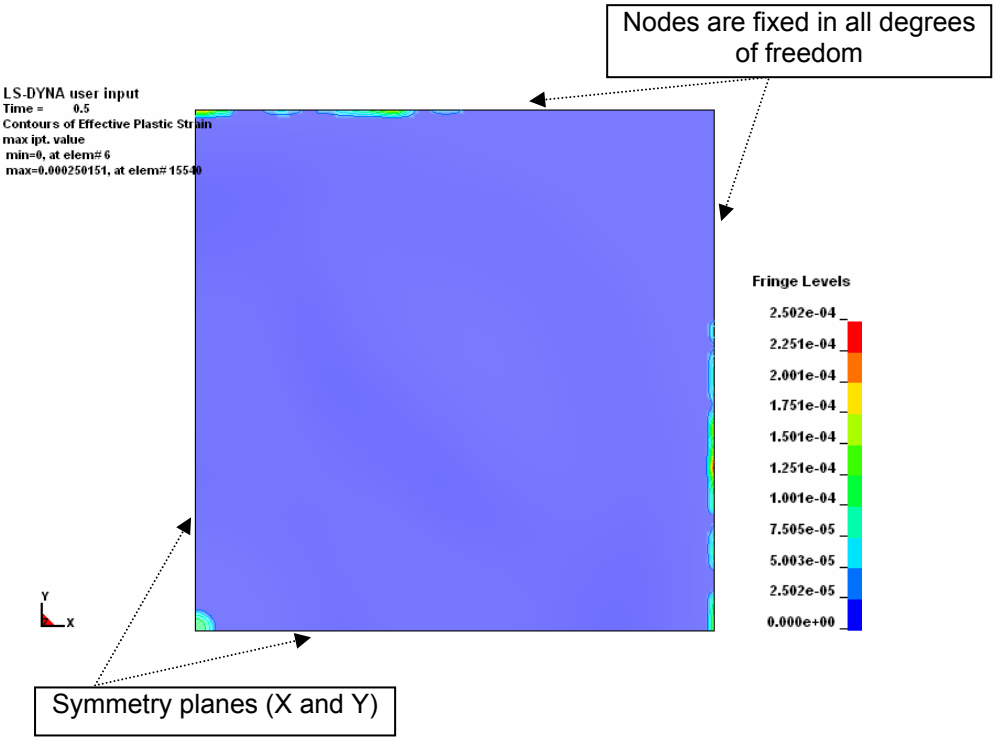

Figure 4.33 Plastic strain contour plot of a quarter model (2.5 x 2.5 x 0.006 m in full plate dimension) after 0.5 seconds

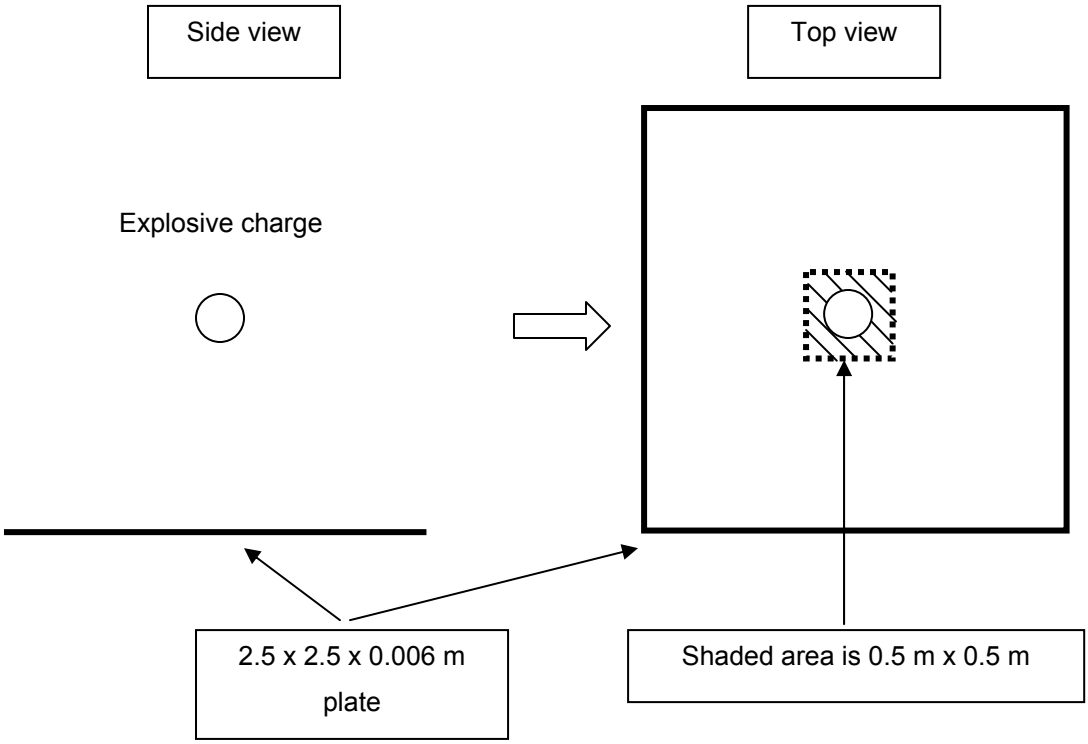

Figure 4.34 Schematic drawing showing the shaded area on the 2.5 x 2.5 x 0.006 m plate which has the same blast load as on the 0.5 x 0.5 x 0.006 m.

4.4 Conclusions

The effects of a mine blast on a simple structure such as a plate have been modelled using LS-DYNA with CONWEP, AUTODYN 3D remap, and AUTODYN 3D multi-materials methods. The modelling techniques have been verified with Boyd's method and the results seem comparable with his experiments. The models were then used to analyse a double plate structure and compare with Sharple's experiments. The results showed that a spaced structure can mitigate the effect of blast on the further panel and thereby reduce the damaging effects. Although there are lots of uncertainties which can have a significant effect, results have demonstrated reasonable agreement with the experiments.

The use of AUTODYN 3D remap and AUTODYN 3D multi-materials methods have been validated with experimental results in both single and double plate models as described above. The closeness to the explosive may cause the simulations to be more divergent from experimental results. It is the most appropriate action to try to avoid simulation at small stand off distances such as at 0.1 m. In the next chapter vehicle bottom structures with different bottom shape models are developed without further comparisons to the experimental results. From experiences in single and double plate models, because the AUTODYN 3D multi-materials method took so long to run and consumed high computer resources, it is considered not suitable for larger problems like typical vehicle bottom size. AUTODYN 3D remap method is the suitable alternative in further simulations.

CHAPTER 5 Development of vehicle hull numerical simulations

Following the analysis and validation of single and double plate numerical models subjected to a mine explosion, with that of experiments, this chapter extends the study by modelling vehicle hull models. This is assumed to be in a single-floor and a double-floor design and hence, firstly, may be represented as a single plate and a box-shape. They are then developed further to be a single-floor vehicle hull and a double-floor vehicle hull models. The results will be compared in this chapter.

5.1 Introduction

In Chapter 4, it was concluded that AUTODYN 3D remap was going to be used to analyse further simulations in a more realistic scenario because of its suitability, particularly in shorter computational time. The aim of this chapter is to develop numerical simulations, whose methodologies have been validated on single and double plate structure cases, on vehicle hull models of a single and a double floor configuration. This is in order to use the model in a parametric study in Chapter 6. Note that in this Chapter 5, the comparison between single floor and double floor configurations in the form of single plate and box models will not be performed because this comparison will be conducted in the form of single-floor vehicle hull and double-floor vehicle hull models in Chapter 6.

Before starting the analysis, it is important to establish the realistic scenario that is going to be used in the analysis with reasonable analysis time and resources. These are described as follows:

5.1.1 Vehicle bottom geometry

From the study of various literatures on the geometry of armoured vehicle bottom structures, it was noticed that most of the information is classified and is not available in the public domain. The available information is from armoured vehicles which were produced years ago. Foss (2000) shows that most armoured vehicles' hull dimensions are 2.5 m to 3.5 m wide x 5 m to 8.5 m long x 1.7 m high. For computational time reasons, it was decided to use the smaller figure of 2.5 m x 5 m. In reality, it is virtually impossible that the bottom of a vehicle is constructed from a single plate of 2.5 m x 5 m without any

stiffeners. There must be some form of support structure, such as stiffened beams on the plate, to maintain structural integrity. It is assumed conservatively that the vehicle bottom structure comprises of effectively 2 separate plates, each being 2.5 m x 2.5 m, which is equivalent to 2.5 m x 5 m, in total. Each plate essentially has a support structure on its edges from the side plate, as shown in Figure 5.1.

Information on plate thickness is difficult to find. However, Foss (2000) indicates that the most recent available information is: T-62 has the floor thickness of 20 mm, Leopard 1 has floor thickness of 15 mm, and BTR-60P APC (first production in 1961) has plate thickness of 5 mm. It is proposed initially that 10, 20 and 30 mm thickness will be used which will represent variation in thicknesses used in armour vehicles' floor panels. The side panels are assumed to be 10 mm thick throughout.

It is assumed that at the vehicle bottom section, the double floor configuration represents a box-like structure. The bottom plate geometries are varied as 'horizontal', or 'V', shape at a 10 degree angle to the nearest horizontal axis (160 degree internal angle). An angle of more than 10 degrees may cause the vehicle bottom to be too big and out of proportion. In addition, it adds up an undesirable weight to the vehicle, thus reducing mobility. It also increases the simulation running time. The air gap between the main plates is also classified information. Based on a private discussion with a reliable source, it is believed that the height of the internal space (gap) may range between 50 to 100 mm. Having a gap more than this may reduce the useable compartment inside the vehicle and/or increase the vehicle height excessively. For comparison purpose with a 10 degree 'V' bottom hull model in Chapter 6, the height of side panels in a double-floor hull model is 118 mm as shown in Figure 5.2. Note that a ¼ symmetry model is used to reduce the computation time.

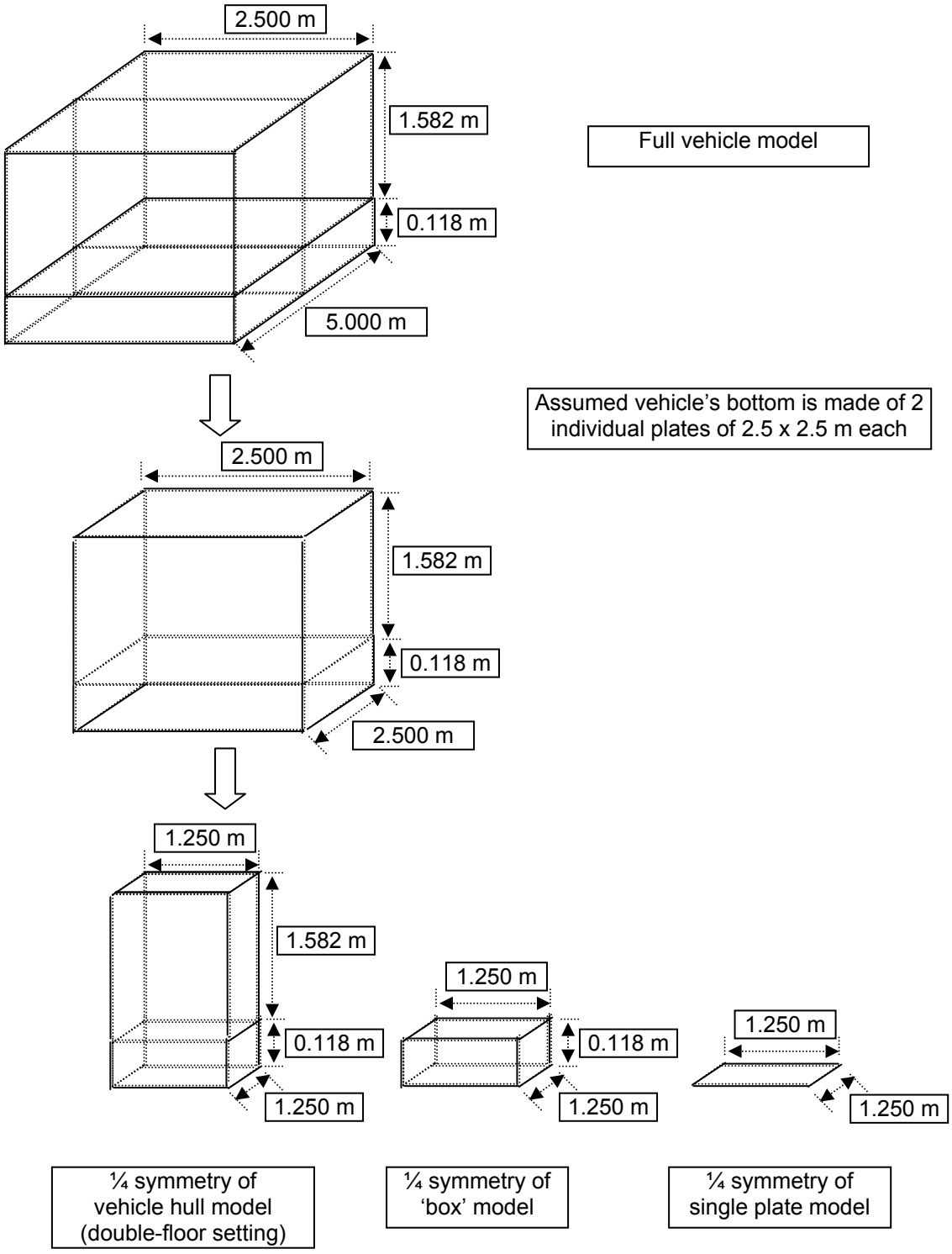

Figure 5.1 Schematic drawing on the derivation of ¼ models used in the numerical simulation based on full armoured vehicle figure (Note that the figure shown may not reflect the dimensions correctly, but the given dimensions have governed the actual size.)

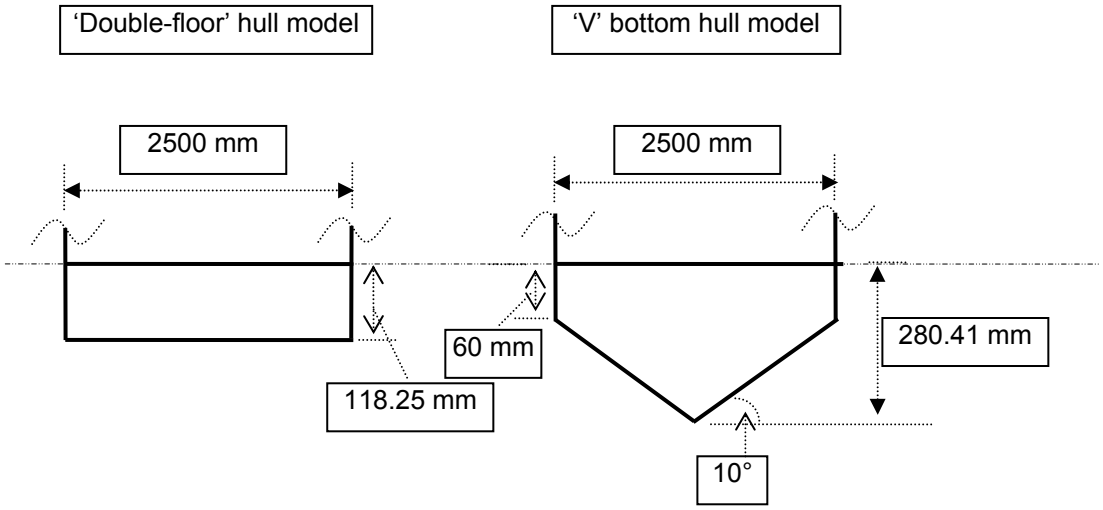

Figure 5.2 Schematic drawing of the vehicle bottom sections in the 'double-floor' hull model and the 'V' bottom hull model

5.1.2 Explosive charge

The research in mine blast loading derived from a mine being buried in the ground is very complex. The study of soil can take time to understand and to model correctly in the numerical simulation. Various soil properties and conditions can influence the blast loading differently. Some organisations and/or companies have heavily invested and dedicated their resources to contribute to this work. In order to simplify the blast loading, it is assumed that the charge is in an hemispherical shape place on a reflected boundary (see Figure 5.3). Later on in Chapter 7, a blast loading from an hemispherical charge on a reflected surface will be compared with a blast loading from a buried charge under 7.7% moisture content soil. The data analysis of available mines in Chapter 2 proposed to use 10 kg and 6.34 kg as explosive charges for modelling. The 10 kg TNT charge represents one of the worst case conditions from available AT mines, because few AT mines weigh more than this. The 6.34 kg TNT charge was chosen because the most widely used TM-57 mine (from the Russian Federation) contains this amount of explosive. In this chapter, for model development purpose, the amount of explosive charge used in the analysis is half of the proposed charge weight (mass). In Chapter 6, an explosive charge mass (weight) of 10 kg TNT in an hemispherical shape will be used in the analysis, in addition to 5 kg TNT and 3.17 kg TNT in an hemispherical shape. Based on the TNT density of 1.63×10^3 kg/m^3, Lee, Finger, and Collins (1973), it is found from the calculation that: 10 kg TNT charge in an hemispherical

shape has a radius of 143 mm, 5 kg TNT charge in an hemispherical shape has a radius of 114 mm, and 3.17 kg TNT charge in an hemispherical shape has a radius of 98 mm.

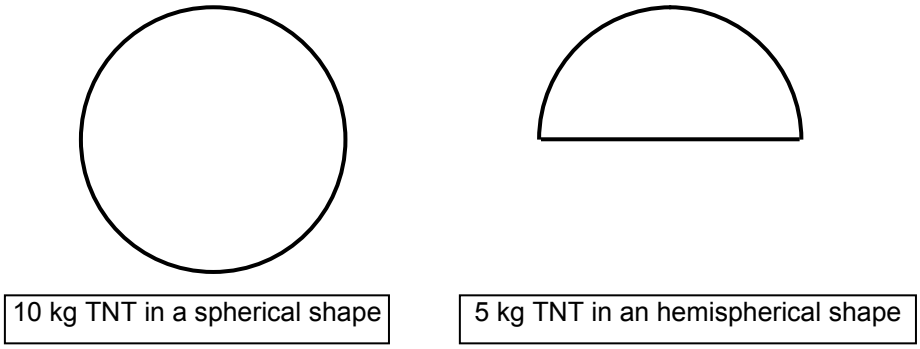

Figure 5.3 Formation of explosive charge in an hemispherical shape

5.1.3 Material property of the plate

Aluminium or steel (Rolled Homogeneous Armour (RHA)) armoured material is used mostly in the manufacture of armoured vehicles. For this study, properties of RHA were derived in the form of Johnson and Cook material model using split Hopkinson experiments by Gray *et al* (1994). These are presented in Table 5.1. The principal stress/strain failure model was used, where the parameters were from Riedel *et al* (2004), as shown in Table 5.2.

Parameter	Parameter value
A	1225 MPa
B	1575 MPa
n	0.768
C	0.0049
m	1.09
T_m	1783 K

Table 5.1 RHA steel material parameters for Johnson and Cook material model

Parameter	Parameter value
σ_{fail}	3800 MPa
ε_{fail}	50%

Table 5.2 RHA steel material parameters for principal stress/strain failure model

5.1.4 Stand-off distance

Fiserova *et al* (2004) has stated that, based on Foss (1999), most vehicles have a ground clearance between 200 – 600 mm. Because the scenario is of a surface-laid mine on a hard ground surface, the stand-off distance will be assumed to be the same as the vehicle ground clearance. Generally, from Foss (2000), ground clearance in armoured vehicles is around 0.4 m, e.g., BTR-60P is 0.475 m, T-72 is 0.43 m, M1A1 is 0.48 m, Alvis Vickers Saxon APC is 0.41 m. The results in Chapter 4 showed that, at a greater distance from the explosive charge, the results seemed to compare better with the experiment. Hence the proposed stand-off distances are 300, 400, 450, 500, and 600 mm. Note that the stand-off used in the simulation will be the distance between the centre of the explosive to the centre of the plate. In addition, the stand-off of one particular vehicle in the real scenario will also be varied depending on different factors, such as the ground property, ground conditions, and the tyre pressures. So this proposed stand-off distance will sufficiently cover the ranges of the real scenario.

5.2 Preliminary model

5.2.1 2D model

The first stage of the preliminary model was to create a model in AUTODYN 2D Euler multi-materials method in order to get the required blast loading from the given explosive charge. This axis-symmetric model consisted of TNT explosive charge and air, which was developed as shown in Figure 5.4. Mesh sensitivity analysis was performed to find the suitable mesh size which would provide acceptable results at a reasonable analysis time. Maximum pressure and maximum specific impulse were recorded at points on 300, 350, 400, 450, and 500 mm stand-off from the charge using 1.5 (0.135 million elements) , 1.25 (0.194 million elements), 1.0 (0.303 million elements), 0.75 (0.539 million elements), 0.5 (1.21 million elements), and 0.4 (1.891million elements) mm mesh size. The results are shown in Figures 5.5 – 5.9. Note that using a mesh size smaller than 0.4 mm gave 'memory allocation error' as this overloaded computational resources. The time taken to run 3000 cycles of each simulation on a computer with Intel ® Xeon 3.4 GHz and 3.0 GB of RAM was also recorded.

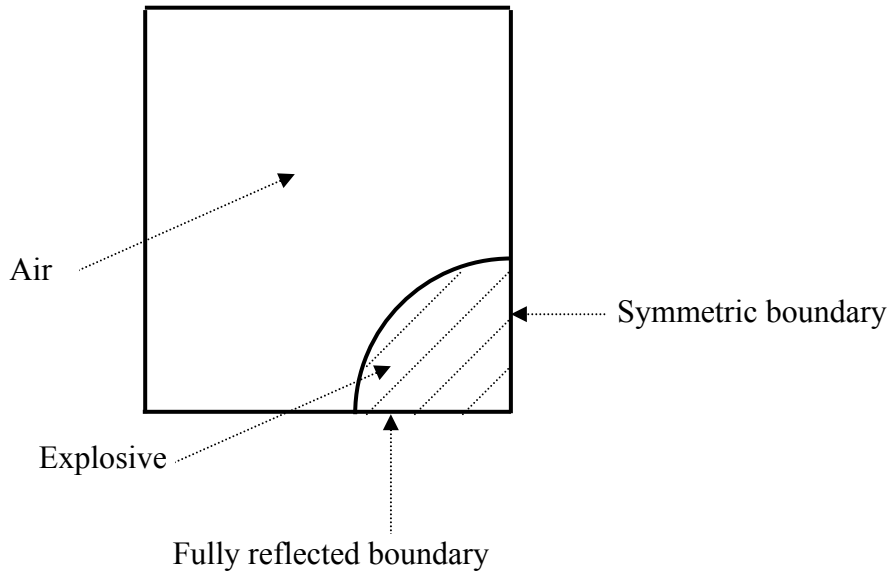

Figure 5.4 Schematic drawing of a 2D axis-symmetric quarter model used in the preliminary AUTODYN 2D model

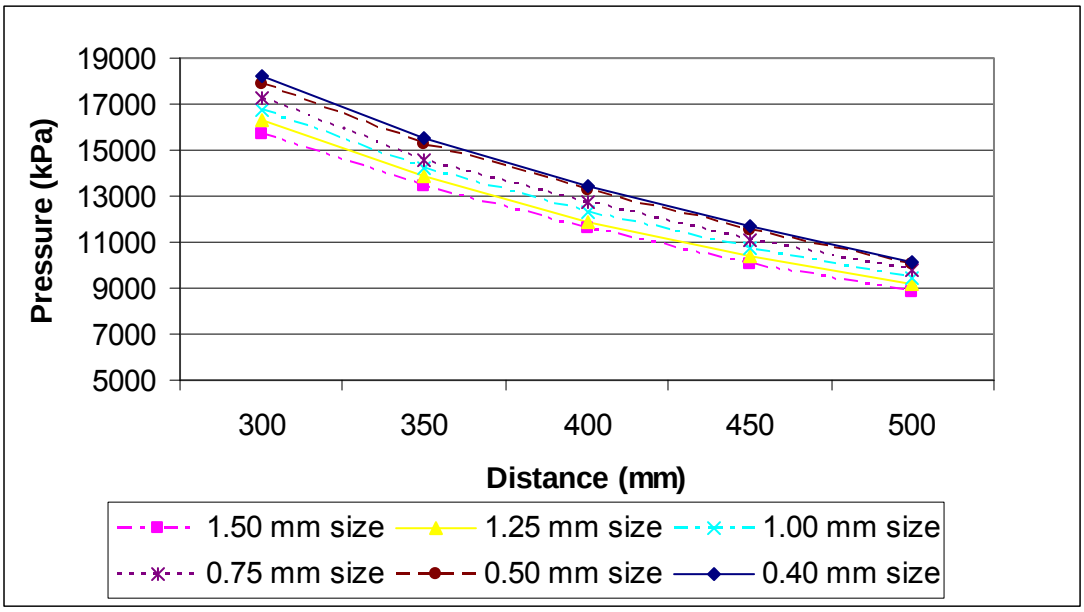

Figure 5.5 Mesh sensitivity results on recorded maximum pressure at different distances and different mesh size

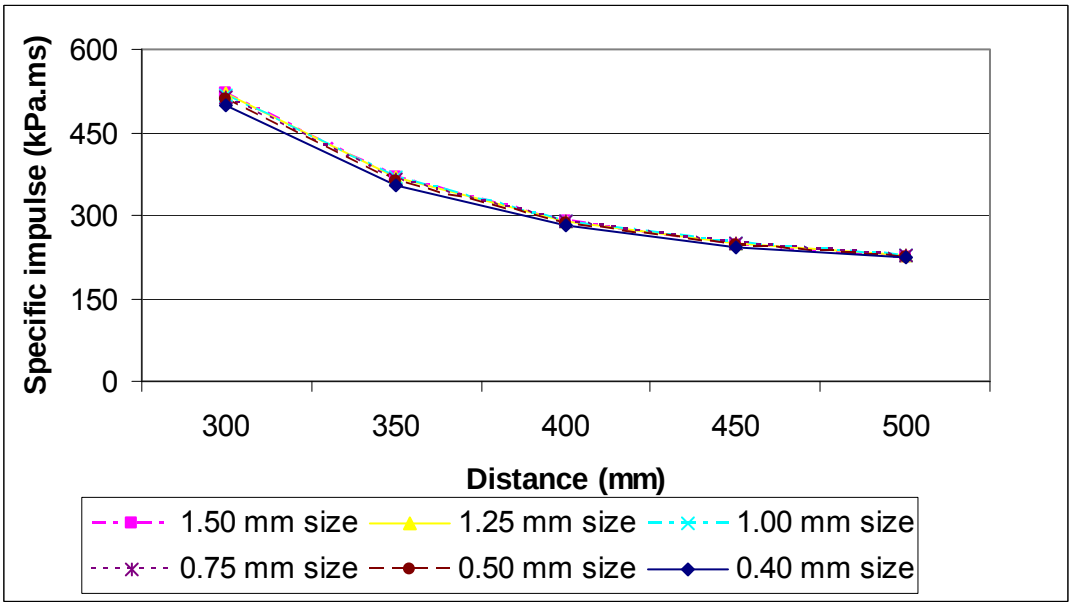

Figure 5.6 Mesh sensitivity results on recorded maximum specific impulse at different distances and different mesh size

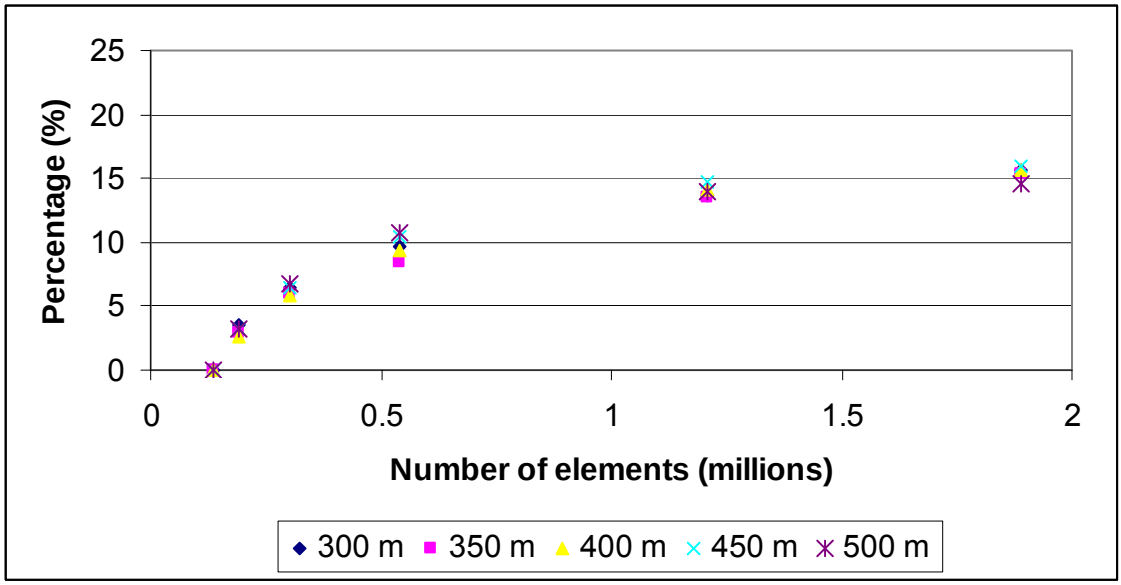

Figure 5.7 Mesh sensitivity results on percentage difference of maximum pressure from 1.5 mm element size (0.135 million elements) results at different number of elements and different recorded distances

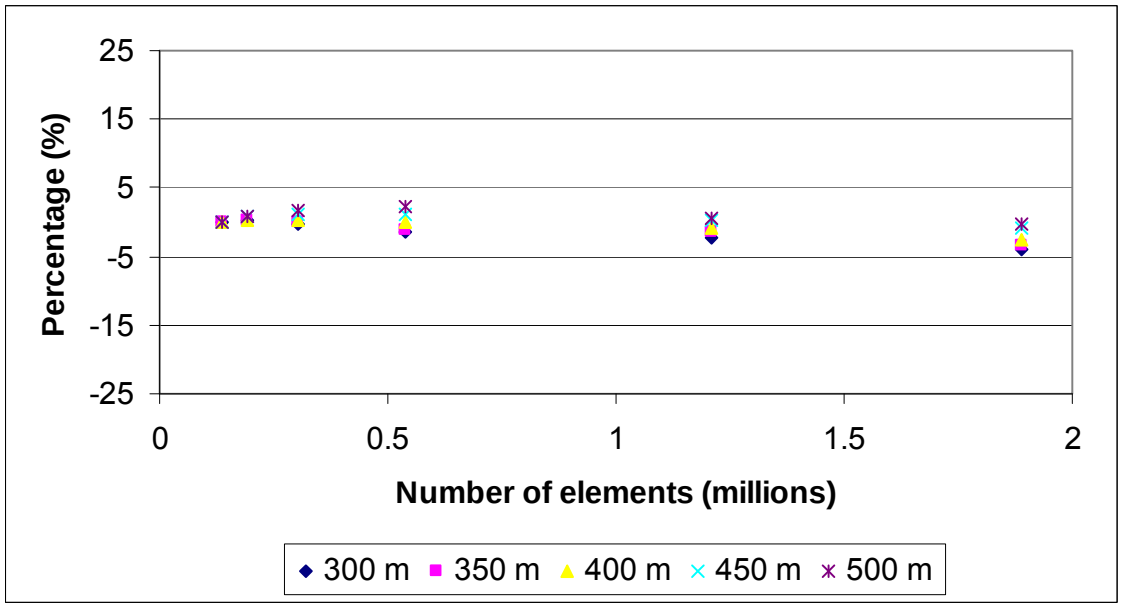

Figure 5.8 Mesh sensitivity results on percentage difference of maximum specific impulse from 1.5 mm element size (0.135 million elements) results at different number of elements and different recorded distances

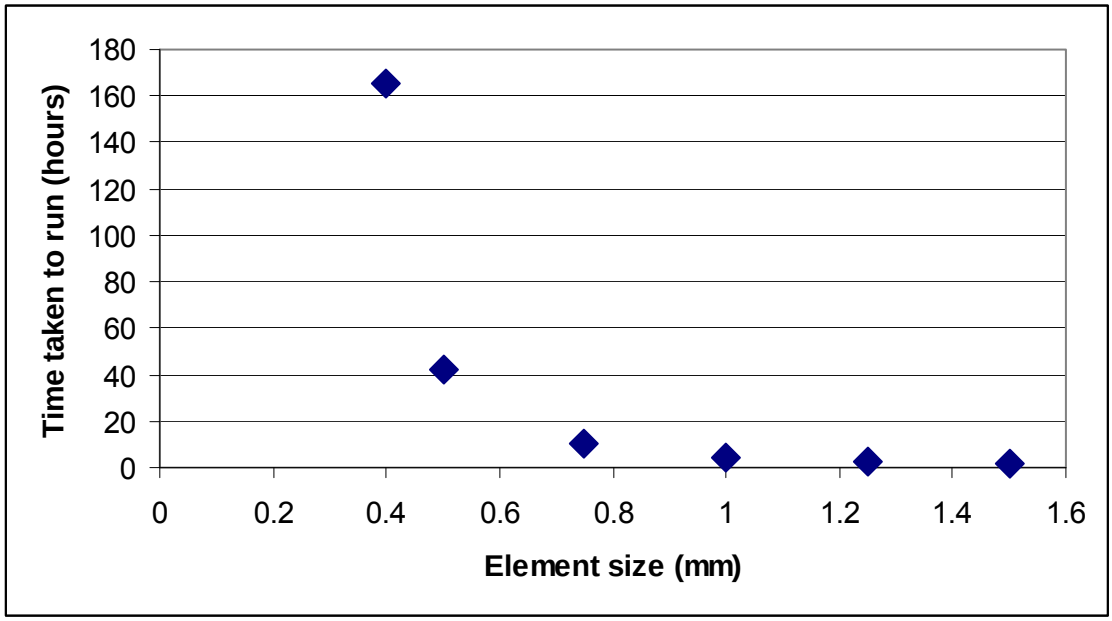

Figure 5.9 Mesh sensitivity results on time taken to run using different element sizes of 1.5, 1.25, 1.0, 0.75, 0.5 and 0.4 mm on AUTODYN 2D.

It is commonly known in Finite Element analysis that the smaller the mesh size the better it represents the actual domain. From the results shown in Figure 5.7 and Figure 5.8, the percentage of pressure and specific impulse change was getting smaller and smaller once the number of elements was increased or the element size was reduced. Figure 5.8 demonstrates that the effect on specific impulse is between 2% to 4% upon increasing the number of elements. It was also noticed in Figure 5.9 that as the element size was reduced, time taken to complete the solution increased exponentially.

It is important to optimise the mesh size (element size) so that reasonable and accurate results are achieved in good time. From the results, it seemed that any elements having a size less than 1 mm was reasonable to use because the pressure did not change much and the specific impulse changed very little. Therefore it is concluded that the 0.75 mm element size will be used in further analysis.

5.2.2 3D model

Although it was mentioned in the last section that 0.75 mm Eulerian elements would be used in the 2D model to provide blast loading, in order to speed up the mesh sensitivity analysis in the 3D model, it was decided that 1 mm Eulerian elements would be used instead. A 2D model was created in the same way as in section 5.2.1 to provide blast loading in a remapped file. A 3D model with symmetry in X and Y was created with Eulerian elements and shell elements representing air and a single RHA steel plate respectively, as shown in Figure 5.10. A 300 mm stand-off distance was selected to run a mesh sensitivity analysis. Note that the Eulerian mesh size needs to be smaller than the shell or Lagrangian mesh size so that the interaction process can work effectively. However, too small Eulerian mesh size may use too much computational resources. Shell element size is governed by the plate thickness (10 mm thick), therefore element size of 10 mm was used. Mesh sensitivity analysis was then performed using 9, 8, and 7 mm Eulerian elements while 10 mm shell elements were used for the plate. The boundary of the plate was fixed in all degrees of freedom; while the boundary at the Eulerian elements was set to allow flow out from all faces except at the Eulerian face, which is at a right angle to the plate nearest to the charge origin and was set to fully reflective boundary. The final stage of modelling was to remap the pressure profile from the 2D model onto the 3D model. Results of maximum dynamic deformation were recoded and are shown in Figure 5.11.

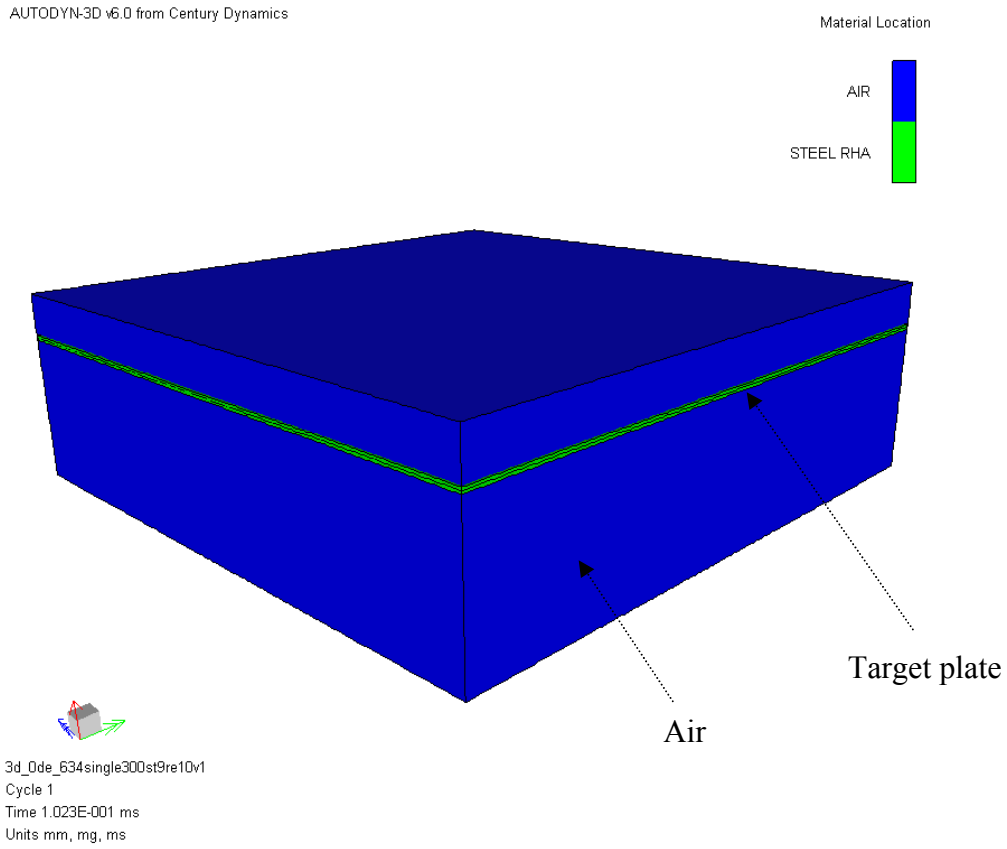

Figure 5.10 A quarter model used in the preliminary AUTODYN 3D model for mesh sensitivity analysis

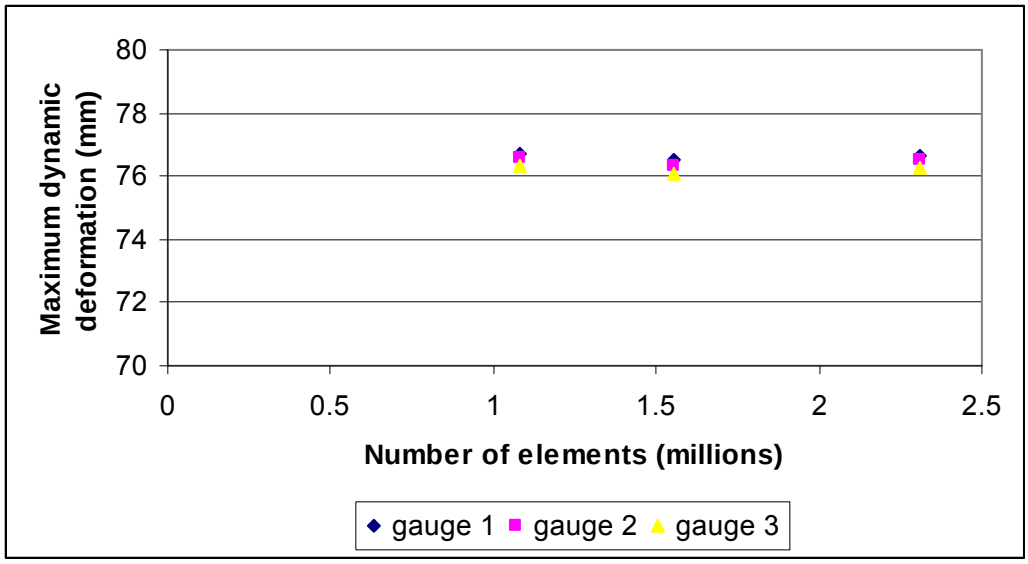

Figure 5.11 Mesh sensitivity results on maximum dynamics deformation at different number of elements (9, 8, and 7 mm element sizes having 1.082 millions, 1.553 millions, and 2.307 millions elements respectively) recorded at gauge 1, 2, and 3 (7, 21 and 35 mm distances from the corner)

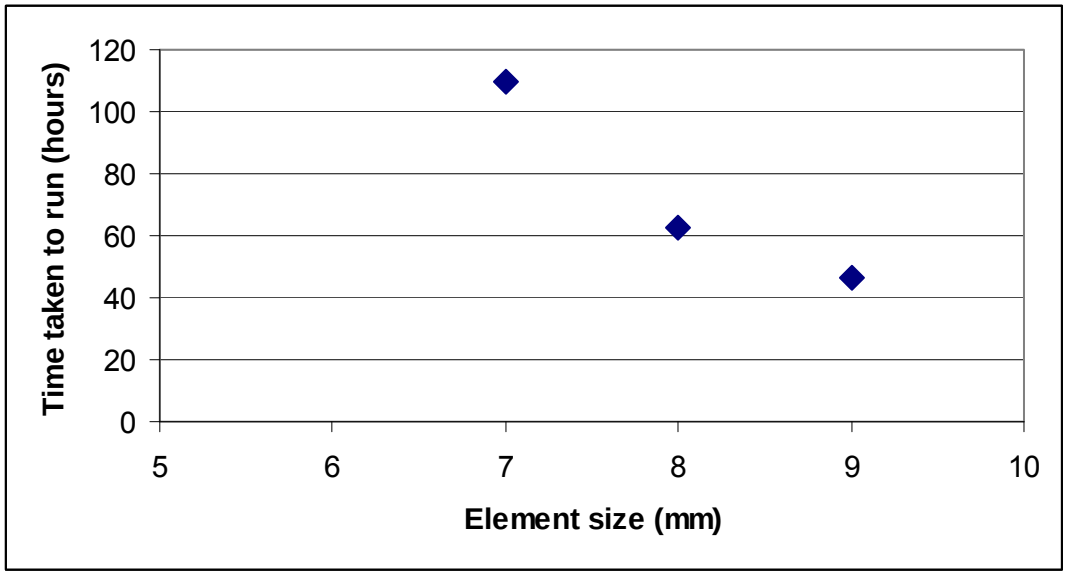

Figure 5.12 Mesh sensitivity results on the time taken to run using different element size of 7, 8 and 9 mm on AUTODYN 3D.

A negligible difference in dynamic deformation as shown in Figure 5.11 was observed as a result of changing Eulerian element size from 9 mm to 7 mm. On the other hand, it took 110 hours to achieve a solution for a 300 mm stand-off distance using 7 mm element size, compared to 47 hours using 9 mm element size. It was therefore decided to use 9 mm mesh for the current 3D analysis.

5.3 Single plate models

5.3.1 Single plate numerical simulations

This section will concentrate on a single floor configuration of the vehicle bottom, which is represented by a single plate simulation. A quarter symmetry model of a single plate and air was developed in AUTODYN 3D using 300, 400, 450, 500, and 600 mm stand-off distances as shown in Figure 5.13. The geometry of the plate was the same as discussed in section 5.1. A 2D blast loading was remapped into a 3D model using Eulerian and shell elements to represent air and RHA steel plate. The 3D Eulerian model was developed to cover plate geometry; this allows the blast to interact with the plate and thus cause plate deformation. The material properties of air and the target plate were taken as an ideal gas and RHA steel respectively. The plate was fixed in all degrees of freedom on its edges. The boundary on the air Eulerian elements was set to 'flow out' for all the outer faces, except at the face perpendicular to the blast direction nearer to the explosive charge. Results are shown in Figures 5.14 – 5.19. Extended results are displayed in Figures C.1 – C5 (Appendix C).

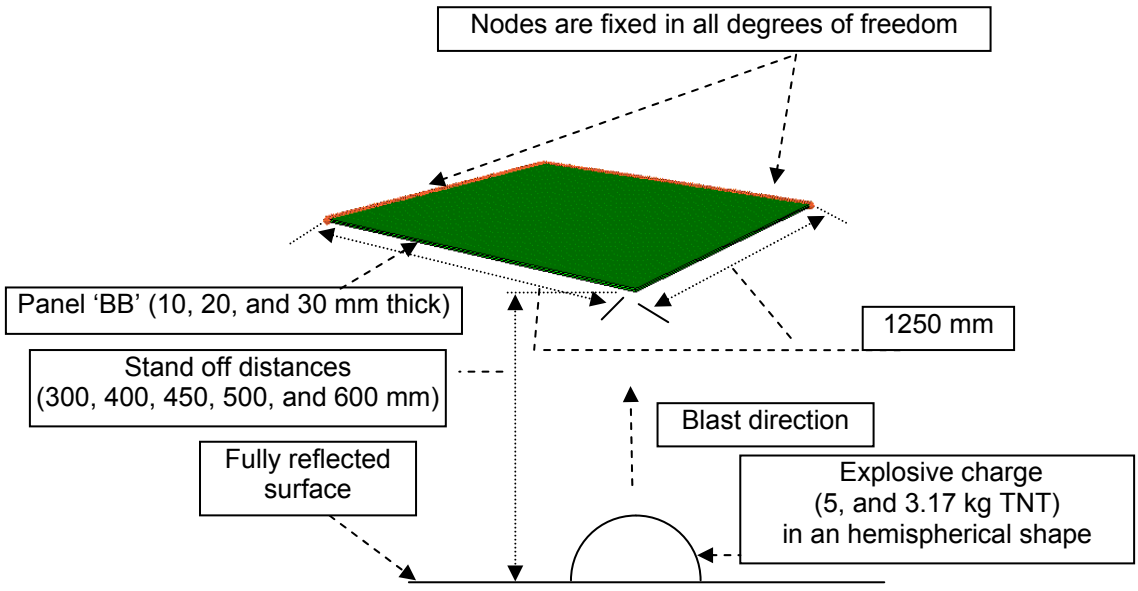

Figure 5.13 ¼ 'single plate' model

5.3.2 Single plate results

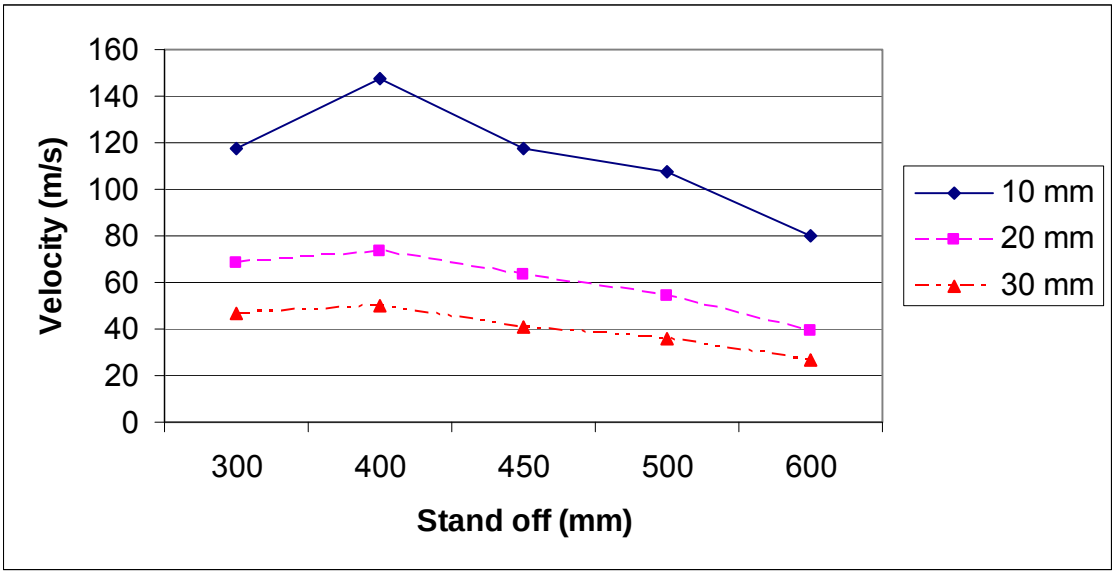

Figure 5.14 Maximum velocity results of single plate simulations having various thicknesses and stand-off distances subjected to 5 kg TNT in an hemispherical shape on reflected surface

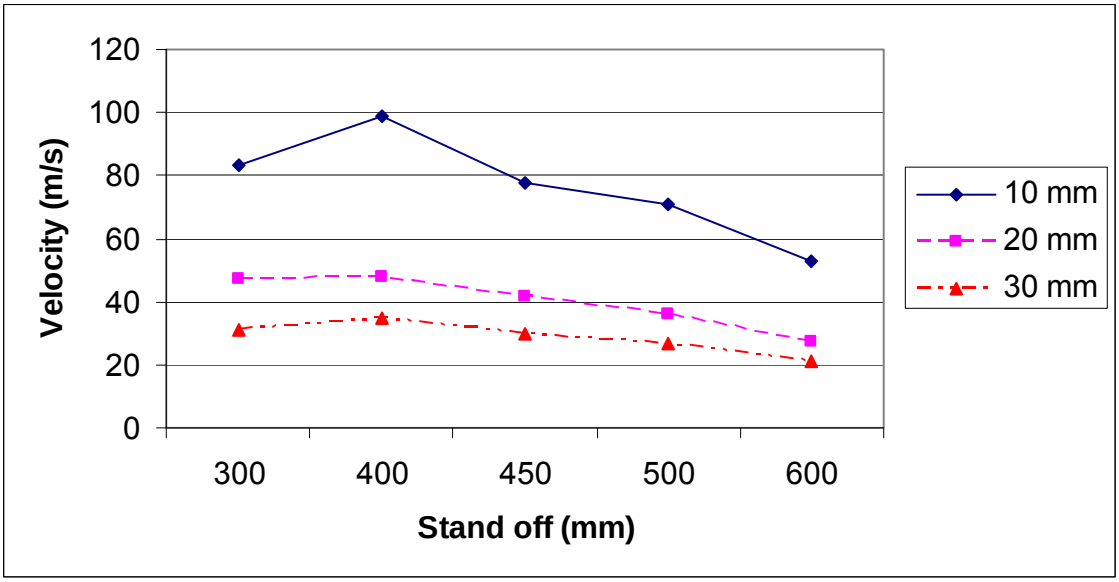

Figure 5.15 Maximum velocity results of single plate simulations having various thicknesses and stand-off distances subjected to 3.17 kg TNT in an hemispherical shape on reflected surface

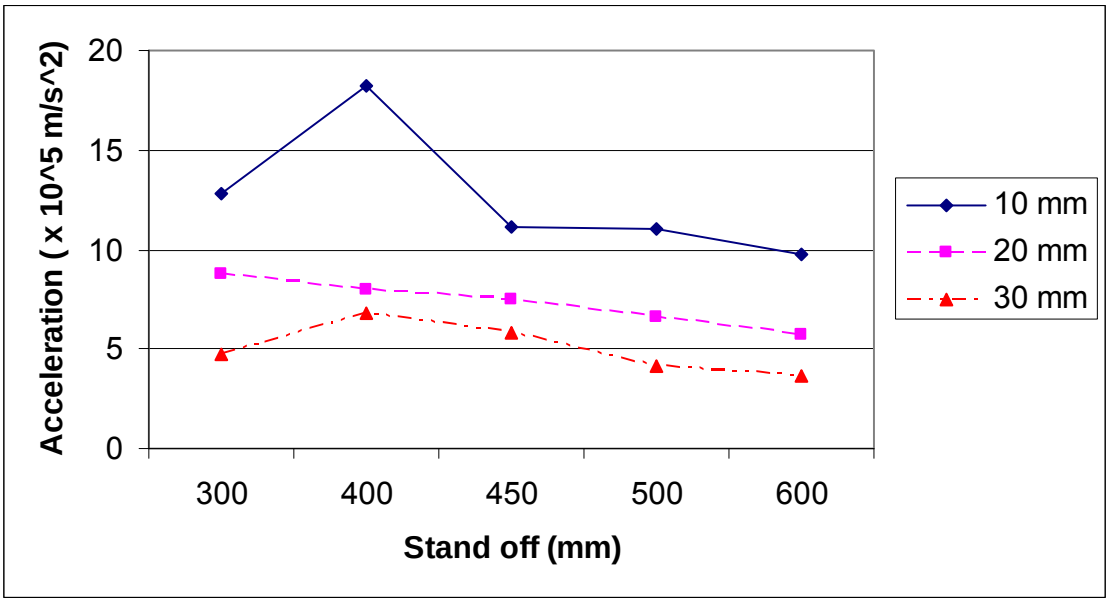

Figure 5.16 Maximum acceleration results of single plate simulations having various thicknesses and stand-off distances subjected to 5 kg TNT in an hemispherical shape on reflected surface

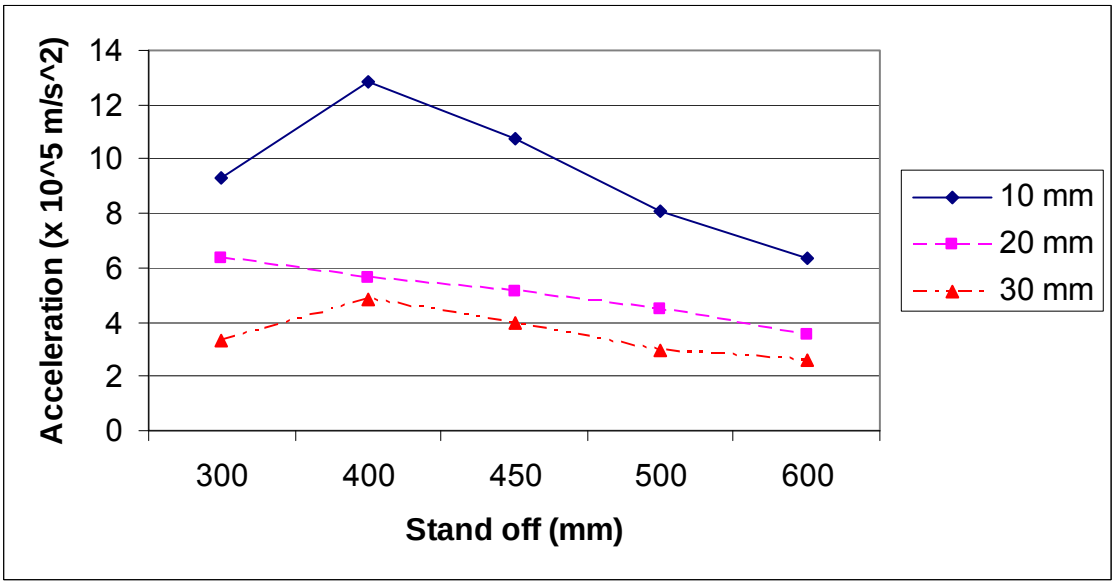

Figure 5.17 Maximum acceleration results of single plate simulations having various thicknesses and stand-off distances subjected to 3.17 kg TNT in an hemispherical shape on reflected surface

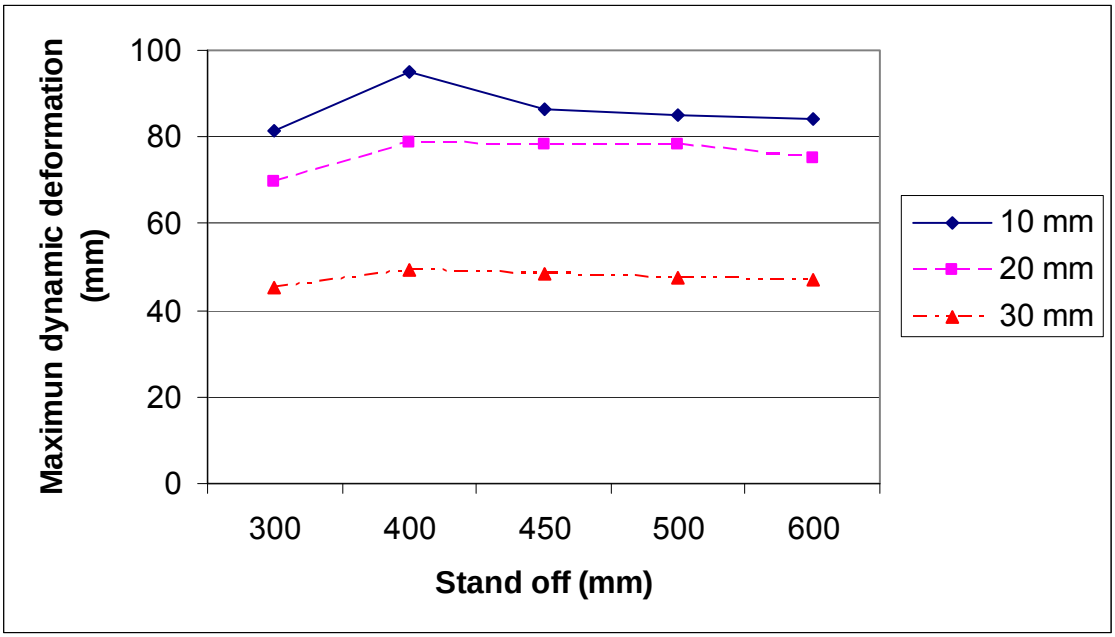

Figure 5.18 Maximum dynamic deformation results of single plate simulations having various thicknesses and stand-off distances subjected to 5 kg TNT in an hemispherical shape on reflected surface

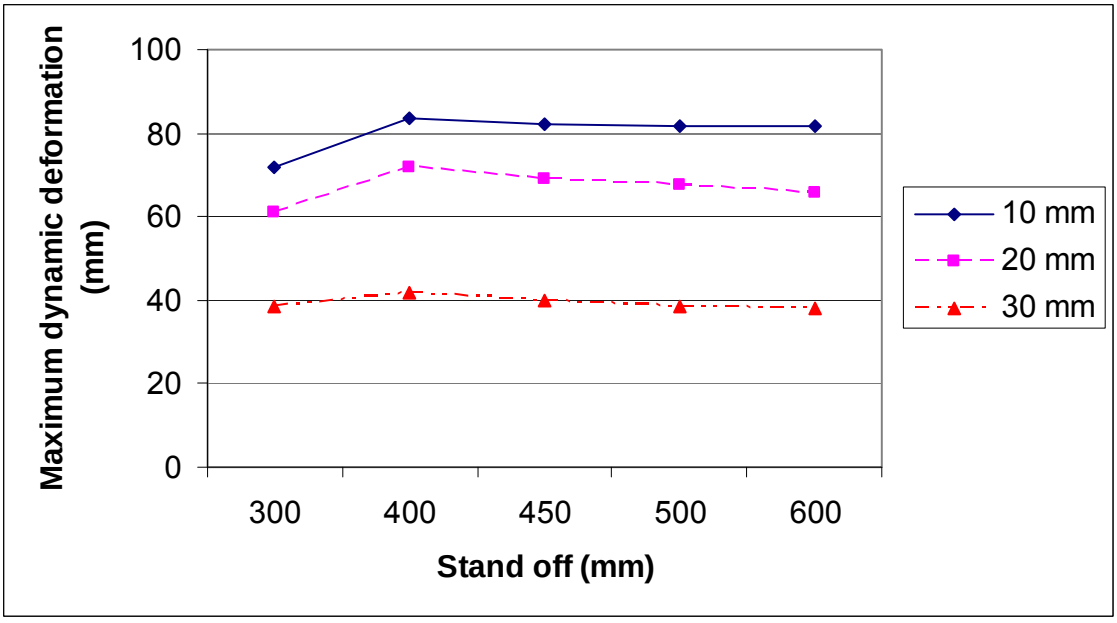

Figure 5.19 Maximum dynamic deformation results of single plate simulations having various thicknesses and stand-off distances subjected to 3.17 kg TNT in an hemispherical shape on reflected surface

5.3.3 Single plate discussion

The result in figure C.1 and C.2 (Appendix C) shows that the maximum deformation at panel BB in the single plate model occurred at the middle of the panels. From single plate simulation results in Figure 5.14 – 5.19, with the exception of the 300 mm stand-off case, the results show that the further the target plate was from the blast mine the fewer effects it experienced. For a given stand-off distance as the plate thickness increased, damage effect on the plate reduced. As the plate thickness was doubled from 10 mm to 20 mm, the velocity, acceleration and maximum dynamic deformation were, on average, reduced by 48%, 43%, and 14% respectively, while increasing the plate thickness from 10 mm to 30 mm, the results were decreased by 64%, 61%, and 48%.However, with the increase in plate thickness, vehicle mass will increase- which affects its mobility.

The velocity, acceleration and dynamic deformation results at 300 mm stand-off distance were less than expected, when compared with the trend in the other stand-off distances. It is believed that this is due to the assumption that the explosive expands large enough to behave as an ideal gas. In all other stand-off distances, the material compression of the explosive reached the value of less than -0.99, which is the recommended value in AUTODYN manual, Century Dynamics Inc (2003) that assumes the explosive to behave as an ideal gas. In Figure 5.20 and Figure 5.21, at 300 mm stand-off distances, the material compression of both charges did not reach this value. However, the pressure front had just arrived at 300 mm distance which forced the simulation to stop and provide blast loading.

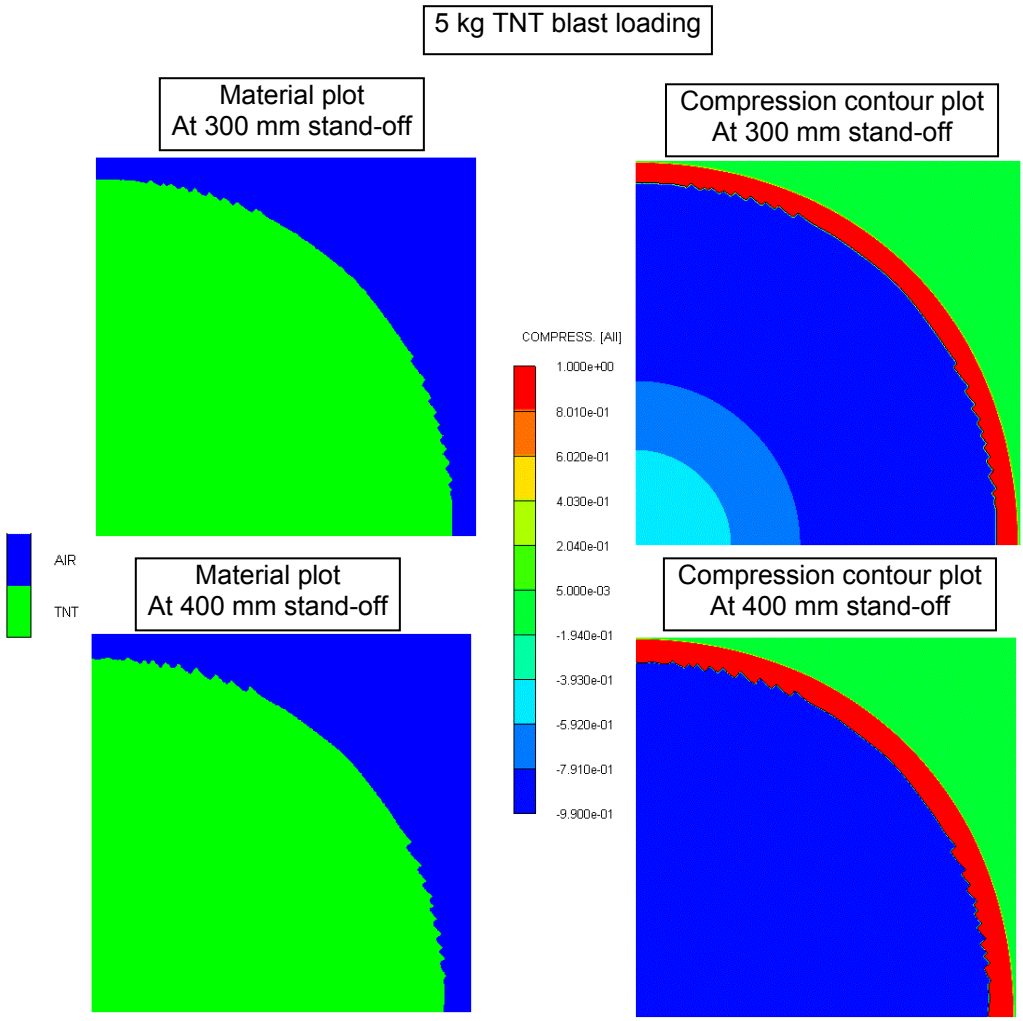

Figure 5.20 Material plots and material compression contour plots in AUTODYN 2D during the blast loading generation stage using 5 kg TNT.

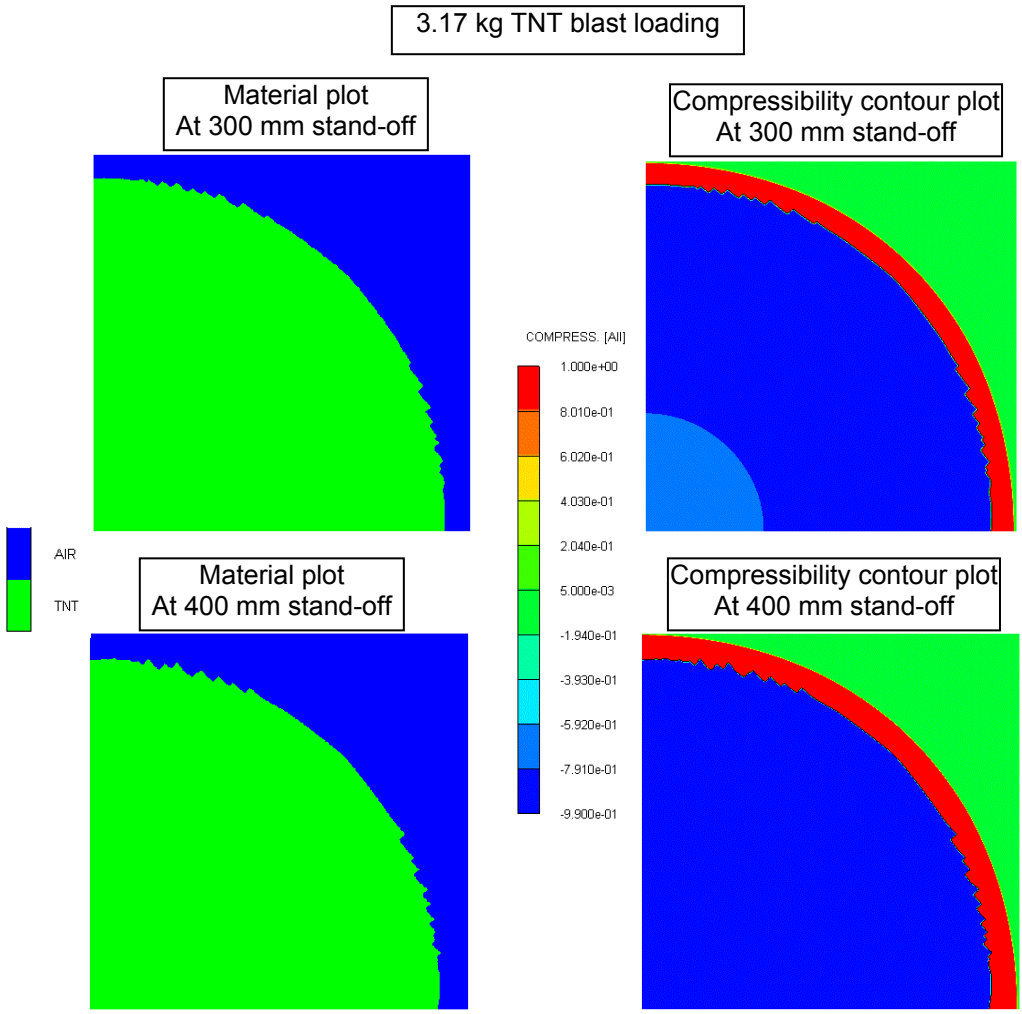

Figure 5.21 Material plots and compressibility contour plots in AUTODYN 2D during the blast loading generation stage using 3.17 kg TNT.

In order to confirm that the 300 mm stand-off distance results are too low, further investigations are performed by developing the same numerical models using LS-DYNA with CONWEP. The blast loading from LS-DYNA with CONWEP is pre-calculated by specifying the actual amount of charge in kg TNT. All other configurations are kept the same. The results are shown in Figures 5.22 – 5.27.

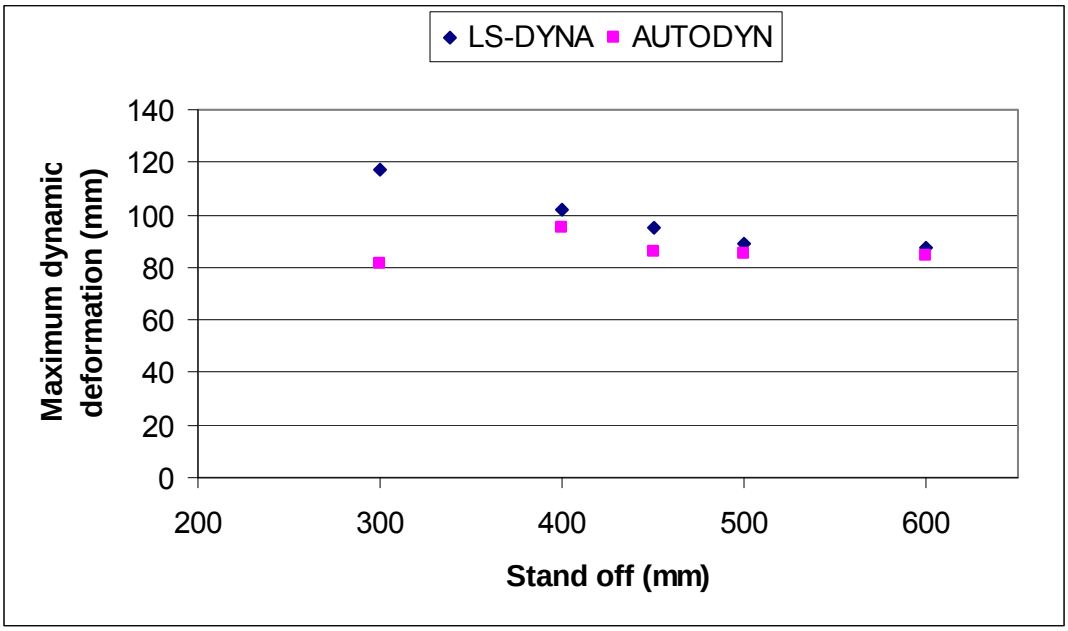

Figure 5.22 Comparison of maximum dynamic deformation results of single RHA steel plate simulations having 10 mm thickness and various stand-off distances subjected to 5 kg TNT in an hemispherical shape using LS-DYNA and AUTODYN.

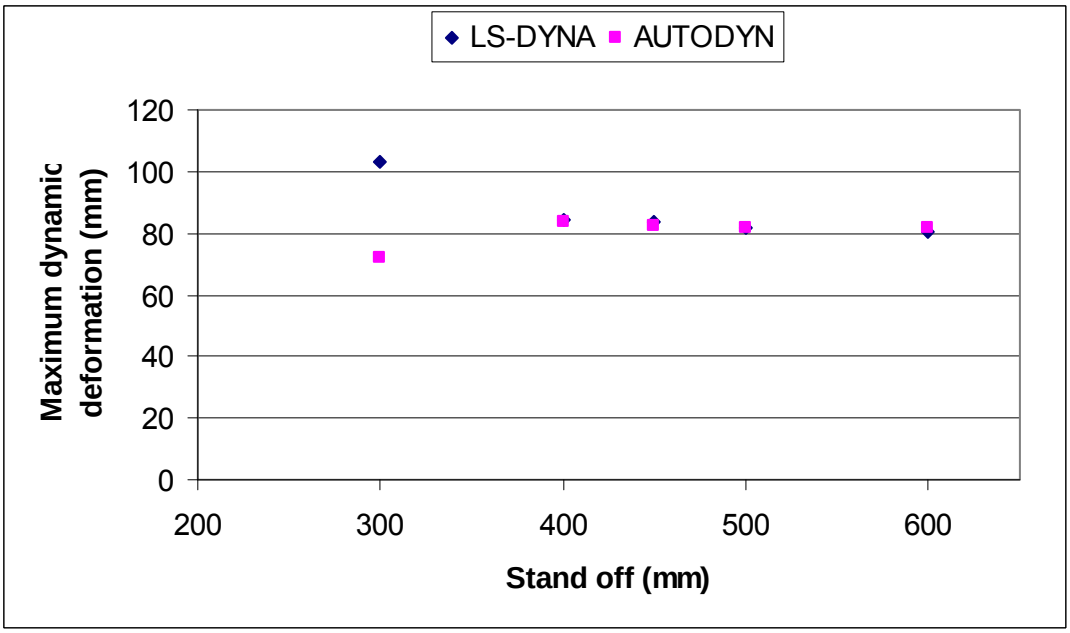

Figure 5.23 Comparison of maximum dynamic deformation results of single RHA steel plate simulations having 10 mm thickness and various stand-off distances subjected to 3.17 kg TNT in an hemispherical shape using LS-DYNA and AUTODYN.

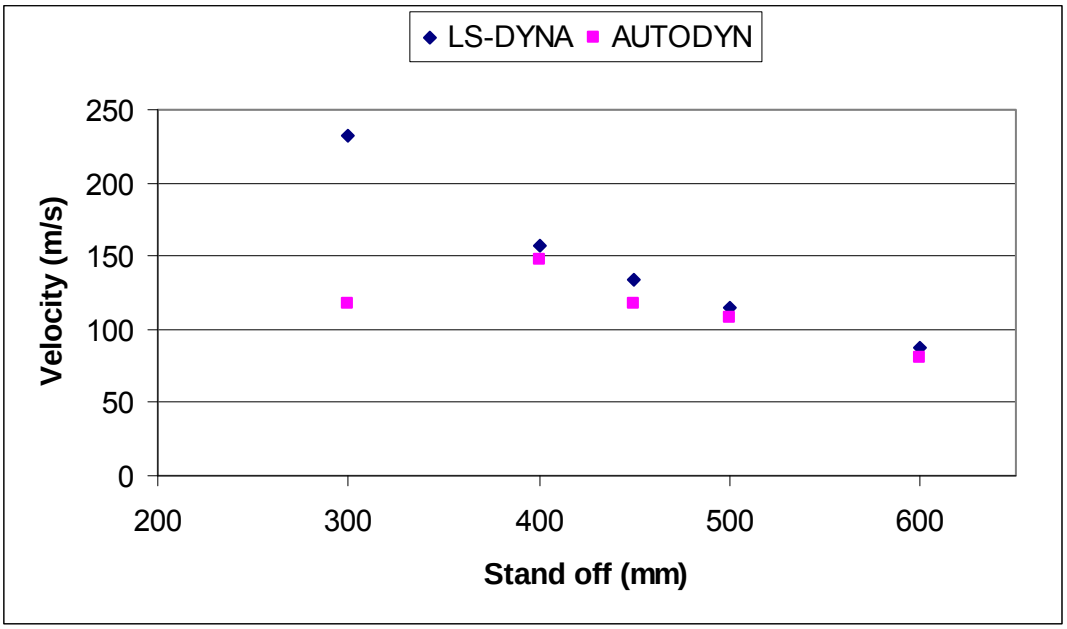

Figure 5.24 Comparison of maximum velocity results of single RHA steel plate simulations having 10 mm thickness and various stand-off distances subjected to 5 kg TNT in an hemispherical shape using LS-DYNA and AUTODYN.

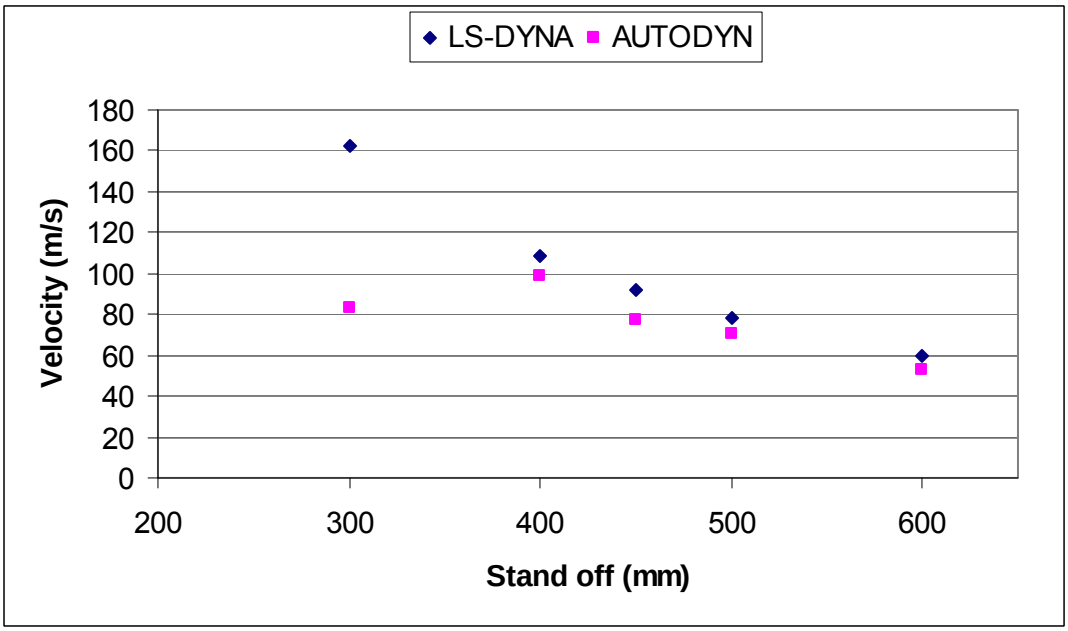

Figure 5.25 Comparison of maximum velocity results of single RHA steel plate simulations having 10 mm thickness and various stand-off distances subjected to 3.17 kg TNT in an hemispherical shape using LS-DYNA and AUTODYN.

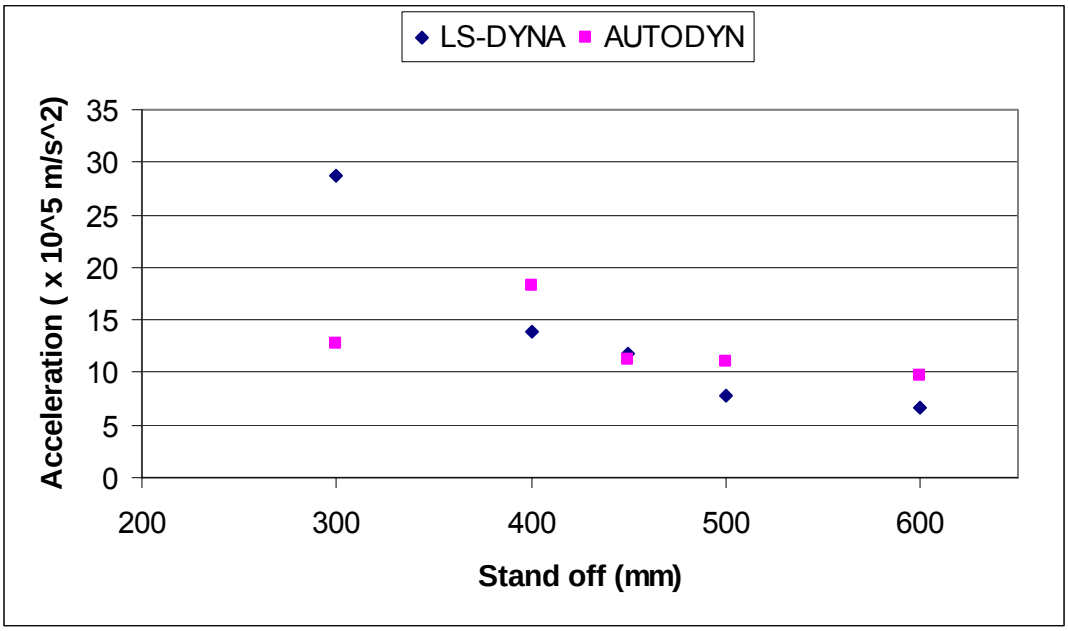

Figure 5.26 Comparison of maximum acceleration results of single RHA steel plate simulations having 10 mm thickness and various stand-off distances subjected to 5 kg TNT in an hemispherical shape using LS-DYNA and AUTODYN.

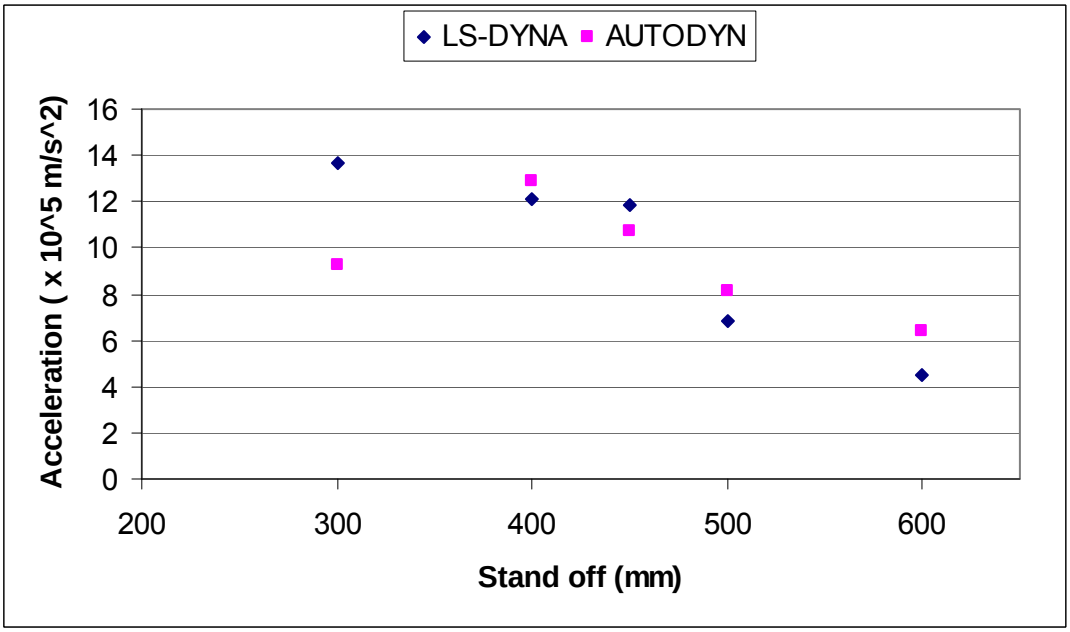

Figure 5.27 Comparison of maximum acceleration results of single RHA steel plate simulations having 10 mm thickness and various stand-off distances subjected to 3.17 kg TNT in an hemispherical shape using LS-DYNA and AUTODYN..

From Figures 5.22 – 5.27, LS-DYNA results at 300 mm stand-off distance are in a similar trend with the other stand-off distances, while AUTODYN results at 300 mm stand-off distance does not follow the same trend. The reason for this has been discussed earlier. Thus it was decided to ignore 300 mm stand-off distance for further analysis.

Based on the deformation plot in Figure C.3 and Figure C.4 (Appendix C), it is estimated that the permanent deformation of a single plate subjected to 5 kg TNT in a spherical shape blast on reflected surface at 400 mm stand-off, is virtually zero. This case is the most extreme case compared to the other cases used in this section, because of the amount of charge, the plate thickness, and the stand-off distance (ignoring 300 mm stand-off distance cases). The target plate, which was fixed around all its edges, might have prevented it from deforming beyond a certain limit. In the box model, the plate may deform more because of the different boundary conditions. There is however, some plastic strain occurring, with the maximum of 0.31 occurring at the edge of the plate at 750 ms, which can be seen in Figure C.5 (Appendix C).

5.4 'Box' models

5.4.1 'Box' numerical simulations

Based on single plate numerical simulations in the previous section, a plain bottom box ('box' model) simulation was developed, using the same method. The model geometry in section 5.1 was used to create a ¼ symmetric model using AUTODYN 3D remapping method. This model represented the bottom part of a vehicle where there were 2 floors, one at the very bottom and the other at the floor of the crew's compartment. These floors, combined with side panels, created the box with the internal space and with a constant gap of 118.25 mm. Blast loading from AUTODYN 2D was remapped into AUTODYN 3D. Air and box structure were represented by Eulerian and shell elements respectively. The boundary condition at the edges of panel BB was fixed along its edges as shown in Figure 5.28. The boundary of the air was set to 'flow out' of all outer faces, except the face representing the ground was set to be a reflected boundary.

Note that only one 'box' model was developed at this stage because it needed to compare with a double-floor vehicle hull model in the next section, and subsequently a better model will be chosen to be used in Chapter 6 to compare different vehicle model configurations. Results are in Figure 5.29 and the extended results are shown in Figures C.6 – C.9 (Appendix C).

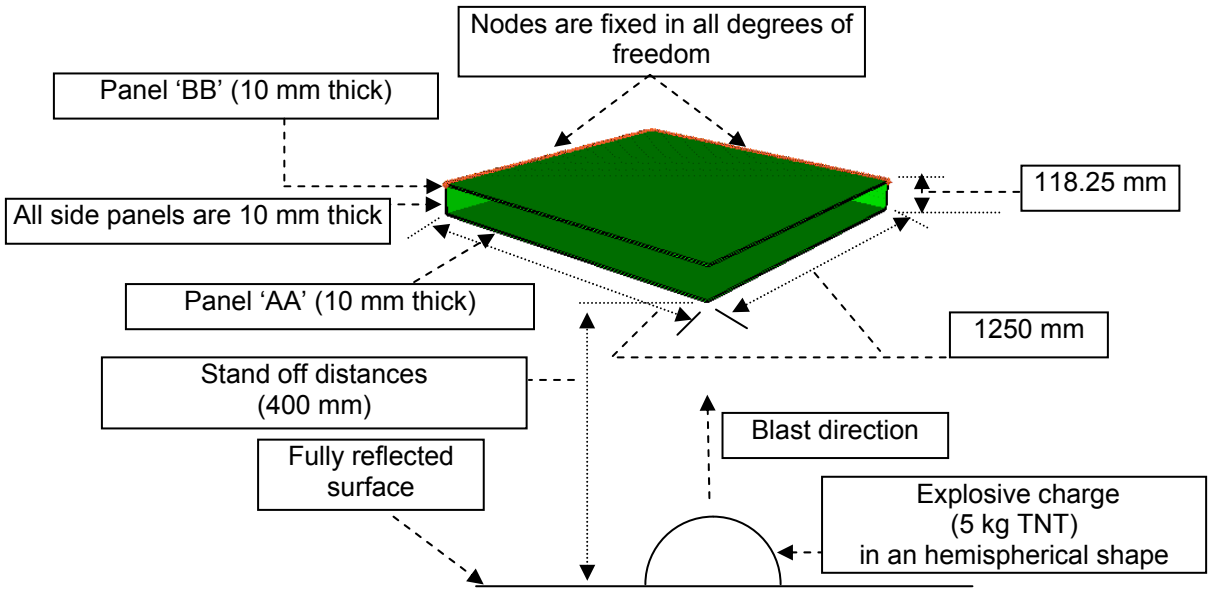

Figure 5.28 ¼ 'box' model

5.4.2 'Box' results

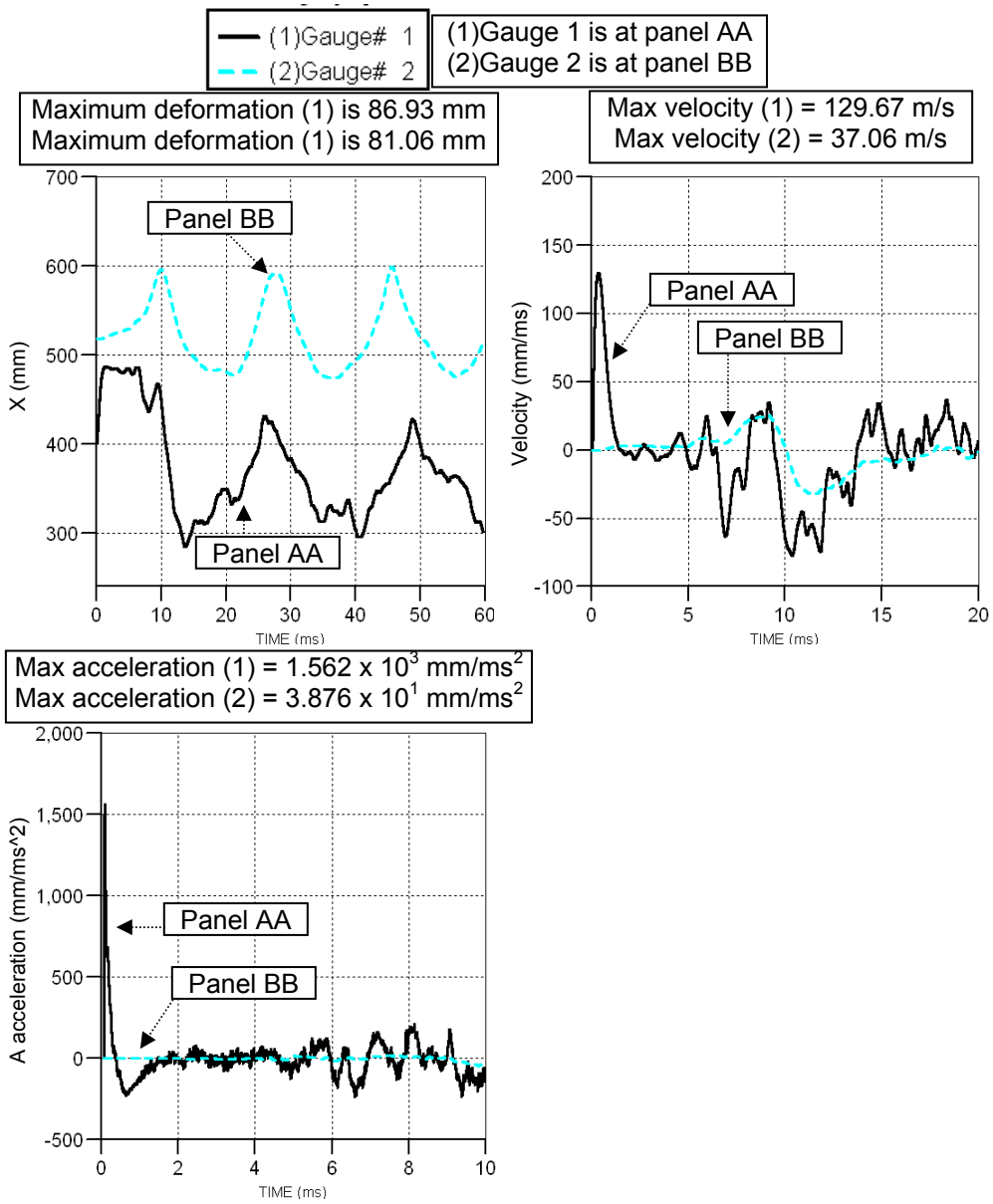

Figure 5.29 'box' model results subjected to 5 kg TNT in an hemispherical shape on a reflected surface at 400 mm stand-off distance (deformation curves are based on the actual gauge positions.)

5.4.3 'Box' discussion

The result in Figure C.7 (Appendix C) shows that the maximum deformation at panel AA in the single plate model occurred at the middle of the panel (when it is viewed in full scale). The results in Figure C.7 (Appendix C) shows that gauge xy1 deformed inwards in z-direction to the maximum of around 7 mm and then sprung back. Gauge xy2, which was very near to the fixed edge, virtually did not move at all in x-direction, and deformed very little in z-direction. This is in agreement with the boundary condition setting, which was fixed along its edges.

Figure C.9 (Appendix C) shows that the plastic strain mostly occurred along the edges of the side panel and panel AA, around the corner area of panel AA, and around the middle of panel AA. The maximum plastic strain of 0.047 recorded at 40 ms, was at a side panel edge, which was rigidly joined to panel AA. This shows that plastic deformation occurred more on the edge areas than at the centre of the panel, which was the closest position to the blast. It is thought that in reality, these edges may be welded, which will weaken the structure integrity and subsequently the damage may occur in these areas.
In general, the maximum deformation, velocity, and acceleration at panel AA are greater than panel BB. The result in Figure 5.29 has shown that there is around 81.06 mm deformation at panel BB. Although panel AA did not impact with panel BB, panel BB moved quite significantly. The following section investigates the causes of the movement by using the 'basic' model, which was defined as a box model of 10 mm thickness with 118.25 mm internal gap subjected to 5 kg TNT in an hemispherical shape, placed on the reflected surface at 400 mm stand-off distance.

Firstly, the model was rechecked again to confirm that the model was set up correctly in every aspect such as material properties, model symmetry, fluid structure interaction, boundary condition, etc. An additional check was done by a staff at Century Dynamics and it was confirmed that the model was developed correctly.

The interaction thickness, which is an artificial Eulerian element thickness used in the interaction calculation to ensure that an Eulerian element is large enough to cover a

Lagrangian element (so that interaction calculation is undertaken effectively), was increased from 12.5 mm to 30 mm (3 times the actual plate thickness) in order to be certain that there would be no leakages from the air through the panels. However, the results are very similar to the basic model, as shown in Figure 5.30. Panel BB still moved quite significantly.

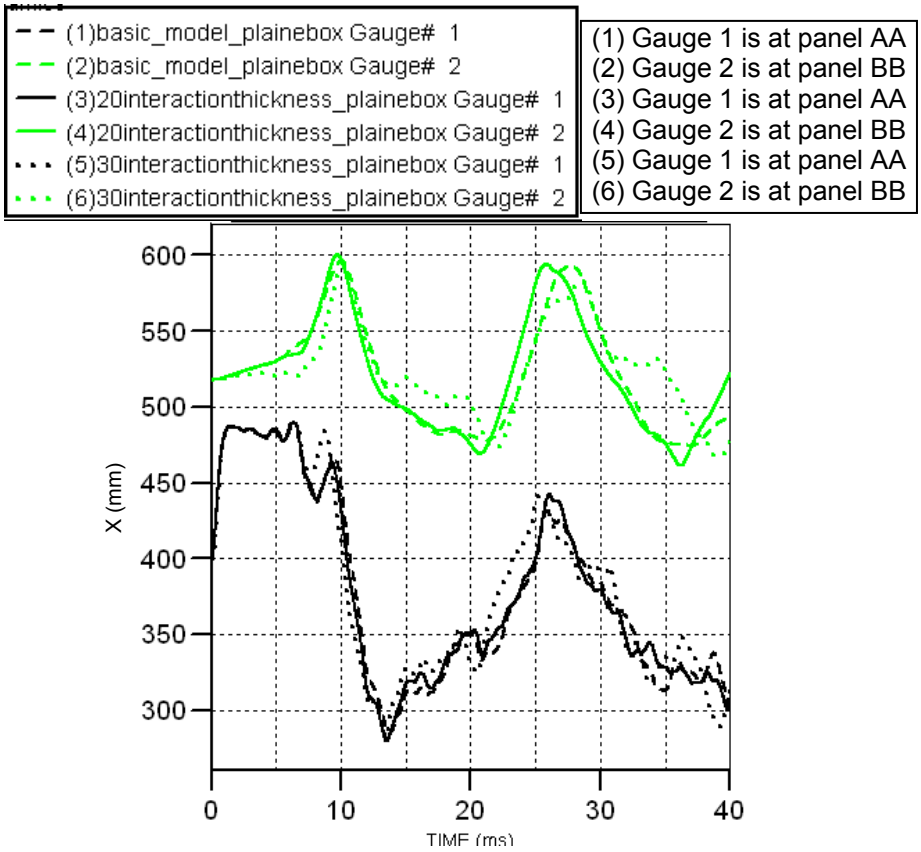

Figure 5.30 Comparison of maximum deformation results (mm) using different interaction thicknesses (each curve is based on the actual gauge position)

The gap was then extended to 250 and 500 mm to see if panel BB moves. The result is in Figure 5.31. The result shows that by extending the gap from 118.25 mm to 250 and 500 mm, there are still some movements at the top panels, though it is getting less as the gap is wider. At the bottom panels which were 400 mm from the blast, '500 mm gap' deforms slightly more than the '250 mm gap' and 'basic' model respectively. This maybe due to the increased size of the side panels which allows the bottom panel to deform more. Note that panel BB deformations from the 3 models started from different original positions because the position of these panels are extended due to the increase in the gaps.

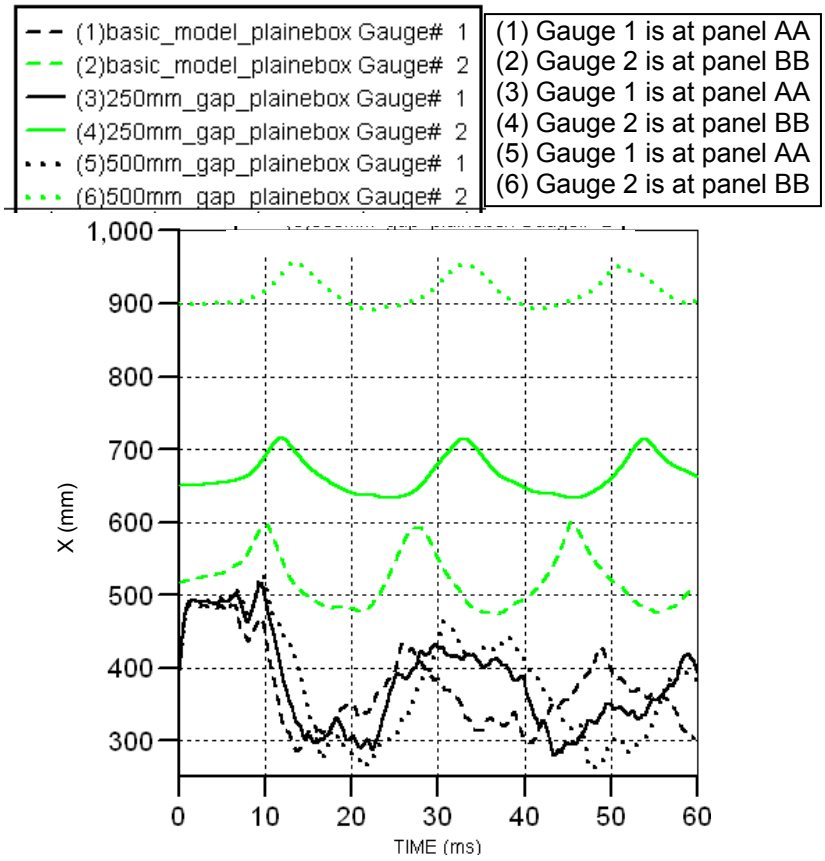

Figure 5.31 Comparison maximum deformation results (mm) between 'basic' model, '250 mm gap model', and '500 mm gap model' (each curve is based on the actual gauge position)

The next stage was to try to apply the fixed edge boundary condition at panel AA only ('bottom only') and also at both panel AA and BB ('both panels') rather than at panel BB only ('top only') which was used previously in the 'basic' model. From the result in Figure 5.32, the deformation at panel AA from 'bottom only' and 'both panels' are almost identical. The small differences maybe due to panel BB and side panels in the 'bottom only' were allowed to deform and transfer the moment to each other and subsequently to panel AA. Although the bottom panels are fixed in all degrees of freedom, it does not prevent the moment to be transferred. Panel AA deformation in the 'top only' is different due to its boundary condition, which allowed panel AA to deform and stay at the maximum position longer. The result in Figure 5.32 shows that panel BB still deformed quite significantly, hence further investigation was needed. Note that applying a fixed edge boundary condition at panel AA or both panels restricts the deformation at panel AA, which subsequently reduces the deformation at panel BB.

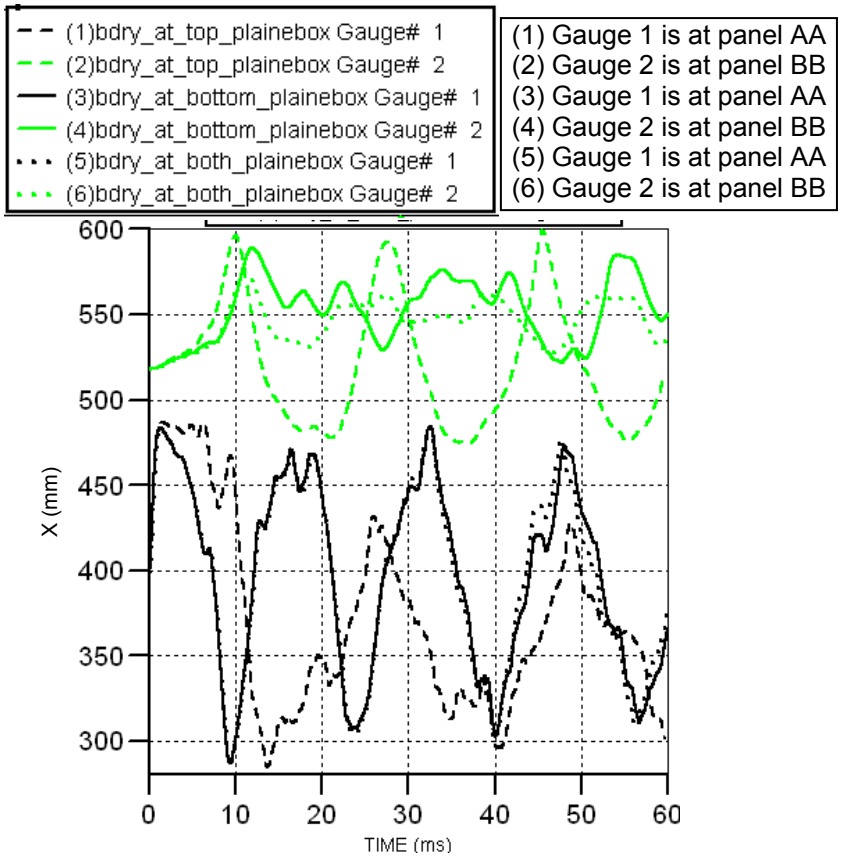

Figure 5.32 Comparison of maximum deformation results (mm) using different boundary conditions in 'top only', 'bottom only', and 'both panels' (each curve is based on the actual gauge position)

At this stage, the side panels in the 'box' model were deleted. The 'basic' model was then compared with 'no side panels' model in order to see if the side panels influenced the top panel deformation. Likewise, '250 mm gap' and '500 mm gap' were compared with their corresponding 'no side panels' models. Note that the fixed edge boundary condition (all degrees of freedom) was applied on Panel AA and BB in all 'no side panels' models. The results are in Figures 5.33 – 5.35. The results show that even without the side panels, the top panels in all 3 cases still deformed, though it was less as the gap was bigger. The top panel at '500 mm gap' case deformed very little.

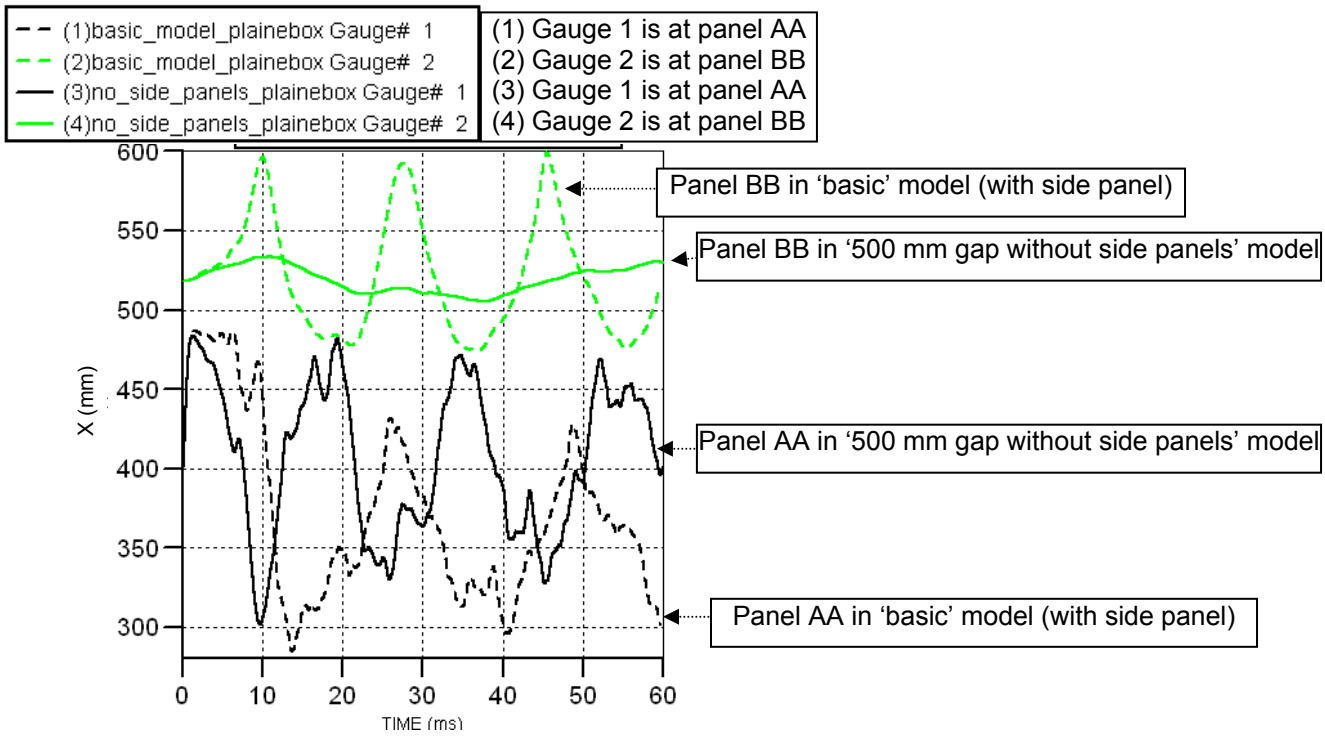

Figure 5.33 Comparison of maximum deformation results (mm) between the 'basic' model and 'without the side panels' model (each curve is based on the actual gauge position)

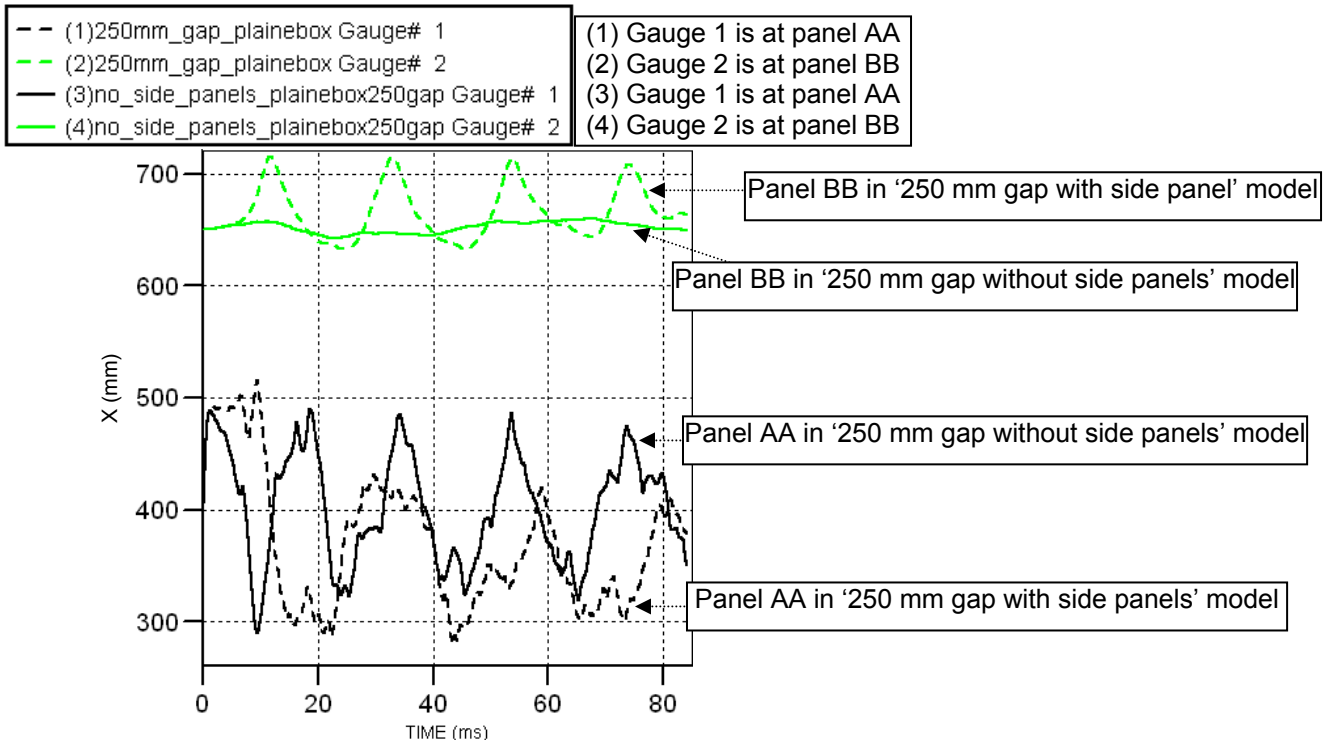

Figure 5.34 Comparison of maximum deformation results (mm) between 'with side panels' and 'without side panels' using 'box model with 250 mm gap' (each curve is based on the actual gauge position)

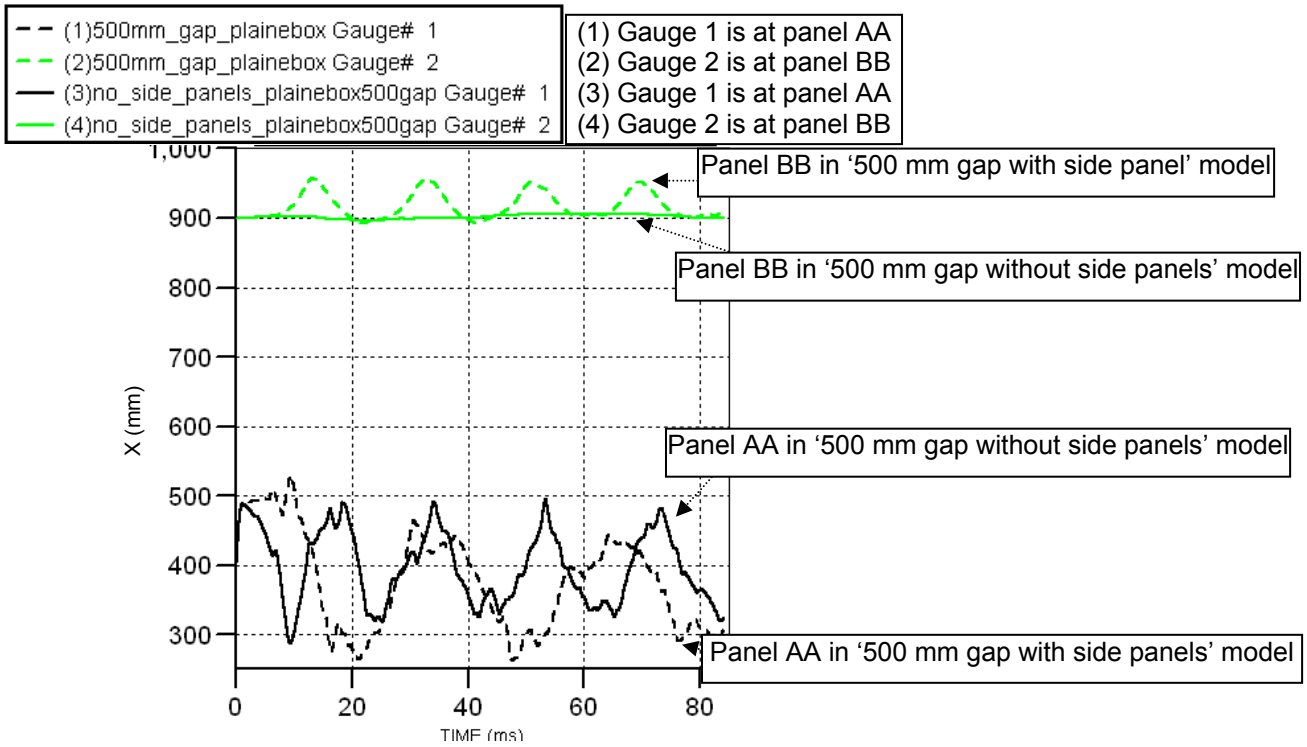

Figure 5.35 Comparison of maximum deformation results (mm) between 'with side panels' and 'without side panels' using 'box model with 500 mm gap' (each curve is based on the actual gauge position)

It is possible that the compressed air, which was contained within the gap, might cause the deformation at panel BB. Therefore it was important to estimate the likely pressure arisen from the air being compressed. In order to simplify the calculation, it was assumed that the bottom panel deforms in a 'piston' manner as in Figure 5.36. Further assumptions were made to assume that the air inside the box behaved as an ideal gas, and the air temperature within the gap in stages 1 and 2 is equal.

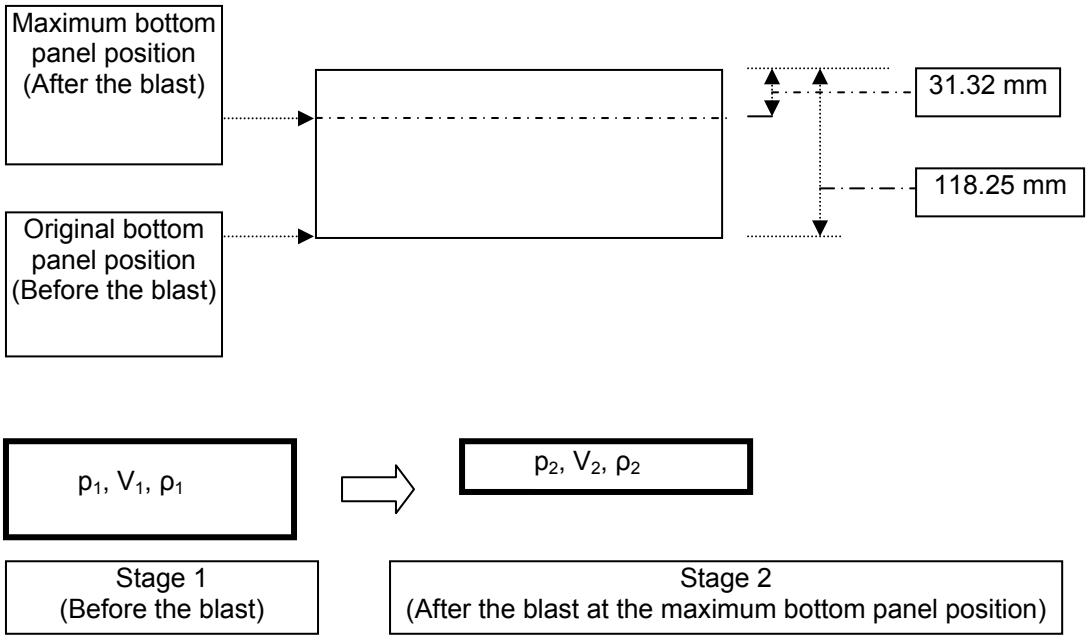

Figure 5.36 Schematic drawing of the box model showing the assumed 'piston' deformation shape.

From 'Boyle's law' equation,

$$\frac{p_1}{V_1} = \frac{p_2}{V_2} \qquad \textbf{(5.1)}$$

Or

$$p_2 = \frac{p_1 V_2}{V_1} \qquad \textbf{(5.2)}$$

p_1 = atmospheric pressure = 1.013 x 10^5 N/m^2, V_1 = 0.11825 x 2.5 x 2.5 m^3, and V_2 = 0.03132 x 2.5 x 2.5 m^3

So p_2 = 3.826 x 10^5 N/m^2

This calculated pressure in stage 2 was used to interact with panel BB. However, there was also the atmospheric pressure acting against panel BB in the opposite direction. Therefore the net pressure is estimated to be = 3.826 x 10^5 -1.013 x 10^5 = 2.812 x 10^5 N/m^2.

In order to see how much panel BB moved when this net pressure (2.812 x 10^5 N/m^2) was applied, an initial estimate was done by using the 'rectangular plates under uniform load producing large deflection' table in Young and Budynas (2002). Panel BB was assumed to behave as a single plate having its edges fixed in all degrees of freedom, and the applied pressure was uniform over the entire plate. The table in Young and Budynas (2002) showed that:

$$\frac{y_{\max}}{t} = f\left(\frac{qb^4}{Et^4}\right) \qquad (5.3)$$

Where y_{max} was the maximum deformation, E was Young's modulus for steel = 210 GPa, t was the thickness of the plate = 10 mm, b was the width of the plate = 2.5 m, and q was the load per unit area = 2.812 x 10^5 N/m^2. Hence $\frac{qb^4}{Et^4}$ in this case was 5230.7 but the maximum value in the table is 250. So a further estimate was done by forecasting the trend of the graph from available pairs of data in the table using Excel. The estimated y_{max}/t was 16.13 and hence the estimated maximum deformation (y_{max}) of panel BB was 161.3 mm.

However, panel BB deformation from the 'basic' box model using AUTODYN was 81.75 mm. The estimated value shows that it is possible that the compressed air can force the top panel to deform as much as 161.3 mm, though it is a very rough estimation, which was based on several assumptions.

Further analysis was done by deleting all air elements and creating a 'pressure boundary' model. The stress (pressure) boundary condition (triangular shape) was then applied at panel BB. From the plot in Figure 5.29, it was roughly estimated that the net pressure was applied at a maximum value at 0.05 ms and went down to zero at 10 ms. The results were compared together with the 'basic' box model in Figure 5.37.

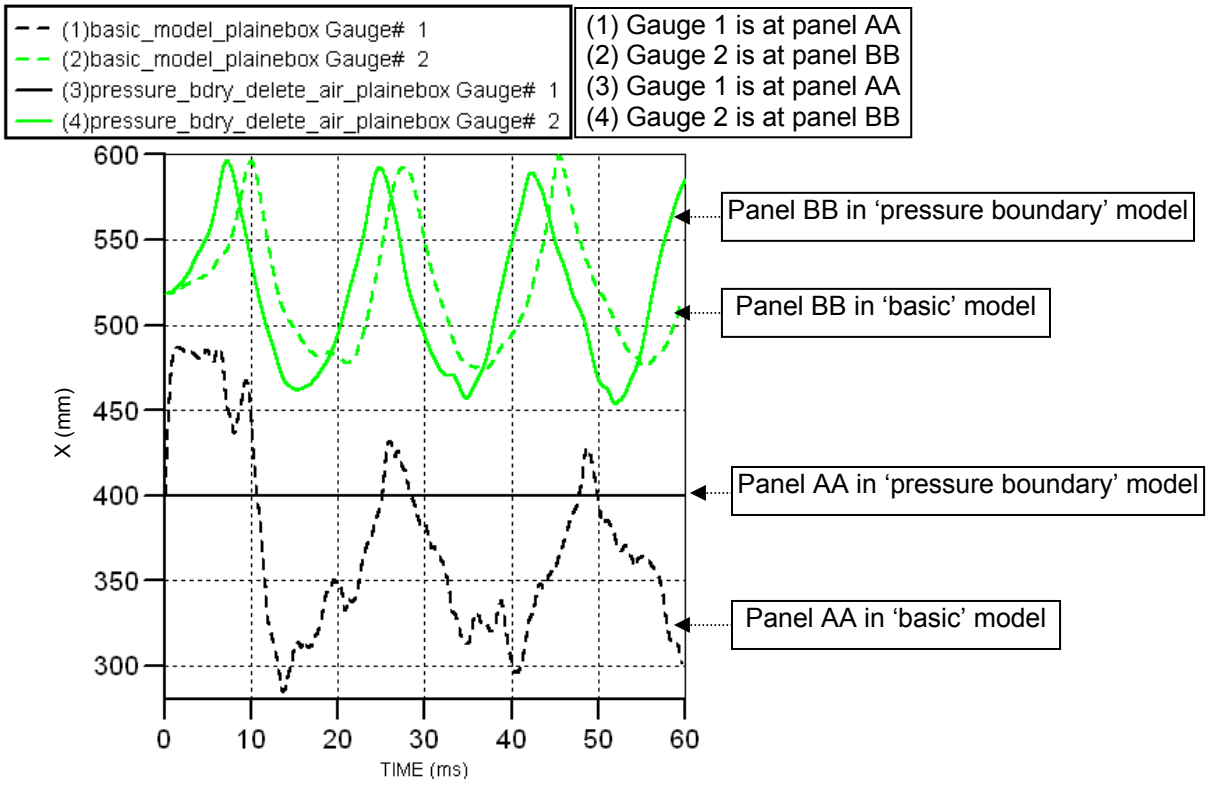

Figure 5.37 Comparison of maximum deformation results (mm) between 'basic' and 'pressure boundary' box model (each curve is based on the actual gauge position)

From the result in Figure 5.37, panel BB deformation curve in 'basic' and 'pressure boundary' models are very similar. It is evident that applying pressure on panel BB, which was calculated from the estimated compressed air (arising due to the deformation of the panel AA), produced maximum deformation and curve pattern similar to the 'basic' case, where actual air was allowed to interact with the structure. Note that panel AA deformation in the 'pressure boundary' model was zero for the whole duration, because the amount of stress boundary applied at panel BB was not large enough to force panel AA, which was rigidly joined to the structure to deform.

A further question arises as to what will happen if the compressed air inside the box model does not interact with panel BB. In other words, if the compressed air does not exist in the box model, will the deformation from the bottom panel alone force the top panel to deform in the case where panel AA does not impact with panel BB? For this case, a 'deleted air elements' box model was developed in exactly the same way as in the 'basic' box model, but the air elements close to the top panel were deleted so that there is no interaction

between the panel BB and the air, as shown in Figure 5.38. Note that it was important to keep the other air elements in the model in order to provide the blast loading to the bottom panel. The result is in Figure 5.39.

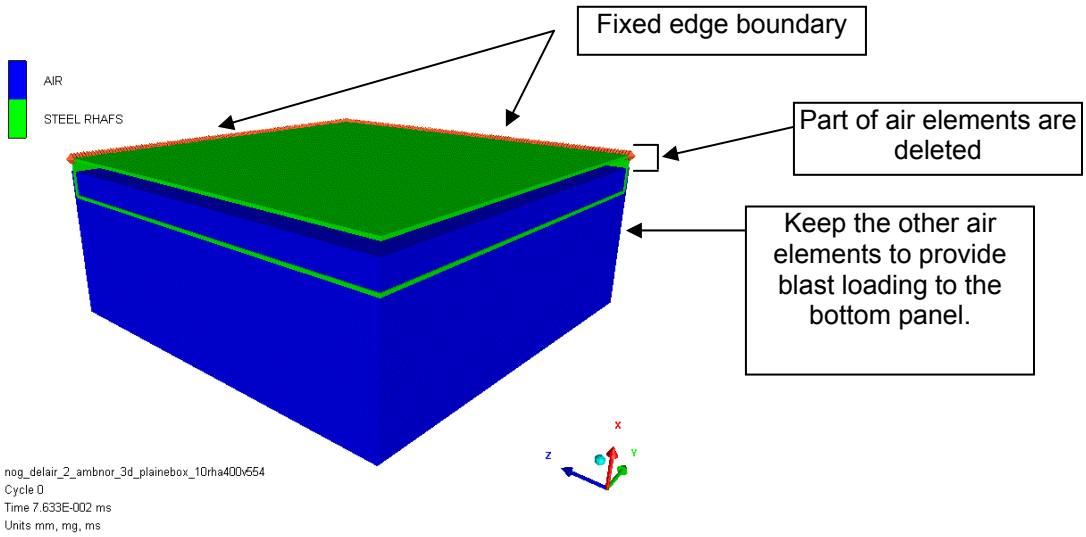

Figure 5.38 'deleted air elements' box model

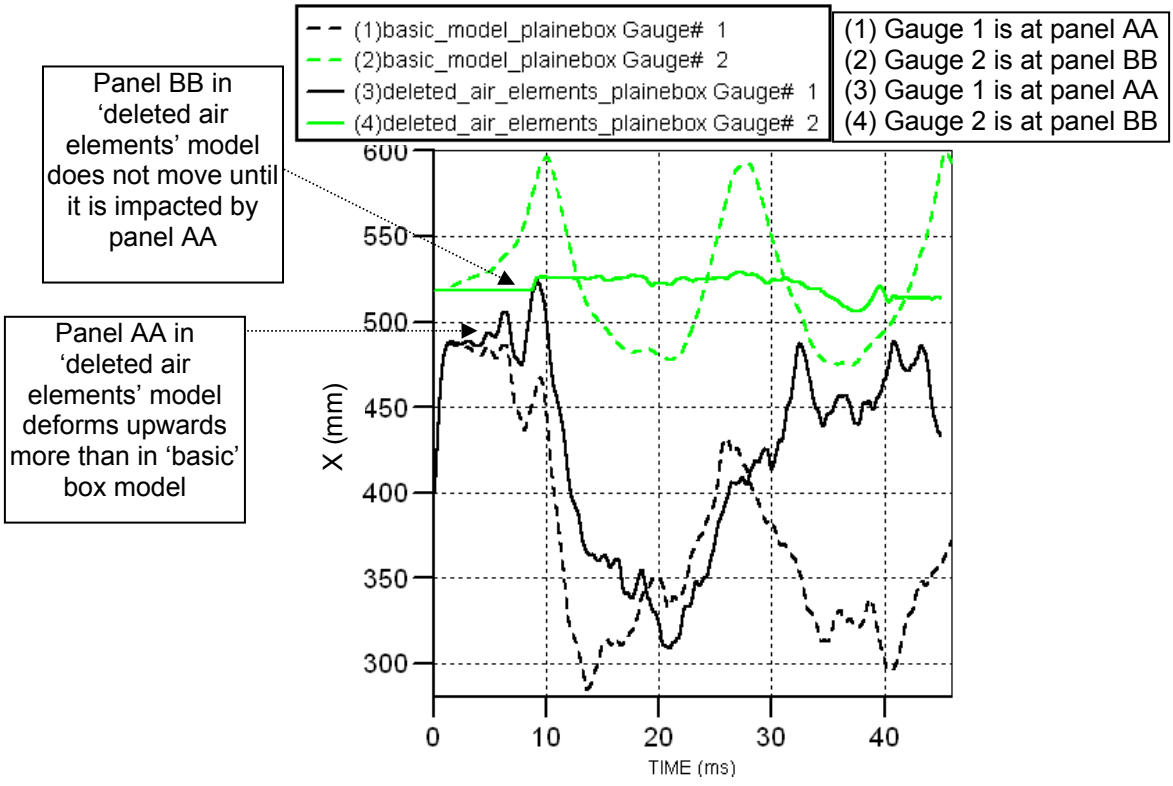

Figure 5.39 Comparison of maximum deformation results (mm) between 'basic' and 'deleted air elements' box model (deformation curves are based on the actual gauge positions)

From the deformation result in Figure 5.39, there are two principal results, which should be commented on. Firstly, panel BB in the 'deleted air elements' box model did not move at all up to about 8 ms whereas panel BB in the 'basic' box model moved significantly. This means that without the presence of compressed air, panel BB does not move. Secondly, panel AA in the 'deleted air elements' box model deformed more than in the 'basic' box model, and impacts with the panel BB. Both models are exactly the same except that parts of the air elements in the 'deleted air elements' model were deleted so the compressed air pressure was not allowed to interact with panel BB. It is thought that with the presence of the air in the 'basic' model, compressed air inside the box does not only force panel BB to deform, but it also ultimately acts as a 'cushion' to counter and prevent panel AA to deform upwards further. Unlike the 'basic' box model, the 'deleted air elements' box model did not have this 'cushion' and hence the bottom panel was allowed to deform more.

Figure 5.40 and Figure 5.41 show the contour pressure plot of the 'basic' box model in different stages. The graded contour scale was fixed to be the same at all stages. The plots show that, as panel AA started to deform in stage 1-3, the pressure started to build up at the corner (inside the box) in the ¼ model (or at the middle if it is viewed in a full model). Stages 4-7 show that the compressed air pressure started to propagate from the corner to the side panels. During Stages 8-10 the pressure moved back to the corner. At Stage 11, which occurs at 5.14 ms, the pressure was very condensed at the corner, as a result of the pressure flew back. By looking at deformation plot in Figure 5.30, at 5 ms, panel BB in the 'basic' model deformed about 10 mm. Stages 12-14 indicate that the compressed air pressure forced panel BB to deform much more than in the previous stages. At Stage 15 the deformation of panel BB created more internal volume inside the box and hence the compressed air pressure was less.

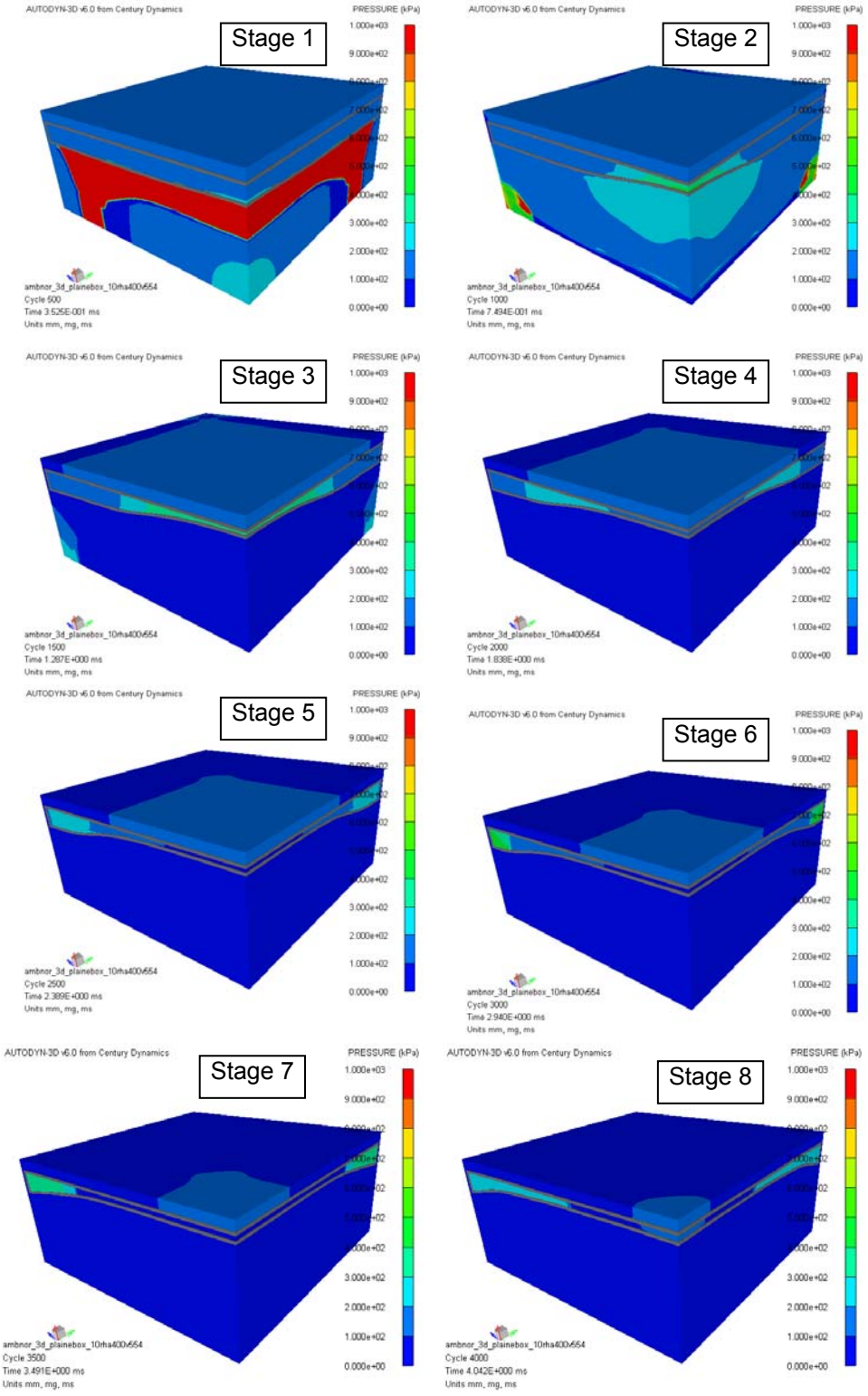

Figure 5.40 Pressure contour plot of the 'basic' box model (1)

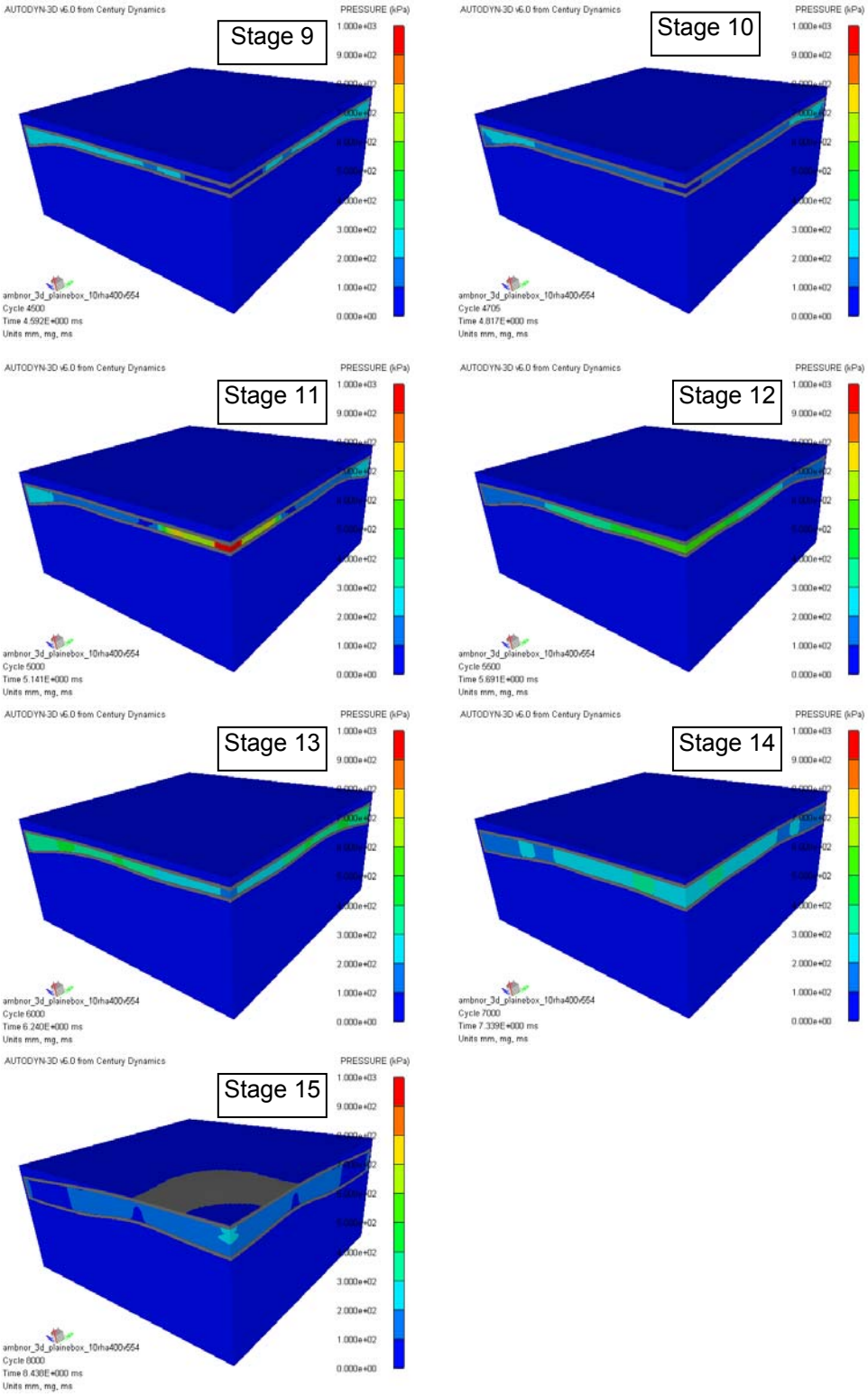

Figure 5.41 Pressure contour plot of the 'basic' box model (2)

5.5 'Vehicle hull' models

5.5.1 'Vehicle hull' numerical simulations

In this section a 'single plate' model, which represented a single floor in the vehicle, was developed further to include a vehicle hull. This model is defined as a 'single-floor hull' model. Likewise, a 'box' model, which denoted a double floor vehicle, was developed to become a 'double-floor hull' model.

The overall height of the vehicle was kept at 1700 mm, which was previously estimated in section 5.1.1. The thickness of the hull (side panels and the uppermost panel) was kept at 10 mm, the same as in the side panel in the 'box model'. For comparison purposes, only 400 mm stand-off distance was used. The explosive charge was 5 kg TNT in a spherical shape. Figure 5.42 and Figure 5.43 show the model configurations.

A numerical model of the 'hull model' was developed in exactly the same way as in the 'box model'. However, it is impossible to create the air elements to cover the whole hull using the same element size as in the 'box model' because of limited computing resources. Considering that the main interest of this thesis is at the bottom part of the vehicle not at the uppermost panel (panel CC), and the likely possibility that the compressed air will have little effect on the uppermost panel, due to the large hull volume, the effects of compressed air (inside the hull) to the uppermost panel is not considered. Hence modelling the air elements to cover the whole model is not necessary. In order to keep the influence of the air inside the smaller box at the bottom part of the model, the air elements in the 'hull model' were then created to cover the vehicle box bottom only. Results are in Figure 5.44 and Figure 5.45 and extended results are in Figures C.10 – C.17 (Appendix C). Unless otherwise stated, all gauges were at the centre of the panels in the full model.

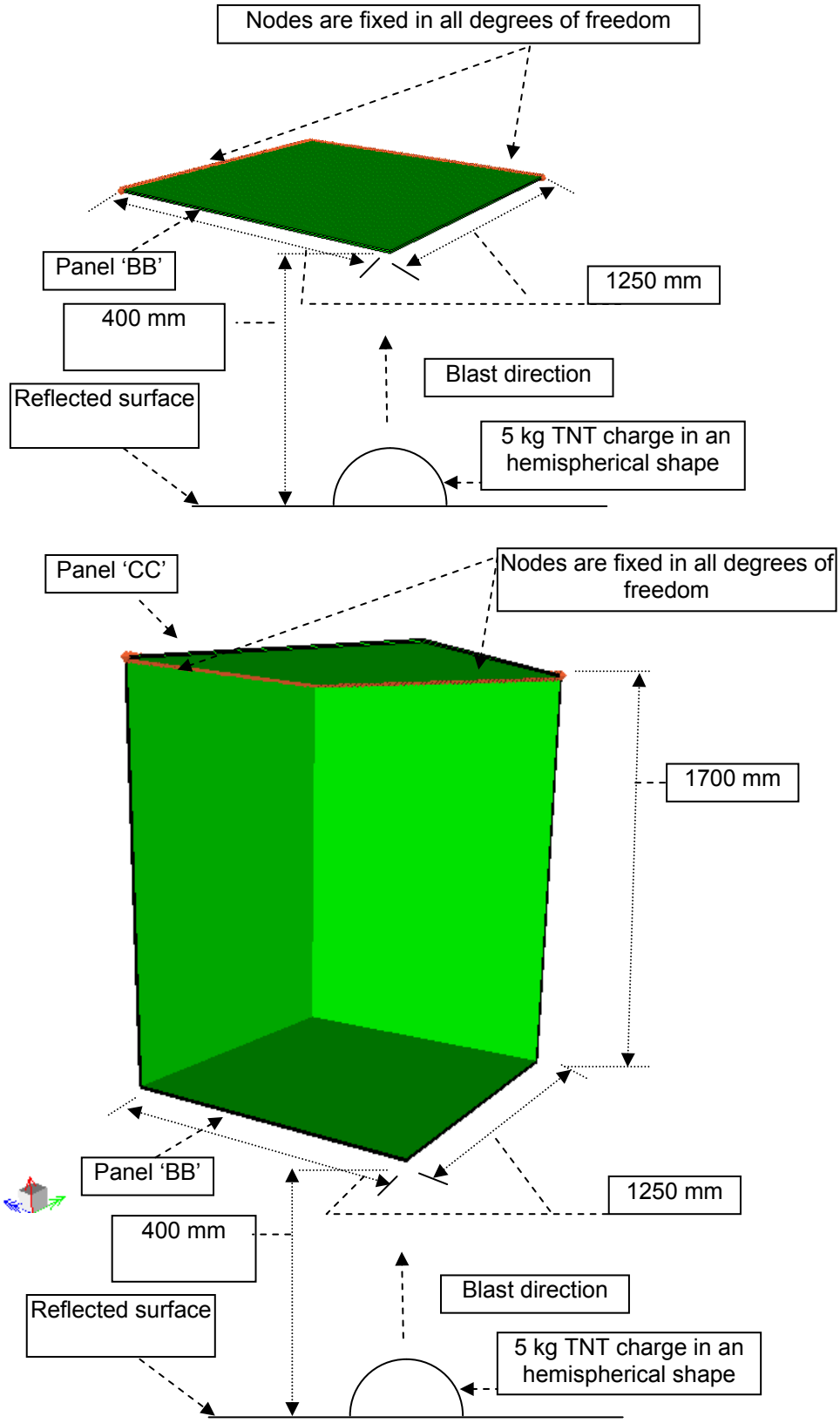

Figure 5.42 'single plate' and 'single-floor hull' models

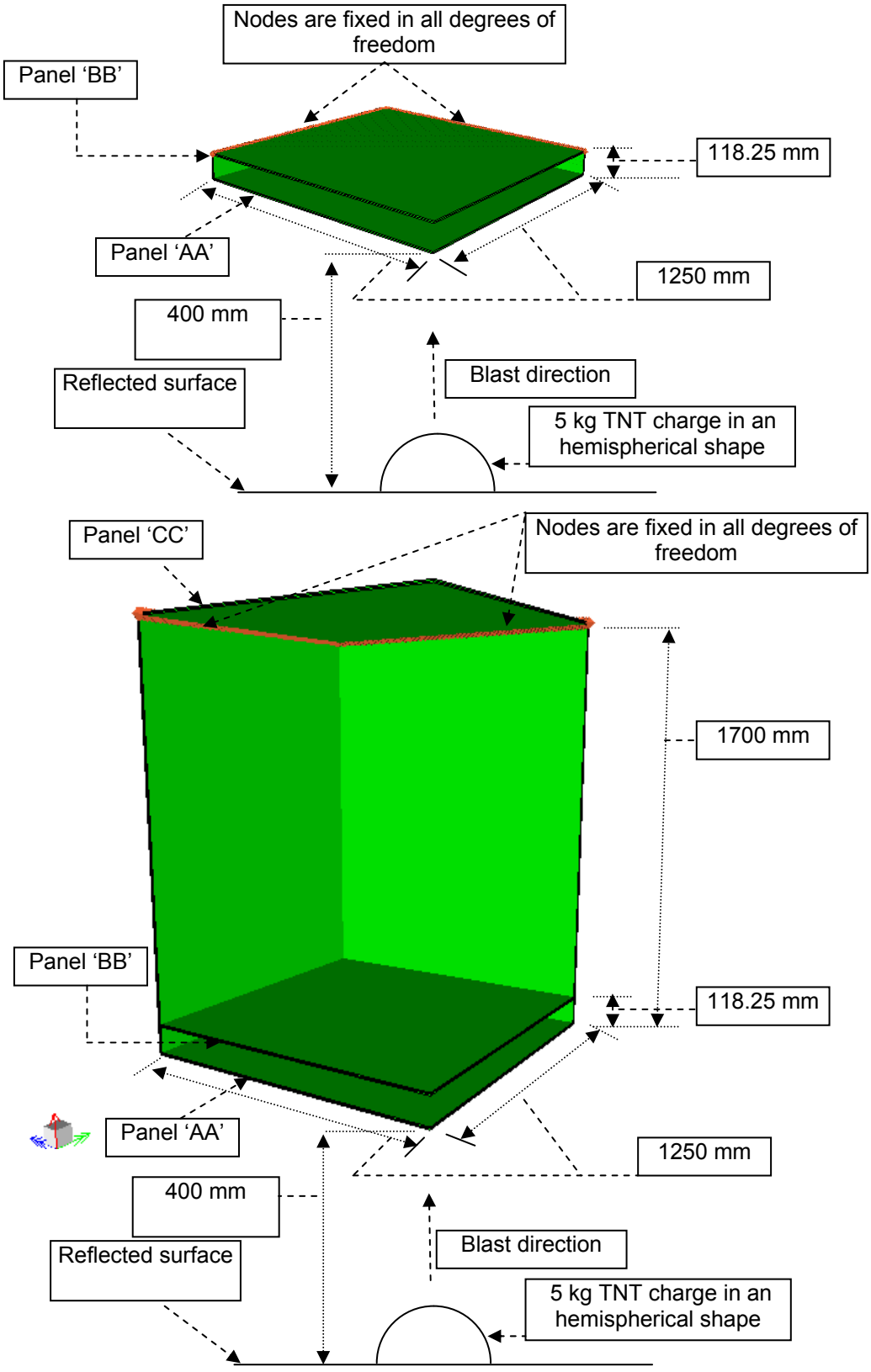

Figure 5.43 'box' and 'double-floor hull' models

5.5.2 'Vehicle hull' results

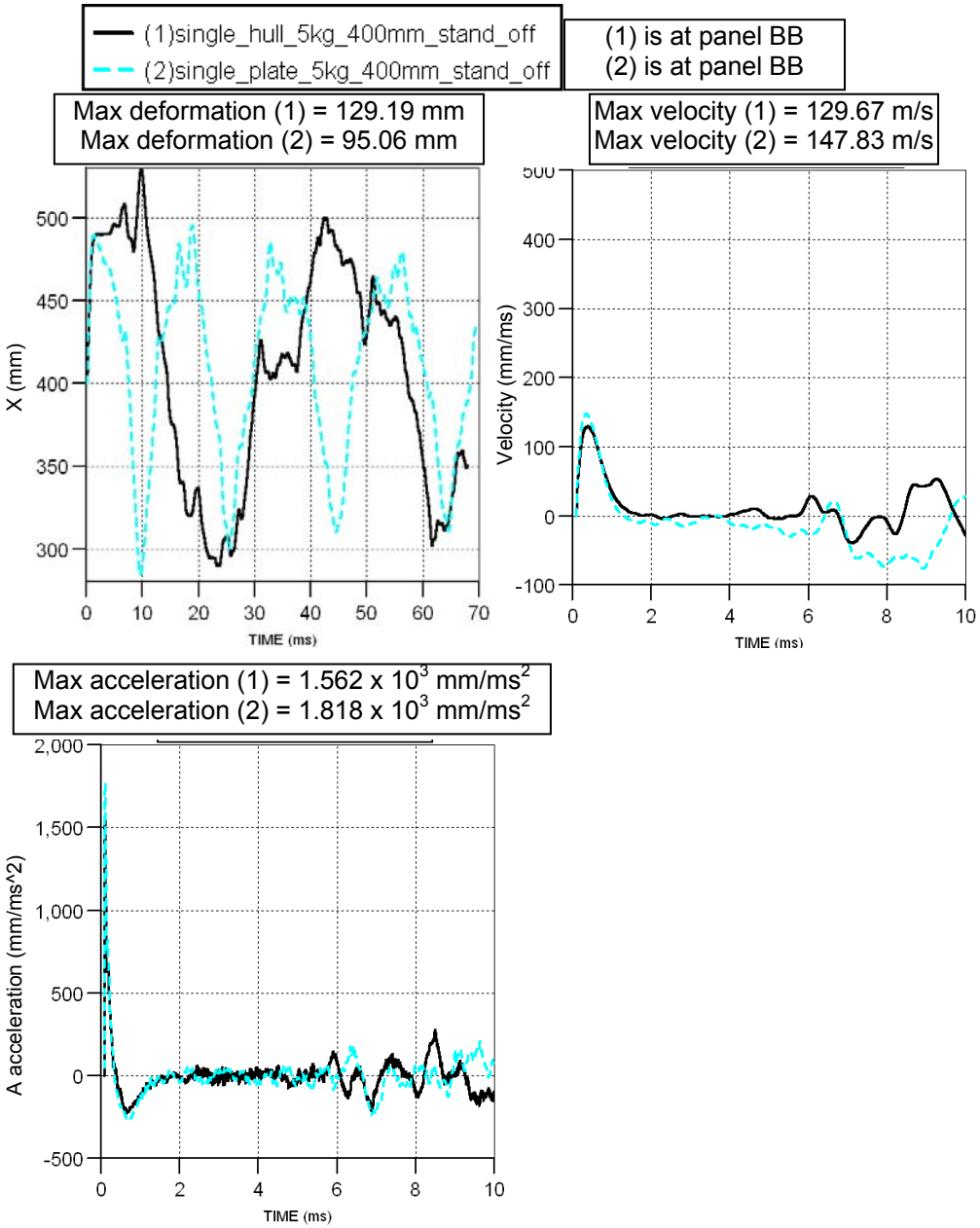

Figure 5.44 Dynamics deformation, velocity, and acceleration results on panel BB of 'single plate' and 'single-floor hull' models subjected to 5 kg TNT in an hemispherical shape blast at 400 mm stand-off distance (deformation curves are based on the actual gauge positions)

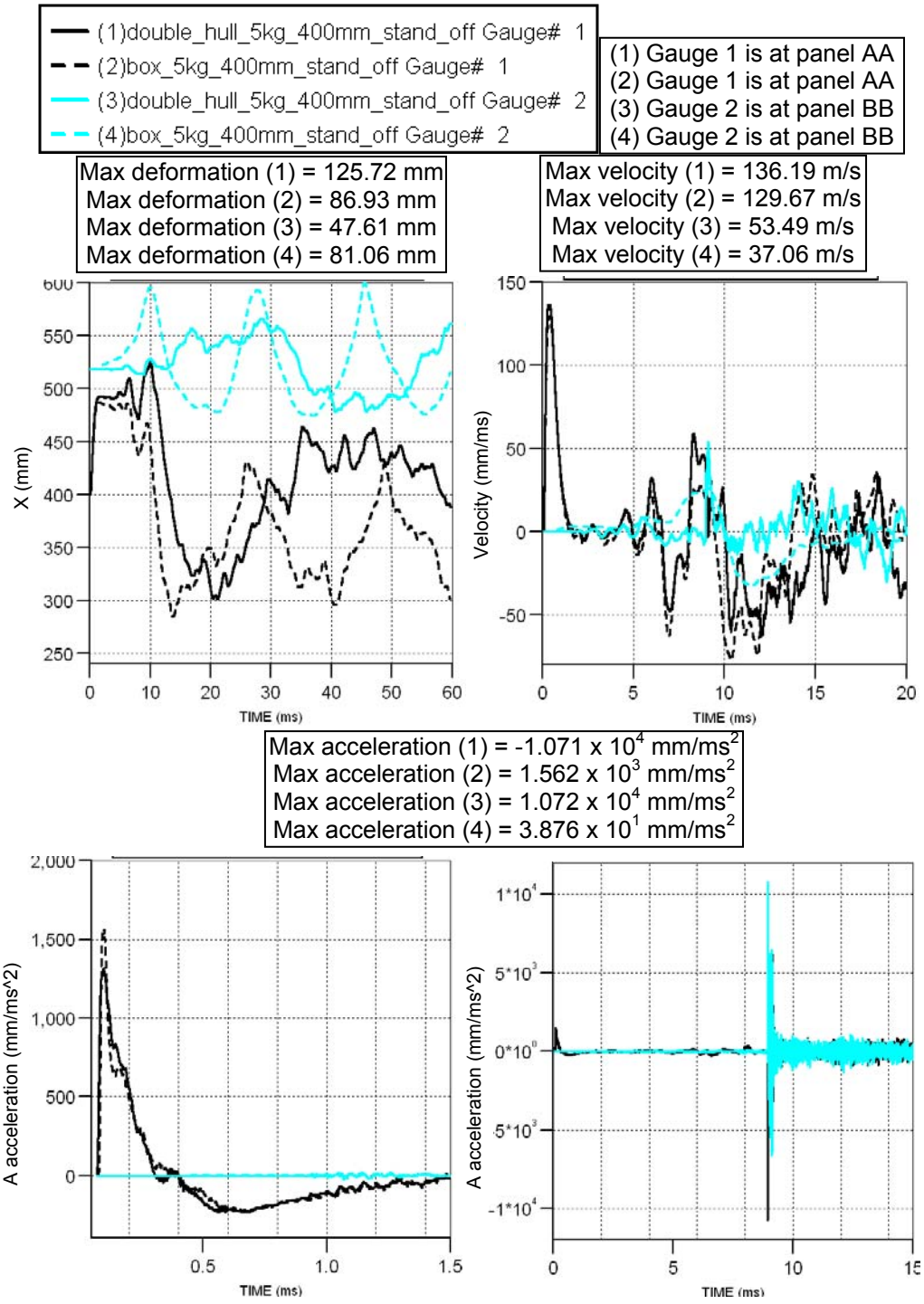

Figure 5.45 Deformation, velocity and acceleration results on panel AA and BB of 'box' and 'double-floor hull' models subjected to 5 kg TNT in an hemispherical shape blast at 400 mm stand-off distance (deformation curves are based on the actual gauge positions)

5.5.3 'Vehicle hull' discussion

Section 5.5 developed a 'single-floor vehicle hull' model and a 'double-floor vehicle hull' model, to compare with a single plate model and a 'box' model. Note that the comparison between a vehicle with single floor and double-floor settings is not discussed in this chapter; it will be investigated in Chapter 6. The results in Figure C.11 and Figure C.17 (Appendix C) show that the maximum deformation at panel BB in a 'single-floor hull' model, and maximum deformation at panel AA in a 'double-floor hull' model occurred at the middle of the panels.

Figure C.12 (Appendix C) indicates that gauge xy1 deformed inwards in z-direction first, while in x-direction, it deformed upwards up to about 5 mm. Gauge xy2 deformed outwards first in z-direction and upwards in x direction. It is thought that in the 'single-floor hull' model, as panel AA deformed in x-direction, the side panel is bent inwards and hence part of it (at gauge xy2) deformed outwards relative to its position. Because at the other end (top) the side panel is rigidly joined to panel CC, whose edges are fixed in all degree of freedom. Figure C.13 (Appendix C) shows around 4 mm deformation occurred at panel CC. It is thought that the movement of panel CC was due to the moment transfer from the side panel. In the double-floor hull model, Figure C.15 (Appendix C) indicates an inwards deformation first in z-direction at gauge xy1, while in x-direction the movement is limited to around 1 mm. At gauge xy2, the deformation in z-direction is small (~1 mm), while at gauge xy3, the deformation in x-direction is also small. (~1 mm). In Figure C.16 (Appendix C), panel CC in the 'double-floor hull' model deformed around 4 mm, which is similar to panel CC in 'single-floor hull' model. As the deformation of panel CC is relatively small, in the further comparisons in Chapter 6, the effects on panel CC will not be discussed.

The comparison between a single plate model and a 'single-floor hull' model in Figure 5.44 shows that the maximum deformation in the single-floor hull model is 36% more, while the maximum velocity and acceleration are 12% and 14% less. The comparison between a 'box' model and a double-floor hull model in Figure 5.45 shows 76%, 5% and 586% increase in maximum deformation, velocity, and acceleration at panel AA in the double-

floor hull model, while at panel BB, 41% decrease in maximum deformation, 44% increase in velocity, and 377 times maximum acceleration are observed. It is thought that by modelling as a vehicle hull, the longer side panels and the changes in the boundary condition allowed panel BB in the single-floor setting to deform more, while in the double-floor setting, it allowed panel AA to deform more and subsequently impacted panel BB. After the impact, higher velocity (44% increase) and undesirable high acceleration (377 times) was recorded at panel BB. Panel AA and BB did not go through each other, which indicates that the model was set to provide a realistic scenario. Note that the deformation at panel BB in the double-floor hull model is less than in the 'box' model because, in the 'box' model, the side panel is short and rigidly joined with panel BB. This panel is fixed in all degrees of freedom on its edges, while in the 'double-floor hull' model the side panel is much longer and the boundary condition is moved to panel CC. As a result, the load at panel BB in the double-floor hull model is dissipated through the deformation at the joint between the side panel and panel BB, while at the same position in the 'box' model, the joint is fixed in all degrees of freedom. This can be seen in gauge xy2 results in Figure C.8 and Figure C.15 (Appendix C).

The important observation is that the impact between panel AA and BB occurred in a vehicle hull rather than in a box model even though they had the same configurations, such as the same stand-off distances, the same thickness, etc. The high acceleration associated with the impact may cause injury or death to the occupants. Not only can the high acceleration be transmitted through their feet or seats, but it may also cause equipment lying on the crew compartment floor to fly around and impact them at high velocity/acceleration. Therefore, it is decided that the comparison in Chapter 6, which compares different vehicle bottom geometries, will be developed as a single-floor hull model or a double-floor hull model.

5.6 Conclusions

At the start of this chapter, work had been done to find information in order to form relevant parameters for simulations. After initial analyses, simulations of horizontal single RHA plate subjected to mine blast based on realistic vehicle geometry, were developed and analysed in terms of different thicknesses (10, 20, and 30 mm), in terms of different stand-off distances (300, 400, 450, 500, and 600 mm) and in terms of different amount of charges (5 kg and 3.17 kg TNT). The results showed good trends, although at 300 mm stand-off distance the results seemed too low. This was a problem in AUTODYN remap method, which assumed the mixture of air and explosive to behave as an ideal gas at the stand-off distance being too close to the explosive.

A 'box' model of 10 mm thickness subjected to 5 kg TNT blasts at 400 mm stand-off distance was then developed. The result indicates that panel BB deformed even though panel AA did not impact and force panel BB to deform. Following a series of investigations, it is evident that the compressed air contained within the gap is the main reason that panel BB deformed. In cases where the compressed air was allowed to interact with panel BB, the effects would depend on how the structure was set up. Different boundary conditions may result in different panel BB responses, but panel BB still deformed. Side panels may have also contributed to the panel BB deformation by transferring moments to it, though without the side panels, panel BB still deformed.

The single plate and 'box' model were developed further to be 'single-floor hull' and 'double-floor hull' models. By modelling as a 'double-floor hull' model, the results captured the impact between panel AA and BB, which was observed by the deformation and high acceleration results.

The development of these models has resulted in 'single-floor hull' and 'double-floor hull' models being selected as suitable models to use to compare the effects of a vehicle having single floor and double floor settings subjected to a mine blast in Chapter 6. The experiences gained in this chapter are valuable to the numerical modelling of a vehicle against a mine blast.

CHAPTER 6 Comparison on different vehicle hull models

Chapter 5 compared the 'single plate' and 'single-floor hull' models and 'box' and 'double-floor hull' models and established that vehicle hull models ('single-floor hull', and 'double-floor hull') would be used for future investigations. This chapter will investigate the comparison between a single-floor vehicle and a double-floor vehicle by comparing the 'single-floor hull' and 'double-floor hull' models.

Case no.	Types of hull (single/ double/ 'V' bottom)	Amount of charge in hemispherical shape (kg TNT)	Distance from the charge to the nearest panel (mm)	Thickness of panel BB (mm)	Thickness of panel AA (mm)	Thickness of side panels (mm)	Gap between panel AA and BB (mm)
1	Single	10	400	10	n/a	10	n/a
2	Double	10	400	10	10	10	118.25
3	Single	10	518.25	10	n/a	10	n/a
4	Single	10	400	20	n/a	10	n/a
5	Single	10	518.25	20	n/a	10	n/a
6	Double	10	450	10	10	10	118.25
7	Double	10	500	10	10	10	118.25
8	Double	10	600	10	10	10	118.25
9	Double	5	400	10	10	10	118.25
10	Double	3.17	400	10	10	10	118.25
11	Double	10	400	10	10	10	270
12	Double	10	400	10	10	10	315
13	Double	10	400	10	20	10	118.25
14	Double	10	400	10	30	10	118.25
15	Double	10	400	10	40	10	118.25
16	Double	10	400	20	10	10	118.25
17	Double	10	400	10	10	20	118.25

18	Double	10	400	20	20	10	118.25
19	'V' bottom	5	400	10	10	10	280.41 (max)
20	Single (1581.75 mm height)	10	718.25	21.66	n/a	10	n/a
21	'V' bottom (1862.16 mm height)	10	437.84	10	10	10	280.41 (max)
22	Single	3.17	518.25	10	n/a	10	n/a
23	Single	10	518.25	40	n/a	10	n/a

Table 6.1 Summary of different configurations from different cases.

6.1 Initial comparisons

6.1.1 'Initial comparisons' numerical simulations

Firstly, the 'single-floor hull' model is compared with the 'double-floor hull' model (case 1 vs. case 2) keeping the distance of the vehicle from the ground (on which lies the hemispherical charge) constant, at 400 mm. The overall vehicle height is kept constant by making the height of the crew compartment of the double-floor vehicle 118.25 mm less than the single-floor vehicle in order to accommodate the double-floor. Note that the 118.25 mm gap is chosen in order to allow subsequent comparison with the 'V bottom' vehicle of 160° internal angle. Then the distance from the charge is increased to 518.25 mm (case 3) in order to maintain a constant stand-off distance for panel BB in cases 2 and 3 – see Figure 6.1. Initially the thicknesses of each individual panel are all 10 mm, and the explosive charge is 10 kg TNT. In the subsequent sections, parameters in the amount of explosive charge, stand-off distance (from the charge to the nearest panel), thickness of panel BB and AA may vary. Table 6.1 summaries these changes. The results of case 1, 2, and 3 are in Figure 6.2 – 6.5.

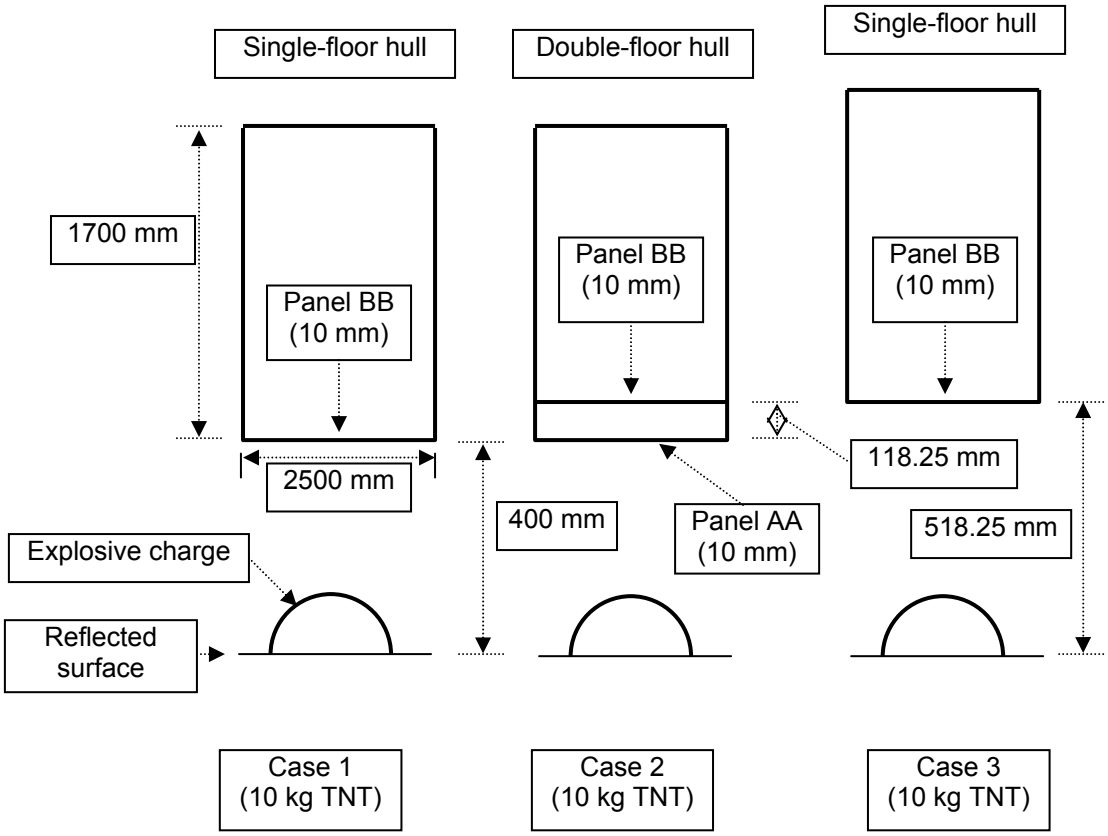

Figure 6.1 Schematic drawing of a comparison between cases 1, 2, and 3 (It is not drawn to scale).

6.1.2 'Initial comparisons' results

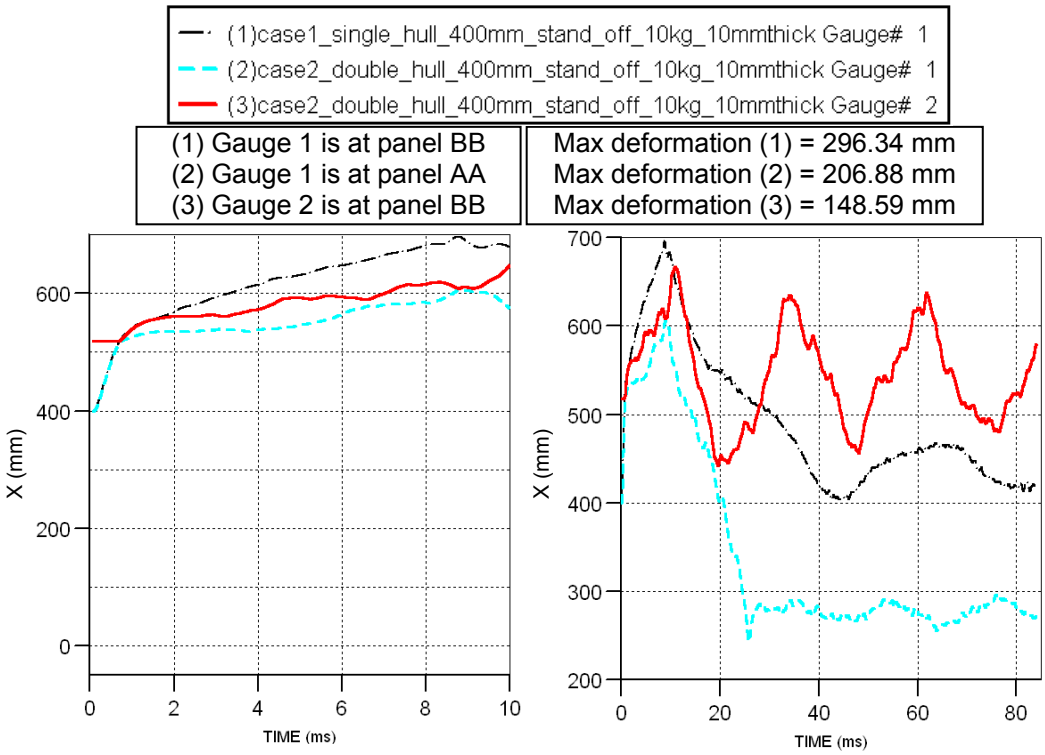

Figure 6.2 Dynamics deformation results of panel BB in case 1, panel AA in case 2, and panel BB in case 2. Note that deformation curves are based on the actual gauge positions.

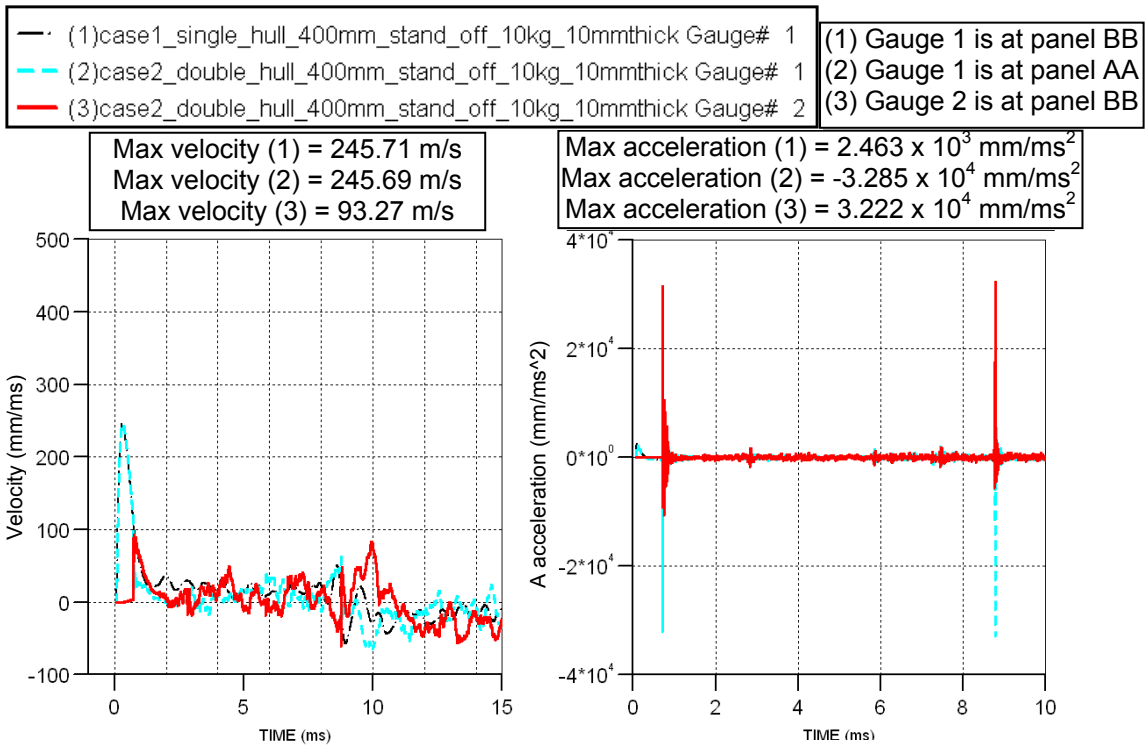

Figure 6.3 Velocity and acceleration results of panel BB in case 1, panel AA in case 2, and panel BB in case 2.

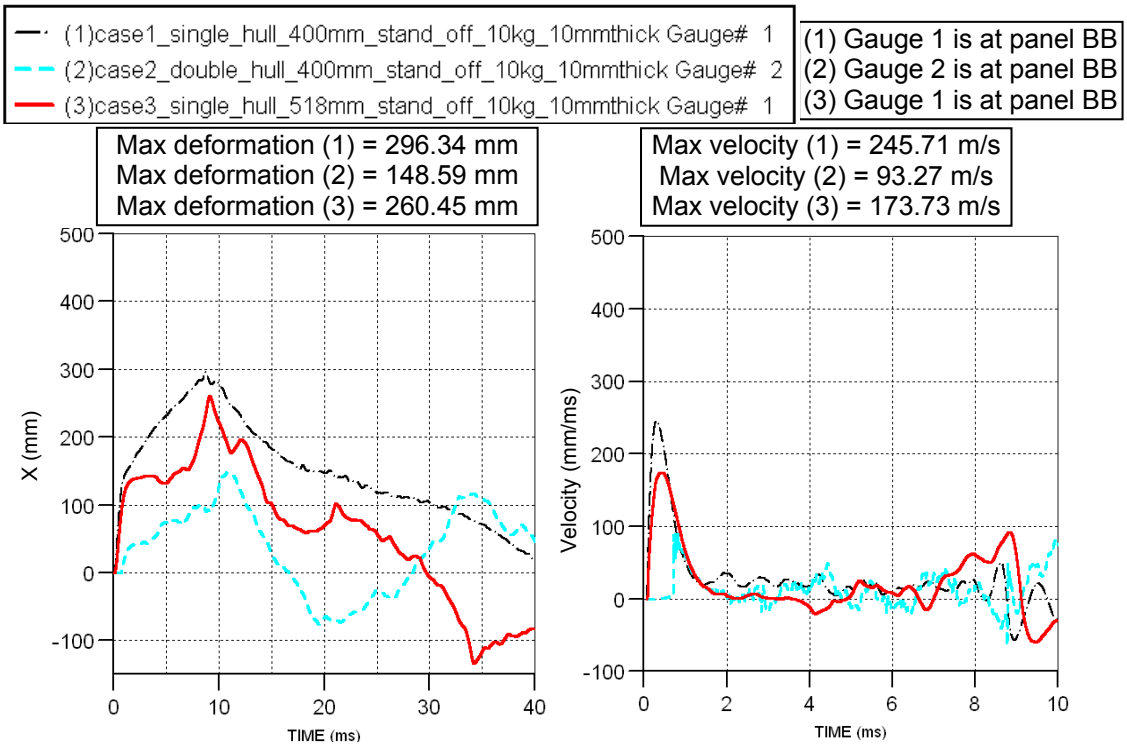

Figure 6.4 Deformation and velocity results at panel BB in cases 1, 2, and 3. Note that deformation curves are based on the net deformation.

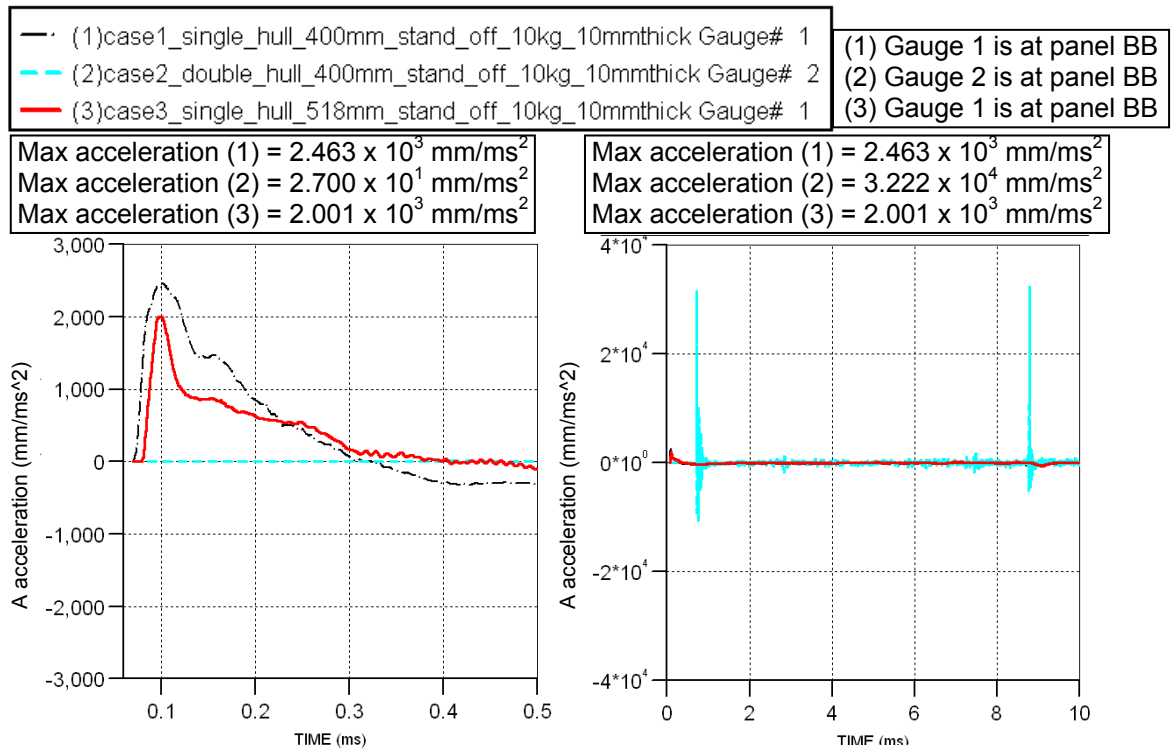

Figure 6.5 Acceleration results at panel BB in cases 1, 2, and 3.

6.1.3 'Initial comparisons' discussion

From the results in Figure 6.2 and Figure 6.3, panel AA in case 2 has impacted with panel BB at approximately 1 and 9 ms. As a result, extremely high acceleration can be observed at these two points. By looking at the panel which encountered the blast first, the results show that panel BB in case 1 has deformed more than panel AA in case 2. This is due to the obstruction from panel BB in case 2, which prevent panel AA to deform further. The maximum velocity from panel BB in case 1 and panel AA in case 2 are very similar because these peaks occurred at the time before the impact in case 2, where the same blast loading were encountered on the same panel of the same thickness.

When panel BB is considered, which represents the crew compartment floor, the maximum deformation and velocity in case 1 and 3 are more than case 2, as shown in Figure 6.4. As the mass of the overall vehicle (structure only) in case 1 is increased 489 kg by adding another floor panel as in case 2, the maximum deformation and velocity are reduced by 49.9%, and 62.0% respectively. In case 3, the stand off distance is increased from 400 mm in case 1 to 518.25 mm, the maximum deformation and velocity are reduced by 12.1% and 29.3% correspondingly. This shows that adding another floor panel into the blast path has reduced the effects on the crew compartment floor more than increasing the stand-off distance, although this requires that the total vehicle mass is not constrained. Figure 6.5 shows that the peak acceleration on panel BB in the double-floor hull model (case 2) is much higher (13 and 16 times more than in case 1 and 3 respectively) than in the single-floor hull model (case 1 and 3) due to the impact between panel AA and BB. However, if one considers the acceleration before the impact, case 2 has much lower acceleration than in case 1 and 3. Compared with cases 1 and 3, acceleration in case 2 is reduced by 99%.

6.2 'single-floor hull' and 'double-floor hull' models

6.2.1 'single-floor hull' and 'double-floor hull' numerical simulations

In this section, the total vehicle weight (mass) and height of single and double floor hull models were kept constant by increasing the thickness of panel BB in single floor hull model to be 20 mm. The stand off distances in case 4 and 5 remain the same as in cases 1 and 3 respectively, which can be seen in Figure 6.6. Results of panel BB in cases 4 and 5 are compared with case 2 in Figure 6.7 and Figure 6.8.

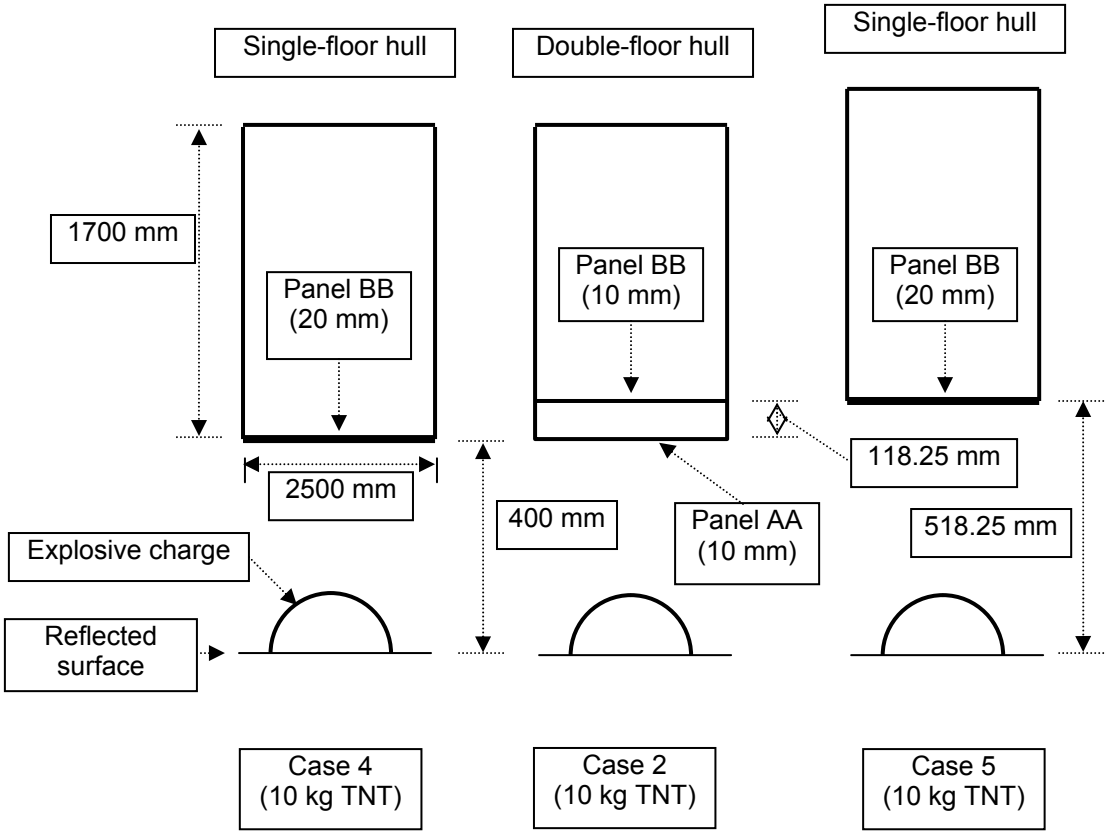

Figure 6.6 Schematic drawing of a comparison between 'single-floor hull' and 'double-floor hull' models (cases 4, 2, and 5).

6.2.2 'single-floor hull' and 'double-floor hull' results

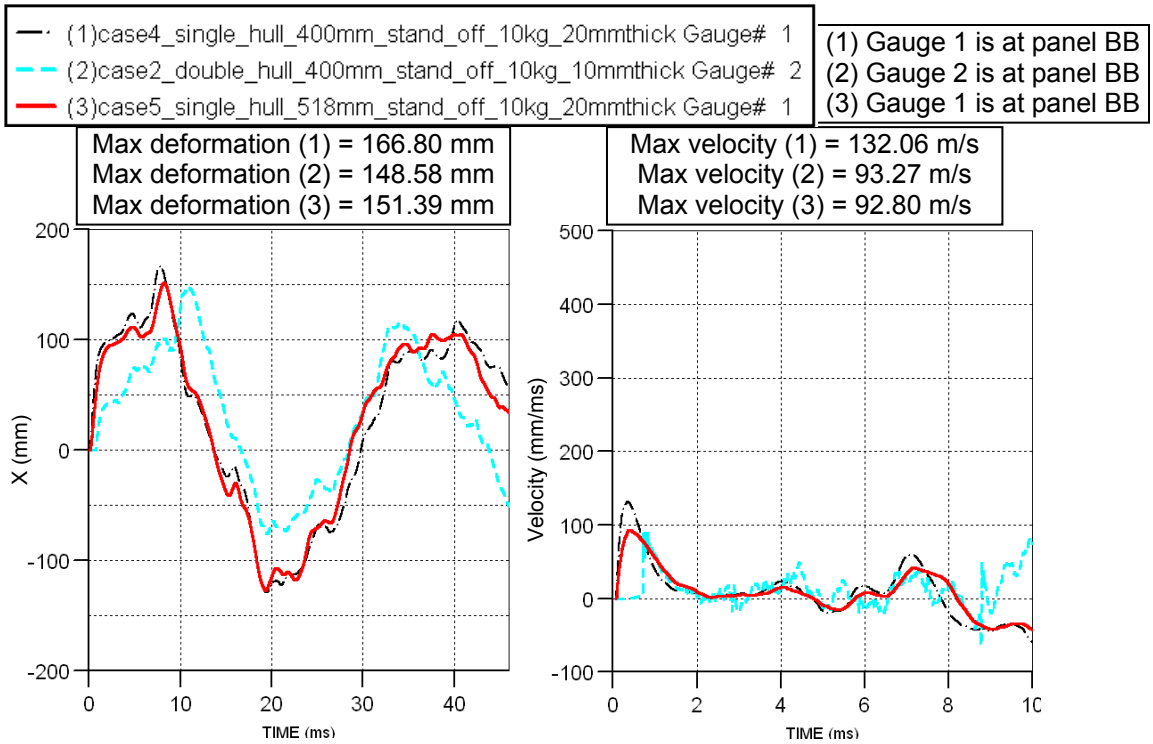

Figure 6.7 Deformation (net deformation) and velocity results at panel BB in cases 4, 2, and 5. Note that deformation curves are based on the net deformation.

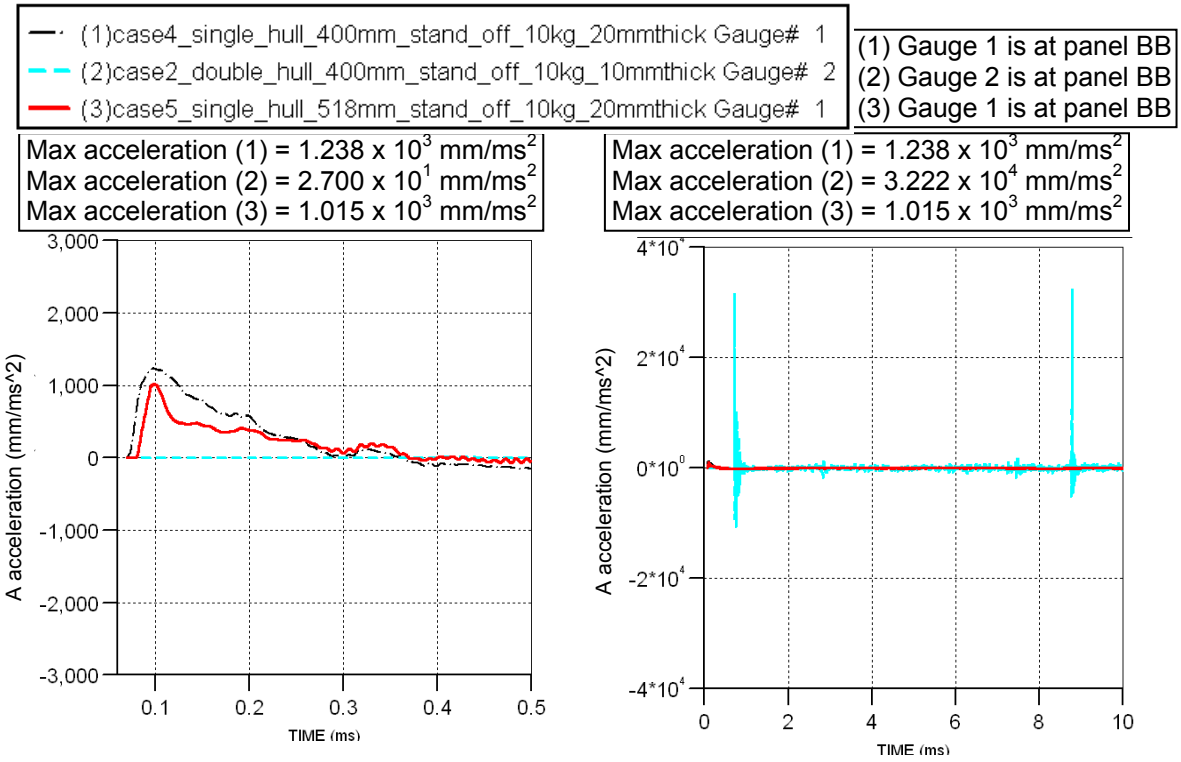

Figure 6.8 Acceleration results at panel BB in cases 4, 2, and 5.

6.2.3 ‘single-floor hull’ and ‘double-floor hull’ discussion

The analysis has progressed further by keeping the total vehicle weight (mass) in the single-floor hull model, in cases 4, and 5, to be the same as in double-floor hull model as in case 2. Compared with panel BB in case 4 as shown in Figure 6.7, maximum deformation in cases 2 and 5 is reduced by 10.9%, and 9.2%, whilst the corresponding maximum velocity is reduced by 29.4% and 29.7%. It shows that the deformation and velocity results at panel BB in cases 2 and 5 is very similar, however, the big differences is in the acceleration as shown in Figure 6.8. Compared with panel BB in case 4 before collision with panel AA, maximum acceleration in cases 2 and 5 is decreased by 98% and 18% respectively. The impact between panel AA and BB in case 2 has created very high acceleration as much as 26 times more than case 4. At this point, it seems that in the double-floor system, it is important to avoid the impact between panel AA and BB, which is due to the maximum deformation in panel AA exceeding the gap distance, so that the undesirable high acceleration does not occur for panel AA and BB.

6.3 Varying stand off distances

6.3.1 'Varying stand off distances' numerical simulations

The response of the vehicle hull to increasing stand-off distance was investigated. Numerical simulations were developed in the same way using a range of stand-off distances: 400, 450, 500 and 600 mm as shown in Figure 6.9. The explosive charge remained a 10 kg hemisphere of TNT. Results are shown in Figures 6.10 – 6.12.

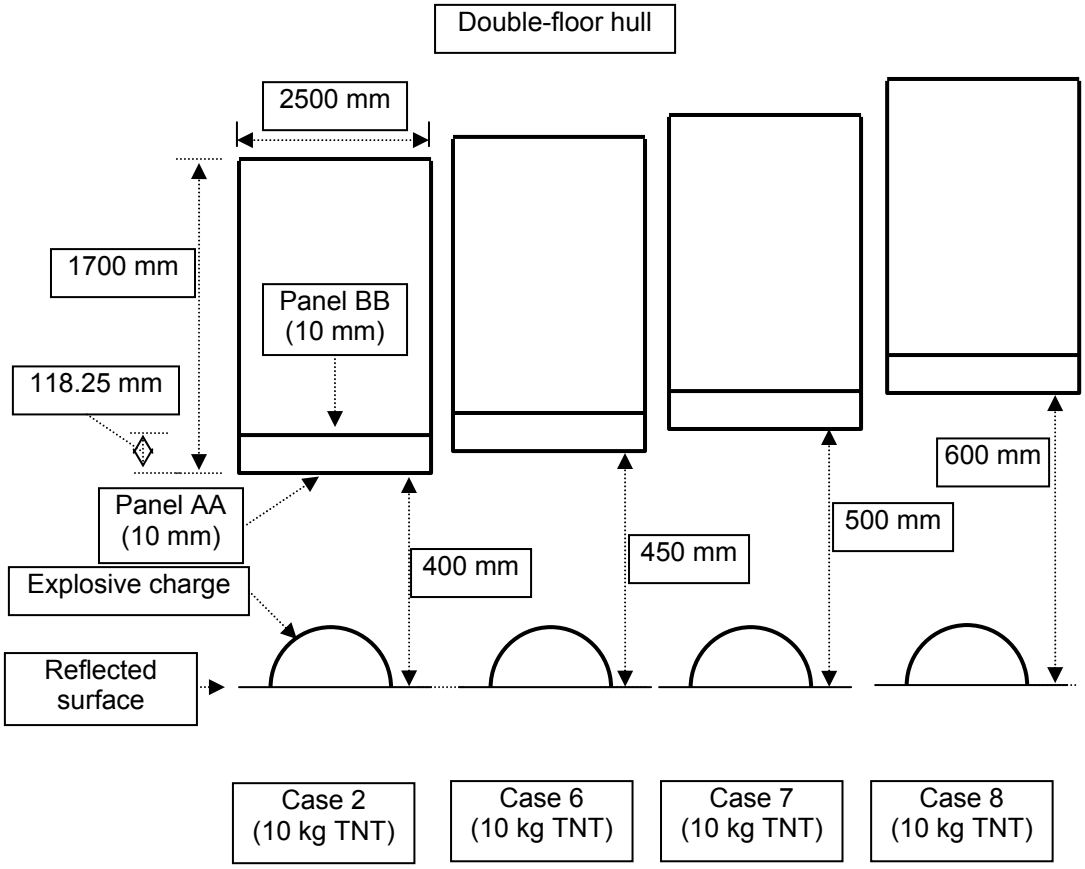

Figure 6.9 Schematic drawing of a comparison in 'double-floor hull' models (cases 2, 6, 7, and 8).

6.3.2 'Varying stand off distances' results

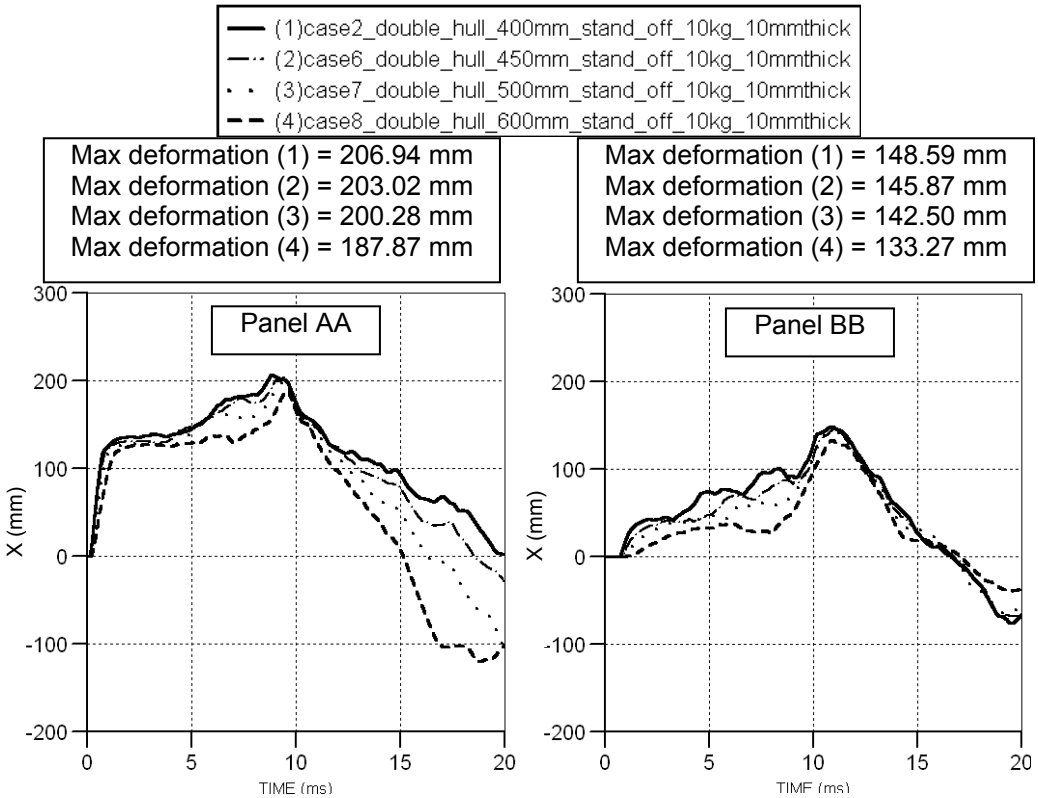

Figure 6.10 Maximum deformation results of panels AA and BB in cases 2, 6, 7, and 8. (Deformation curves are based on the net deformation.)

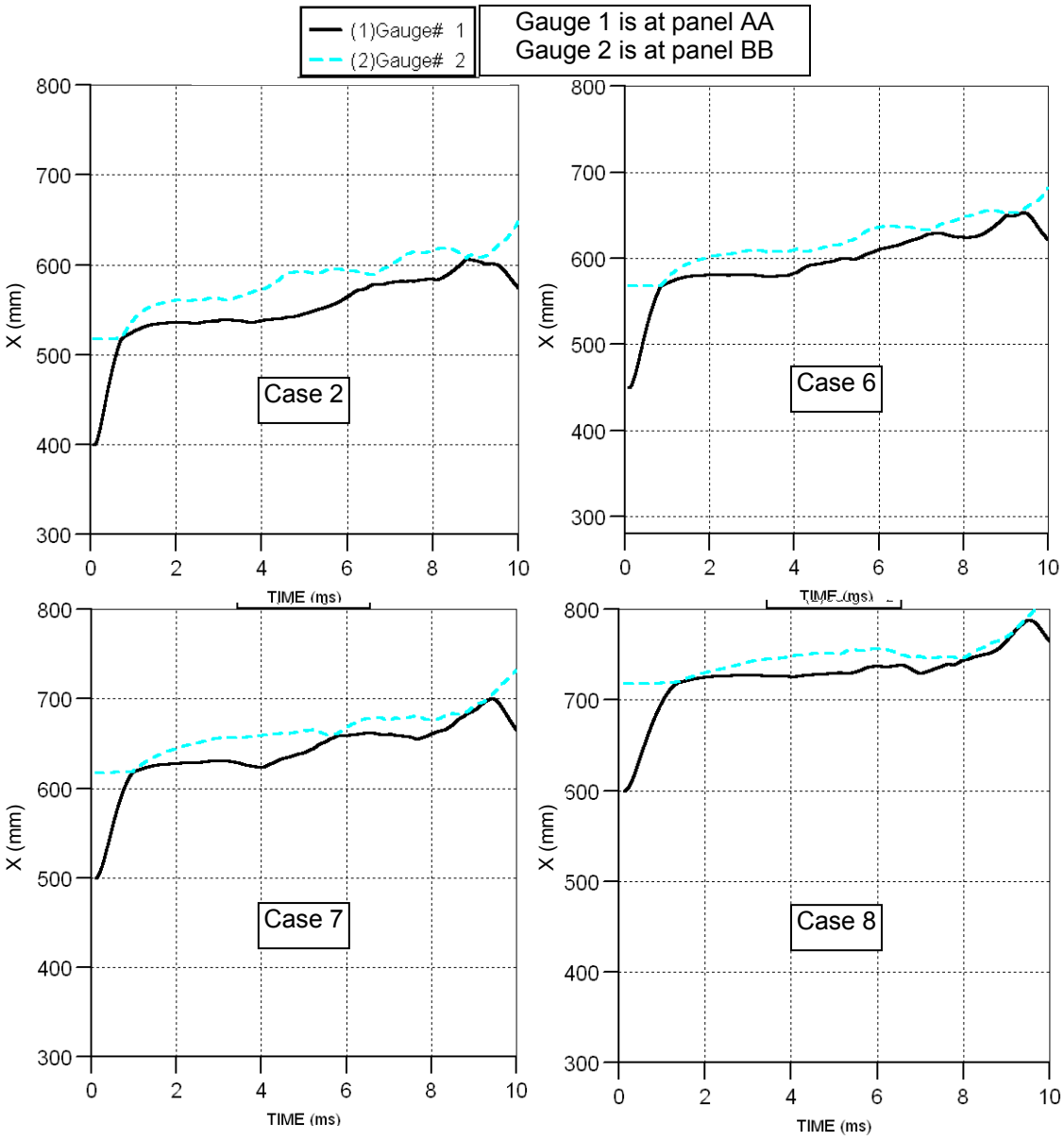

Figure 6.11 Deformation results in cases 2, 6, 7, and 8. (Deformation curves are based on the actual gauge positions.)

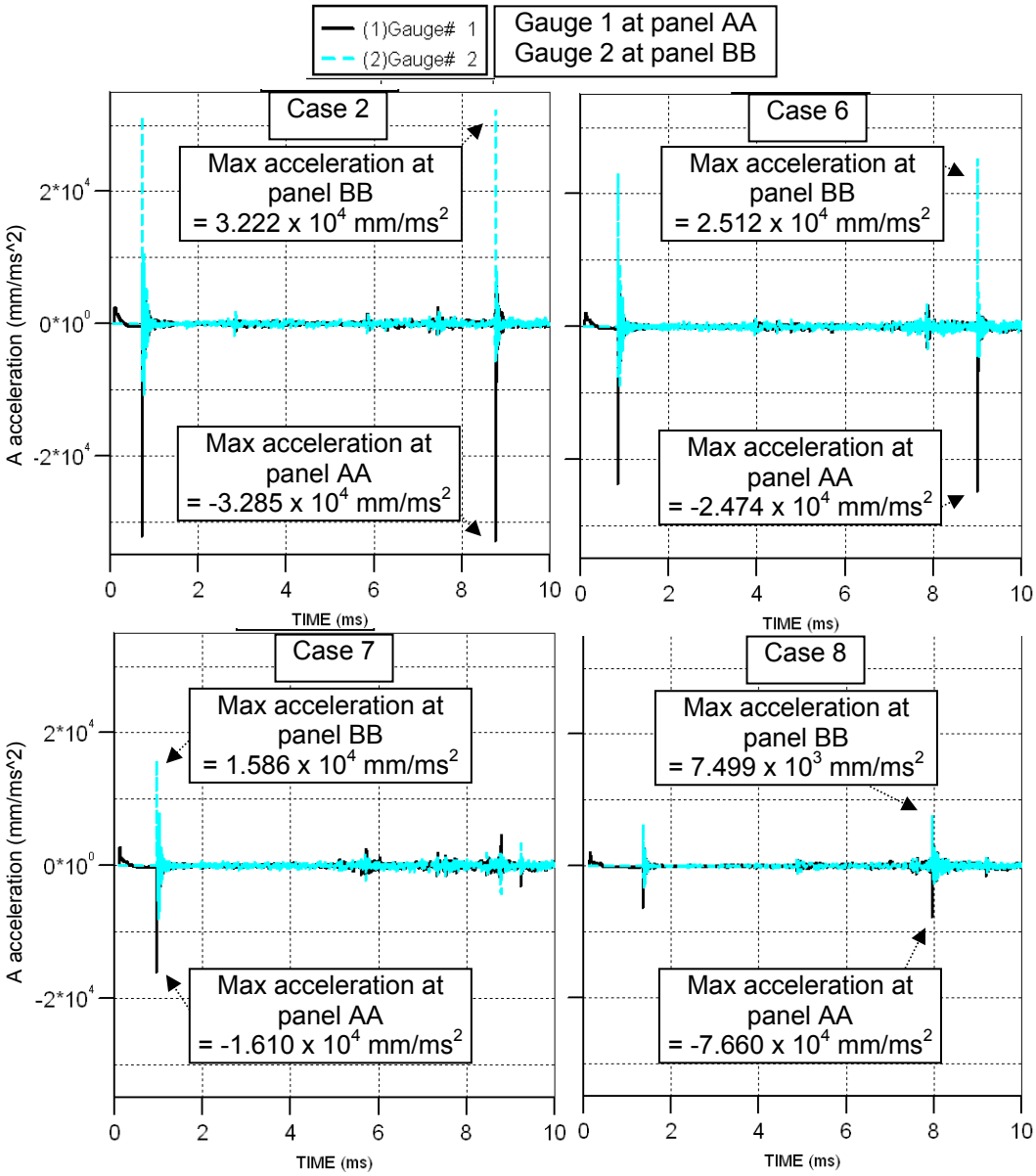

Figure 6.12 Acceleration results at panel AA and BB in cases 2, 6, 7, and 8. Note that all cases contain the same scales.

6.3.3 'Varying stand off distances' discussion

In cases 6, 7, and 8, the stand off distance in case 2 has extended to 450, 500, and 600 mm. Results in Figure 6.10 shows that panel BB in cases 6, 7, and 8 has deformed 2%, 4%, and 10% less than case 2. This indicates that the further away from the blast the less the effect on panel BB. By looking at Figure 6.11, panel AA still impacts with panel BB in case 2, 6, 7, and 8, even though the stand off distances are increased. As a result, the maximum acceleration results in Figure 6.12, illustrates very high acceleration at the time of impact in each case, though the peak is decreasing as the stand off distance is increasing. Cases 6, 7 and 8 respectively show 22%, 51% and 77% reductions of the maximum acceleration of Panel BB compared with case 2.

6.4 Varying amounts of explosive charge

6.4.1 'Varying amounts of explosive charge' numerical simulations

In this section the blast loading was reduced from 10 kg TNT to 5 kg TNT, equal to half the amount of TNT found in the majority of AT mines, and to 3.17 kg TNT, equal to half the amount of TNT found in the most used AT mines (TM-57). In each case, hemispherical charges were used, at 400 mm stand-off distance from the 'double-floor hull' model, as shown in Figure 6.13. The results are in Figures 6.14 – 6.16.

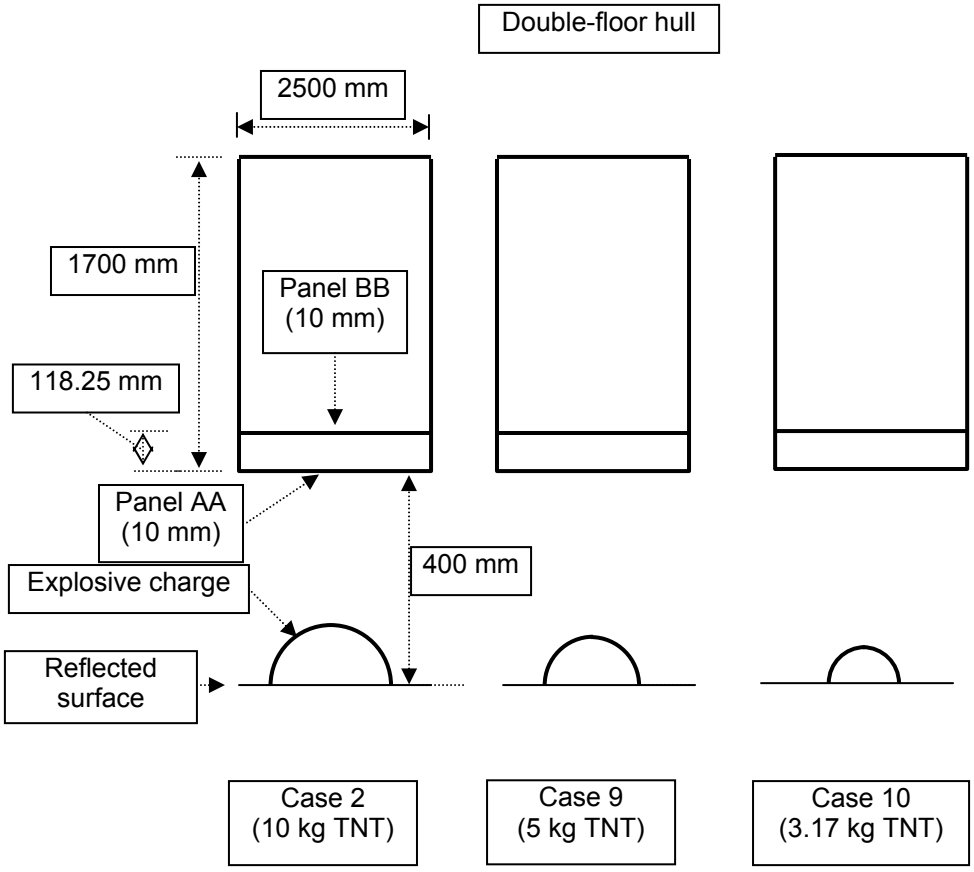

Figure 6.13 Schematic drawing of a comparison in 'double-floor hull' models (cases 2, 9, and 10).

6.4.2 'Varying amounts of explosive charge' results

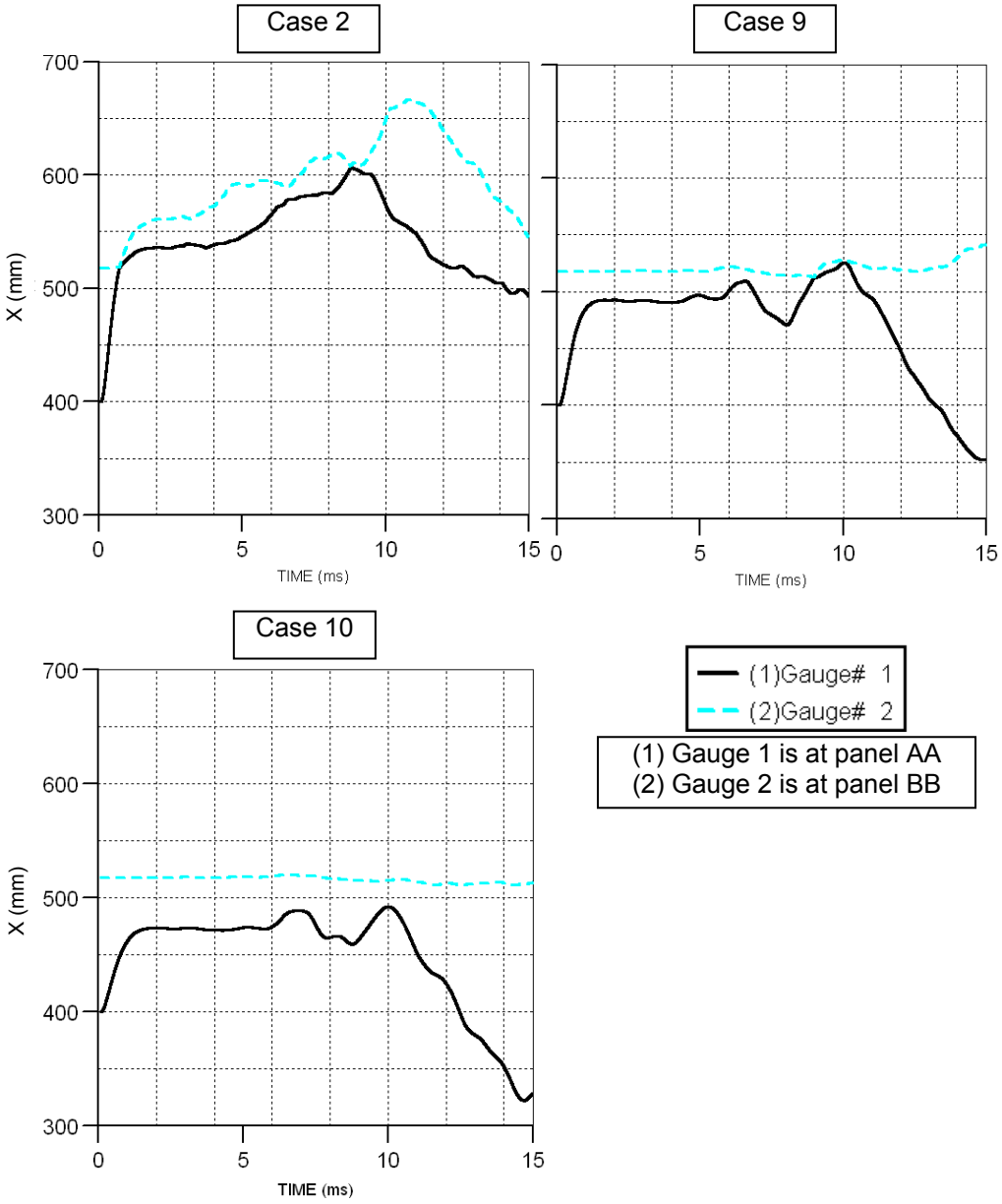

Figure 6.14 Deformation results of cases 2, 9, and 10 up to 15 ms. Note that all cases contain the same scales and deformation curves are based on the actual gauge positions.

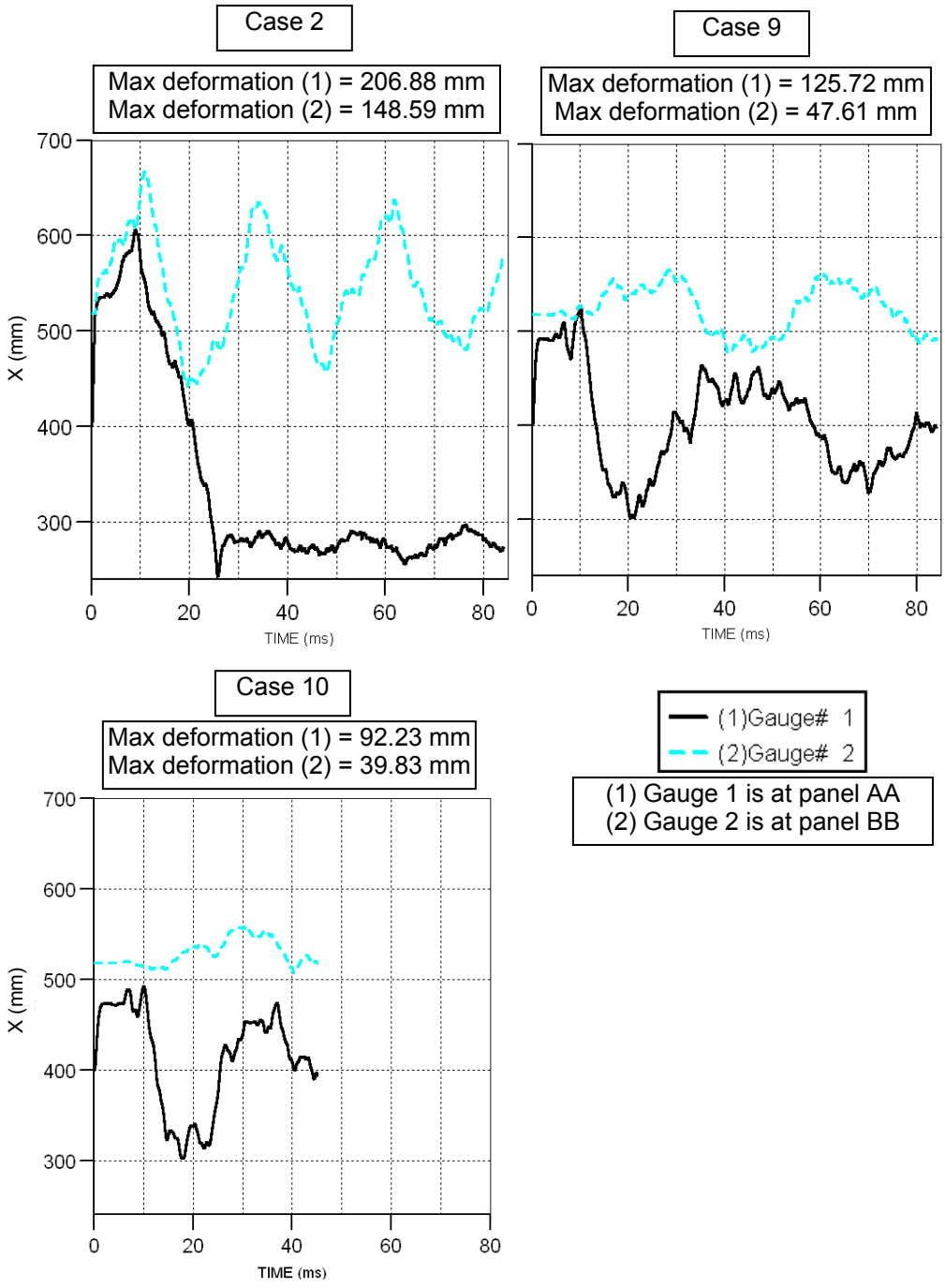

Figure 6.15 Deformation results of cases 2, 9, and 10 after 15 ms. Note that all cases contain the same scales and deformation curves are based on the actual gauge positions.

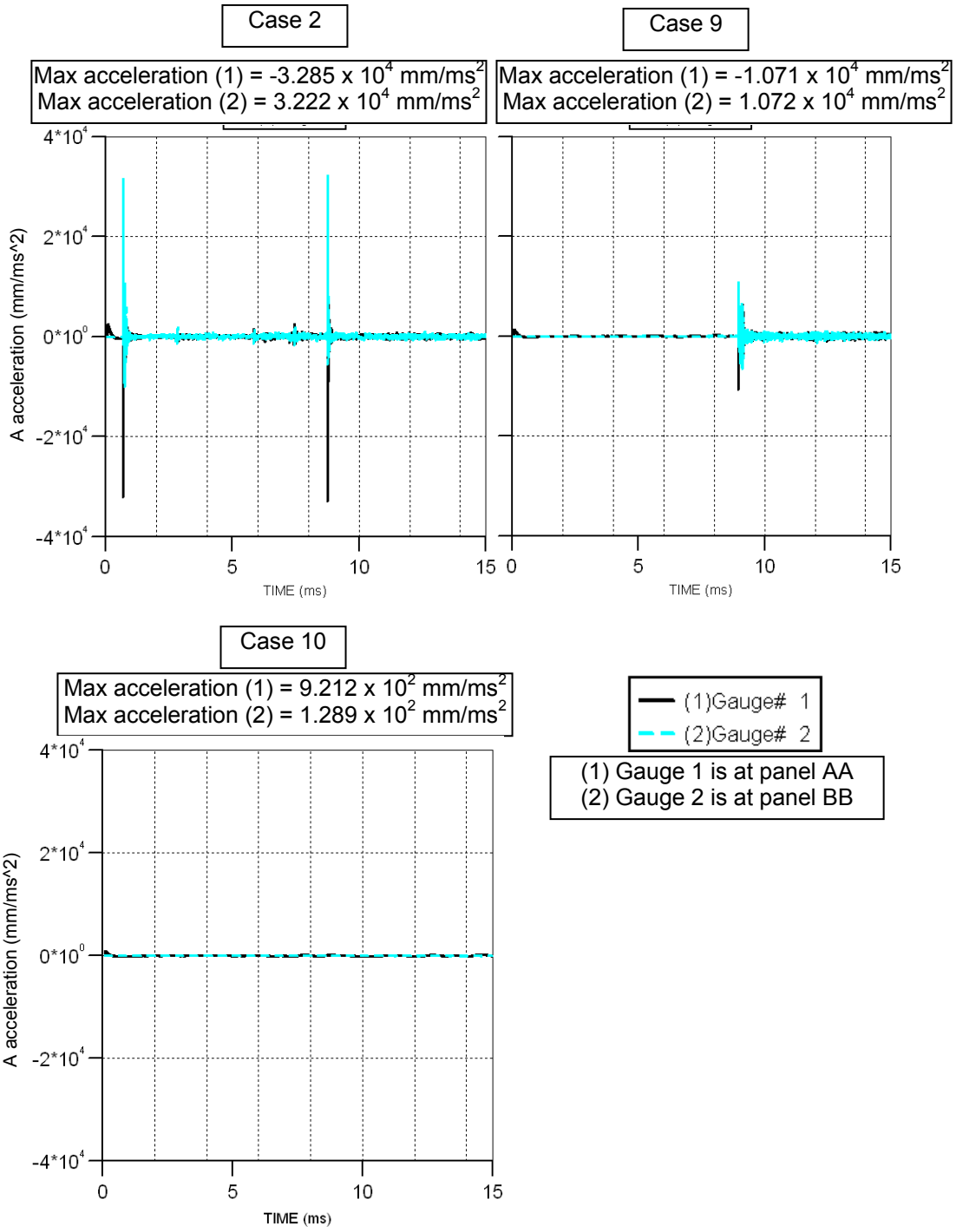

Figure 6.16 Acceleration results of cases 2, 9, and 10. Note that all cases contain the same scales.

6.4.3 'Varying amounts of explosive charge' discussion

It seems that the method of increasing the stand off distance as in case 6, 7, and 8, does not prevent the impact between panel AA and BB. Therefore, for trial purposes, the amount of explosive charge is reduced from 10 kg TNT as in case 2 to 5 kg TNT as in case 9 and 3.17 kg TNT as in case 10. The results in Figure 6.14 and Figure 6.15 show that there is an impact between panel AA and BB in case 9; the corresponding high peak acceleration in Figure 6.16 can be observed. However, there is no impact between the two panels in case 10, where no very high peak acceleration is present. By looking at the deformation plot in case 10, panel BB still deforms even though there is no impact between panel AA and BB. This is mainly due to the compressed air pressure which has already been discussed in Chapter 5, where the top panel in the 'box model' model has deformed without the impact from the bottom panel.

6.5 Varying the gap distances

6.5.1 'Varying the gap distances' numerical simulations

A range of numerical simulations were conducted, during which the gap between panels AA and BB was varied from 118.25 mm, 270 mm and 315 mm in cases 2, 11 and 12 respectively as shown in Figure 6.17. Results are in Figure 6.18 and Figure 6.19.

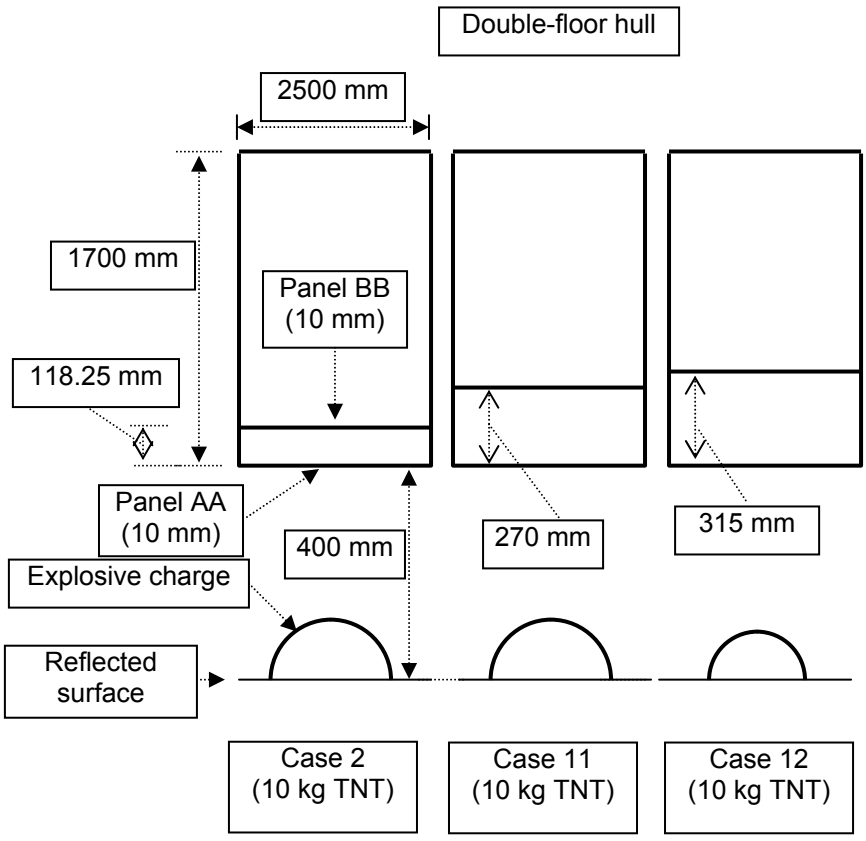

Figure 6.17 Schematic drawing of cases 2, 11 and 12.

6.5.2 'Varying the gap distances' results

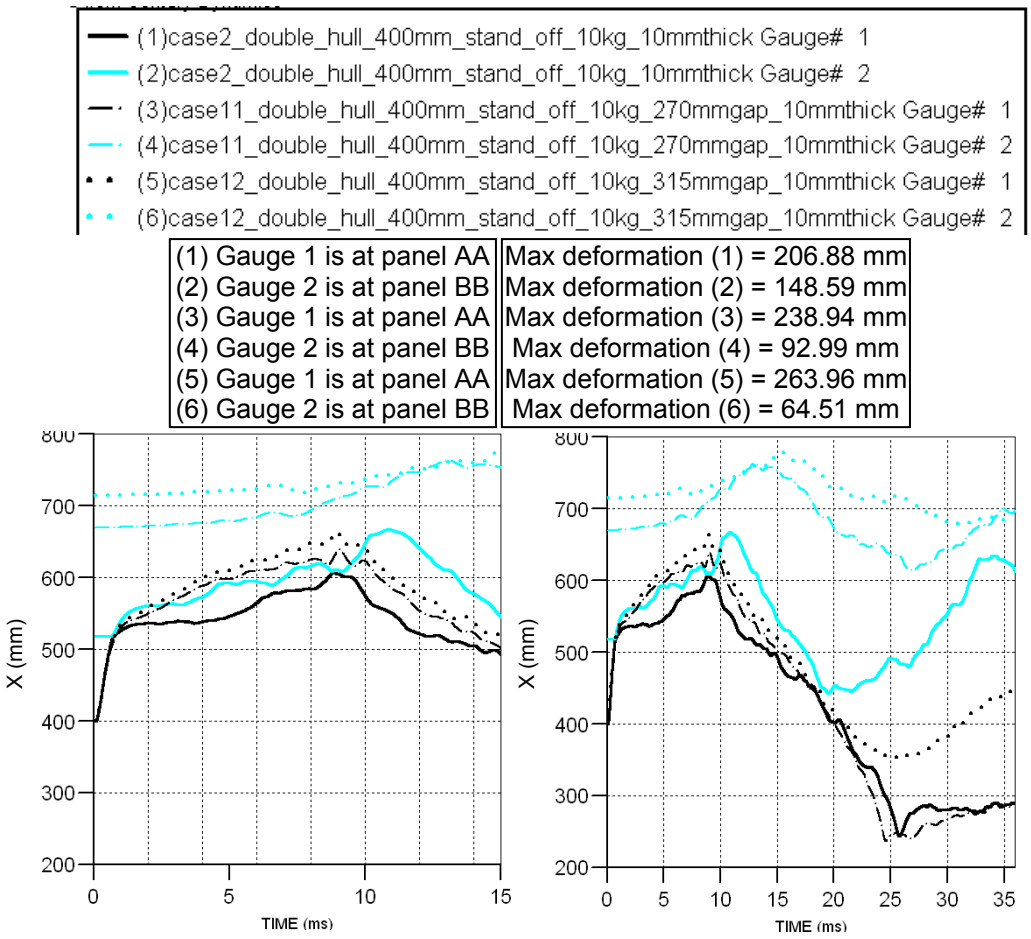

Figure 6.18 Deformation results of cases 2, 11, and 12. Note that all cases contain the same scales and deformation curves are based on the actual gauge positions.

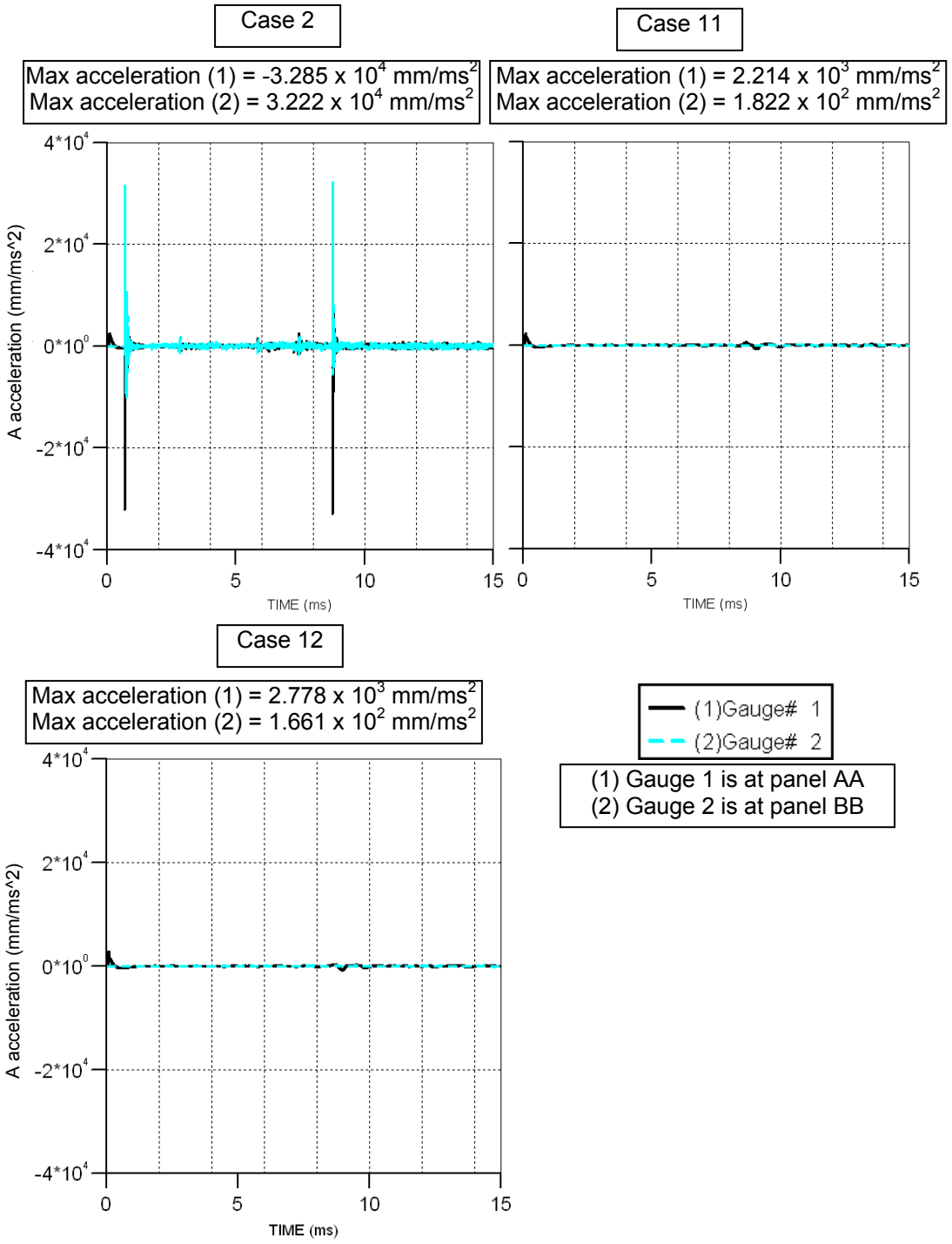

Figure 6.19 Acceleration results of cases 2, 11, and 12. Note that all cases contain the same scales.

6.5.3 'Varying the gap distances' discussion

By extending the gap from 118.25 mm (case 2) to 270 mm (case 11) and 315 mm (case 12), the results in Figure 6.18 indicate that panel BB in cases 11 and 12 does not impact with panel AA. The acceleration plot in Figure 6.19 also supports this finding because there is no evidence of high acceleration peaks in cases 11 and 12. Results in Figure 6.18 shows that as the gap is increased, maximum deformation of panel AA is also increased even though cases 2, 11, and 12 encountered the same blast loading. This may be explained that as the gap is increased, the volume of air inside the gap is also increased. As a result, the air inside the bigger gap may be compressed more than the air inside the smaller gap. In case 11, the gap has increased from case 2 by 151.75 mm, while the maximum deformation on panel AA in case 11 has increased from case 2 by 32.06 mm. Likewise, case 12 has extended the gap from that in case 2 by 196.75 mm, while panel AA has deformed 57.08 mm more than in case 2. However, Figure 6.18 shows that panel BB has deformed less as gap is increased. Maximum deformation on panel BB in cases 11 and 12 are reduced by 37%, and 57%. As the gap is increased, the air volume inside the gap is also increased. When panel AA has deformed at its maximum, the air volume inside the gap is still more than in the smaller gap cases because the increase in deformation is less than the increase in gap. Hence, the compressed air pressure inside the gap in case 12 is less than in case 11. Panel BB in case 12 therefore has deformed less than in case 11. In case 2, panel BB has deformed more because the impact from panel AA.

6.6 Varying thicknesses

6.6.1 'Varying thicknesses' numerical simulations

In this section, the thickness of panel AA, BB, and side panels were increased in various cases. By increasing the thickness, the weight of the vehicle was also increased. It was assumed in this section that the total weight of the vehicle was not required to remain constant. The thicknesses are increased in cases 13, 14, 15, 16, 17, and 18, which can be seen in Figure 6.20 and Figure 6.21. Results are in Figures 6.25 – 6.34.

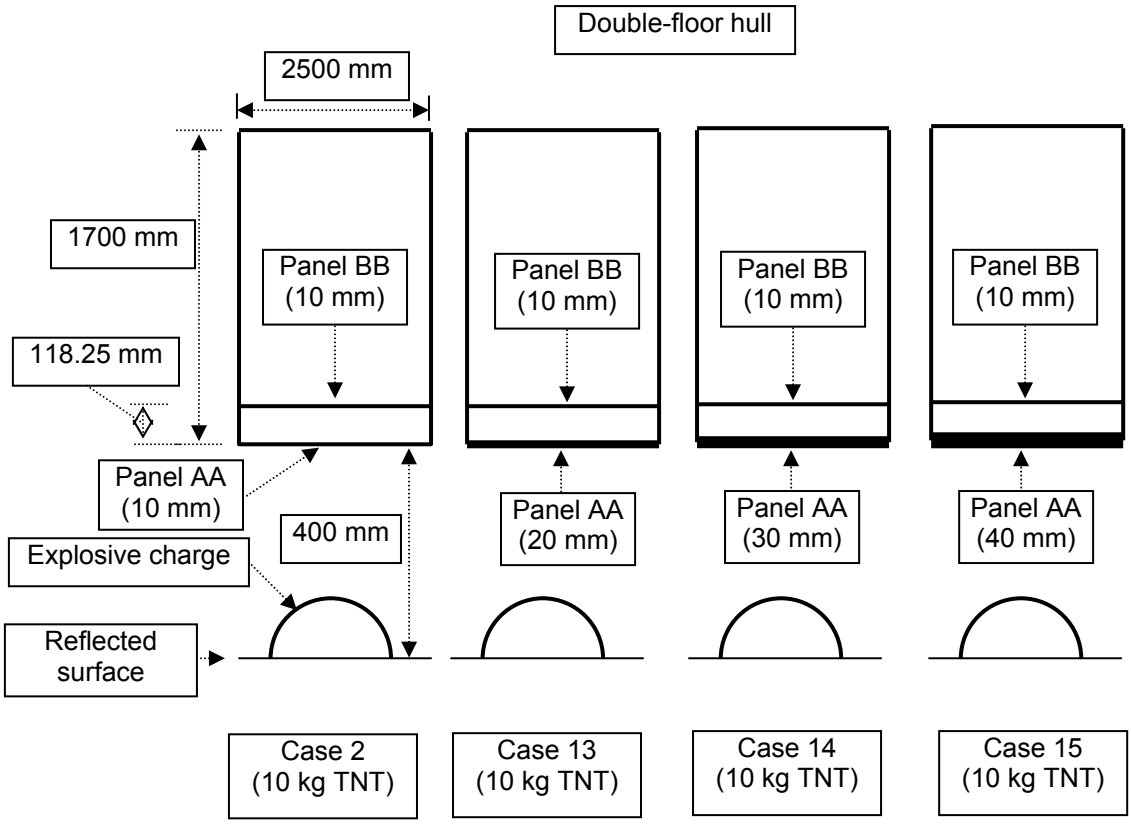

Figure 6.20 Schematic drawing of a comparison in 'double-floor hull' models (cases 2, 13, 14, and 15).

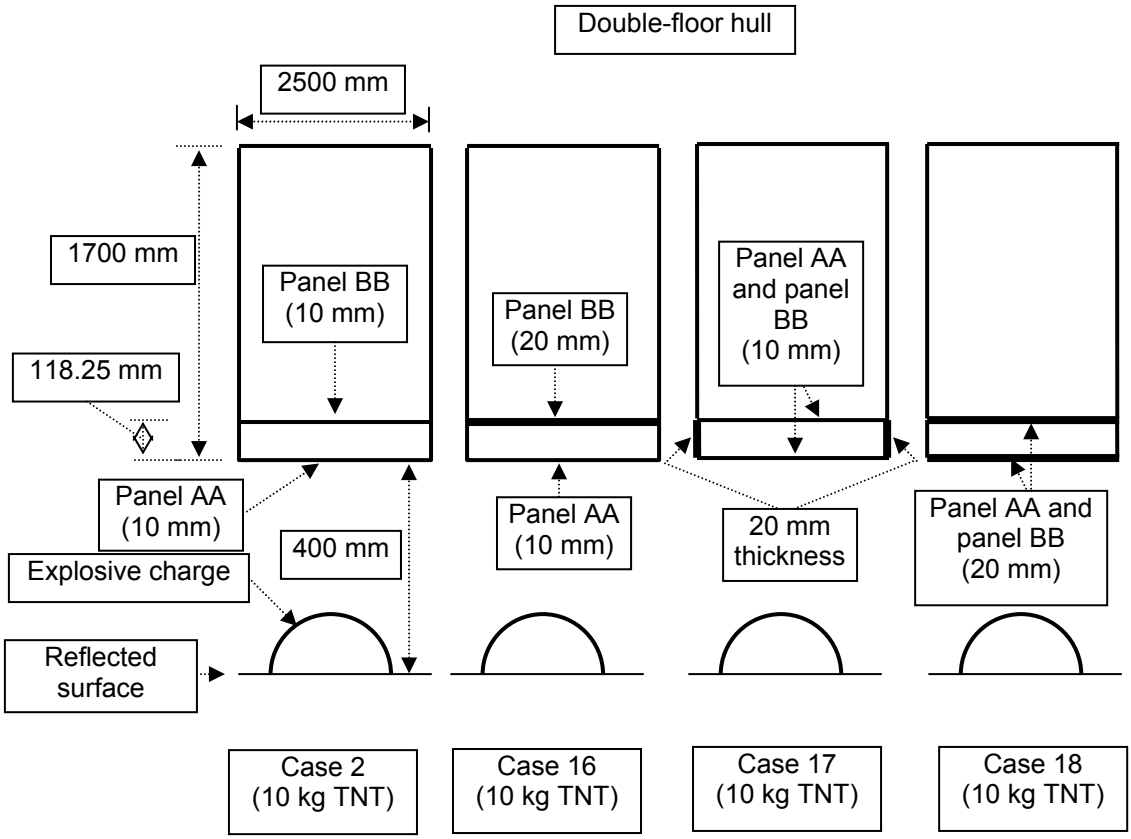

Figure 6.21 Schematic drawing of a comparison in 'double-floor hull' models (cases 2, 16, 17, and 18).

6.6.2 'Varying thicknesses' results

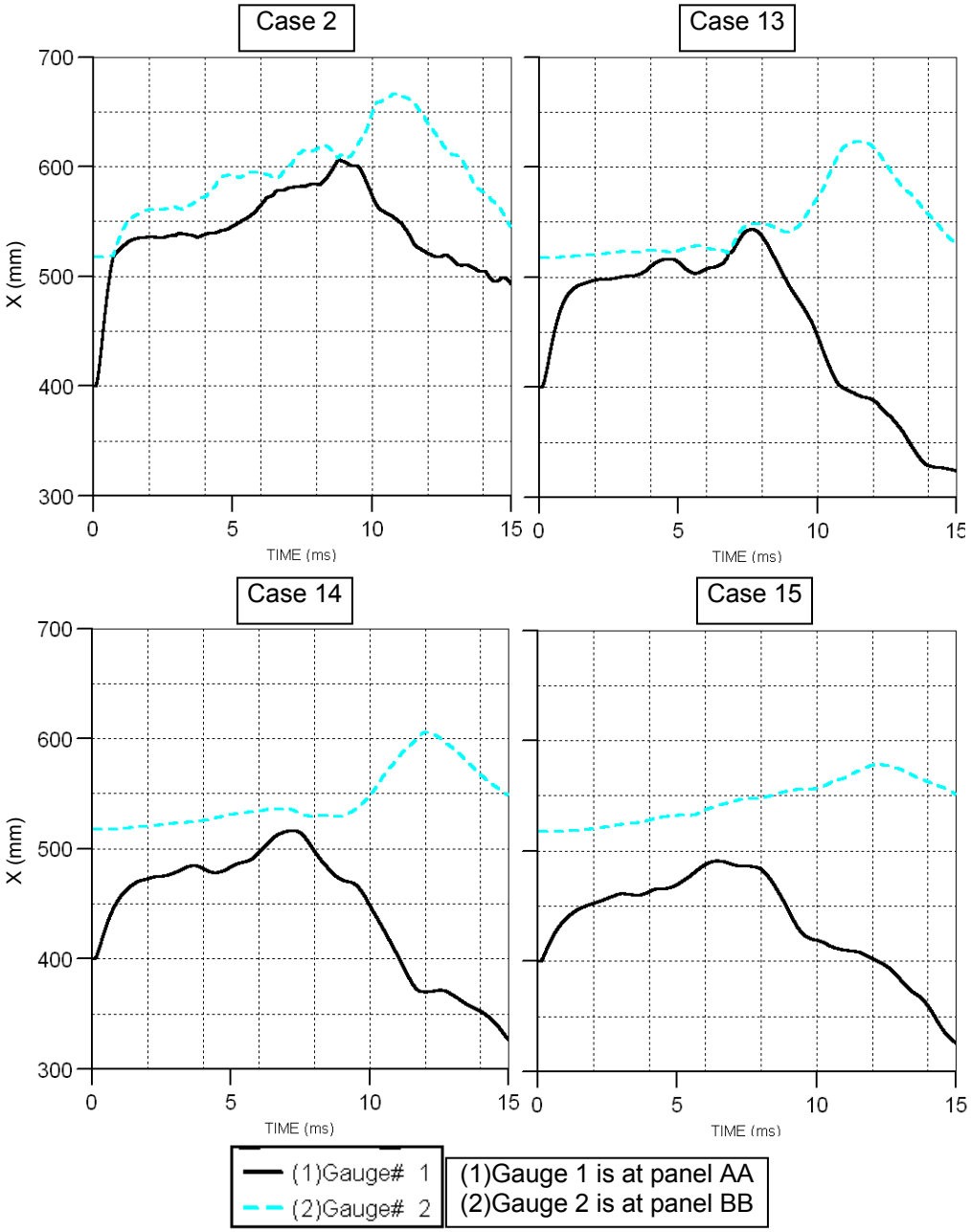

Figure 6.22 Deformation results of cases 2, 13, 14, and 15 up to 15 ms. Note that all cases contain the same scales and deformation curves are based on the actual gauge positions.

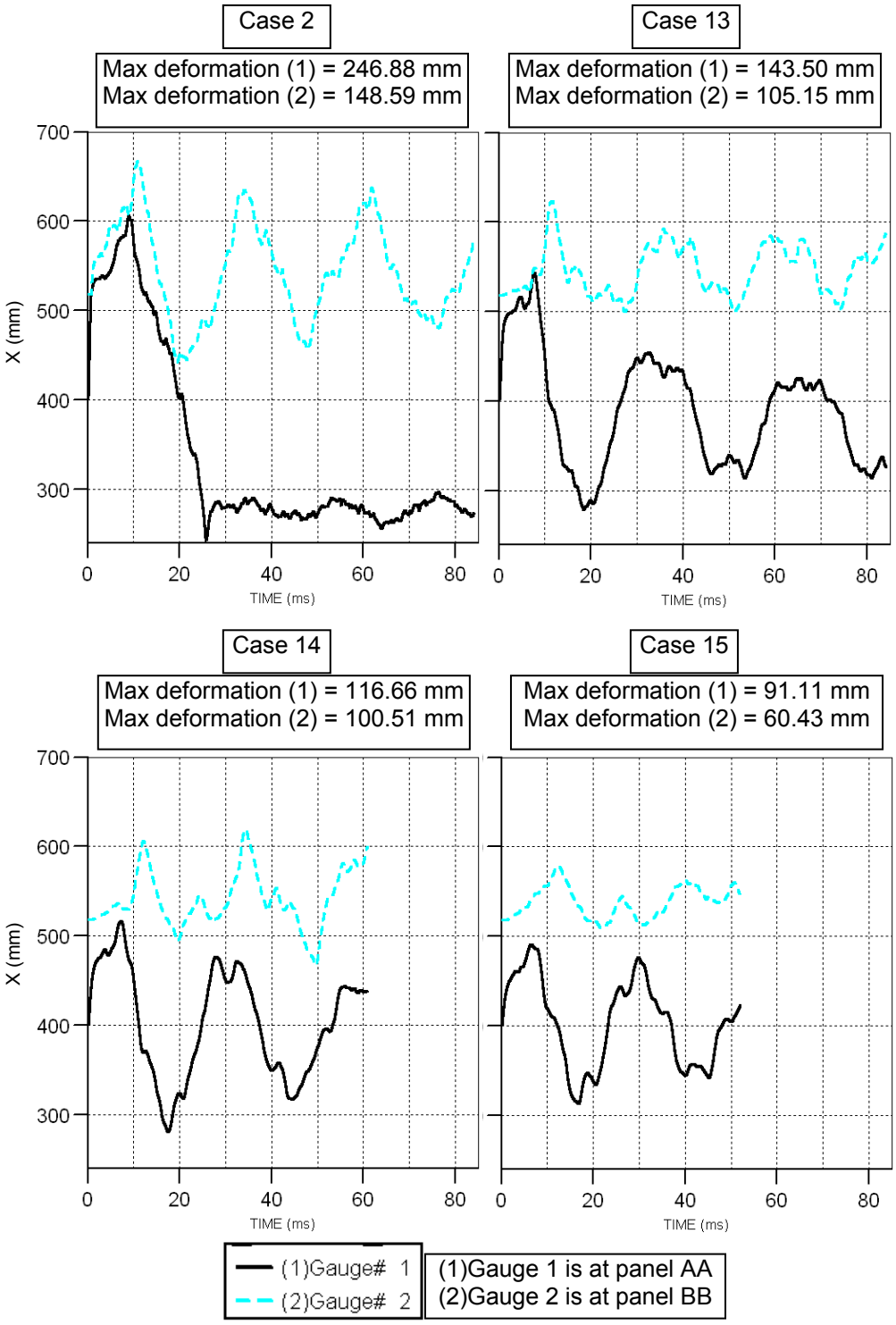

Figure 6.23 Deformation results of cases 2, 13, 14, and 15. Note that all cases contain the same scales and deformation curves are based on the actual gauge positions.

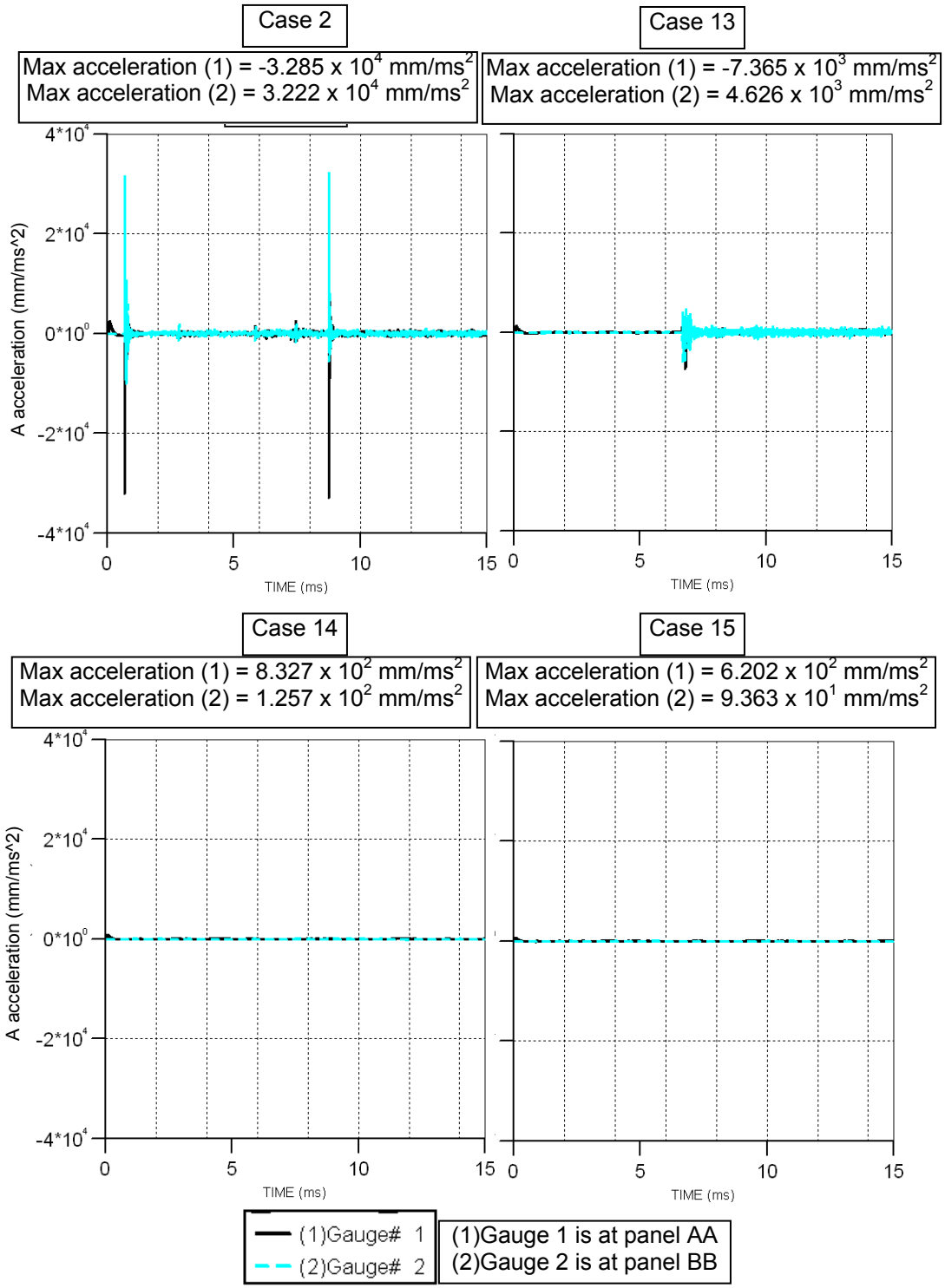

Figure 6.24 Acceleration results of cases 2, 13, 14, and 15.

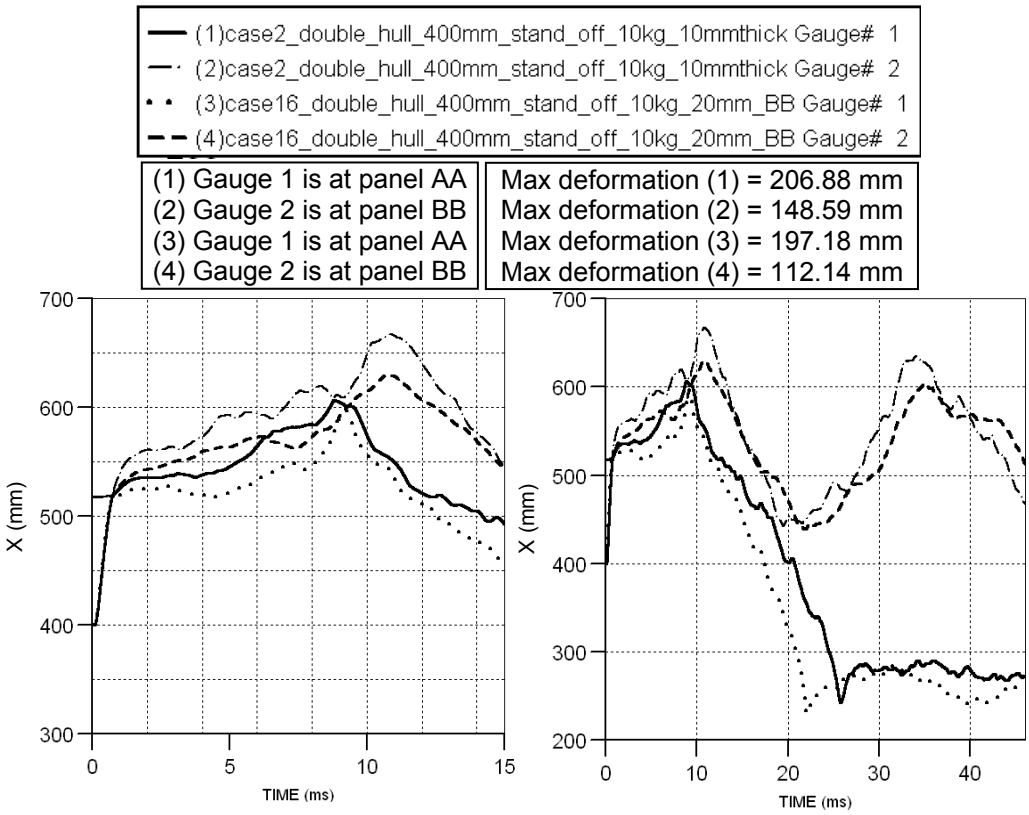

Figure 6.25 Deformation results of cases 2, and 16. Note that deformation curves are based on the actual gauge positions.

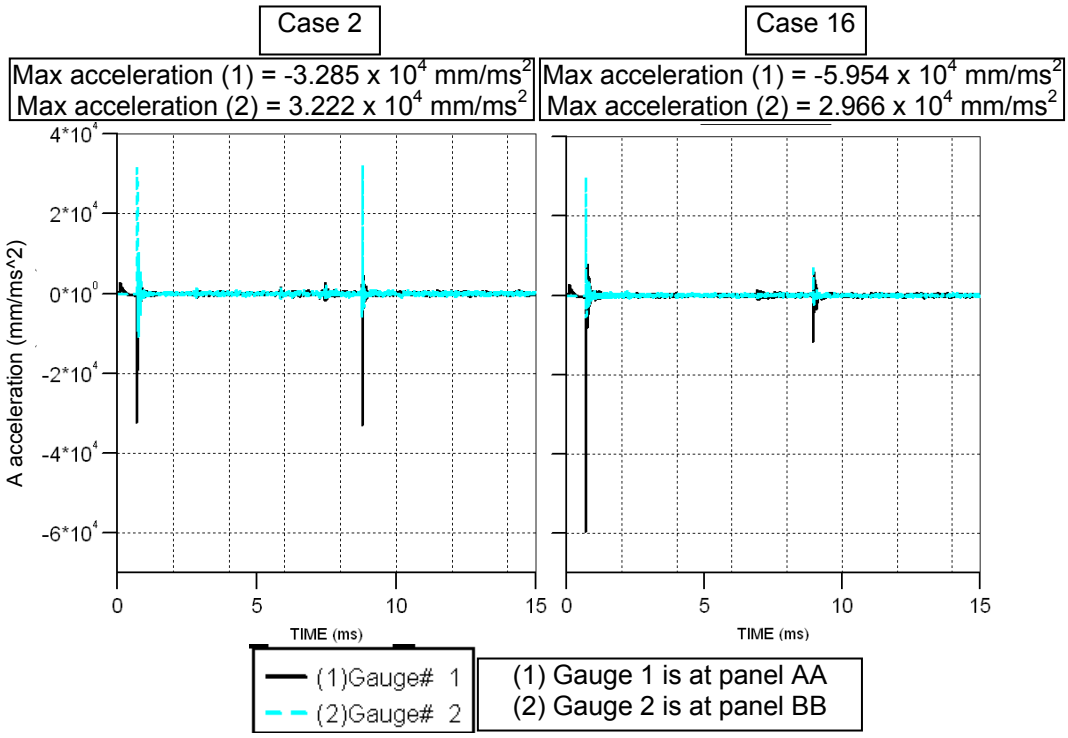

Figure 6.26 Acceleration results of cases 2, and 16.

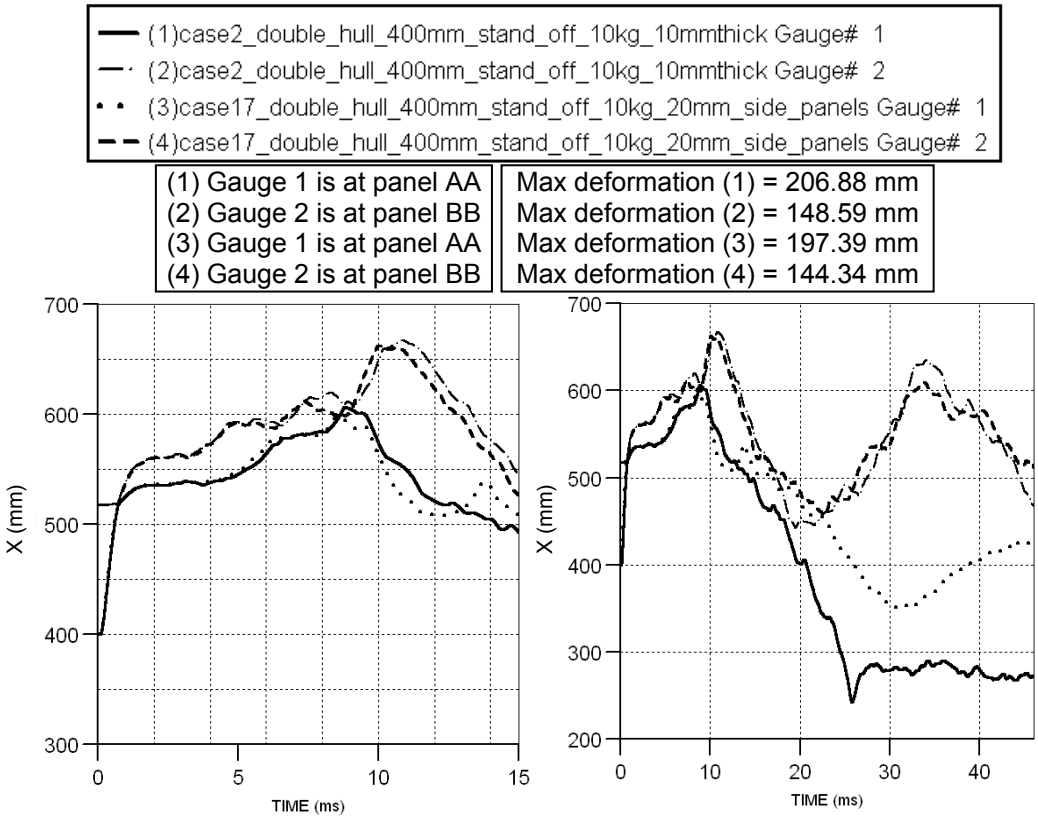

Figure 6.27 Deformation results of cases 2 and 17. Note that all cases contain the same scales and deformation curves are based on the actual gauge positions.

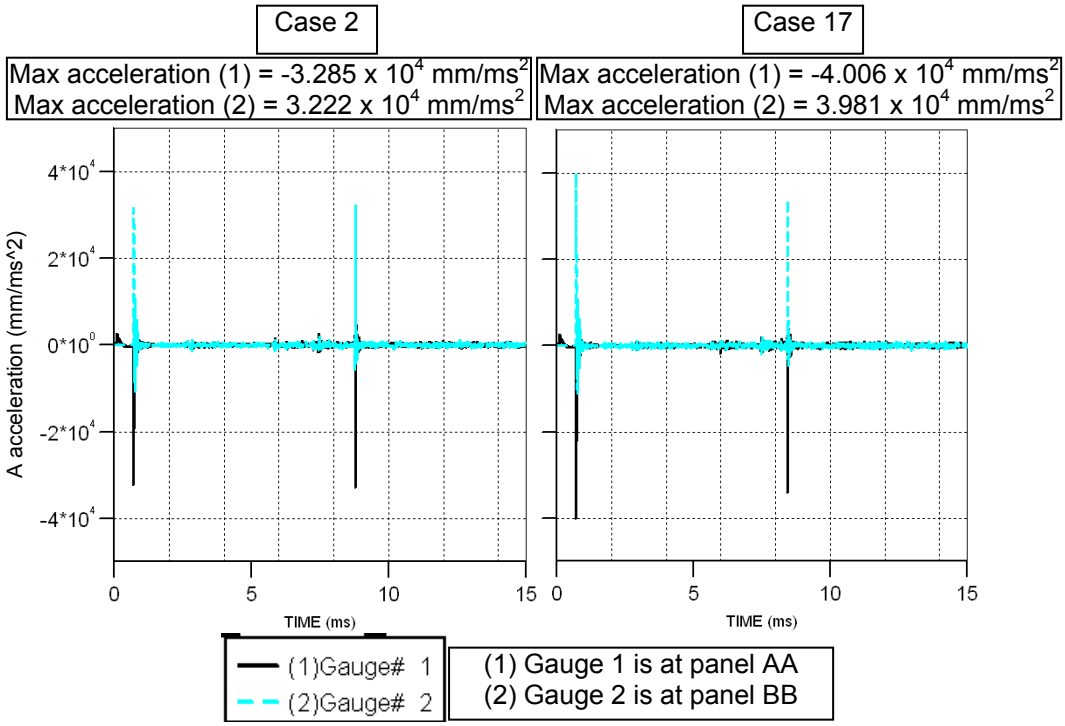

Figure 6.28 Acceleration results of cases 2 and 17. Note that all cases contain the same scales.

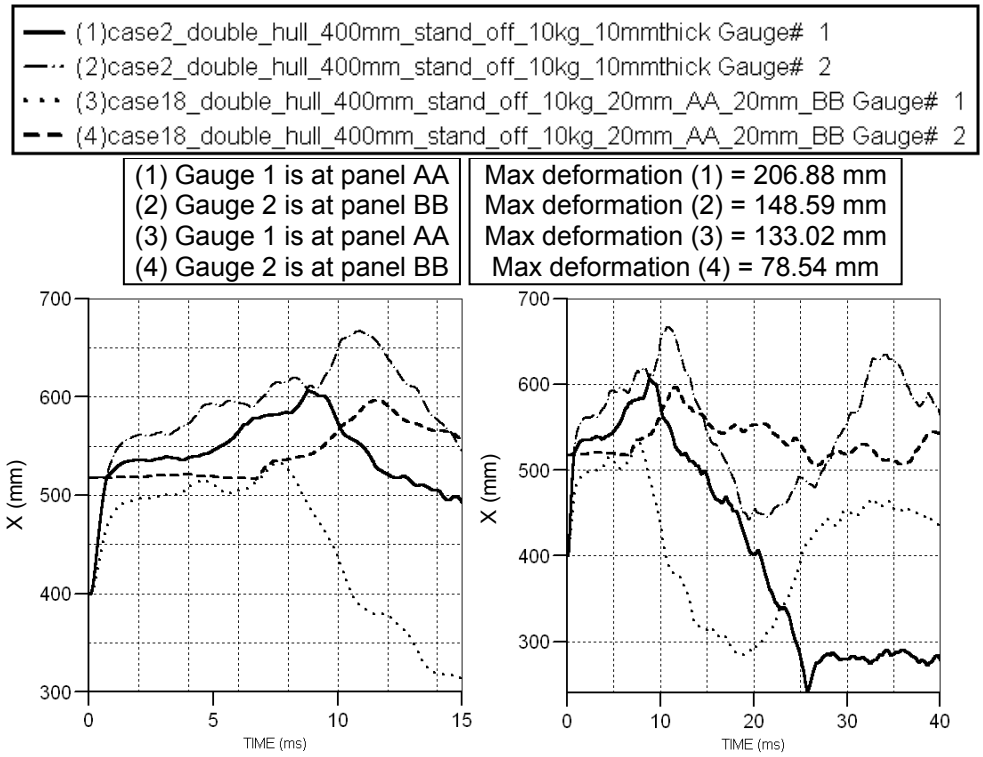

Figure 6.29 Deformation results of cases 2, and 18. Note that all cases contain the same scales and deformation curves are based on the actual gauge positions.

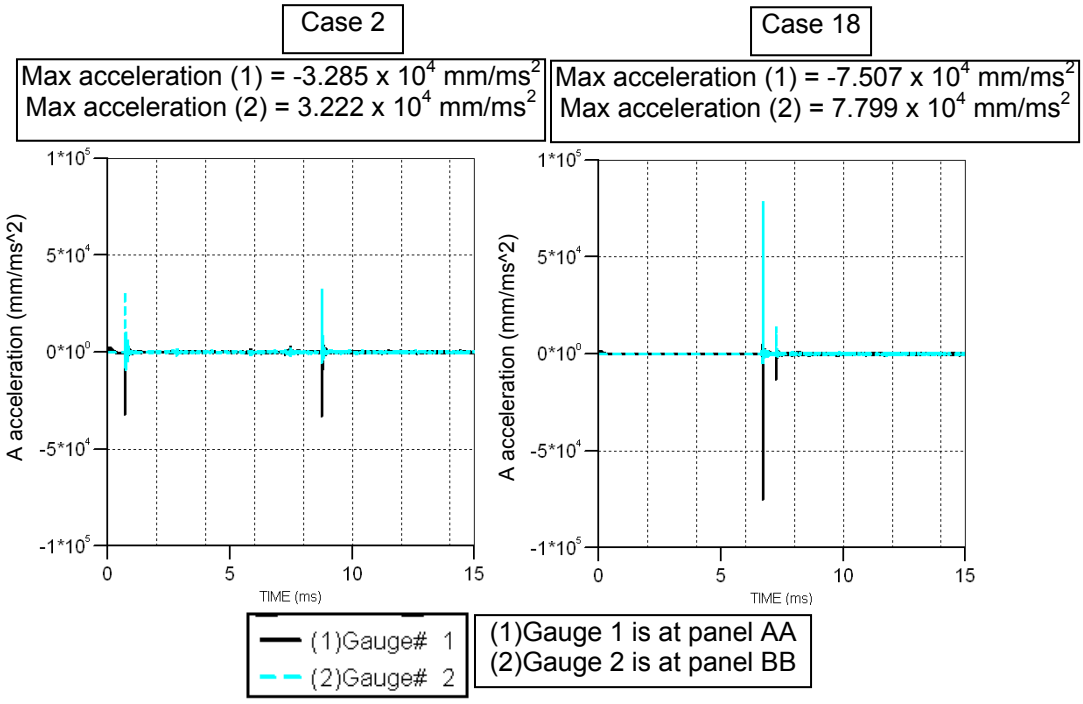

Figure 6.30 Acceleration results of cases 2, and 18.

6.6.3 'Varying thicknesses' discussion

In section 6.6, the thickness of panel AA has increased from 10 mm as in case 2 to 20, 30, and 40 mm in case 13, 14, and 15 respectively. Figure 6.22 and Figure 6.23 demonstrate that panel AA in cases 2 and 13 impacted with panel BB whilst this does not occur in cases 14 and 15 as evident by the acceleration plot in Figure 6.24. Compared with case 2, the maximum deformation of panel AA in cases 13, 14, and 15 is reduced by 42%, 53%, and 63%, whilst the maximum deformation of panel BB is decreased by 29%, 32%, and 59% correspondingly. In terms of velocity results as shown in Figure D.3 (Appendix D), the maximum velocity of panel AA is reduced by 46%, 65%, and 75%, whilst the maximum velocity of panel BB is decreased by 34%, 57%, and 82%. Note that for every 10 mm thickness increase to the floor panel, the mass of the vehicle increases by 489 kg.

Instead of increasing thickness on panel AA, case 16 has increased thickness of panel BB from 10 mm to 20 mm. However, Figure 6.25 and Figure 6.26 show that panel AA still impacts with panel BB, which creates undesirable high peak acceleration, although panel BB in case 16 has deformed less because the panel is thicker. Deformation curves in case 2 and case 16 are exactly the same before the first impact between panel AA and BB in both cases. After the impact panel AA in case 16 has deformed backwards more because panel BB is thicker and has more mass than in case 2. Case 17 has increased the thickness on the side panels to 20 mm but the results in Figure 6.27 are similar to case 2 (5% and 3% reduction in panel AA and panel BB maximum deformations), and panel AA still impacted with panel BB which created undesirable high acceleration as shown in Figure 6.28. The side panels in case 17 were stiffened by thickening them, hence after the impact, panel AA deformed and moved less than in case 2 as shown in Figure 6.27. Case 18 increased the thickness of panels AA and BB to 20 mm each; but the impact between panels AA and BB still occurred, though the maximum deformation on panels AA and BB is reduced by 36% and 41% as shown in Figure 6.29.

From the results in cases 13, 14, 15, 16, and 17 it demonstrates that increasing the thickness on panel BB, and side panels does little to prevent the impact between panels AA and BB. The best solution is to increase the thickness on panel AA which is the first structure to

encounter the blast so that it does not deform more than the gap, thus preventing the undesirable high acceleration.

It would hence be interesting to ascertain whether the double-floor hull model would be better than the single-floor hull model of the same weight (mass) in the case where the impact between panels AA and BB is avoided. Case 10 is used for comparison with case 22, the configuration of which can be seen in Figure 6.31, and the results are in Figure 6.32.

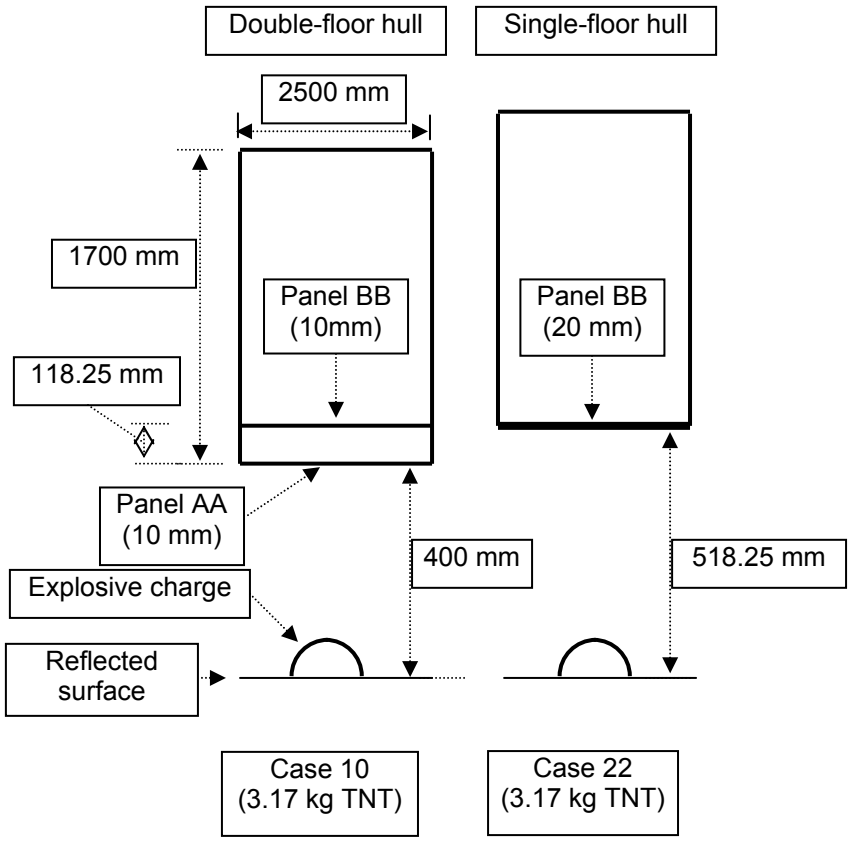

Figure 6.31 Schematic drawing of cases 10 and 22.

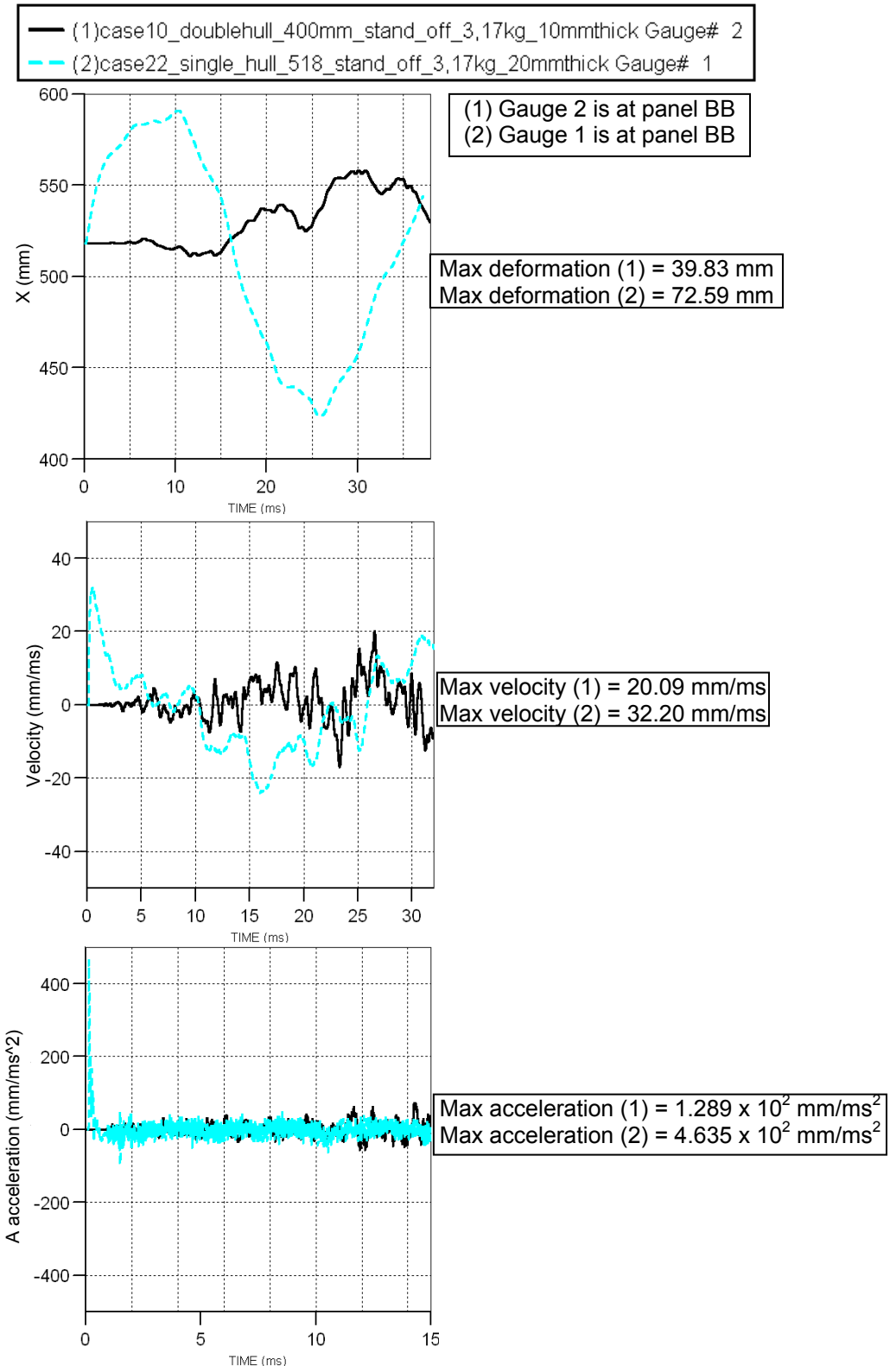

Figure 6.32 Deformation, velocity, and acceleration results on panel BB in cases 10 and 22. Note that deformation curves are based on the actual gauge positions.

Considering the results at panel BB only, the crew compartment floor, Figure 6.32 illustrates that, when comparing results from the 'single-floor hull' model (case 22) with those from the 'double-floor hull' model (case 10) of the same mass and the same stand-off distance from the charge to panel BB, the effects on panel BB in case 10 are less than in case 22. Maximum deformation, velocity and acceleration on panel BB in case 10 are decreased by 45%, 38% and 72% respectively when compared with case 10.

The comparison between the single-floor hull model and the double-floor hull model is extended (in cases 14 and 23) by using the higher blast loading produced by an explosive charge of 10 kg. The configurations of cases 14 and 23 can be seen in Figure 6.33, and the results are in Figure 6.34.

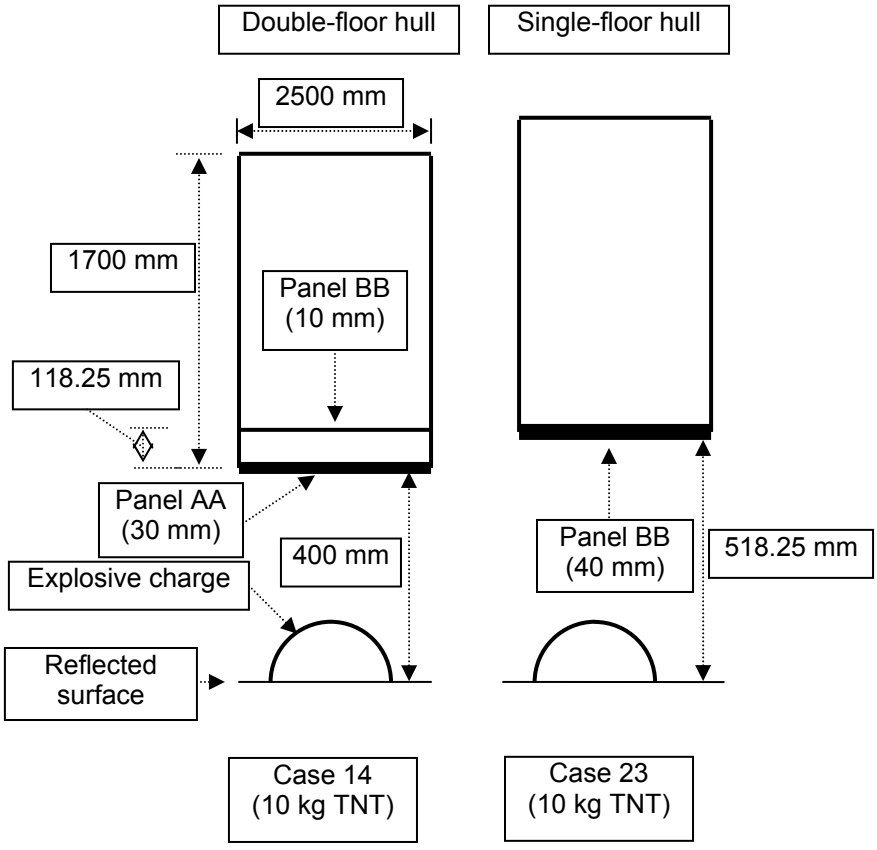

Figure 6.33 Schematic drawing of cases 14 and 23

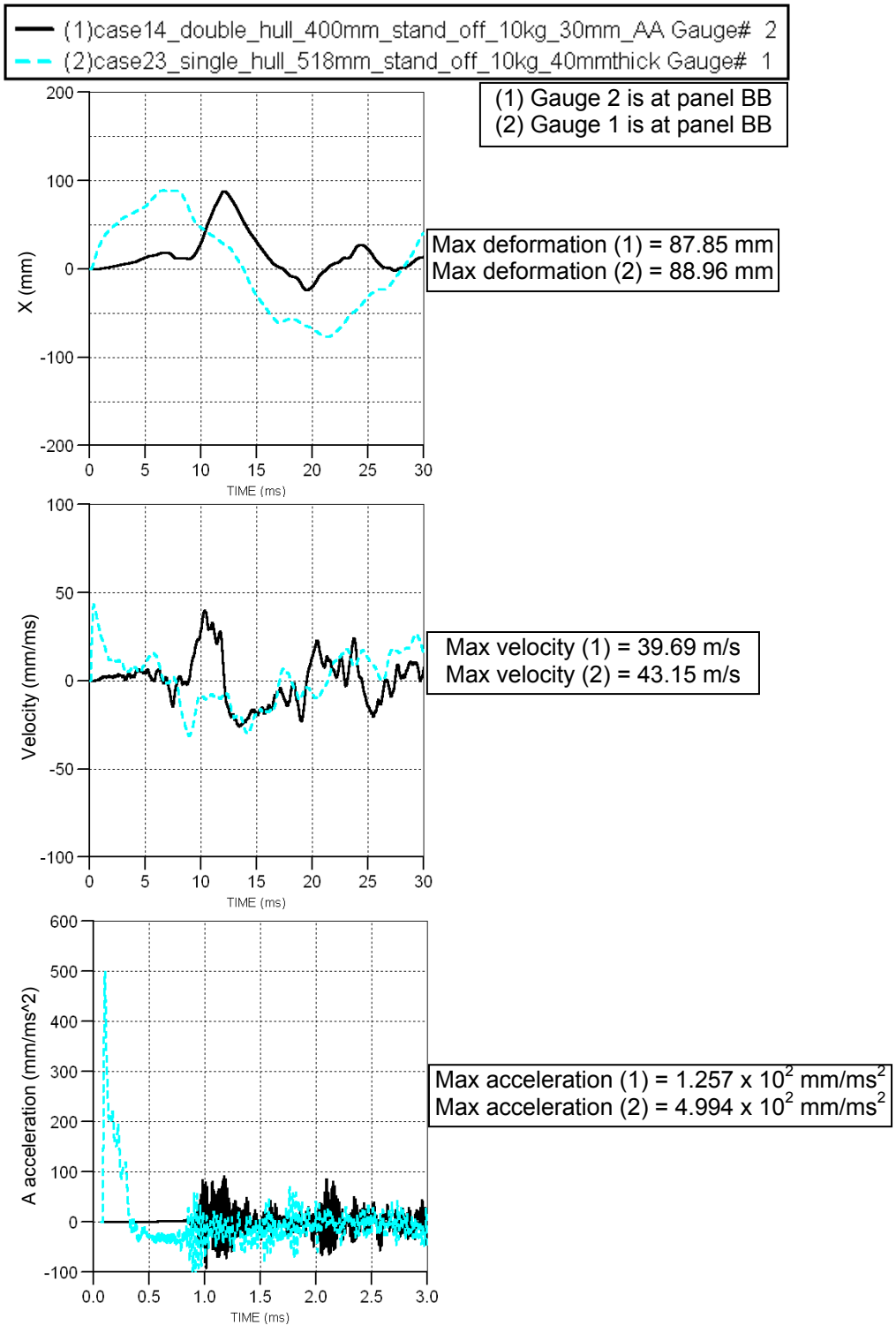

Figure 6.34 Deformation, velocity, and acceleration results on panel BB in cases 14 and 23. Note that deformation curves are based on the net deformation.

Figure 6.34 shows that the maximum deformation and velocity in case 14 (double-floor) is similar to case 23 (single-floor), where maximum deformation in case 23 is reduced by 1% and the maximum velocity is reduced by 8% compared to case 14. Significant difference is observed in the acceleration plot where the maximum acceleration in case 14 is reduced by 75%. This is in line with the difference between results from case 10 and 22. It is thought that the difference between the single-floor hull model and double-floor hull model which accounted for the higher acceleration due to panel BB in the double-floor system did not receive the blast loading directly but rather due to the compressed air inside the gap. In addition, panel BB has acted as a stiffener on the side panels, which may reduce the acceleration. The comparison between the two pairs of cases 10 and 22, and 14 and 23, indicates that when the load is more extreme (10 kg TNT), the difference between the 'single-floor hull' model and 'double-floor hull' model is similar in terms of maximum deformation and velocity at panel BB but when the load is less extreme (3.17 kg TNT) the difference is more apparent.

6.7 Initial 'V' bottom hull model

6.7.1 'Initial 'V' bottom hull' numerical simulations

In this section, the bottom of vehicle was modelled as 'V' shape in case 19 – as in Figure 6.35, by inclining panel AA at 10° to the horizontal axis. It was developed as a ¼ symmetry model to compare the deformation shape with that from the ½ symmetry model of the same configuration. Results are in Figure 6.36 and the extended results are in Figure D.4 – D.9 (Appendix D).

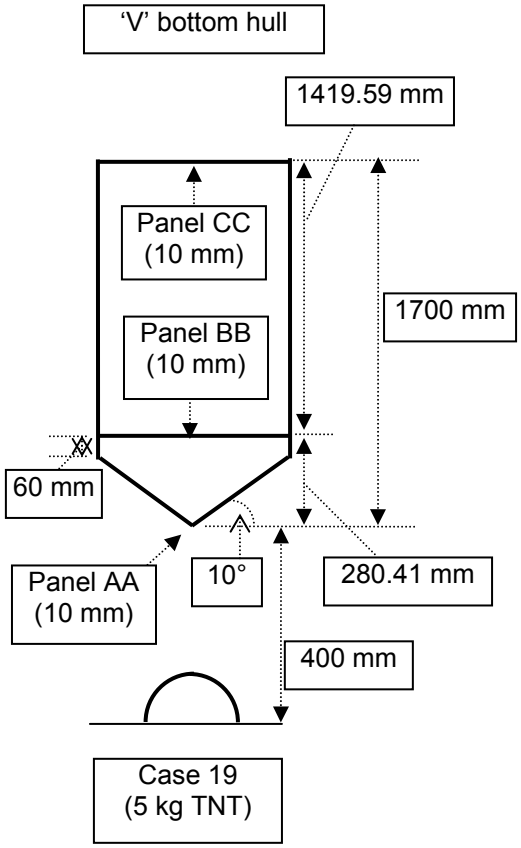

Figure 6.35 Schematic drawing of case 19.

6.7.2 'Initial 'V' bottom hull' results

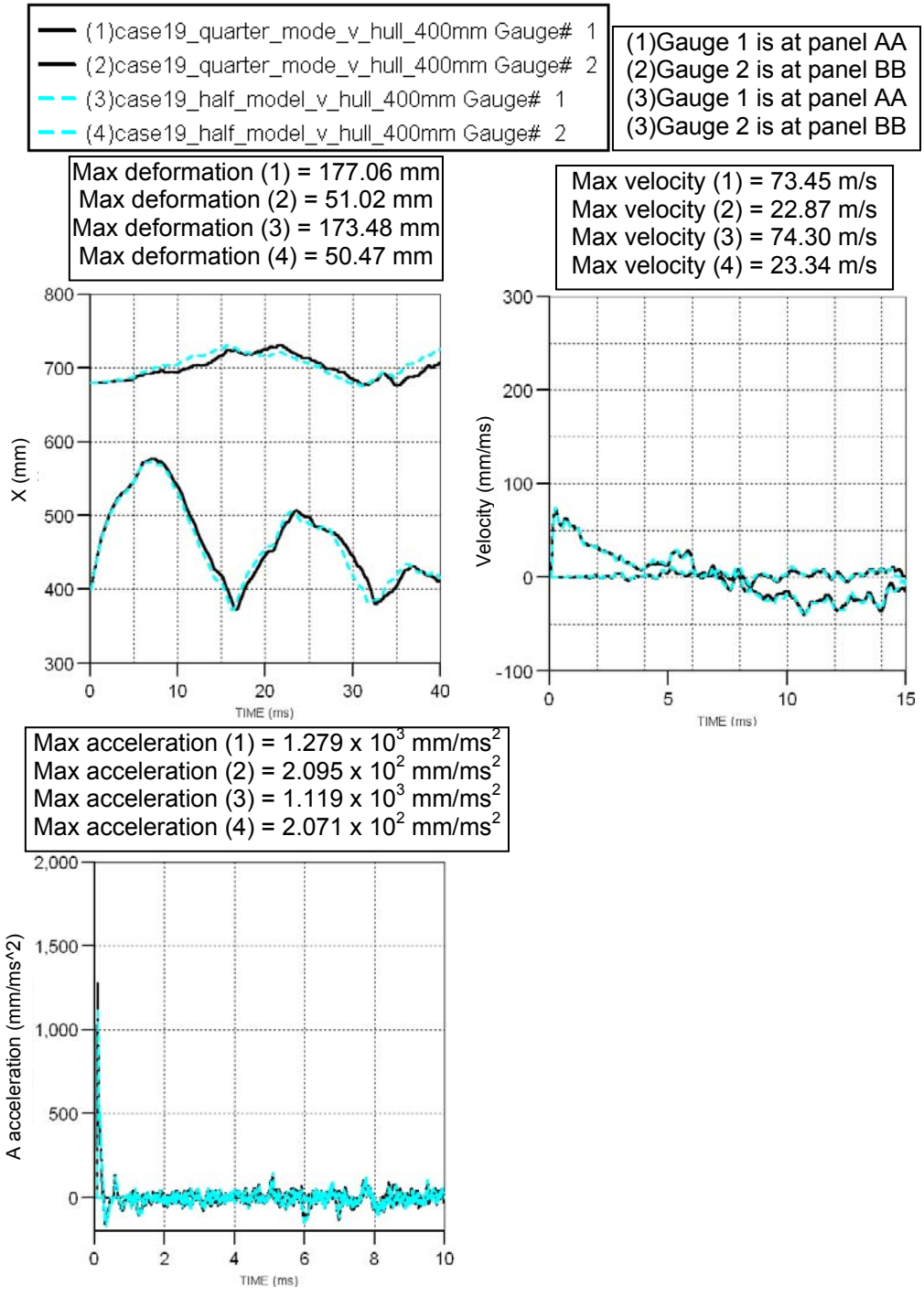

Figure 6.36 Deformation, velocity, and acceleration results between half and quarter model in case 19. Note that deformation curves are based on the actual gauge positions.

6.7.3 'Initial 'V' bottom hull' discussion

In section 6.7 panel AA was changed into a 'V' shape. Figure D.5 (Appendix D) examines the deformation on the nearby gauges around the middle of panel AA. The position of gauges 13, 14, 15, 16, 17, and 18 is at 5, 25, 45, 66, 86, and 106 mm in the horizontal direction. The increases in maximum deformation from gauge 13 are 2.24%, 3.63%, 3.95%, 3.39%, and 2.09% at gauges 14, 15, 16, 17, and 18 respectively. It is noticed that maximum deformation on gauges 14, 15, and 16 gradually increased from that at gauge 13 but then have gradually dropped in gauge 17 and 18. However, these changes are very small. The results also show that the curve trends from different gauges are very similar. Therefore in the future analysis on the 'V bottom hull model, the maximum deformation on gauge 13 will be used to compare with other models at the same gauge position on panel AA, even though this deformation value may not be the highest maximum deformation value on panel AA.

Figure D.6 (Appendix D) shows the deformation on the XZ side panel of the 'V' bottom hull model. At gauge xz1, XZ side panel, which is shorter than XY side panel, deformed outwards first due to panel AA being compressed by the blast pressure. Once panel AA deformed downwards, XZ side panel started to deform inwards and so on, with gauge xz1 has more movements than gauge xz2. In terms of deformation in the x-direction, the plot shows only 1-2 mm movement at gauge xz1 and xz3. In contrast, Figure D.7 (Appendix D) demonstrates that, XY side panel deformed inwards first and then deform outwards up to around its original location. Figure D.8 shows that panel CC has 0.0 deformation, velocity and acceleration.

Figure 6.36 compares the modelling methods between modelling as a ¼ and ½ symmetry models. The deformation plots are very similar; the ¼ symmetry model gave 2% and 1% higher maximum deformation, 1% and 2% lower maximum velocity, and 14% and 1% higher maximum acceleration respectively on panels AA and BB compared with ½ symmetry model. The curve trends between the two cases are also very similar. Therefore it is thought that in the future analysis, V' bottom hull model will be modelled as a ¼ symmetry model because the results are very similar to the ½ symmetry model and the running time is shorter. Although there are 14% differences in acceleration on panel AA,

modelling as a ¼ symmetry model is a conservative approach because the acceleration is higher. Note that modelling as a full model is not performed in this analysis because too many computational resources would be needed to model the same element size as in ¼ symmetry model.

6.8 'single-floor hull', 'double-floor hull' and 'V bottom' hull models

6.8.1 'single-floor hull', 'double-floor hull' and 'V bottom' hull numerical simulations

In this section, 3 different vehicle hull models: 'single-floor hull', 'double-floor hull' and 'V bottom' hull were compared as in Figure 6.37. In all 3 models both the height of the crew compartment and total vehicle weight were kept constant. This required panel BB in case 20 to be 21.66 mm thick, while panel AA and BB in cases 8 and 21 were each 10 mm thick. The stand-off distance from the charge to panel BB is maintained at 718.25 mm.

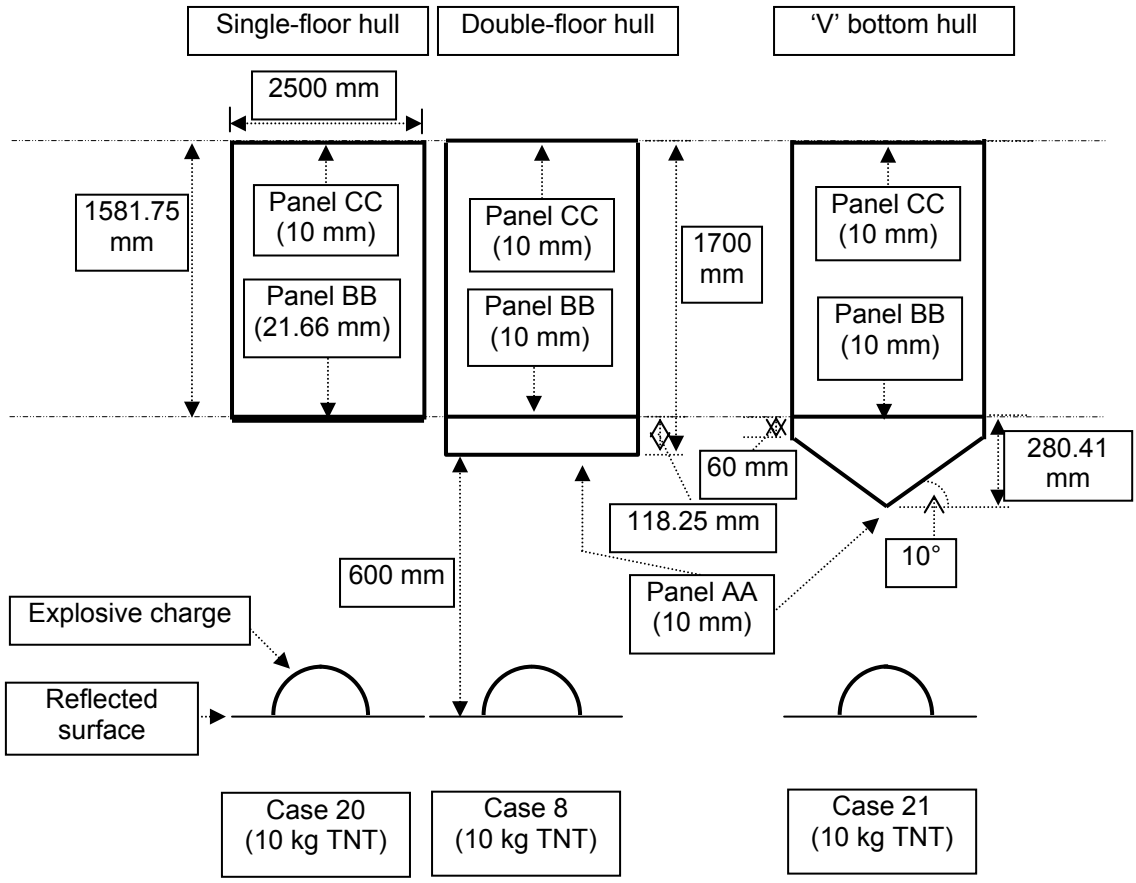

Figure 6.37 Schematic drawing of a comparison in case 20, 8, and 21.

6.8.2 'single-floor hull', 'double-floor hull' and 'V bottom' hull results

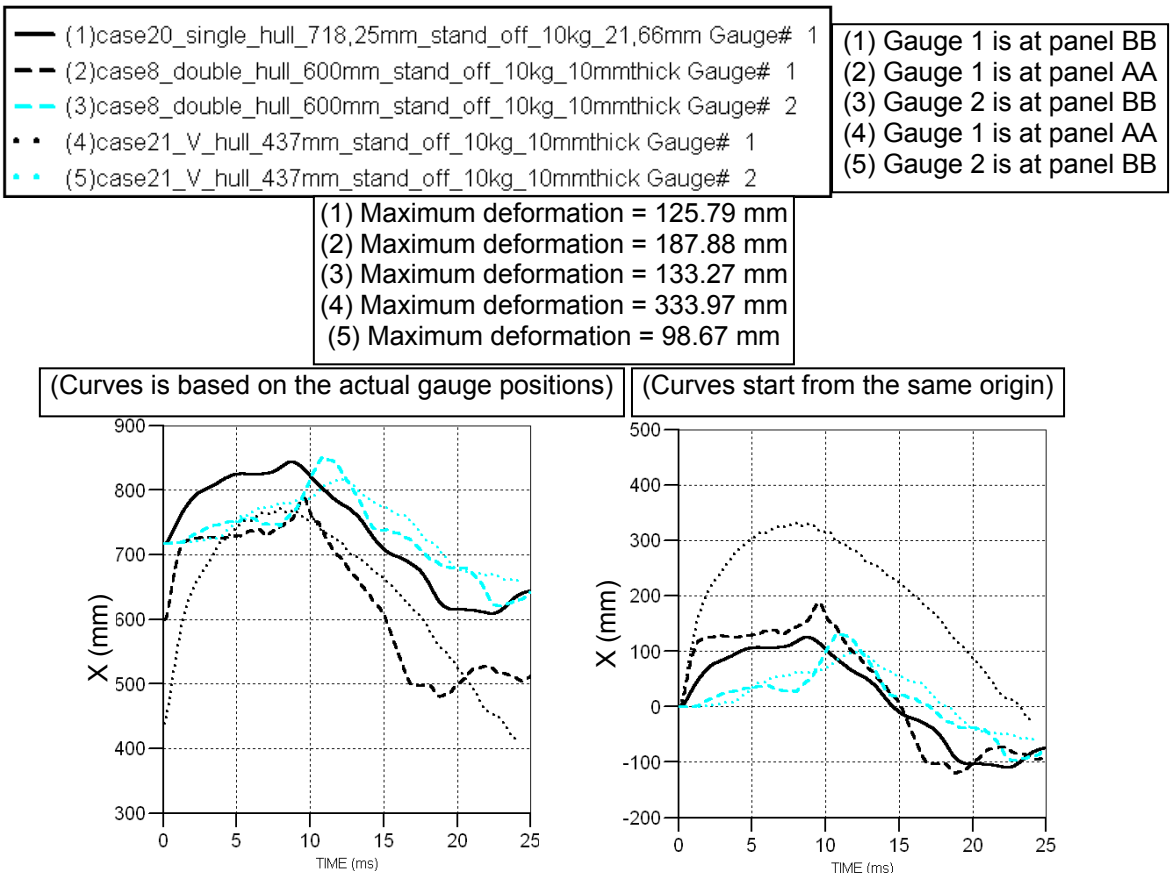

Figure 6.38 Deformation results of cases 20, 8, and 21.

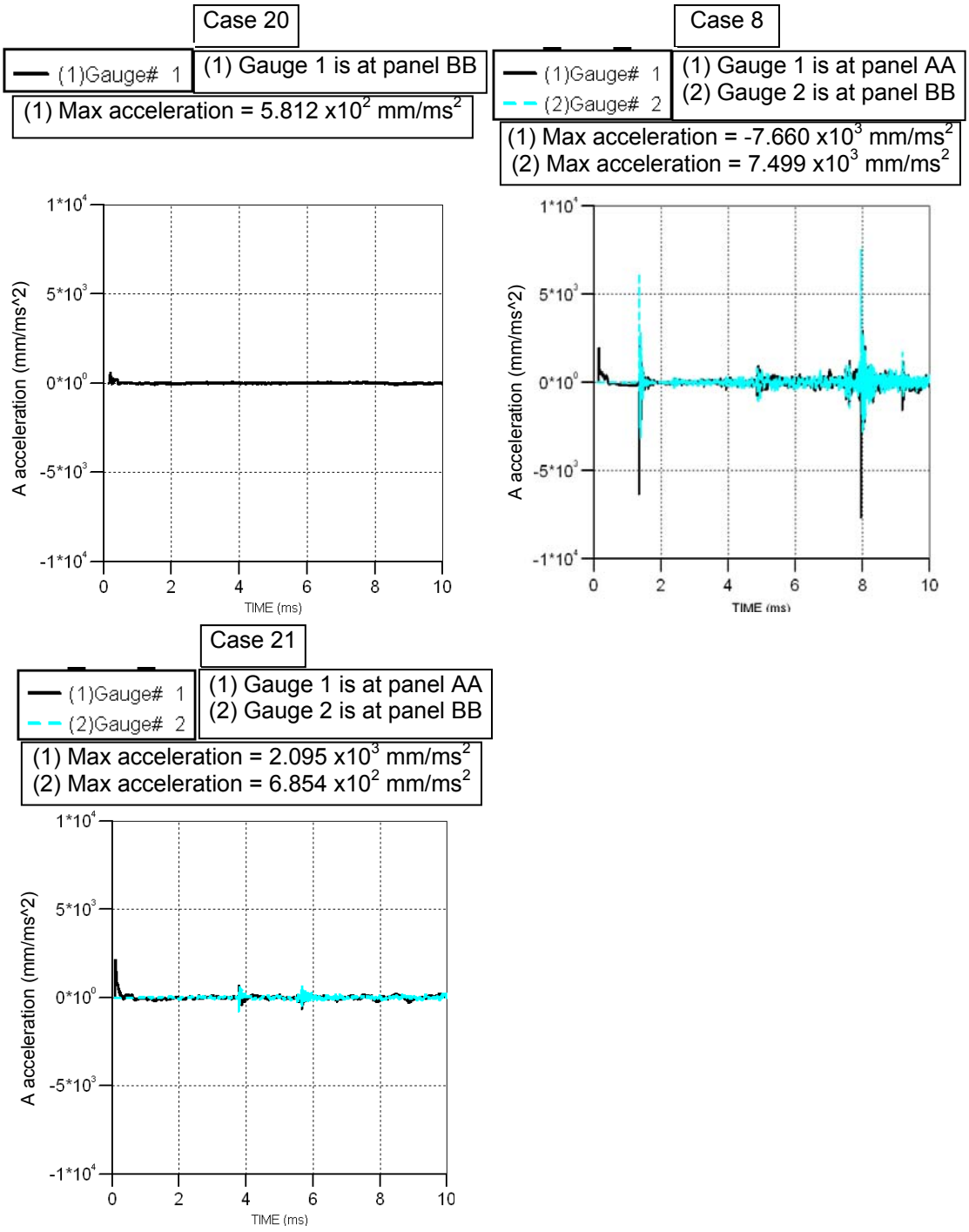

Figure 6.39 Acceleration results of cases 20, 8, and 21.

6.8.3 'single-floor hull', 'double-floor hull' and 'V bottom' hull discussion

Section 6.8 compares the 'single-floor hull' (case 20), 'double-floor hull' (case 8), and 'V bottom hull' (case 21) where the vehicle's weight (mass) in each case is the same. In Case 20, panel BB is 21.66 mm thick instead of 20 mm thick. The extra thickness accounting for the extra material was from the side panels at the bottom part of the vehicle model. The vehicle's height was shortened to 1581.75 mm, rather than 1700 mm as used in case 20. Figure 6.38 shows that panel AA in case 8 and 21 impacted with panel BB, which subsequently caused panel BB to deform. Compared with case 20, the maximum deformation at panel BB in case 8 is increased by 6%, while the maximum deformation at panel BB in case 21 is decreased by 22%. Figure 6.39 demonstrates that the maximum acceleration at panel BB in case 8 is increased from case 20 by 1,190% because of the impact, while the maximum acceleration at panel BB in case 21 is only increased by 18% even though impact also occurs. The acceleration at panel AA from the impact in case 21 (~ 4 ms and 6 ms), which is similar to the acceleration at panel BB from the impact but different in the opposite direction, is actually lower than the acceleration occurred due to the deformation movement (~0.2 ms). Considering at the crew compartment floor in cases 8 and 21, where impacts occurred in both cases, case 21 is preferable to case 8 because of the lower maximum deformation and acceleration. Based on the previous comparison of results between the single-floor hull and the double-floor hull cases of the same mass (weight), where there is no impact between panel AA and BB in the double-floor hull, the acceleration in the double-floor hull cases is lower than the single-floor hull cases. Hence it is likely that without the impact, the acceleration at panel BB in the 'V bottom hull' model will be less than the acceleration at panel BB in the single-floor hull model. This implies that, in cases where there is no impact between panel AA and BB, for the same vehicle weight (mass) and a constant crew compartment height, but changing the bottom section, the 'V bottom hull model is a better alternative than the 'double-floor hull model and the single-floor hull model.

For simplification, it is assumed that the averaged blast pressure acting on the 2.5 m x 2.5 m panel, inclined at 0°, is 1×10^5 kN/m^2. By inclining the panel, the averaged pressure acting at right angle on the 10° inclined panel AA is = $\cos(10)*(1 \times 10^5) = 9.848 \times 10^4$

kN/m^2. In case 21, the area of panel AA has increased from 6.25 m^2 to 6.346 m^2. Generally, if the area is increased, the pressure will be reduced. Therefore the averaged pressure at panel AA acting on the 10° inclined panel AA is reduced further from 1 x 10^5 kN/m^2 to 9.848 x 10^4 kN/m^2, and to 9.698 x 10^4 kN/m^2. This has accounted for 1.52% reduction in the averaged pressure. However, this figure is based on numerous assumptions. In reality, the blast pressure progresses dynamically due to the flow of the air and explosive mixture.

Considering the blast pressures measured at gauges A1 – A9, as shown in Figure 6.41 and Figure 6.42, the location of which can be seen in Figure 6.40, at gauges A1, A2, and A3, the maximum pressure in case 21 ('V bottom hull') is higher than in case 8 ('double-floor hull') and case 20 ('single-floor hull'). Gauge A2, which is 100 mm from the x-axis, in all cases recorded a higher maximum pressure than gauge A1, which is on the x-axis. However at gauges A4 – A9, the maximum pressure in case 21 dropped to be less than cases 8 and 20. By looking at the gauge positions, gauges A4 and A5 in case 21 are actually closer to the centre of the charge (571 mm and 643 mm) than in cases 8 (666 mm and 717 mm) and 20 (774 mm and 818 mm). From the pressure contour plots in Figures D.10 – D.15 (Appendix D), as the blast pressure started to interact with panel AA, the reflected pressure is built up. The contour plot indicates that the layer of the 'more than 1.0 x 10^4 kN/m^2' pressure range in cases 20 and 8 has built up more than in case 21, which is evident by the thickness of the pressure plot in that range. The results have shown that by changing the angle of incidence to 10°, the reflected pressure dropped even though the gauges are at a shorter stand off distance from the blast and the thickness of high pressure plot is less than in the 0° angle of incidence case. This is due to the reflected pressure being allowed to propagate sideways to the lower pressure region more easily. The finding can be further supported by the reflection coefficient (reflected pressure divided by the incident pressure) vs. angle of incidence plots in Hetherington (1994) and US Department of the Army (1991). The plot shows that the reflected pressure at 10° angle of incidence is less than the reflected pressure at 0° angle of incidence in all cases.

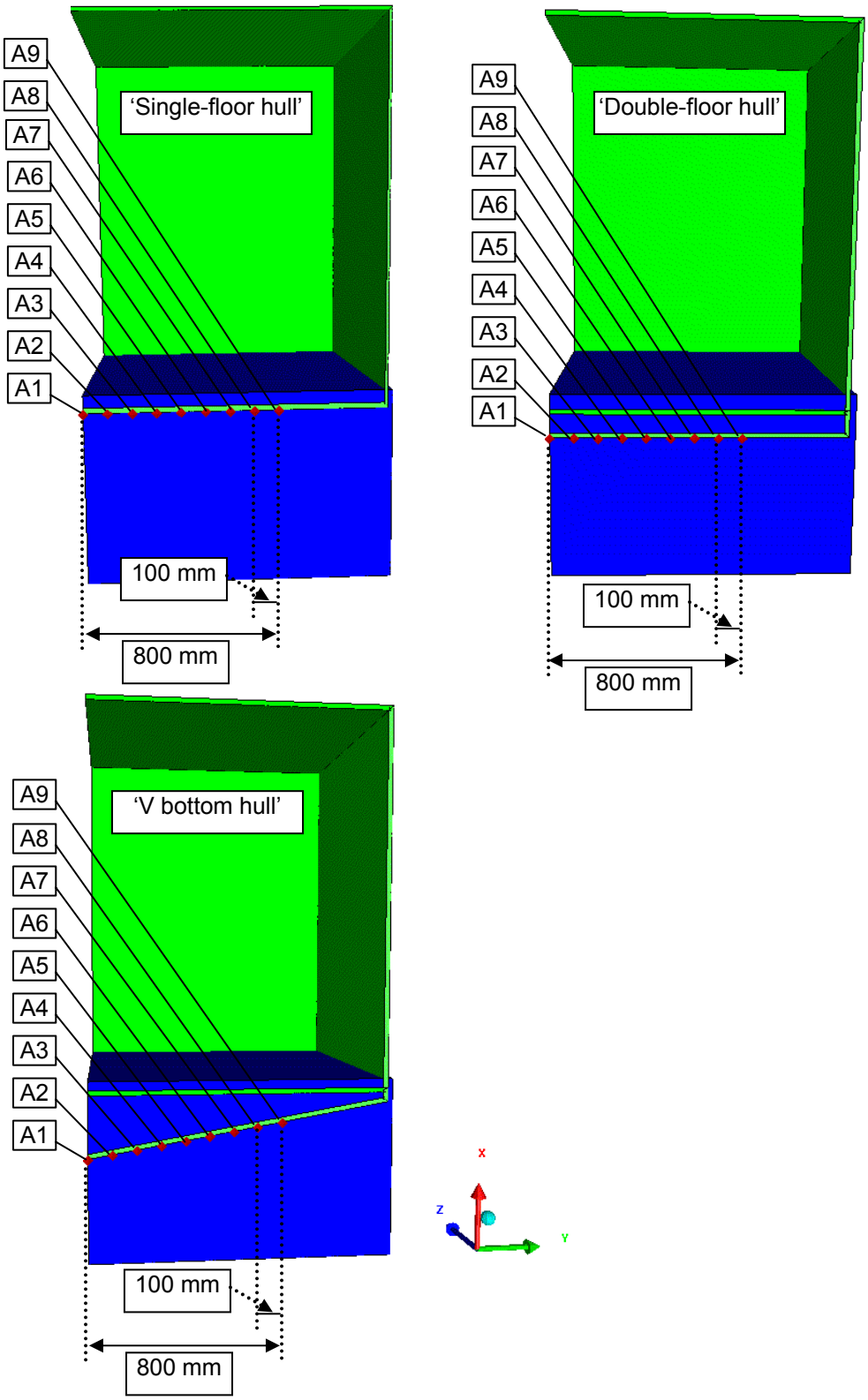

Figure 6.40 Gauge A1 – A9 in cases 20, 8, and 21. Note that each gauge is 5 mm directly below the structure in x-direction.

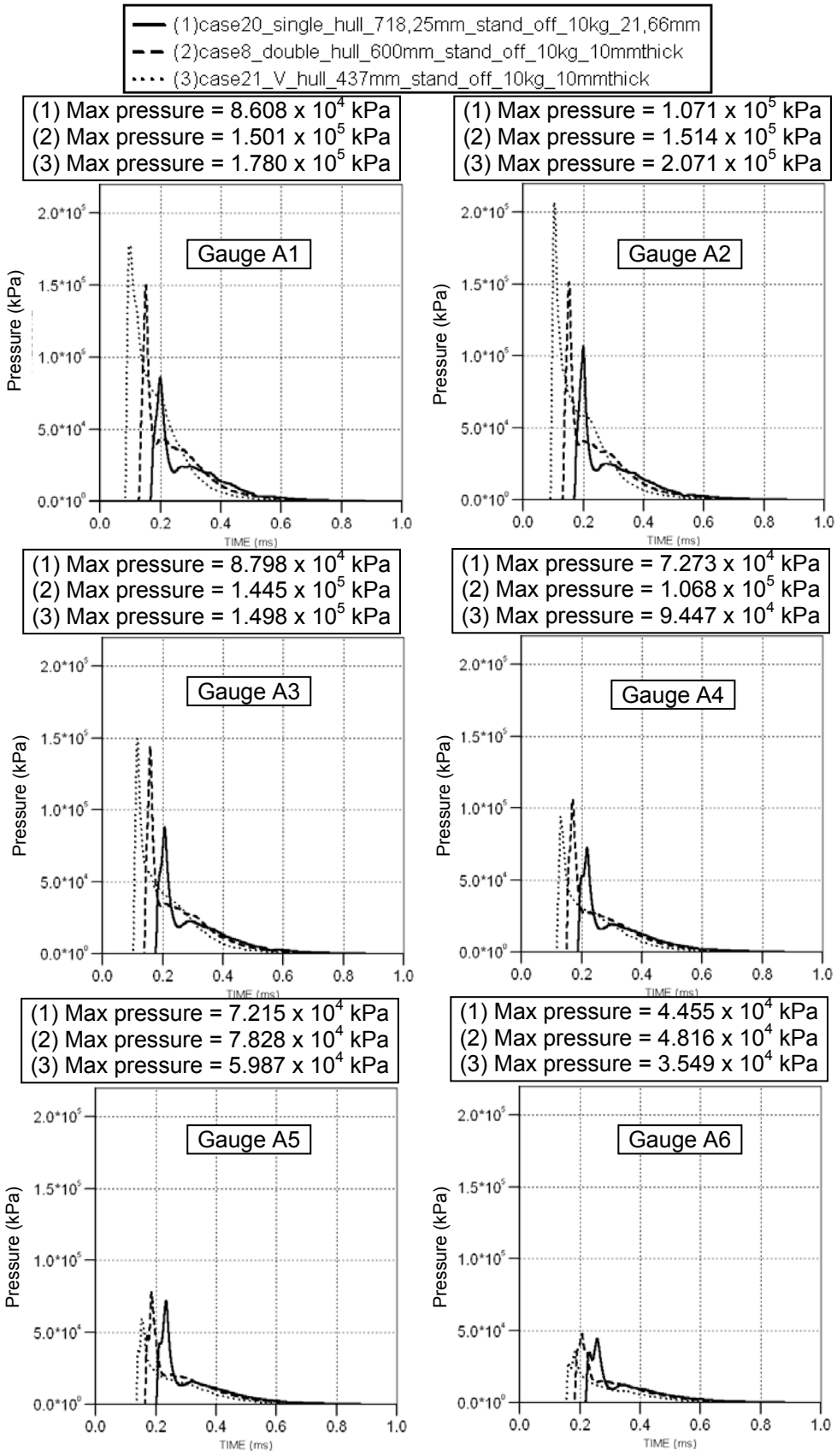

Figure 6.41 Recorded pressure at gauge A1 – A6 in cases 20, 8, and 21.

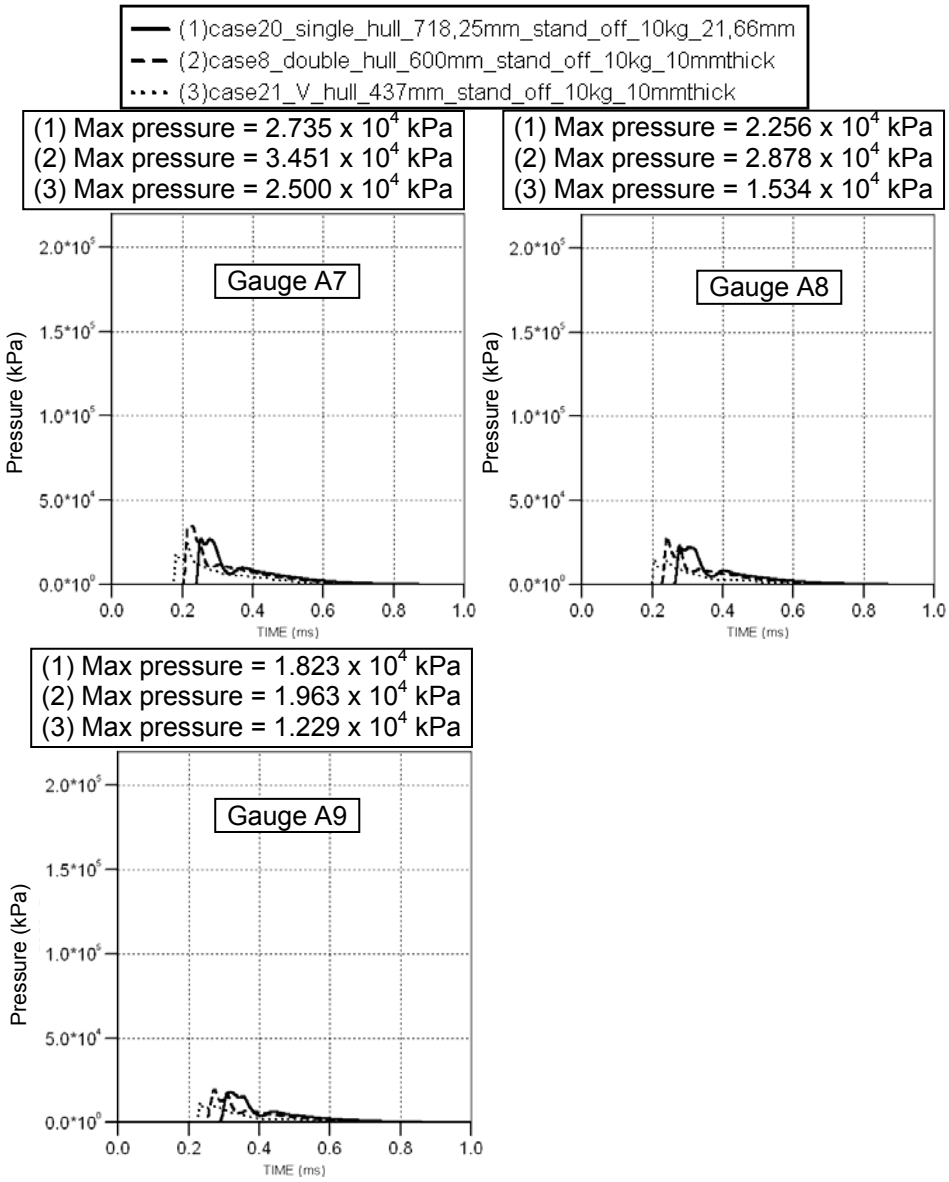

Figure 6.42 Recorded pressure at gauge A7 – A9 in cases 20, 8, and 21.

Based on the results from gauges A1 – A9, it may be possible that the averaged pressure acting on panel AA in case 21 is less than in cases 8 and 20. However, the results show that the deformation on panel AA in case 21 is more than case 8 and panel BB in case 20. It is thought that panel AA in case 21 deformed more because of its closeness to the explosive charge, where higher pressure is observed locally at gauge A1.

Figure 6.43 shows the comparison between the incident pressure and the reflected pressure at gauges A1 and A6. The incident pressures were recorded by deleting all the vehicle structures and allowing the blast pressure to propagate. At gauge A1, the reflection coefficient (reflected pressure divided by the incident pressure) is 9.9, 13.5, and 9.3 in case 20, 8, and 21 respectively, while at gauge A6, the reflection coefficient is 5.5, 5.6, and 3.5 in case 20, 8, and 21 correspondingly. This is in agreement with Smith and Hetherington (1994), which states that at very close range, the experimental measurements of reflection coefficient up to 20 have been made.

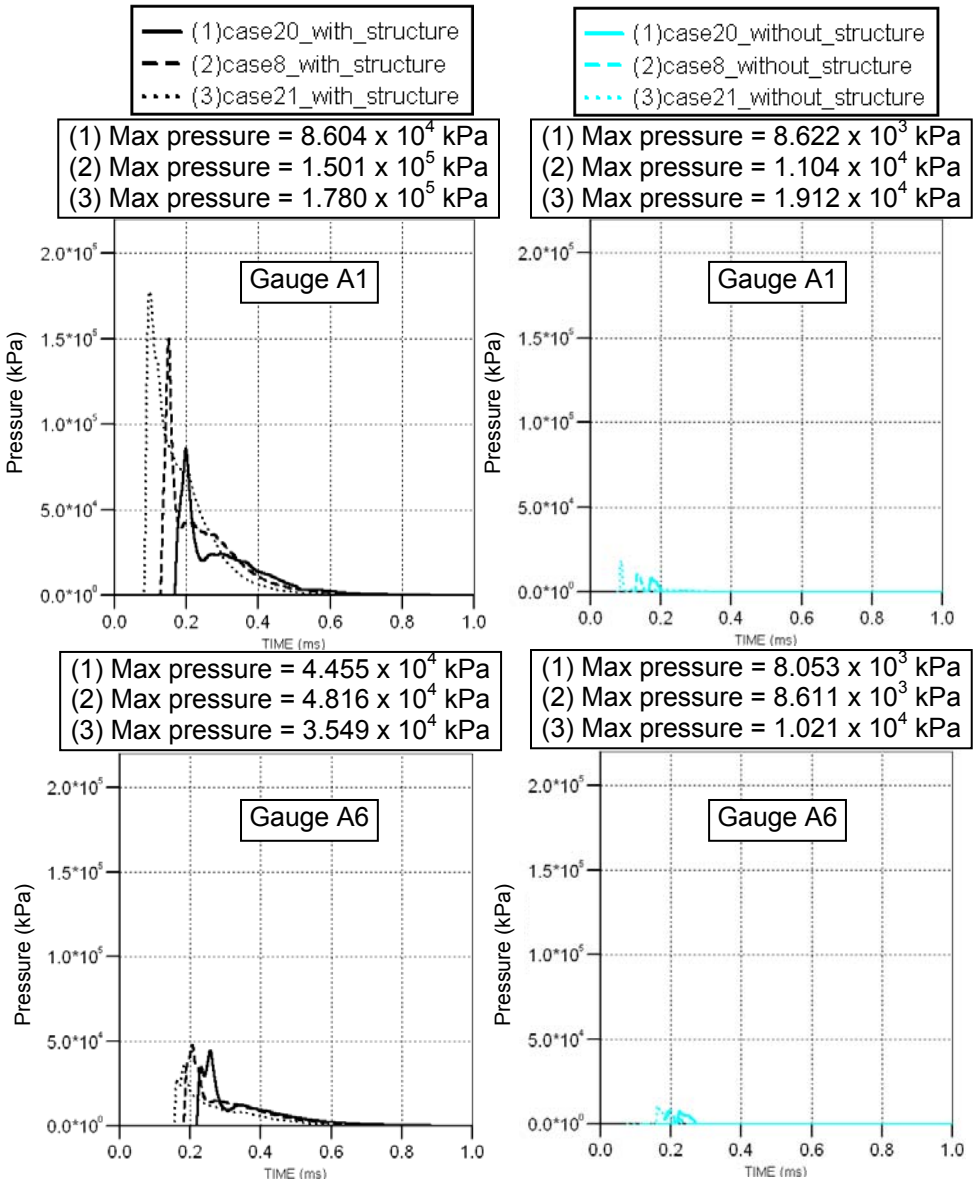

Figure 6.43 Comparison between reflected pressures (cases 20, 8, and 21 with vehicle hull structures) and incident pressures (cases 20, 8, and 21 without vehicle hull structures)

6.9 Conclusions

This chapter has performed different analyses on various vehicle hull configurations subjected to mine blasts. The results demonstrate that, for the same vehicle weight (mass), a double-floor vehicle model gives lower maximum deformation, velocity, and acceleration than a single-floor vehicle model, providing that panel AA does not impact with panel BB. Therefore by keeping the stand-off distance of panel BB the same, the method of adding another floor panel is better than adding more thickness to panel BB and extending the stand off distance.

Undesirable high acceleration is observed in the cases where panel AA impacts with panel BB in double-floor hull models. This can be avoided by reducing the amount of explosive charge, increasing the thickness on panel AA, increasing the gap distance, and using 'V bottom' hulls. Using 'V bottom' can reduce or eliminate the impact between panel AA and BB by allowing the blast to propagate sideways more, which reduces the reflected pressure, and subsequently the crew compartment floor experiences less effects in terms of deformation, velocity, and acceleration.

CHAPTER 7 Vehicle hull model subjected to a buried charge under soil numerical simulations

This Chapter compares the blast loading from an hemispherical charge on a reflected surface, which was used in Chapter 5 and 6, to the blast loading from a charge buried under soil using a new soil model.

7.1 Introduction

In May 2006, Fiserova (2006) has developed a framework for deriving the cohesive soil model with different moisture contents, which is composed of fine particles with material strength. This soil model was developed in AUTODYN 2D multi-materials and was validated against the experimental results.

The remap method used in Chapters 4, 5, and 6 was done by remapping from AUTODYN 2D multi-materials, which consisted of air and explosive, to AUTODYN 3D single material, which approximated the mixture to behave like an ideal gas (This thesis defines this method as AUTODYN 3D remap). However, soil cannot be modelled in this way. In 2004, AUTODYN version 5 was made available. This version allowed the remap capability from AUTODYN 2D multi-materials to AUTODYN 3D multi-materials (This thesis defines this method as multi-materials remap). Later in 2005, AUTODYN version 6 has improved its 3D multi-materials solver to have a similar remap capability with the 2D multi-materials. It has also improved the Euler/Lagrange coupling to be more precise.

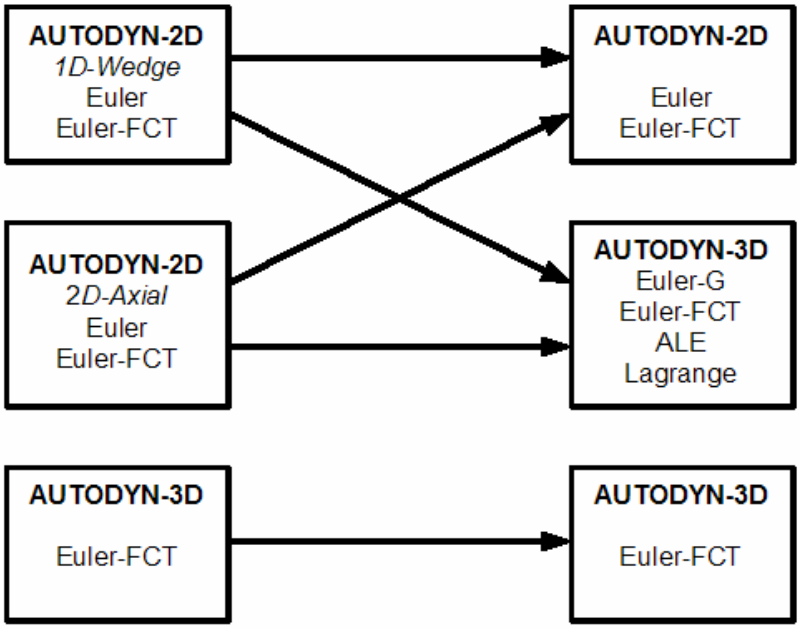

Figure 7.1 Remap options from Century Dynamic Inc. (2005)

This thesis has taken advantage of these developments to implement the blast loading from a buried charge in soil, using the formulation of the soil model derived by Fiserova (2006), into the full model, which includes interaction with a structure. The blast loading from a buried charge in soil with 7.7% moisture content will be used to compare with the blast loading from an hemispherical charge on a reflected surface. By using the multi-materials remap method, this comparison will show whether the blast loading used in Chapter 5, and 6 is a suitable alternative. Because of the limited time available, the work in this chapter will involve only a single plate and a double-floor hull vehicle model.

7.2 Soil parameters

The soil parameters required in AUTODYN were obtained from Appendix E in Fiserova (2006), which used Compaction equation of state, Granular strength model, and Hydro-tensile limit failure model. The derivations of these models are fully described in Fiserova (2006).

7.2.1 Compaction equation of state

In AUTODYN, Century Dynamics Inc. (2003), Compaction equation of state is described by the plastic compaction path, which is defined by a piecewise linear path with ten points on the pressure-density curve.

$$\rho = f(p) \qquad (7.1)$$

Fiserova (2006) has derived this relationship based on Henrych (1979). The density of a three-phase medium soil, which consists of solid particles, water, and air, is related to the pressure relationship from each phase's relative volume. The soil density at pressure p is equivalent to the initial density divided by the total of the relative volumes from all three phases.

The relationship between the relative volume and pressure (the equation of state) for the solid phase is the equation obtained from the curve fitted through the triaxial laboratory data points.

The water phase equation of state is taken from Henrych (1979), and the air phase equation of state is the adiabatic form, with the adiabatic coefficient of 1.4.

As the material compacts, the elastic loading and unloading is a relationship between density and bulk sound speed.

$$\rho = f(v_{sound}) \qquad (7.2)$$

The velocity is divided into longitudinal and shear components, both of which are related to the density.

7.2.2 Granular strength model

AUTODYN describes the Granular strength model as a relationship between the yield stress σ_y, pressure p, and the corresponding density using 10 sets of data.

$$\sigma_y = c + p\tan\phi \qquad (7.3)$$

Where c is the cohesion value and ϕ is the friction angle, which can be found from the triaxial laboratory data.

In addition, the relationship between the shear modulus and the soil density is required in the form of 10 sets of data. As described above, soil density may be found from the relative volume of each phase. The relative volume of each phase also determines the Poisson's ratio, which together with the bulk modulus gives the shear modulus value. Note that the bulk modulus can be found from the ratio of the change in pressure and the change in strain value.

7.2.3 Hydro-tensile limit failure model

$$p_{\min} = -c \qquad (7.4)$$

Where c is the cohesion value. The model is set such that failure occurs when the value of soil cohesion becomes negative (no longer sticks). Once the material fails in a cell, the internal energy is recomputed and the material is assumed to have rehealed so that negative pressures may occur in the next timestep but limited again by the hydrodynamic tensile limit, Century Dynamics Inc. (2003).

7.3 Preliminary models

7.3.1 'Preliminary models' simulations

The initial step was to develop the axis-symmetric model in AUTODYN 2D multi-materials, which contained air, soil, and explosive charge. A spherical charge of 3.17 kg TNT was buried under soil of 7.7% moisture content, 30 mm distance from the ground surface, as shown in Figure 7.2. The mesh sensitivity analysis was done by measuring the pressure and specific impulse at the gauges at 390, 400, 410, 425, and 440 mm from the soil surface. Results are in Figures 7.3 – 7.5.

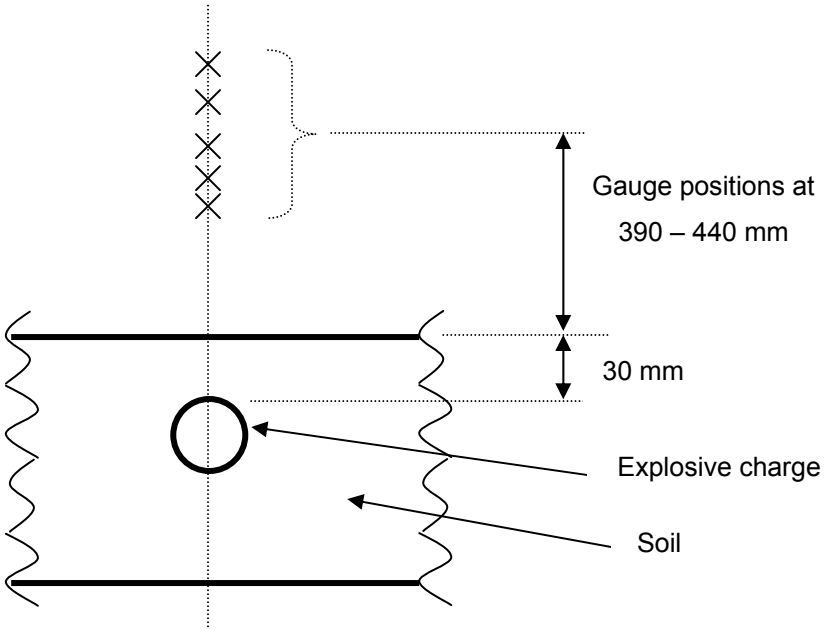

Figure 7.2 Schematic drawing of mesh sensitivity analysis of a spherical charge buried under soil.

7.3.2 'Preliminary models' results

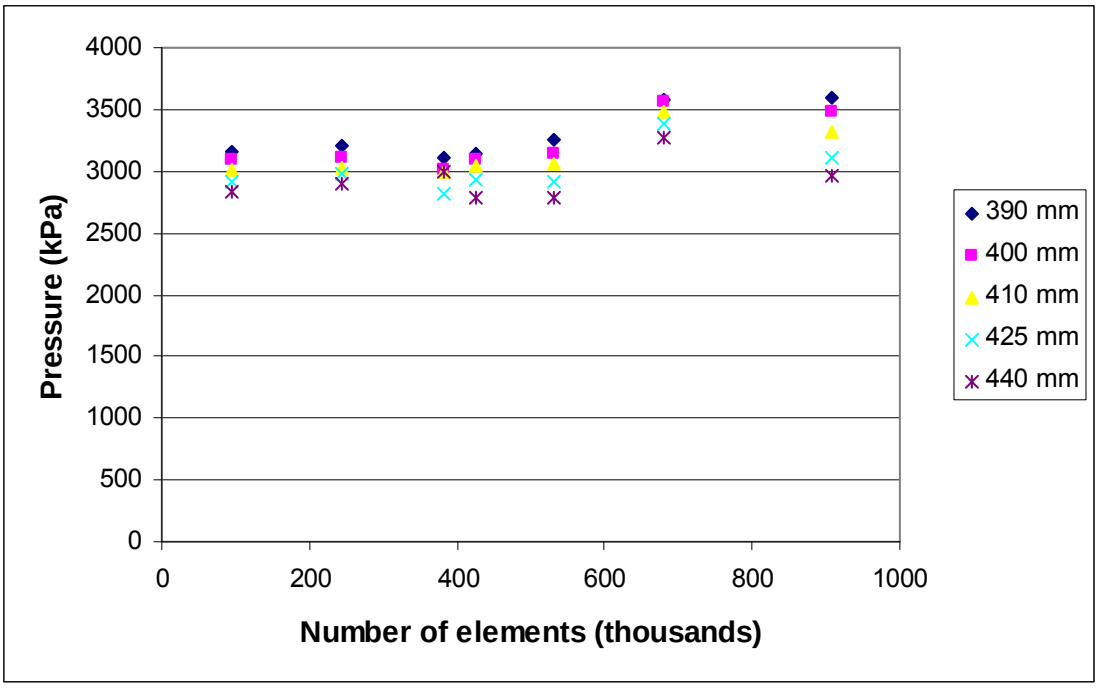

Figure 7.3 Mesh sensitivity results on recorded maximum pressure at different gauges (390, 400, 410, 425, and 440 from the soil surface) using different mesh size: 2.00 mm (96 thousand elements) 1.25 mm (245 thousand elements), 1.00 mm (383 thousand elements), 0.95 mm (425 thousand elements), 0.85 mm (530 thousand elements), 0.75 mm (681 thousand elements), and 0.65 mm (907 thousand elements).

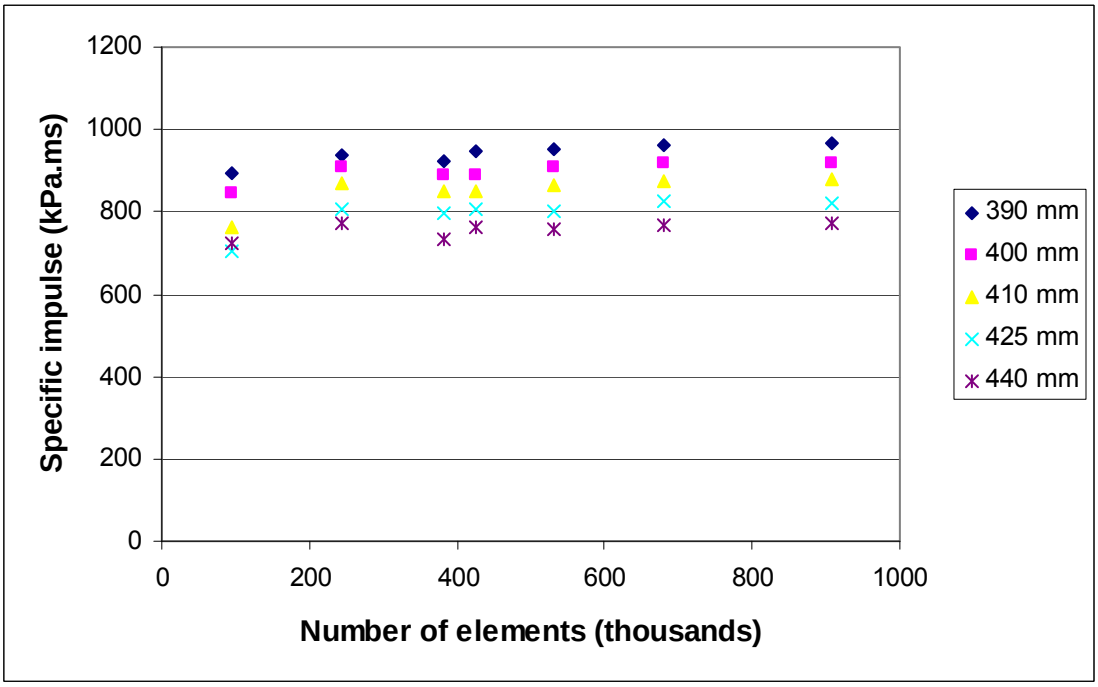

Figure 7.4 Mesh sensitivity results on recorded maximum specific impulse at different gauges (390, 400, 410, 425, and 440 from the soil surface) using different mesh size

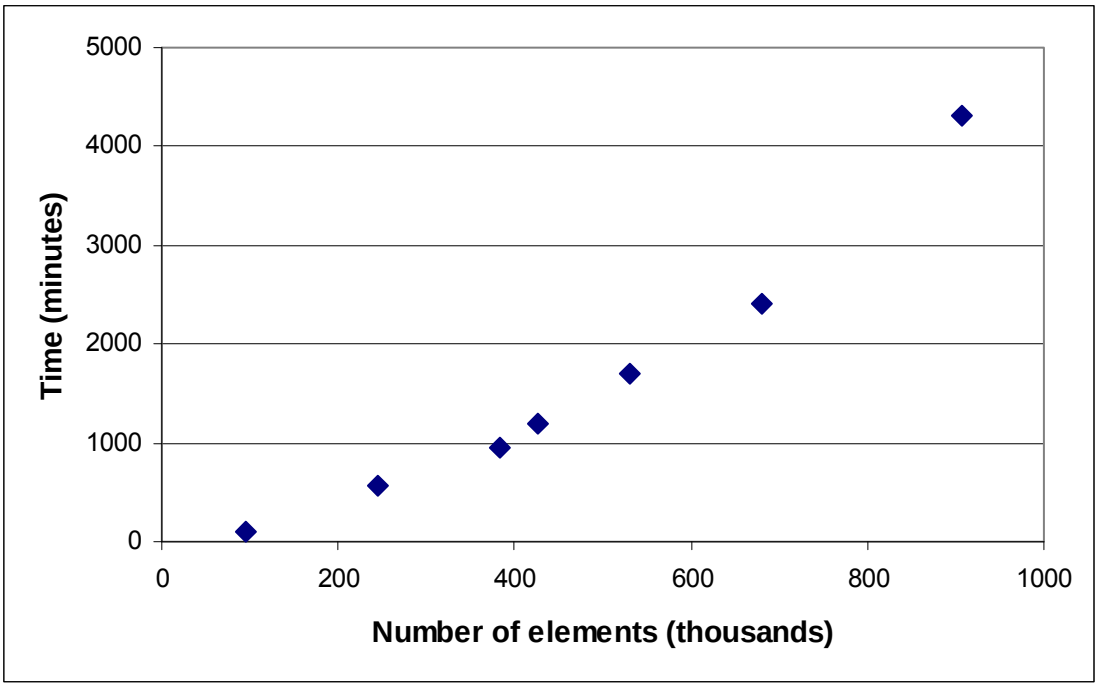

Figure 7.5 Time taken to run using different mesh sizes (number of elements): mesh sensitivity analysis on a buried charge under the soil.

7.3.3 'Preliminary models' discussion

From the results in Figure 7.3 – 7.5, 0.75 mm mesh size is going to be used in the future analysis. Apart from the mesh size of 1.00 mm and 2.00 mm, as the gauge position increases from 390 mm to 440 mm from the blast, the recorded pressure and specific impulse reduces. This shows that the further it is away from the blast, the less the effect it receives. At '1 mm mesh size' and '2 mm mesh size', the recorded pressure and specific impulse at 425 mm and 440 mm vary slightly from the trend respectively. As the mesh size reduces from 2.00 mm to 0.65 mm, the recorded specific impulse seems to change little. Changes are more in terms of recorded pressure. Overall, the pressure starts to go up until using 0.75 mm mesh size and then drops when using 0.65 mm. The variations of results may be explained by first looking at the material plots at cycle 0 in Figure 7.6. It can be seen that the explosive charge (TNT) in the '2.00 mm mesh size' is not really in a spherical shape, while the '0.75 mm mesh size' is much closer to the intended spherical shape. This is due to the restriction in AUTODYN that each Euler element is allowed to contain only one material at the initial set up (cycle 0) and the mesh of the Euler element must be in rectangular shape. Because of this, if the element size is smaller, it will represent the

spherical shape better. Subsequently, each mesh sizes will create different explosive shapes, which will give the variation in the blast loading.

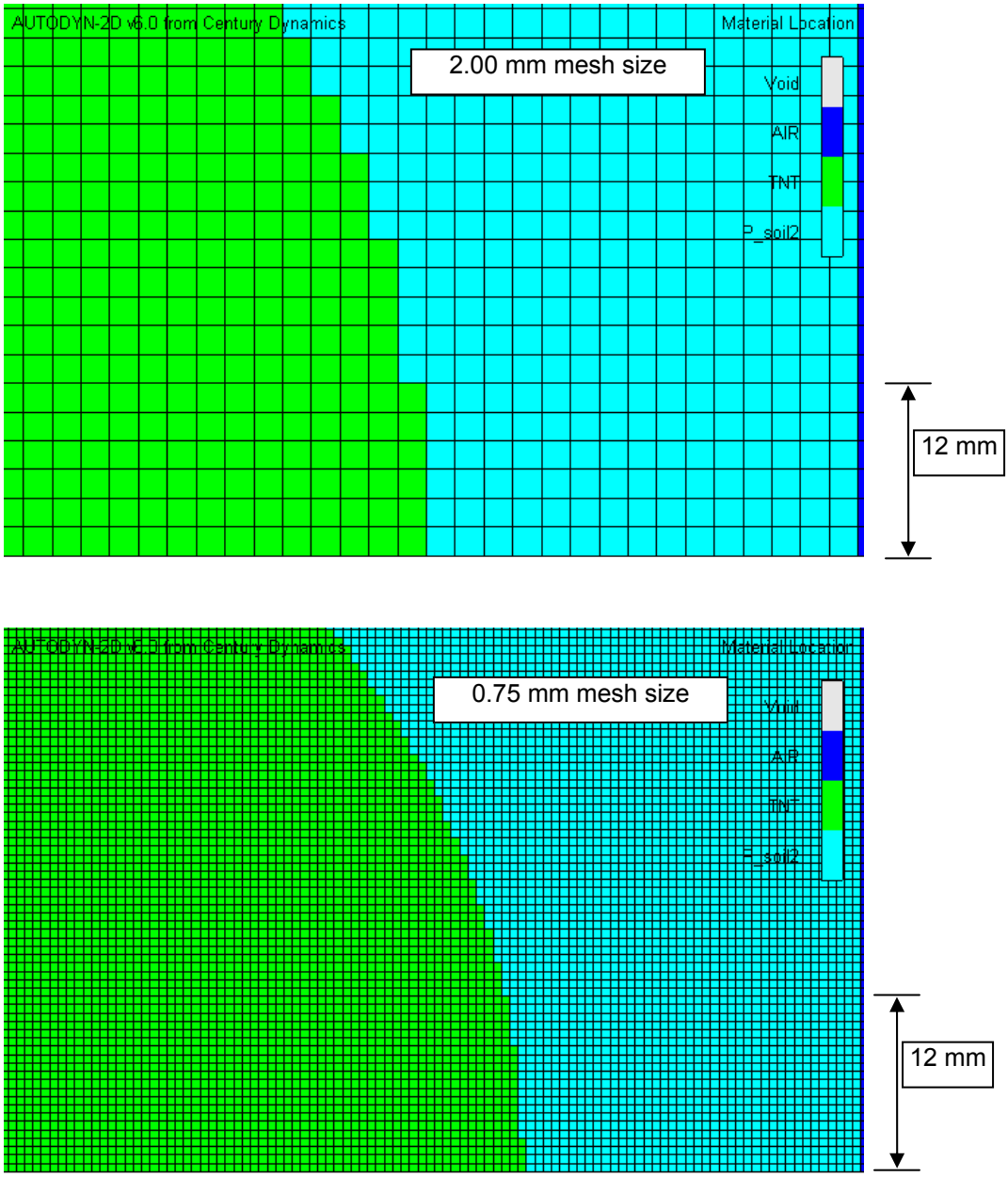

Figure 7.6 Comparing material plot at cycle 0 between 2.00 mm and 0.75 mm mesh size. Note that the plots are zoomed in for clarity and hence they are only one part of the whole models.

AUTODYN partitions the whole model into different elements depending on the mesh size. Within each element, the pressure at a particular position will be estimated based on the nearby pressure points, which are at the element centres and are calculated directly from AUTODYN. The smaller the mesh size and hence the larger number of elements will give the recorded pressure value closer to the actual pressure value at that point. The pressure in a multi-materials element will be determined by pressure averaging. The interface within a multi-materials element uses Simple Line Interface Calculation (SLIC) method, which is shown in Figure 7.7.

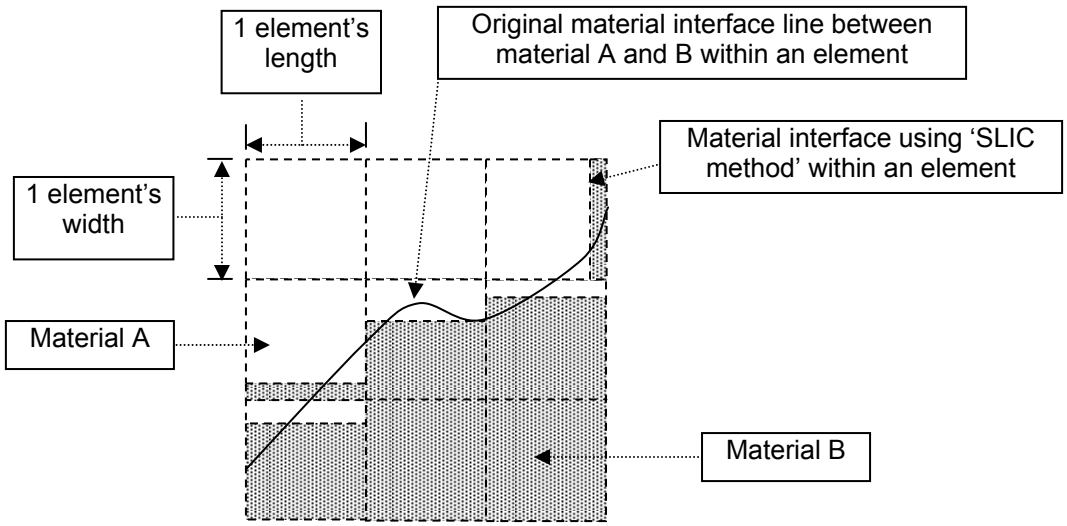

Figure 7.7 'SLIC method', produced based on YOKOI (2007)

From this figure, it indicates that within a multi-materials element, the material interface using SLIC method in AUTODYN does not give the exact material interface. If the original charge shapes are developed to be different because of different mesh sizes, it is likely that the material interface within AUTODYN will add further more variations as the blast is progressed through the soil and air. At a particular element, explosive charge, soil and air materials may be present, which is certainly more complicated than the interface between two materials. It is possible that at the same cycle time, the location of these materials will be slightly different. Figure 7.8 shows the material plots using different material sizes at 0.25 ms, which can be seen that they are slightly different, especially at the interface. As a result, the pressure contour plots, which are recorded at 0.5 ms also differ, as shown in Figure 7.9. Therefore, it is possible that, in some cases, the pressure from the smaller mesh

sizes might be lower than from the larger mesh sizes, especially in a blast loading analysis which involves extremely violent material movements and high pressure. In mesh sensitivity analysis involving multi-materials, it is important to record the pressure from different mesh sizes using different gauge positions as much as possible in order to analyse the trend. In this section, the trend from the plot indicates the mesh size of 0.75 mm is a suitable choice to use to run at a reasonable time. The numerical simulation was then conducted using the same model as in the mesh sensitivity analysis but with slightly bigger model, which accounted for the distance from the soil surface to the intended target.

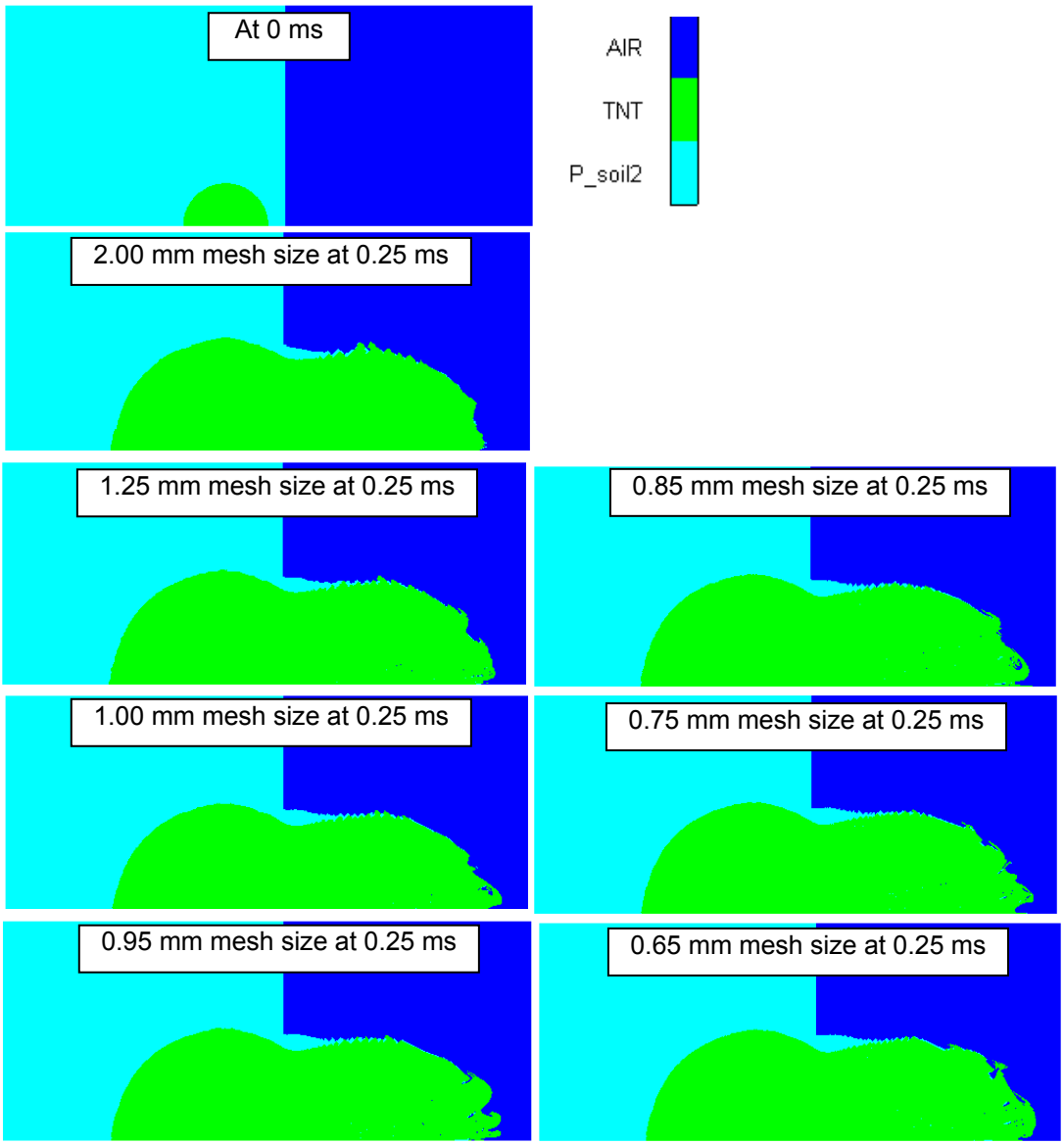

Figure 7.8 Comparing material plots at 0.25 ms from different mesh sizes (2.00, 1.25, 1.00, 0.95, 0.85, 0.75, and 0.65 mm)

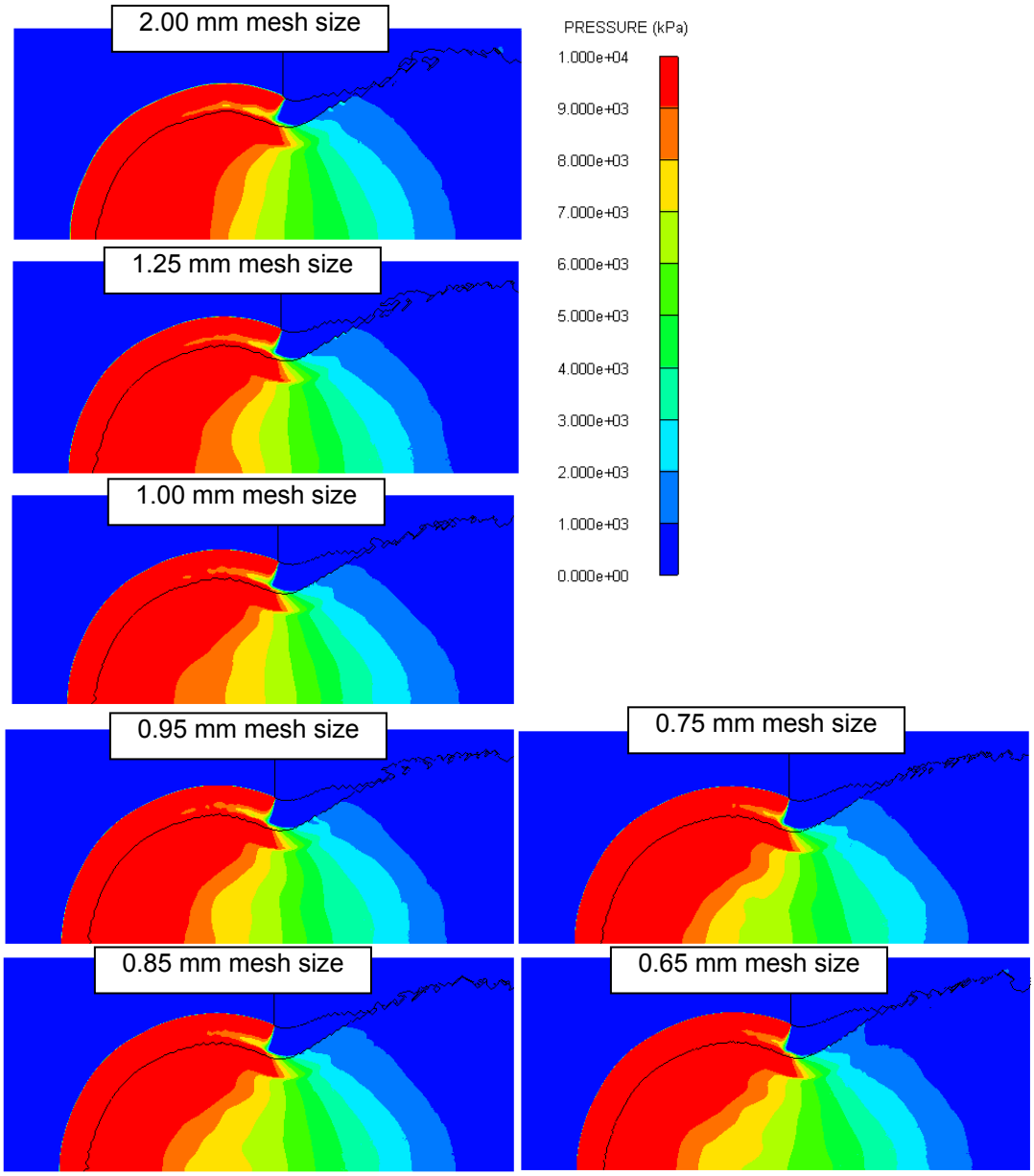

Figure 7.9 Comparing pressure contour plots at 0.5 ms from different mesh sizes (2.00, 1.25, 1.00, 0.95, 0.85, 0.75, and 0.65 mm). Note that the contour scale is same in all cases.

7.4 Buried charge and charge on a reflected surface

7.4.1 'Buried charge and charge on a reflected surface' simulations

This section will compare the blast loadings of the same amount of charge between an hemispherical charge and a buried charge under soil with 7.7% moisture content. Numerical simulations are developed in AUTODYN 2D using the same methodology as in the mesh sensitivity analysis. Figure 7.10 shows the schematic drawing of different cases. Results are in Figure 7.11 – 7.13. Note that gauge 36 and 56 are at 395 mm from the soil surface and are 200 mm apart.

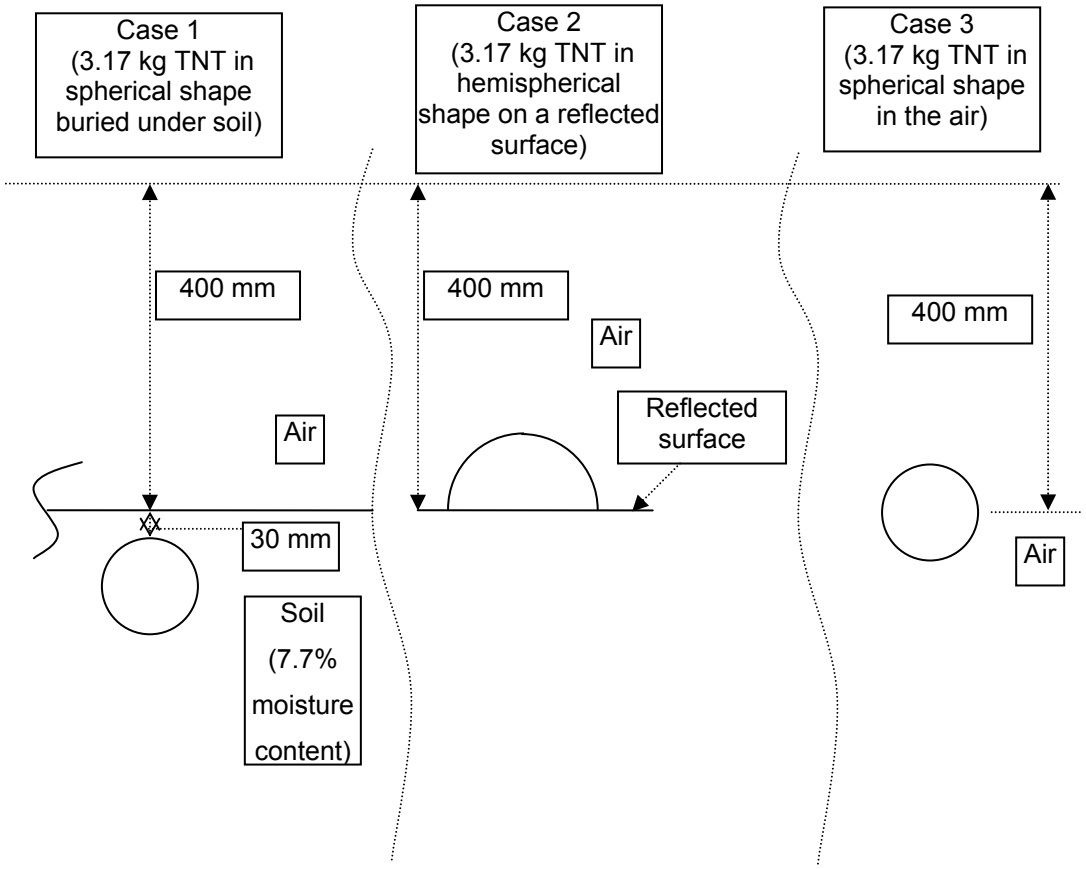

Figure 7.10 Schematic drawing of case 1, 2, and 3.

7.4.2 'Buried charge and charge on a reflected surface' results

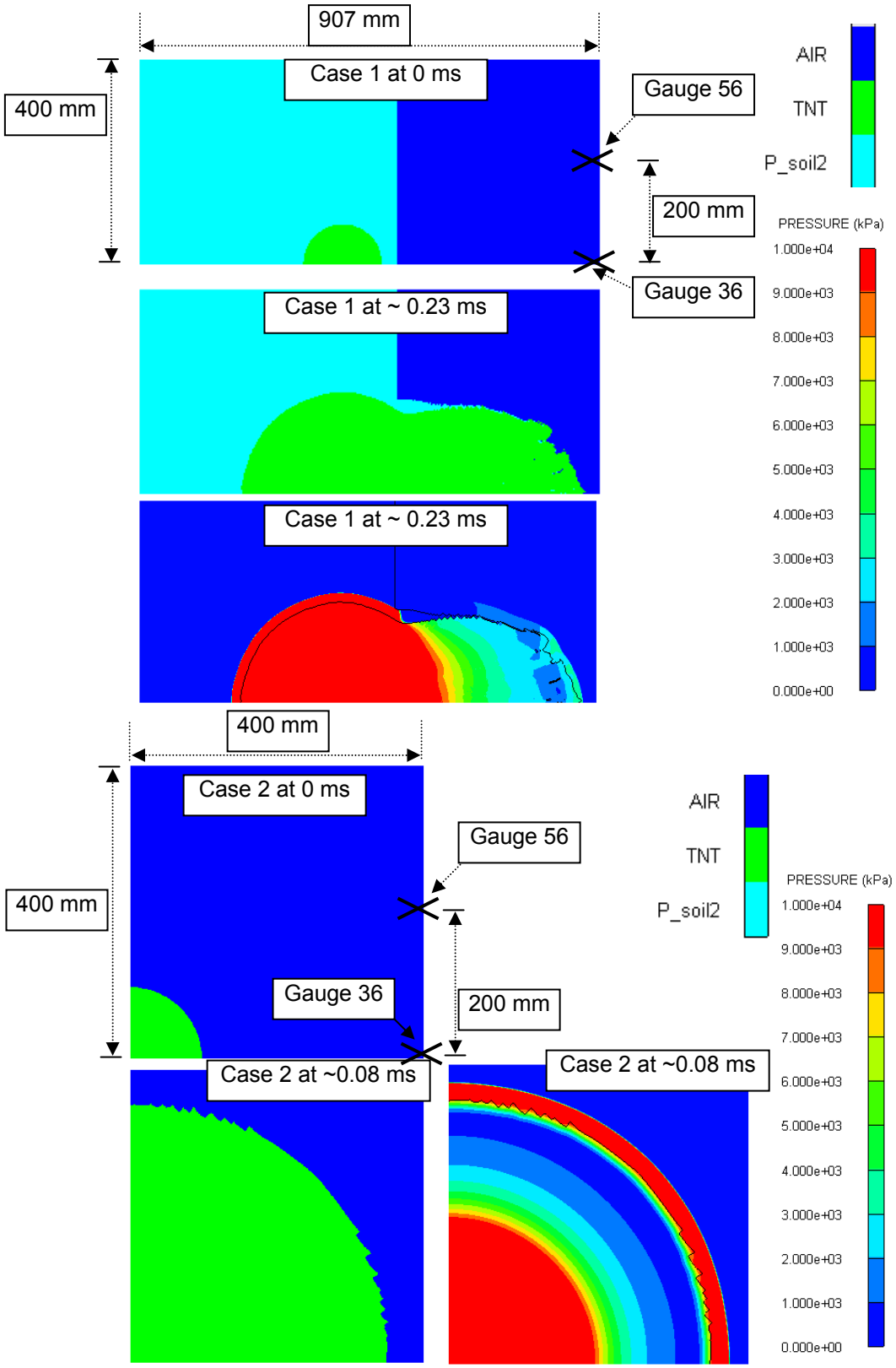

Figure 7.11 Material and pressure contour plots of case 1 and 2

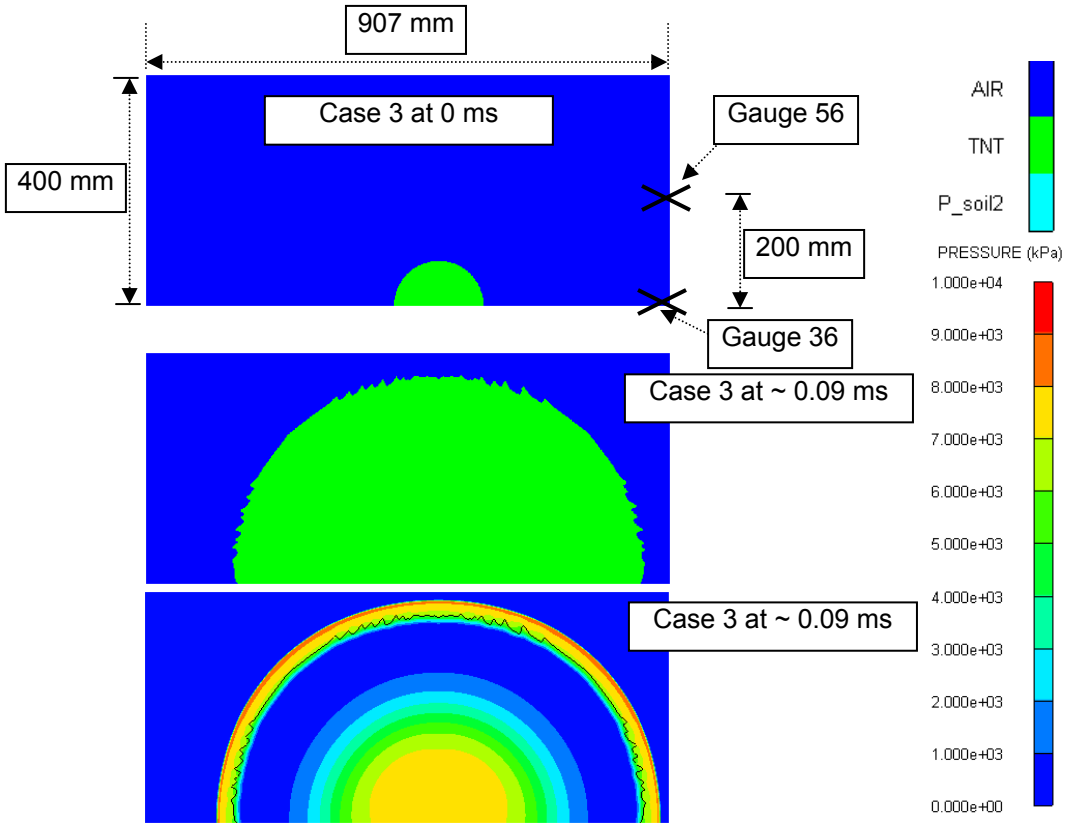

Figure 7.12 Material and pressure contour plots of case 3

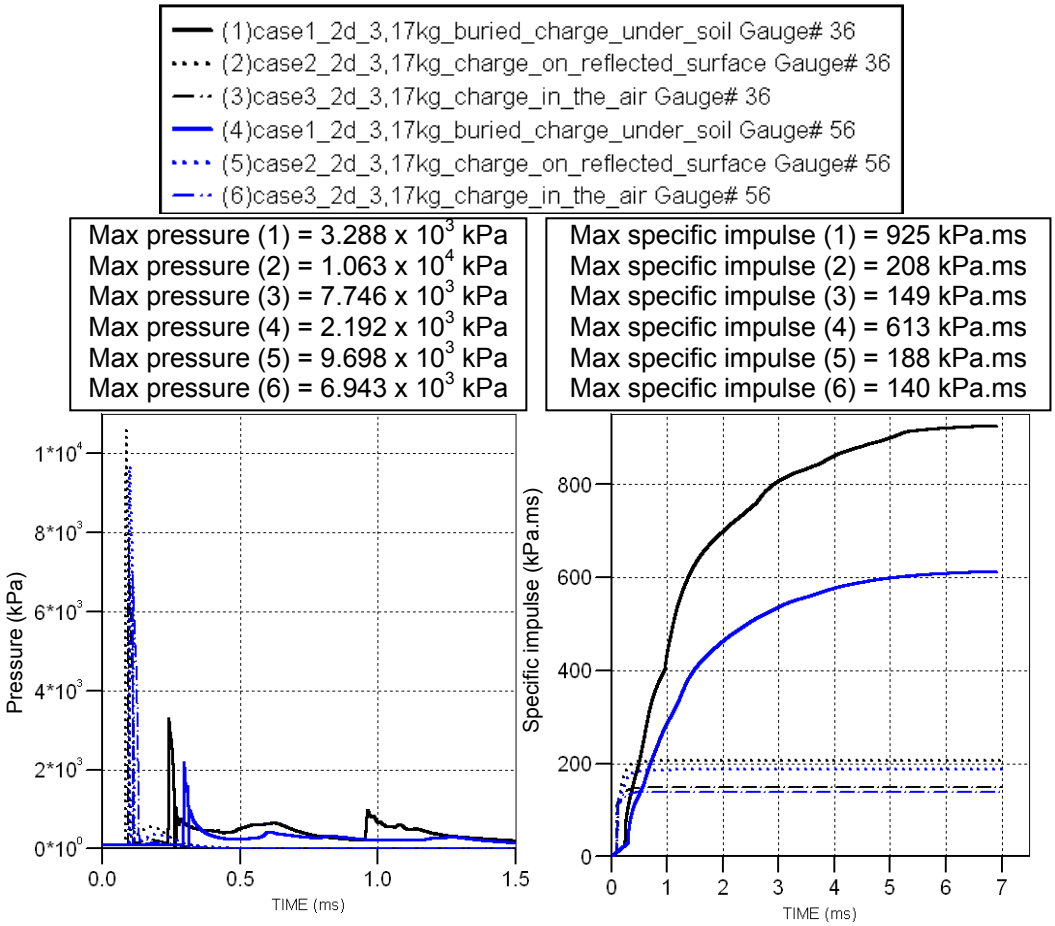

Figure 7.13 Pressure and specific impulse results in case 1, 2, and 3 at gauge 36 and 56.

7.4.3 'Buried charge and charge on a reflected surface' discussion

From material plot in Figure 7.11 and Figure 7.12, TNT in cases 2 and 3 has expanded spherically. However, TNT in case 1 was forced to expand comparatively narrower because of the presence of the soil. By measuring the maximum pressure and maximum specific impulse at gauges 36 and 56, which are 200 mm apart, the pressure in cases 1, 2, and 3 has dropped by 33%, 9%, and 10%, while the maximum specific impulse has dropped by 34%, 10%, and 6%, respectively. It confirms that the blast loading from a buried charge in soil is restricted to a smaller target area than the blast loading on the reflected surface and blast loading in the air. The drop in pressure and specific impulse measured at gauge 36 and 56 occurred in case 1, 2, and 3 even though these two gauges are at 395 mm from the surface because gauge 56 is actually at 443 mm rather than 395 mm from the centre of the charge as in gauge 36. It is expected that the further away from the blast the pressure and specific impulse will be reduced.

Figure 7.13 illustrates that blast loading from an hemispherical charge on a hard surface gives 27% (gauge 36) and 40% (gauge 56) higher maximum pressure, and 40% (gauge36) and 34% (gauge 56) higher specific impulse than the blast loading from a spherical charge in the air having the same weight (mass). The added pressure and specific impulse has come from the reflection on the surface.

Comparing with the blast loading from the spherical charge in the air in case 3, the maximum pressure from spherical charge buried at 30 mm from the soil surface in case 1 is 58% (gauge 36), and 68% (gauge 56) lower, while the maximum specific impulse is 521% (gauge 36) and 338% (gauge56) higher than case3. The decrease in pressure may have come from the obstruction of the soil on the top of the explosive charge, while the increase in specific impulse is due to the soil particles. US Department of the Army (1985) states that, in cohesive soil, moist clay particles deform upon impact, expending some of their kinetic energy in the process, and transmitting an impulse to the impacted structure that has a lower peak load (pressure) but longer in duration than in rocky soil which consists of rock particles.

7.5 Comparison using structural models

7.5.1 Single plate simulations

In this section, blast loading from a 3.17 kg TNT explosive charge in spherical shape buried under soil of 7.7% moisture content is applied to a single plate (2.5 m x 2.5 m x 0.01 m) and compared with 3.17 kg TNT explosive charge in an hemispherical shape on a reflected surface, as in Figure 7.14. The results are in Figure 7.15.

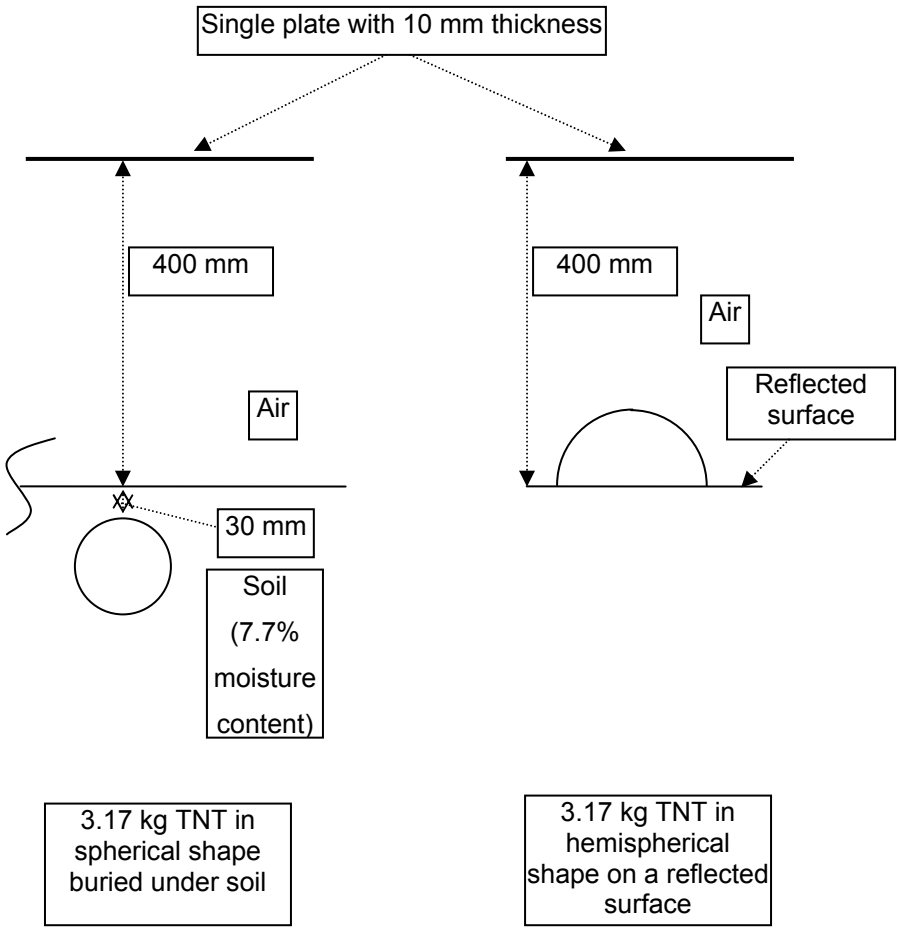

Figure 7.14 Schematic drawing of single plate subjected to 3.17 kg TNT on reflected surface and 3.17 kg TNT buried 30 mm from the soil surface.

7.5.2 Single plate results

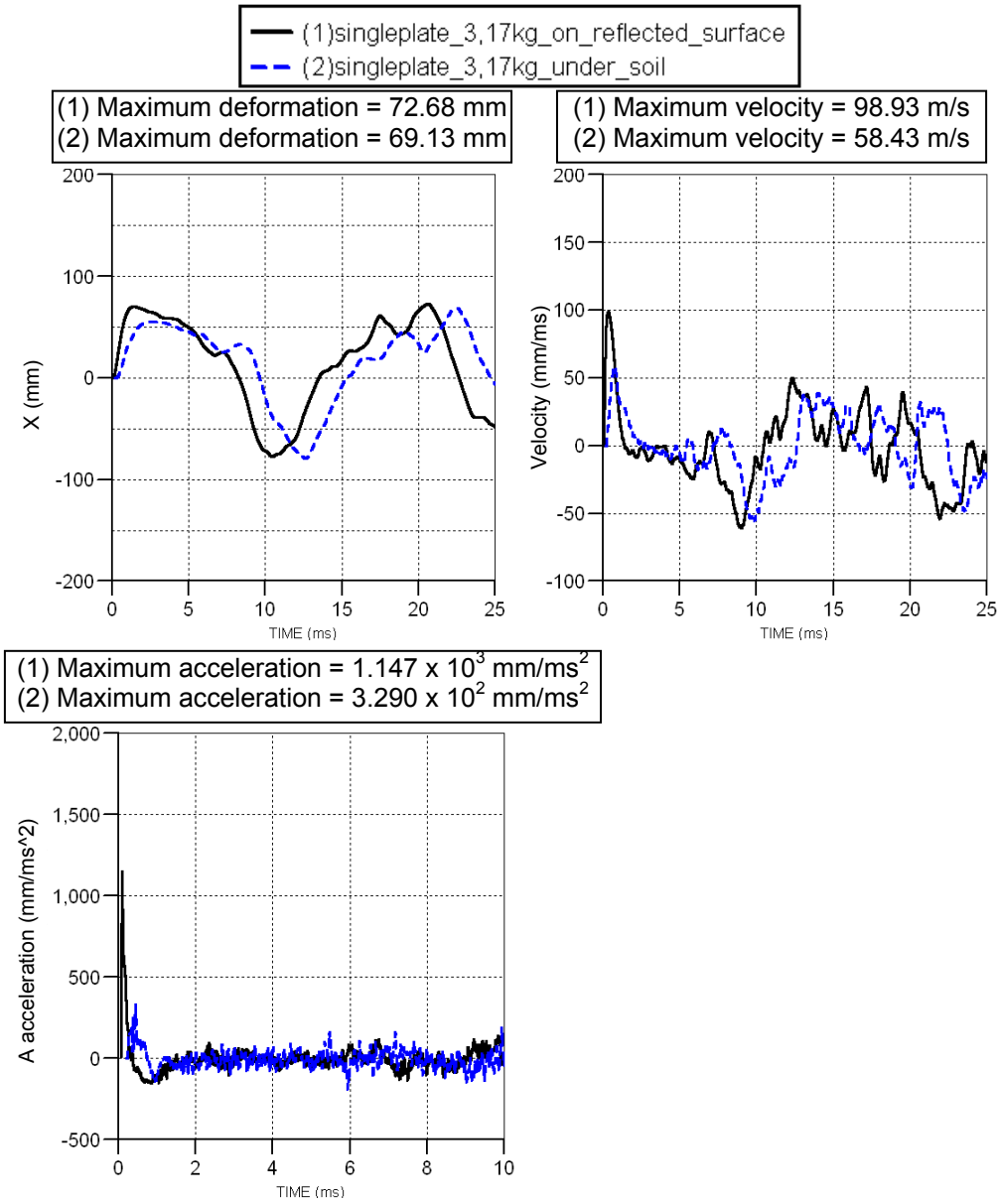

Figure 7.15 Deformation, velocity, and acceleration results of single plate models subjected to 3.17 kg TNT on reflected surface and 3.17 kg TNT buried 30 mm from the soil surface (deformation curves are based on the net deformation)

7.5.3 Double-floor hull simulations

In this section, blast loading from a 3.17 kg TNT explosive charge in spherical shape buried under soil of 7.7% moisture content is applied to the double-floor hull structure and compared with case 10 in Chapter 6 where 3.17 kg TNT explosive charge in an hemispherical shape on a reflected surface, as in Figure 7.16. The results are in Figure 7.17 – 7.19.

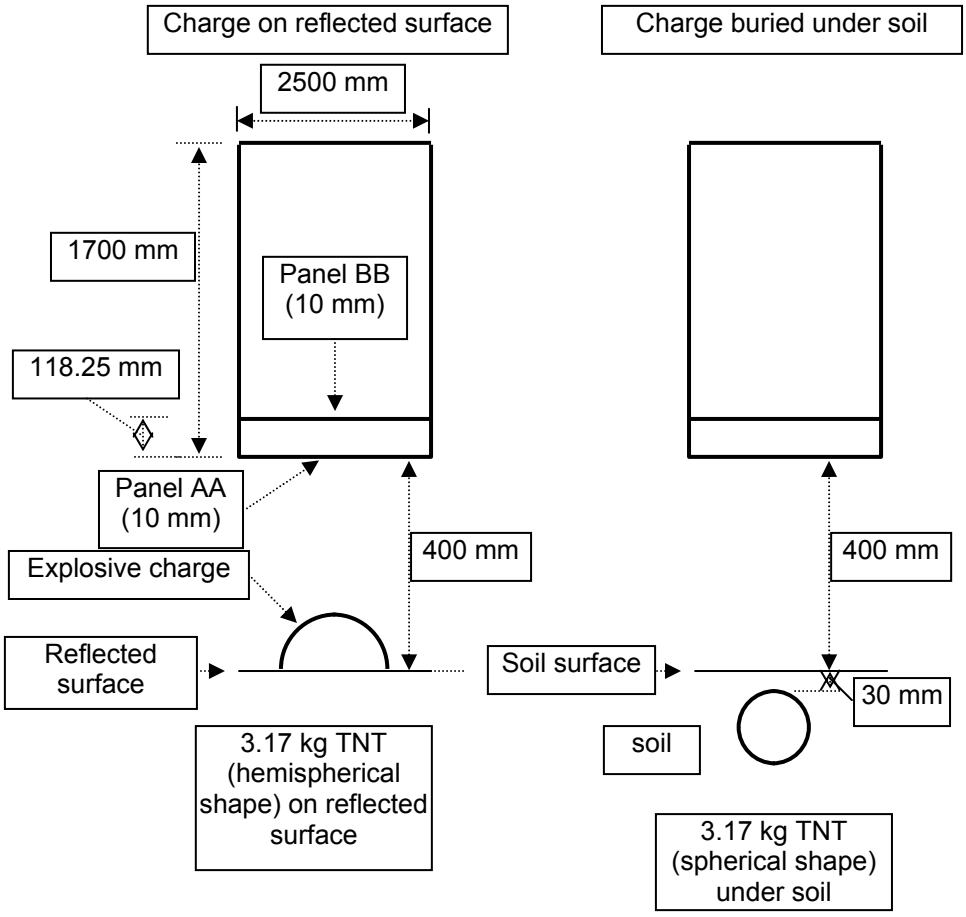

Figure 7.16 Schematic drawing of double-floor hull models subjected to 3.17 kg TNT on a reflected surface and 3.17 kg TNT buried 30 mm from the soil surface.

7.5.4 Double-floor hull results

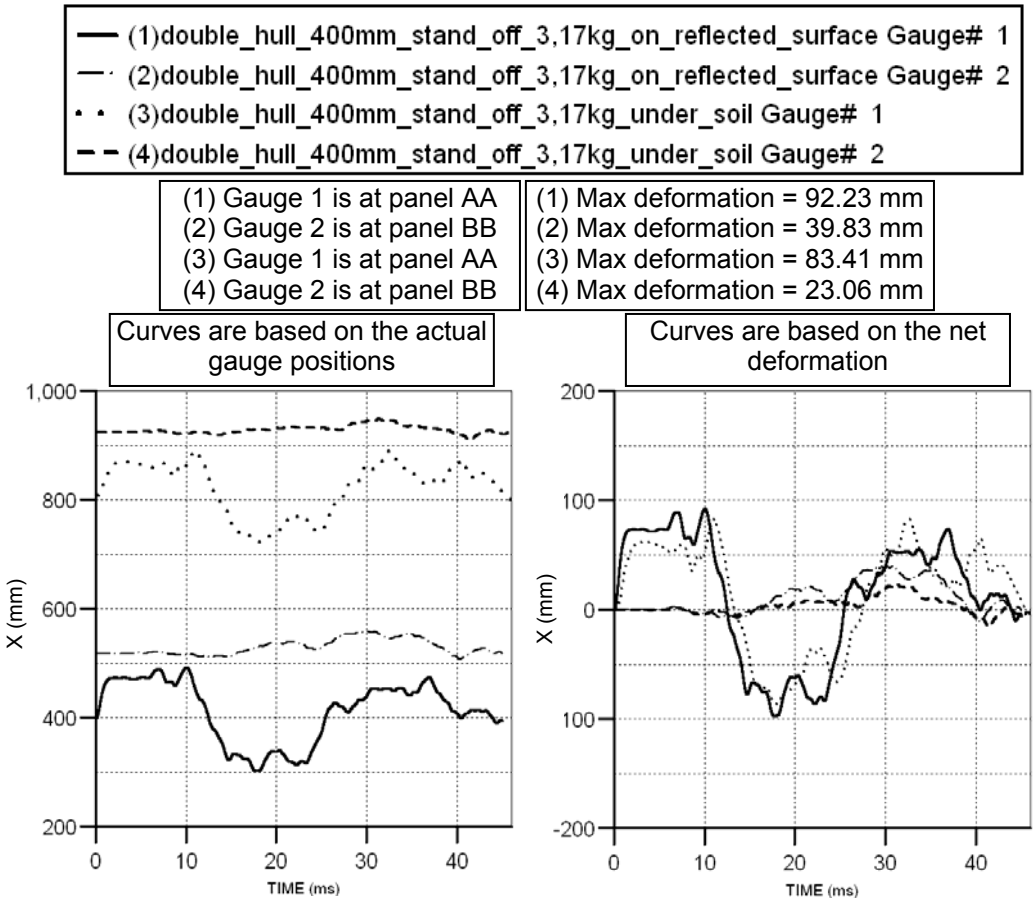

Figure 7.17 Deformation results of double-floor hull models subjected to 3.17 kg TNT on a reflected surface and 3.17 kg TNT buried 30 mm from the soil surface.

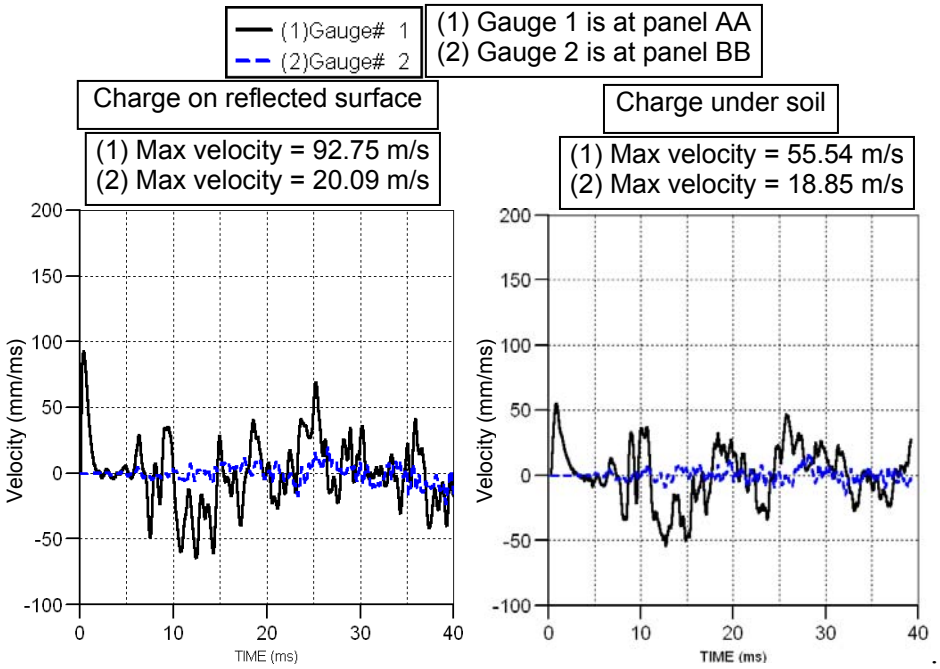

Figure 7.18 Velocity results of double-floor hull models subjected to 3.17 kg TNT on a reflected surface and 3.17 kg TNT buried 30 mm from the soil surface.

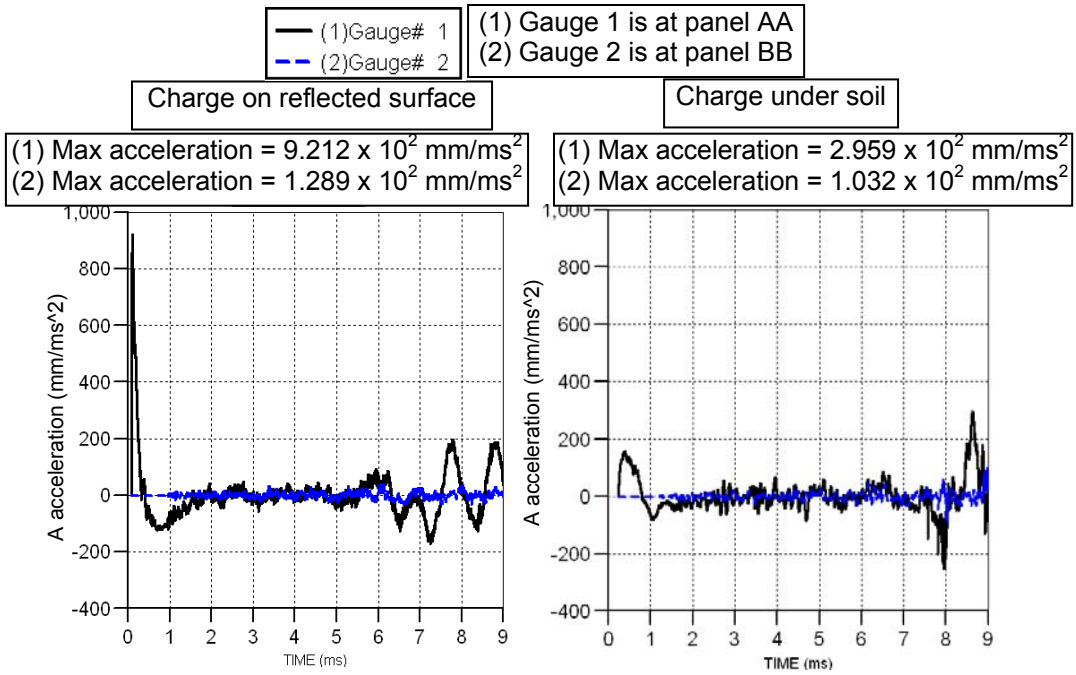

Figure 7.19 Acceleration results of double-floor hull models subjected to 3.17 kg TNT on a reflected surface and 3.17 kg TNT buried 30 mm from the soil surface.

7.5.5 'Structural models' discussion

In section 7.5.1 and 7.5.2, the blast loadings from the buried charge in the soil and the charge on the reflected surface were applied onto the single plate. The maximum deformation, velocity, and acceleration from the soil case are 5%, 41%, and 71% lower than the reflected case, respectively. This is in agreement with the double-floor hull model where a reduction of 10%, 40%, and 68% in maximum deformation, velocity, and acceleration on panel AA are observed in Figures 7.17 – 7.19. Based on these results, it can be said that, by using the multi-materials remap method, the analysis in Chapter 5, and 6, which used the blast loading from an explosive charge of an hemispherical shape placed on a reflected surface, is an alternative to the case where the explosive charge in spherical shape of the same weight is buried under 7.7% moisture content soil at 30 mm from the ground surface. This is in agreement with the literature review in Chapter 3, where Randers-Pehrson and Bannister (1997) indicated that surface detonation of an hemispherical charge can be used as an alternative to the case of a mine buried to the depth of 5 – 20 cm (Although in this Chapter, the mine is buried at 30 mm). It must be stressed that the new soil model, which was developed in AUTODYN 2D, was validated with the experimental results from Defence Research and Development Canada- Suffield (DRDC-Suffield), as shown in Fiserova (2006). However, an AUTODYN 3D structural (such as a single plate) model subjected to a buried explosive charge below the new soil model where an explosive, soil, and air are modelled as Eulerian elements using the multi-materials remap method, has not been validated with the experimental results. Also, it has not been compared directly with the other modelling techniques, such as, modelling soil as Lagrangian elements, which was used by Fairlie and Bergeron (2002), the results of which showed an increase of 125% in the whole pendulum target velocity (rotated about a pivot point) when using a buried charge instead of a bare charge on a rigid surface at 400 mm from the target, although, the details on the depth of burial, soil parameters and charge shape of this result were not shown. It is possible that the multi-materials remap method used in this chapter may give lower results when it is directly compared with the experiment and the other methods. In addition, the comparison of blast loading in this Chapter is only for a particular case of an explosive charge buried at 30 mm below the ground to the nearest charge surface, under 7.7% moisture content cohesive soil. Other

configurations may give different results. For example, it is likely that, if the moisture content in soil is increased more than 7.7%, the blast loading will increase. US Department of the Army (1985) stated that wet soil usually produces larger crater, and hence more ejecta is generated than dry soil. At shorter stand off distances, ejecta may influence more on the target. An optimum depth of buried will provide the maximum amount of ejecta, which may give a greater effects.

7.6 Conclusions

This chapter has compared the blast loading from a buried spherical charge under soil to the blast loading from an hemispherical charge on a reflected surface of the same weight (mass), which was used in Chapter 5 and 6 by using multi-materials remap method. The results showed that, in this configuration, the blast loading from a buried charge gives lower maximum deformation, velocity, and acceleration on the structure than the blast loading from the charge on a reflected surface. Based on the results, the blast loading used in Chapter 5 and 6 may be considered as an alternative to the blast loading from a buried charge at 30 mm from the 7.7% moisture content cohesive soil surface.

The implementation of the new soil model, which accounts for the effects of different soil moisture contents, using multi-materials remap method was carried out for the first time. The soil model has already been validated with the experimental results; however, the structural response result has not been validated with the experimental results or compared with the other techniques.

CHAPTER 8 Further discussion

This chapter discusses important points, which have not been discussed in the previous chapters.

This thesis has demonstrated the use of numerical analysis as a tool to investigate the effect of having different vehicle configurations. Numerical analysis has advantages and disadvantages in comparison to the full-scale experiment. Firstly, it gives designers the flexibility to perform different analyses as many as required to find the optimum solution. This is unlikely to happen in the full-scale experiment, which consumes high resources in terms of time and finances. Numerical analysis can provide straightforward time-history data of different parameters whereas the experimental measurement is very expensive, difficult to perform, and its equipment may be destroyed during the test. However, numerical analysis is not designed to solely replace the experiment, but to reduce the number of experiments. Experimental results are still necessary to calibrate the numerical results because numerical analysis is usually based on assumptions. It is also a requirement in numerical analysis to have sufficient computing resources together with the required software.

In this thesis, bare charges of hemispherical and spherical shapes were assumed to represent AT mines. In reality mines have their charge arranged in different shapes depending upon design and hence provide different effects. Further research could be conducted to account for the mine casing and other possible fragments, so that the effects of fragmentation are evaluated. Several mines might be chosen, which are present in the terrain of a particular country where the mine-protected vehicle is expected to be used. In this way, the vehicle will be designed according the threat it faces.

Different modelling techniques of LS-DYNA with CONWEP, AUTODYN 2D, AUTODYN 3D with remap, and AUTODYN 3D multi-materials were compared and used in this thesis. LS-DYNA with CONWEP method is relatively fast compared to the others but its limitations allow it to be used only in certain cases. Its blast loading from CONWEP is derived empirically, which is based on some assumptions and estimations. In some cases, it extrapolates the load curve in order give the blast load at certain distance. The CONWEP

blast loading model does not take into account the depth of burial, soil moisture content, soil particles, confinement or tunnel effects, the shape of the explosive charge, effect of shadowing objects, and requires explosive contents to be expressed in TNT equivalent mass. AUTODYN 2D takes a relatively shorter time to analyse, and the mesh density can be finer with less time penalty comparing with AUTODYN 3D. However, unlike LS-DYNA with CONWEP and AUTODYN 3D, modelling in two dimensions is restricted to axis-symmetric and planar-symmetric models only. This can make results deviate from the experimental results as shown in Chapter 4. Modelling with AUTODYN 3D multi-materials straight away allows more flexibility with similar results but require a lot of time and computational resources because it needs to calculate further the interaction between different materials and their couplings with the structure. It allows different Eulerian materials to be modelled together. The computational time can be made shorter by modelling in AUTODYN 2D first and then remapping into AUTODYN 3D multi-materials. For example, in Chapter 7, a blast load from a buried charge under soil was remapped into AUTODYN 3D multi-materials; this is not possible in AUTODYN 3D remap method, which restricts to single Eulerian material. AUTODYN 3D remap needs a blast load from AUTODYN 2D multi-materials model which unlike AUTODYN 3D multi-materials model, can have finer meshes with less time penalty. The blast load is then remapped onto AUTODYN 3D single material, which does not need to calculate the interaction process between Eulerian materials. This speeds up the running time enormously. However, it assumes that the mixture of explosive and air just before it is remapped behaves like an ideal gas in order to be able to remap into AUTODYN 3D single material. Because of this reason, the result of a single plate model at 300 mm stand off distance in Chapter 5 was not in the same trend as the others. Therefore it is not suitable for very small stand-off distances. The method of using AUTODYN 2D multi-materials and remapping into AUTODYN 3D multi-materials (multi-materials remap method) was used when modelling a structure subjected to a mine blast from a buried charge in soil as in Chapter 7. This method would also have been used in Chapter 5 and Chapter 6. However, the analysis would be slower than the method of using AUTODYN 2D multi-materials and remapping into AUTODYN 3D single material (AUTODYN 3D remap method) because the computer must calculate the interaction between soils, charge, and air Eulerian materials in addition to the interaction between Shell and Eulerian elements in AUTODYN

3D. The remap process itself requires much more computational resources in order to store and process these additional data and for large models with fine meshes, the complexity may cause the computer to crash. In addition, this multi-materials remap method should be directly compared with the available experimental results. The other modelling techniques to implement the new soil model should also be developed and compared. This will allow the new soil model, which accounts for different moisture contents, to be used in the soil-related applications, such as an effect of a buried charge to the full-scale vehicle or building.

In Chapter 6, different 'double-floor hull' models were used to try to avoid the impact between panel AA and BB. High acceleration was observed during the impact. This is undesirable in the vehicle because the high acceleration at the crew compartment floor can transfer to the occupants through their feet and seats and may cause death or injury. Williams and Fillion-Gourdeau (2002) used head and pelvis injury criterions, from Alem (1996), acquired using a Hybrid III Anthropomorphic Test Device (ATD), which represented a human body. Acceleration of 150g (~ 1472 m/s^2) for 2 ms at the head is a high risk to brain damage, while acceleration of 40g (~392 m/s^2) for 7 ms at the pelvis is a high risk to spinal cord damage. Although the work in this thesis did not cover the analysis of the vehicle's crew, it is possible that the high acceleration caused by the impact between both floor panels can transfer to the occupants and cause death or injury. The impact between both floor panels may also accelerate loose items within the crew compartment to propagate and behave as high velocity projectiles, which could cause death or injury to occupants. In addition, the impact can cause high stress at panel BB, which can be shown in Figure 8.1.

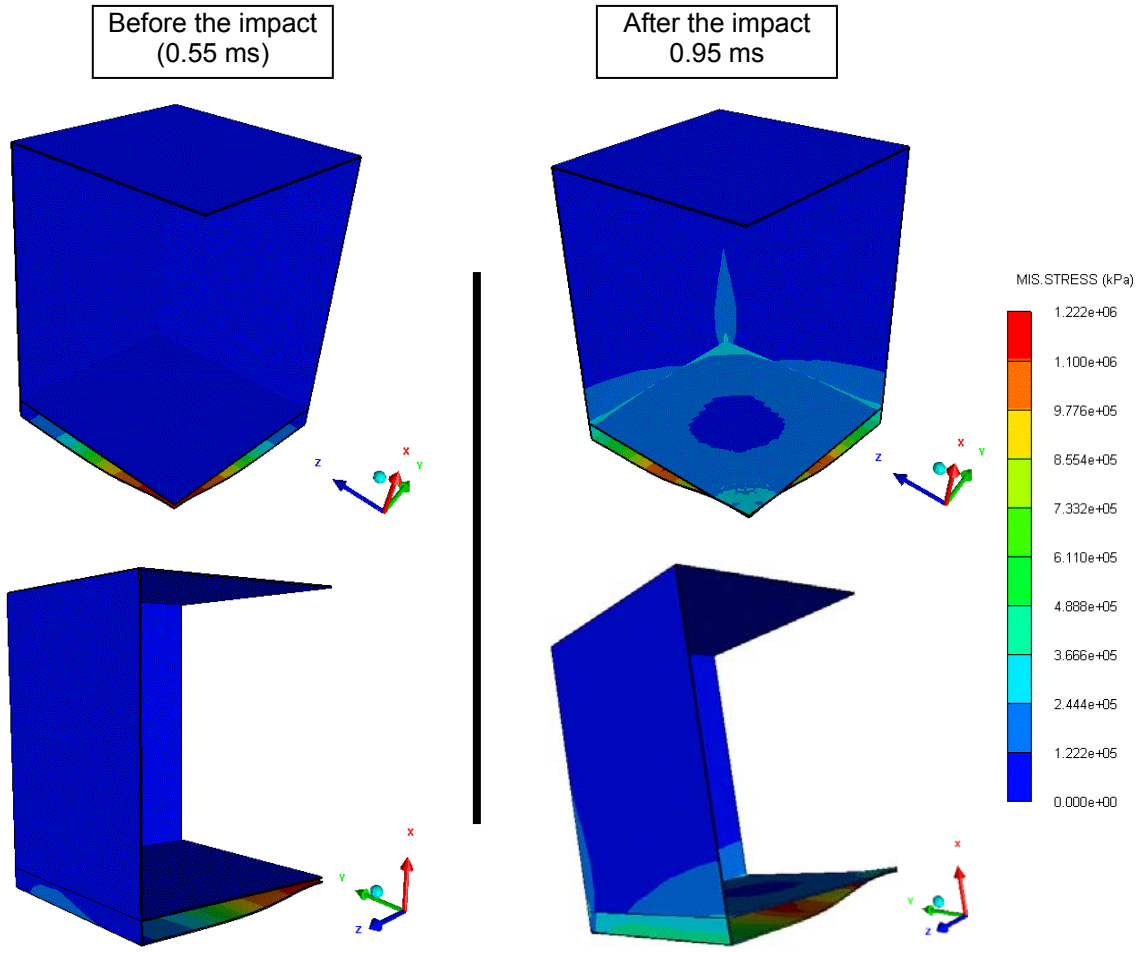

Figure 8.1 Stress contour plot of case 2 in Chapter 6 (¼ symmetric model)

Case 2 and case 1 in Chapter 6 are the worst ‘single-floor hull’ and ‘double-floor hull’ cases used in this thesis because of the amount of charge (10 kg TNT in an hemispherical shape) and the stand off distance (400 mm). Figure 8.2 and Figure 8.3 shows the effective plastic strain plot after 84 ms. Although a principal stress/strain failure model was applied to the vehicle structure, the stress and strain was not high enough to cause failure. However, in some areas, the plastic strain occurred. In the ‘single-floor hull’ model (case 1), at 84 ms, the maximum plastic strain of 0.137 occurred at point S1, while in the ‘double-floor hull’ model (case 2) the maximum plastic strain of 0.064 occurred at point D1. It is evident in both cases that the plastic deformation regions are at the middle of both floor panels (when it is viewed in full model), at the corners, and around the joint areas. In reality, each panel may be welded together as opposed to be rigidly joined together in the numerical model. It is possible that in reality panel AA may tear away from the side panels because of the welded joint was not as strong as in the numerical model.

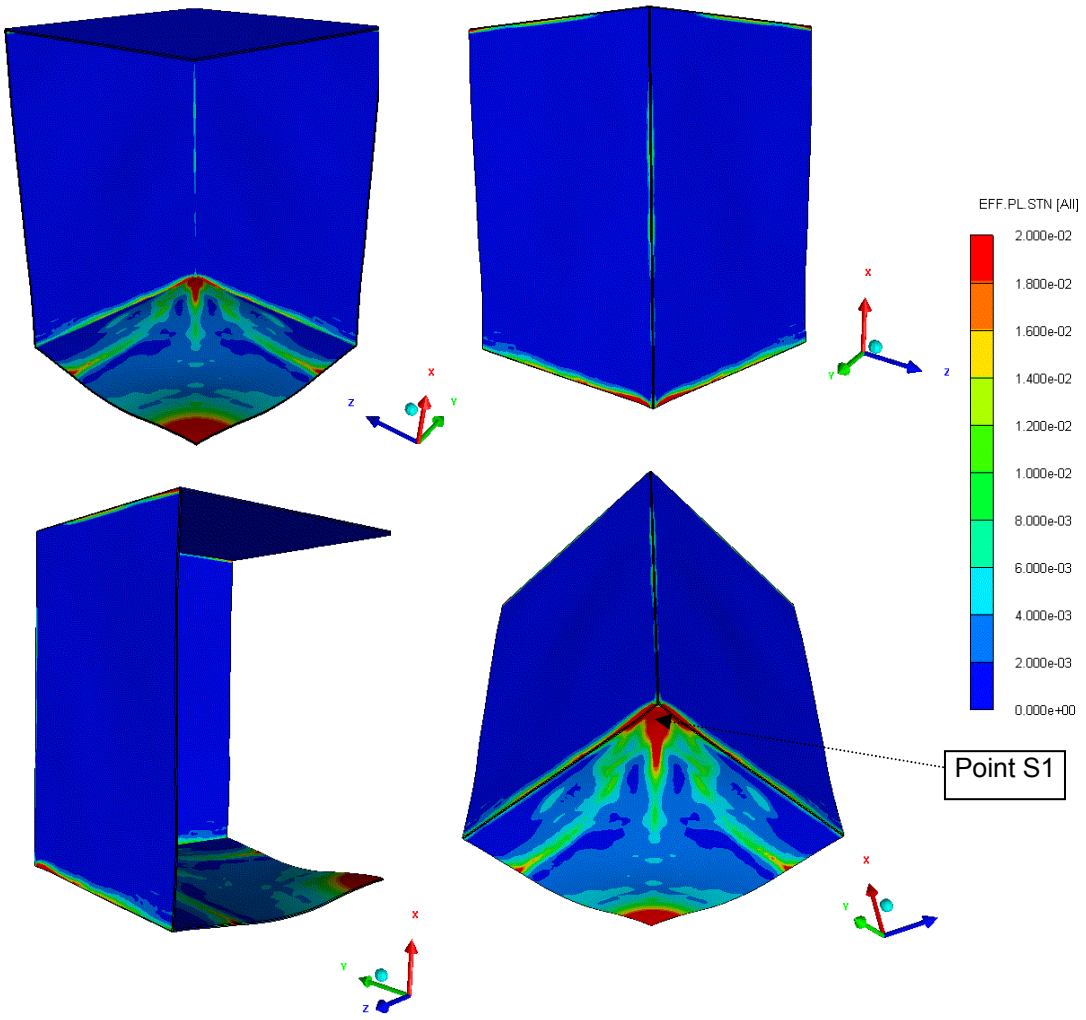

Figure 8.2 Effective plastic strain contour plot of case 1 in Chapter 6 at 84 ms (¼ symmetric model)

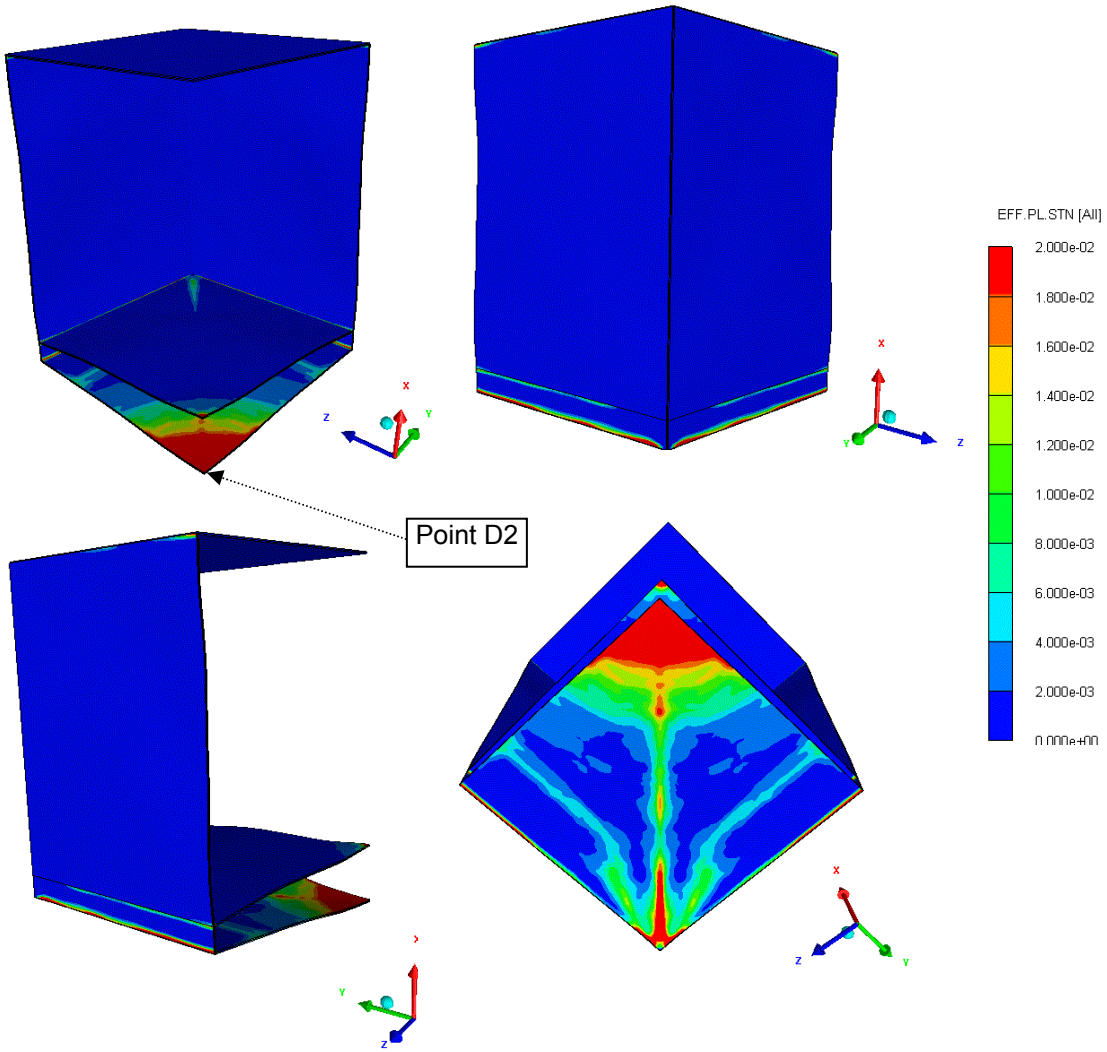

Figure 8.3 Effective plastic strain contour plot of case 2 in Chapter 6 at 84 ms (¼ symmetric model)

Comparison between various models, 'single-floor hull', 'double-floor hull', and 'V bottom', were done and discussed in Chapter 6. Considering the crew compartment floor (panel BB) as the point of interest, at the same vehicle mass (weight), stand off distance at panel BB, and vehicle hull height, 'double-floor hull' model gave less deformation, velocity, and acceleration than the 'single-floor hull' model when the impact between both floor panels was avoided. It is thought that the difference between the 'single-floor hull' model and 'double-floor hull' model due to panel BB in the double-floor system did not receive the blast loading directly but rather due to the compressed air inside the gap. In addition, panel BB has acted as a stiffener on the side panels, which reduced the z-

deformation at the side panels. This can be seen at the comparison at gauge xy2 between case 10 and case 22, as shown in Figure 8.4 and Figure 8.5, where the maximum deformation in z-direction in case 10 is ~ 15 mm, while the maximum deformation in case 22 is ~ 0 were observed. Likewise, the 'V bottom' hull model, which has two floor panels, also possesses the same advantages as the 'double-floor hull' model. In addition, the results and discussion in Chapter 6 also showed that, although the 'V bottom' hull model was at a shorter distance from the blast, the reflected pressure started to be less than the 'double-floor hull' and 'single-floor hull' models at 400 mm from the tip of the 'V'. This was due to the explosive mixture was deflected sideway. This finding was further supported by the theory in Chapter 3, where Smith and Hetherington (1994) and US Department of the Army (1991) has shown that, at the same stand off distance, the reflected pressure at 10° angle of incidence is always less than the one at 0° angle of incidence. The idea of using spaced plates in the form of double-floor hull model in this thesis was also previously used in protection against firearms, which was mentioned in US Department of the Army (1985). It described the disadvantages that additional material is required to keep the plates separated and to maintain structural strength, and the first plate may be made ineffective by repeated attacks. In blast protection application, it is possible that if panel AA is damaged and made ineffective, panel BB (crew compartment floor) will be vulnerable because of its direct path to the blast load and the possible impact from panel AA. In this thesis, each panel was rigidly joined together, where in reality, it may be welded together, which may weaken the structural integrity.

The 'V bottom' hull model seemed to be better than the 'double-floor hull', and 'single-floor hull' models respectively. However, this numerical analysis, which concentrates on its protection against mine blast, is only one part of the vehicle design process. In reality, vehicle designers may need to take other requirements into consideration, for example, the total vehicle mass (weight), payload, numbers of crew inside, vehicle speed, protection against small arms, protection against artillery shells, protection against Nuclear, Biological, and Chemical (NBC) threats, its firepower, manufacturing methods, budget, time, etc.

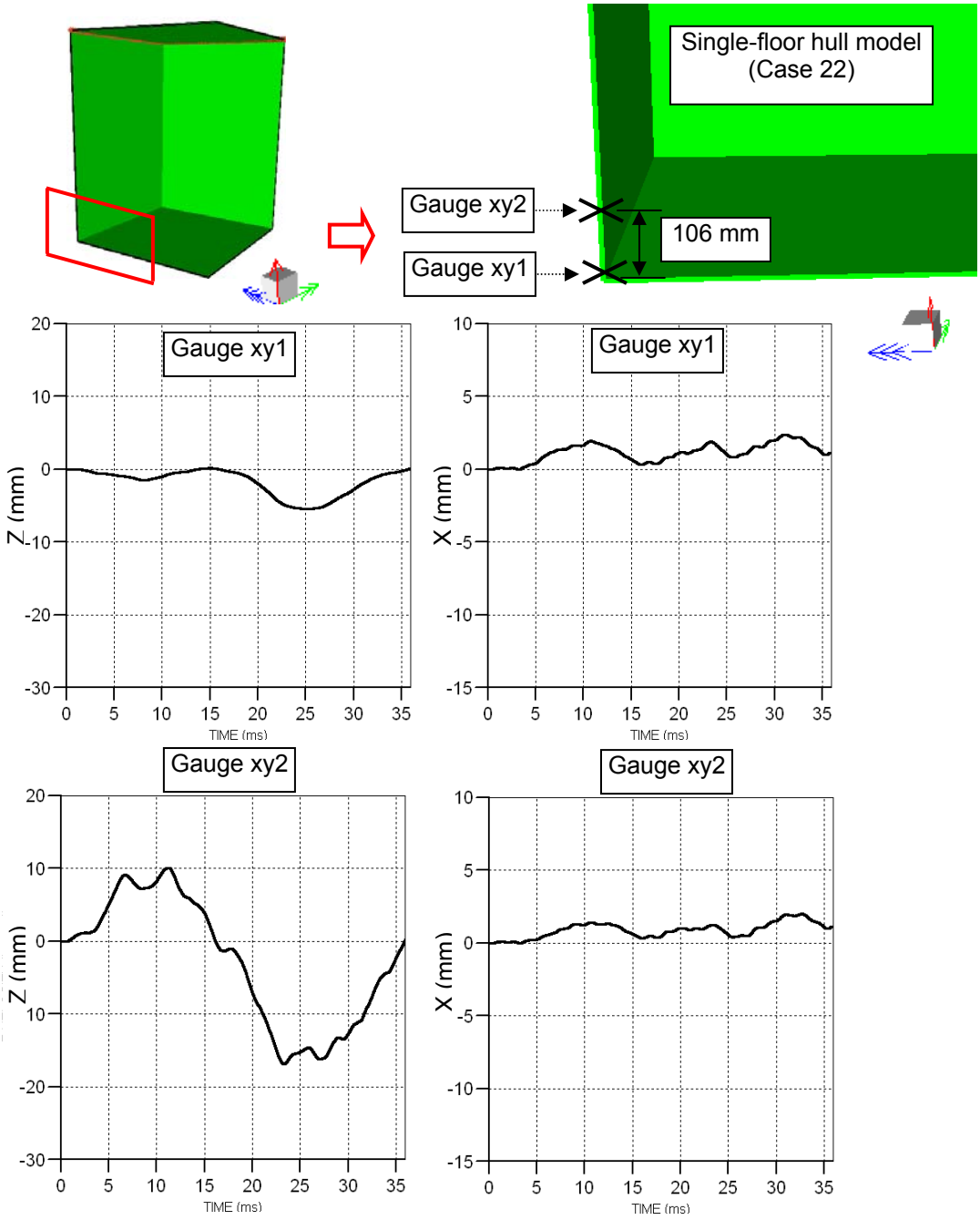

Figure 8.4 Deformation on xy-side panel in case 22 (deformation curves are based on the net deformation)

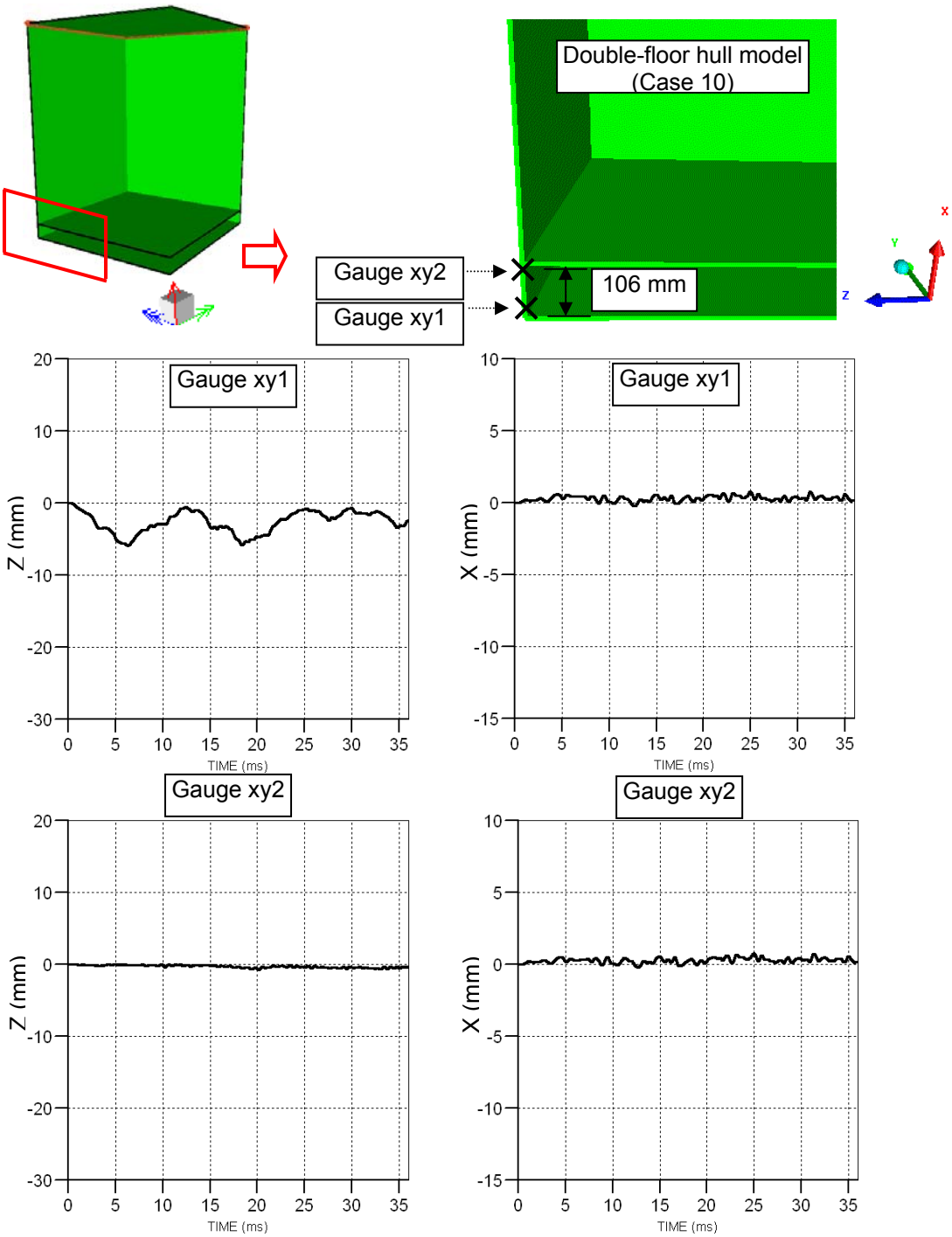

Figure 8.5 Deformation on xy-side panel in case 10 (deformation curves are based on the net deformation)

The models developed in this thesis are based on some assumptions, which are different from the real scenario. For example, in this thesis, each panel was rigidly joined together, while in reality it may be welded together. The works in this thesis focused on the local effects at the vehicle bottom, which was constrained from moving at its top edges (panel CC) while in reality, this is not fixed and the vehicle is allowed to move or overturn. The work does not include global effects, such as the movement of the vehicle which will affect the analysis. The vehicle hull model used was only a structural model, which did not include its engine, gears, suspension system, structural support system, etc. The explosive charge used was a bare hemispherical charge on a reflected surface, This gives similar effects to a buried charge under cohesive soil (fine particle) having 7.7% moisture content, as shown in Chapter 7. In reality, the nature and moisture content of the soil may be different. The multi-materials remap method still needs to be validated with the experimental results and other modelling methods. It is possible that this multi-materials remap method may give comparatively lower structural response results. Further investigation on this method should be carried out. Based on these assumptions, the nature of mine blast, the validated results in Chapter 4, and the comment by Vulitsky and Karni (2002), which mentioned that explosion prediction in many literatures may give discrepancies up to 100% and even higher with respect to the test data, it is possible that the analysis in Chapter 5, 6, and 7 may be 100% difference from the actual experimental data of the same configuration.

Although in Chapter 6, the vehicle model is changed into various configurations in order to avoid the impact between both floor panels, the 'working' vehicle model may not be useful in reality because of the vehicle requirement constraint. For example, the gap between the two floor panels, which was extended, may be too large because the crew compartment space is reduced. Likewise, the increase in thickness at panel AA or BB may result in too much weight increase. A combination of different geometries may also provide the suitable alternative solution given the same constraint. For example, the vehicle may combine its maximum gap allowance with increasing thickness.

Chapter 6 has shown that a vehicle with a double-floor setting is better than a single-floor setting provided that the bottom panel (panel AA) does not impact with the crew

compartment floor (panel BB). Based on the analysis in this thesis, it is estimated that a plain double-floor vehicle having 10 mm armour panels at both floor panels may withstand an AT mine having a charge weight up to 3.17 kg TNT at 400 mm stand off distance without incurring the undesirable high acceleration. By increasing the thickness at the bottom panel (panel AA), increasing the gap distance, and changing the bottom panel into the 'V' shape, it is possible that the vehicle is able to withstand higher charge weight. However, this estimation may represent the case where the explosive charge is buried at 30 mm from the cohesive soil surface having 7.7% moisture content. Different depth of buried, and soil properties may give different results. Further works should be done to provide soil parameters of different moisture contents, other than the soil with 7.7% moisture content. Further numerical simulations should also include effects of soil particle sizes, stand off distances (from a buried charge under soil), amount of charges, depth of buried, etc.

In this thesis, the vehicle models were a single-floor with horizontal flat bottom, double-floor with horizontal flat bottom, and double-floor with 'V' bottom (10 degree angle from the horizontal axis). The estimated vehicle configurations and dimensions were based on a limited vehicle data available in the public domain. In reality, each vehicle is unique and its configuration may be different. For example, a vehicle may have a combination of two 'V' shapes in one vehicle or it may contain attenuation materials within the internal space. It is also necessary to obtain the actual vehicle details, for example, its dimension, panel thickness, how each panel is joined, support structures, total mass (weight), etc. In order to be as accurate as possible all materials should be tested in the laboratory so that all parameters are defined. For example, RHA material may be tested to provide Johnson and Cook parameters. In addition, the model may include wheels (or tracks), engines, suspension system, gun system, etc. This will allow the numerical model to be developed as close to the actual vehicle as possible.

For numerical simulations of a large vehicle, the limitation of computational resources becomes obvious. Some attractive techniques need to be developed. The problem must be reduced to a symmetric model and divided into stages. For example, the first stage may be a blast load generation stage, where a buried charge in soil, developed in AUTODYN 2D

multi-materials with fine mesh is allowed to progress up to a point very close to the vehicle. The second stage may involve an initial blast interaction stage where blast load is remapped into AUTODYN 3D. The Eulerian elements of air, soil and explosive may be removed once the blast load has fully interacted with the vehicle and the numerical simulation may be remapped into a coarser mesh. In addition, the computer needs to a have large enough memory. The model should be as close to the actual vehicle geometry as possible. It might be imported from 3D modelling software into mesh generation software and into AUTODYN. In reality some parts of the vehicle may be welded together, so research into the effects of welding on the strength of the vehicle may be useful instead of assuming that it is rigidly fixed together.

Further research into the use of shock absorbing/attenuating materials in the gap between the double floors of the vehicle should be carried out. This could provide a method of reducing the blast effects. Experiments and numerical simulations may be conducted on this topic although it is more complex than using simple steel structures. Research should investigate whether the materials can be integrated with the vehicle bottom and can actually reduce the blast effects because it is possible that the response of these materials is too slow in response to the blast load interacting with the structure to have any attenuating effect. Also the questions remain whether it is physically viable to contain these materials within the gap.

This thesis does not contain new mine blast experiments for several reasons. Firstly, the available experimental results seemed to be sufficient. Secondly, the nature of mine blast experiment consumes high resources. It is extremely difficult to achieve the required results with accuracy and consistency to a degree that one would like. Based on a two day experience by the author setting up mine blast experiments (which involved two horizontal steel plates), there are many different factors that can influence the results. The amount, shape, location, and depth of charge might be different each time the experiment is performed. The compaction and the composition of the soil might change. Environmental factors such as temperature and rain are uncontrollable, which all is making it difficult to perform repeatable experiments. The rig must be manufactured to the desired geometry. The materials of the target might need to take time to order and manufacture. High quality

measurement equipment is needed and suitably matched to the amount of blast load. The range needs to be booked and authorised in advance. The range may have limitations on the maximum amount of charge that can be used. It may take 6 months for an inexperienced researcher to plan these tests. So it is strongly recommended that experiments should be planned and organised as much in advance as possible by highly experienced technicians. These will minimise the chances of something going wrong at the range and hence provide the required results with as minimum resources as possible.

CHAPTER 9 Conclusions

This chapter highlights the work that has been done for this thesis. The contributions arising from the thesis are also presented.

Research in mine-protected vehicles is normally classified within commercial companies. It is difficult to know how much progress and activities in this research area have been carried out. Some companies do choose to publish their works at conferences. Their works may involve different groups of researchers concentrating on different parts of the research area. This thesis, which has been conducted by one researcher, aimed to fill a gap in the published research by focusing on vehicle bottom structures. This thesis aimed to develop validated numerical simulations of vehicle bottom structures subjected to anti-tank (AT) mine blasts in order to assess their effects without the need of conducting full-scale experiments. Throughout the thesis, the aim has been achieved.

This thesis has made several contributions to knowledge in the research area. Extensive research on AT mines, which were likely to cause damage to vehicles and their occupants has been carried out and arranged mines into different categories using various criteria. As there are so many mines that could cause damage to vehicles and their crews, this thesis has formulated its own criteria based on different literatures in order to classify them. The results were transformed into the percentage form and graphical display for ease of understanding. The present threat from mines can now be identified. It has indicated that the present threat to vehicles depended mainly on first generation blast mines having full width attack capability with a definite deployment pattern and a charge weight up to 10 kg TNT. This thesis has found that 58% of mines are blast mines instead of the 80% figure which was previously quoted in some literatures, such as in Ogorkiewicz (2003). Some of this work was written and accepted for the future publication in the ARMOR magazine.

Different methodologies from two widely used software, LS-DYNA and AUTODYN, were tried and compared together with the experimental results in the form of single and double plate structure subjected to an exploding charge in the air which represented a mine without casing. Results seemed to be comparable with experimental results, especially further from the blast. These are good results considering the nature of mine blast experiments that

contained so many variables. These results illustrate the advantages and disadvantages of these methods, and are detailed in this thesis. Part of this work has been published in Showichen *et al* (2005).

The development of a vehicle hull model has made a contribution by demonstrating that, to model a vehicle with double floor setting, it must be modelled in 'double-floor hull' instead of 'box' geometries. This will allow the numerical simulation to capture the impact between both floor panels, which creates undesirable high acceleration. In case where there is no impact between both floor panels, the results show that the upper floor panel deforms mainly because of the compressed air inside the gap. The results also indicate that at the distance too close to the blast, numerical modelling using AUTODYN remap method gave comparatively lower results from the trend. This is due to the assumption that the mixture of explosive and air behaves as an ideal gas.

Chapter 6 has made several contributions. It investigated the effects of mine blast on various vehicle hull configurations. This, effectively, has demonstrated the advantage of using numerical method in finding the suitable vehicle configuration instead of performing numerous full-scale experiments. The results showed that in cases where the impacts between both floor panels were avoided, a vehicle with double-floor setting was better than a vehicle with single-floor setting of the same mass (weight). As the stand off distance, and/or the plate thickness (panel AA), and/or gap distance was increased the effects were reduced, while as the amount of explosive charge was increased, the effects were also increased. The results indicated that increasing the thickness at panel AA is the better option to avoid the impact between both floor panels than increasing the thickness at panel BB. Chapter 6 has made an additional contribution by comparing 'single-floor hull', 'double-floor hull' and 'V bottom' hull models. Although there is a trend to make the bottom of armoured vehicle a 'V' shape to reduce the blast load, numerical analysis in the published research such as Gupta (2003) has assumed a rigid structure. The results have shown that, the maximum dynamic deformation at the crew compartment floor in the 'V bottom' hull model is the least, although its maximum acceleration is more than the 'single-floor hull' model because of the slight impact between both floor panels. By using the techniques of increasing the gap and/or panel thickness to avoid the impact, it is likely that

the deformation and acceleration in the 'V bottom' hull and the 'double-floor hull' models will be less than the 'single-floor hull' model having the same mass (weight), respectively.

This thesis has shown the implementation of the soil model into numerical simulations of vehicle bottom subjected to buried charge in soil. These parameters which were formed and validated with the experiments by Fiserova (2006) were implemented into structural model analysis for the first time using multi-materials remap method in AUTODYN. It has demonstrated that the successful works by Fiserova (2006) can be expanded further into structural models. A comparison between a blast load derived from an hemispherical charge on a reflected surface was compared to a blast load derived from a spherical charge of the same mass (weight) buried under cohesive soil of 7.7% moisture content. Both blast loads were applied to single plate and 'double-floor hull' models at 400 mm stand off distance. The results showed similar curve trends in deformation, velocity, and acceleration. However, these structural response results and its implementation method need to be compared and validated with the experimental results and the other techniques.

Overall, the results and discussion in this thesis has certainly contributed to the knowledge in this area. In terms of personal benefits, the author has learnt so much from this work. He has spent some time studying a number of software packages for this work. LS-DYNA and AUTODYN were the main interests. Within LS-DYNA, there are FEMB pre-processor, ETA post processor, and LSTC pre/post processor which have to be understood for this work. He has learnt some fundamental skills in SOLIDWORKS for a possible geometry construction, although it was not needed. TRUEGRID was used as a mesh generator in 'single-floor hull', 'double-floor hull', and 'V' hull models and then imported into AUTODYN. These computer software packages can take some time to learn. The skills and knowledge in these software have given extra benefit to the author for future employment.

REFERENCES

ALEM, N. M., 1996. *Mine blast acceleration injury assessment: Methods, criteria and software*, Report no. 97-04, USA: U.S. Army Aeromedical Research Laboratory (USAARL).

ASHCROFT, P.S., 1999. *Is there a future for the anti-tank mine?* MA dissertation in Military Studies, Cranfield University.

BAKER, W.E., *et al*., 1983. *Explosion hazards and evaluation.* Amsterdam, Netherlands: Elsevier.

BIRD, R., 2001. Protection of vehicles against landmines. *Journal of Battlefield Technology*. 4, 1 (March 2001), 14-17.

BOYDS, S. D., 2000. *Acceleration of a plate subjected to explosive blast loading-trial results*, DSTO-TN-0270. Australia: Defence Science & Technology Organisation, March 2000.

BRODE, H. L., 1955. Numerical solution of spherical blast waves. *Journal of Applied Physics.* No.6 (June 1955).

CENTURY DYNAMICS INC, 2003. *AUTODYN theory manual revision 4.3*. California, USA.

CENTURY DYNAMICS INC, 2005. *What's new in AUTODYN version 5?* California, USA.

CHENG, Q.H., *et al*., 2002. Response of a box-like structure to near-by explosion. *International Symposium on Defence Construction 2002*, Singapore: April 2002

COLIN, G. S., 2002. *An introduction to hydrocode modelling*, unpublished lecture notes. Arizona, USA: The University of Arizona, August 2002. Available at: <URL: http://www.lpl.arizona.edu/~gareth/publications/sales_2/download/intro.pdf.

DOBRATZ, B.M., and CRAWFORD, P.C., 1985. *LLNL explosive handbook: Properties of chemical explosives and explosive simulants*. Technical report UCRL-52997. California, USA: Lawrence Livermore National Laboratory, January 1985.

DOSQUET, F., PRIVSEK C., NIES, O., and GERWELER M, 2004. Test methodology for protection of vehicle occupants against IED. In *18th Military Aspects of Blast Symposium*, Bad Reichenhall, Germany, 2004.

DUMAS, S. and WILLIAMS, K., 2002. *Mine blast loading pre-processor for LS-DYNA*. QC, Canada: Defence R & D Canada- Valcartier.

ELLIOTT, C.L., MAYS, G.C., and SMITH, P.D., 1992. Protection of buildings against terrorism. *Proceedings of the Institution of Civil Engineers-Structures and Buildings*. 94, 3 (August 1992), 287-297.

ENDEVCO CORPORATION, 2006. *Product models search* [online]. Available at: <URL: http://www.endevco.com> [accessed 27 May 2006].

ENGINEERING TECHNOLOGY ASSOCIATES INC., 2001. *ETA/FEMB-PC user manual version 27*. Michigan, USA: September 2001.

FAIRLIE, G., 2003. Numerical simulation of combined blast and fragment loading on structures. In *11th International Symposium on Interaction of the Effects of Munitions with Structures*, Mannheim, Germany, May 2003.

FAIRLIE, G., and BERGERON, D., 2002. Numerical simulation of mine blast loading on structures. In *17th Military Aspects of Blast Symposium*, Nevada, USA, June 2002.

FISEROVA, D., 2006. *Numerical analyses of buried mine explosions with emphasis on effect of soil properties on loading*. Ph.D. thesis, Cranfield University.

FISEROVA, D., *et al*, 2004. Evaluating numerical approaches in explosion modelling using a surface-laid mine. *Journal of Battlefield Technology*, 7-2 (March 2004), 1-5.

FOSS, C. F. ed., 1999. *Jane's armour and artillery: 1999 – 2000*. Great Britain: Jane's Information Group Limited. Also available at: <URL: http://jaa.janes.com >

FOSS, C. F. ed., 2000. *Jane's armour and artillery: 2000 – 2001*. Great Britain: Jane's Information Group Limited. Also available at: <URL: http://jaa.janes.com >

GAUDREAULT, P., BOUAMOUL, A., DUROCHER, R., and ST-JEAN, B., 2005. Finite element modelling of light armoured vehicle welds heat affected zone subjected to an anti-vehicular blast landmine loading, a summary of the numerical model and field experiment. *In: 22nd International Symposium on Ballistics*, Vancouver, Canada: November 2005.

GENSON, K., 2006. *Vehicle shaping for mine blast damage reduction*. MSc thesis. University of Maryland.

GRAY III, G. T., *et al*, 1994. *Constitutive equations for annealed metals under compression at high strain rates and high temperatures.* LA-12669-MS. New Mexico, USA: Los Alamos National Laboratory, January 1994.

GUPTA, A. D., 2001. *Modelling and analysis of a 3-D asymmetric mine-soil-hull floor interaction problem with mine buried in dry and wet sand,* ARL-RP-29. MD, USA: U.S. Army Research Laboratory, Aberdeen Proving Ground, September 2001.

GUPTA, A. D., 2003. *Effect of hull bottom shapes on mine-blast loading from detonation of an explosive on a rigid surface*, AMSRL-WM-TB. MD, USA: U.S. Army Research Laboratory, Aberdeen Proving Ground, September 2003.

HALLQUIST, J., 1998. *LS-DYNA theoretical manual v970*. California, USA: Livermore Software Technology Corporation, May 1998.

HLADY, S. L., 2004. Effect of soil parameters on landmine blast. *In: 18th International Symposium on the Military Aspects of Blast and Shock*. Bad Reichenhall, Germany, September 2004.

HELD, M., 1984. Anti-tank mines. *In: 4th International Seminar on Defence Technology, Rawalpindi-Pakistan, 1984*. (s.l.): (s.n.)

HENRYCH, J., 1979. *The dynamics of explosion and its use*. Development in civil engineering. Amsterdam, the Netherlands: Elsevier Science Publishers.

HYDE, D., 1991. *CONWEP: Conventional Weapons Effects Program.* Vicksburg, MS, USA: US Army Waterways Experimental Station.

JOHNSON, G., and COOK, G., 1983. A constitutive model and data for metals subjected to large strains, high strain rates and high temperatures. *In: 7th International Symposium on Ballistics*. Hague, Netherlands, April 1983.

KEVIN, B., 2006. *How landmines work* [online]. Available at: <URL: http://people.howstuffworks.com/landmine.htm> [accessed 11 May 2006].

KING, C., ed., 2002. *Jane's mines and mine clearance: Seventh Edition 2002 – 2003* [online]. Great Britain: Jane's Information Group Limited. Available at: <URL: http://jmmc.janes.com > [accessed 5 June 2003].

KING, C., ed., 2003. *Jane's mines and mine clearance: Eight Edition 2003 – 2004* [online]. Great Britain: Jane's Information Group Limited. Available at: <URL: http://jmmc.janes.com > [accessed 1 April 2004].

KING, C., ed., 2004. *Jane's mines and mine clearance: Ninth Edition 2004 – 2005* [online]. Great Britain: Jane's Information Group Limited. Available at: <URL: http://jmmc.janes.com > [accessed 5 February 2005].

KNIGHTS, M., 2005. *Jane's intelligence review: 1 November 2005* [online]. Great Britain: Jane's Information Group Limited. Available at: <URL: http://janes.com > [accessed 31 May 2007].

KINGERY, C. N., and BULMASH, G., 1984. *Air-blast parameters from TNT spherical air burst and hemispherical surface burst,* ARBRL-TR-02555. MD, USA: U.S. Army Ballistic Research Laboratory, Aberdeen Proving Ground, April 1984.

KINNEY, G.F., and GRAHAM, K. J., 1985. *Explosive shocks in air: 2nd edition*. USA: Springer-Verlag.

LANDMINE MONITOR EDITORIAL BOARD, 2002. *Landmine monitor report 2005: toward a mine-free world* [online]. Canada: International Campaign to Ban Landmines Annual Report. Available at: <URL: http://www.icbl.org/lm/2002> [accessed 5 January 2003].

LANDMINE MONITOR EDITORIAL BOARD, 2005. *Landmine monitor report 2005: toward a mine-free world* [online]. Canada: International Campaign to Ban Landmines Annual Report. Available at: <URL: http://www.icbl.org/lm/2005> [accessed 11 May 2006].

LEE, E., FINGER, M. and COLLINS, W., 1973. *JWL equation of state coefficients for high explosives.* UCID-16189. California, USA: Lawrence Livermore National Laboratory, January 1973.

MAYS, G.C., and SMITH, P.D., ed., 1995. *Blast effects on buildings*. Great Britain: Thomas Telford Publications.

MCGLAUN, J.M., THOMPSON, S.L., and ELRICK, M.G., 1990. CTH: A three-dimensional shock wave physics code. *International Journal Impact Engineering*, 10, 1-4, 351-360.

MUZYCHUK, E., MAYSELESS, M., and BELSKY, 2005. Influence of the post-detonation burning process on blast wave parameters in air. *In: 22nd International Symposium on Ballistics*, Vancouver, Canada: November 2005.

NGO, T., MENDIS, P., GUPTA, A., and RAMSAY, J., 2007. Blast loading and blast effects on structures- An overview. *Electric Journal of Structure Engineering*, Special issue 2007 (Feb 2007), 92 – 101.

NORTH ATLANTIC TREATY ORGANIZATION, 2004. *Protection levels for occupants of logistic and light armoured vehicles: NATO STANAG 4569 (Edition 1).* May 2004.

NORTH ATLANTIC TREATY ORGANIZATION, 2006. *Procedures for evaluating the protection level of logistic and light armoured vehicles: NATO AEP-55 (Volume 2 for mine threat, Edition 1).* September 2006.

OGORKIEWICZ, R. M., 2003. *Impact of mines on armoured vehicle design*. Shrivenham, UK: Survivability of light armoured vehicles course, Cranfield University, Oct 2003.

PIKE, J., 2005. *Improvised explosive device (IEDs)/ Booby traps* [online]. Available at: <URL: http:www.globalsecurity.org> [accessed 7 April 2008].

PCB PIEZOTRONICS INC., 2006. *Online product catalogue* [online]. Available at: <URL: http://www.pcb.com> [accessed 27 May 2006].

RIEDEL, W., WEBER, K., WICKLEIN, M., THOMA, K., and FARBER, J., 2004. Reduction of fragment effects behind layered armour experimental and numerical analysis. *In: 21st International Symposium on Ballistics*, Adelaide, Australia: 19 – 23 April 2004.

RANDERS-PEHRSON, G. and BANNISTER, K., 1997. *Airblast loading model for DYNA2D and DYNA3D*, ARL-TR-1310. MD, USA: Army Research Laboratory, Aberdeen Proving Ground.

SHARPLES, N., 2002. *Resistance of homogeneous spaced and honeycomb core sandwich panels to explosive blast.* MSc Project report. Swindon, UK: Cranfield University (RMCS Shrivenham), July 2002.

SHOWICHEN, A., et al., 2005. Simulation of plate structures subjected to Anti-tank mines. *Journal of Battlefield Technology*. 8, 1 (March 2005), 1-7.

SHOWICHEN, A., HAMEED, A., and IREMONGER, M.J. Anti-tank mines. *ARMOR magazine*. Accepted and scheduled to be published in future issue. Kentucky: U.S. Army Armor Center.

SLOAN, C. E., 1986. *Mine warfare on land.* London: Brassey's Defence Publishers.

SMITH, C., 1996. *The Military utility of landmines.* London: Centre for Defence and Studies, King's College, June 1996.

SMITH, P. D., and HETHERINGTON J. G., 1994. *Blast and ballistic loading of structure.* Great Britain: Butterworth-Heinemann Ltd.

THE U.S. DEPARTMENT OF STATE, 1998. *Hidden killers: the global landmine crisis.* Washington DC: Bureau of Political Military Affairs, Office of Humanitarian Demining Programs, September 1998.

U.S. DEPARTMENT OF THE ARMY, 1985. *Fundamentals of protective design for conventional weapons*, Technical Manual TM855-1.

U.S. DEPARTMENT OF THE ARMY, 1991. *Design of structures to resist the effects of accidental explosions*, Technical Manual TM5-1300.

UNITED NATIONS ASSOCIATION OF THE USA, 2002. *Landmine crisis* [online]. Available at: <URL: http://www.landmines.org/crisis > [accessed 5 January 2003].

UNITED NATIONS ASSOCIATION OF THE USA, 2006. *Landmine crisis* [online]. Available at: <URL: http://www.landmines.org/crisis > [accessed 11 May 2006].

VULITSKY, M., and KARNI Z., 2002. Ship structures subject to high explosive detonation. *In: 7th International LS-DYNA Users Conference.* Michigan, USA: Livermore Software Technology Corporation (LSTC) and Engineering Technology Associates (ETA).

WESTINE, P. S., *et al*., 1985. *Development of computer program for floor plate response from a land mine explosions*, Technical report no. 13045. MI, USA: US Army Tank-Automotive command.

WILLIAMS, J. R., 2000. Anti-tank landmines - the threat, *In: RMCS Symposium, 2000.* (s.l.): (s.n.)

WILLIAMS, K., and FILLION-GOURDEAU, F., 2002. Numerical simulation of light armoured vehicle occupant vulnerability to anti-vehicle mine blast. *In: 7th International LS-DYNA Users Conference.* Michigan, USA: Livermore Software Technology Corporation (LSTC) and Engineering Technology Associates (ETA).

WILLIAMS, K., and MCCLENNAN, S., 2003. *A numerical analysis of mine blast effects on simplified target geometries: Validation of loading models*, TM 2002-260. Valcartier, Canada: Defence R&D Canada- Valcartier.

WILLIAMS, K., and POON, K., 2000. *A numerical analysis of the effect of surrogate anti-tank mine blasts on the M113*, TM 2000-007. Valcartier, Canada: Defence R&D Canada-Valcartier.

XYZ SCIENTIFIC APPLICATIONS INC., 2001. *TRUEGRID manual version 2.1.0* California, USA: September 2001.

YOKOI, K., 2007. Efficient implementation of THINC scheme: A simple and practical smoothed VOF algorithm. *Journal of computational Physics,* 226-2 (1 October 2007), 1985 – 2002.

YOUNG, W.C., and BUDYNAS, R.G., 2002. Roark's Formulas for stress and strain, seventh edition, Singapore: McGraw-Hill, 2002.

APPENDIX A List of AT mines

Mine	FMK-3	PRB M3/M3A1	Type 72 (AT)	AT Mine	PT Mi-Ba-II
Country of origin	Argentina	Belgium	China, People's Republic	Cuba	Former Czechoslovakia
Type	AT blast mine	AT blast mine	AT blast mine	AT blast mine	AT blast mine
Weight (kg)	7.10	6.80	6.50	9.00	9.60
Explosive weight (kg)	6.10	6.00	5.40	8.00	6.00
Explosive type	TNT/RDX/wax	TNT/RDX/Al	TNT/RDX	TNT	TNT
Equivalent TNT (kg)	6.10	6.00	5.40	8.00	6.00
No. of countries used	1	10	9	3	5
Fuze options	AP mine	pressure fuze, anti-handling (PRB M3A1)	pressure fuze	pressure fuze	pressure fuze
Laying options	manual	manual or mechanical	manual or mechanical	manual	manual
Maximum attack capability	heavy armoured vehicle	heavy armoured vehicle	heavy armoured vehicle	heavy armoured vehicle	heavy armoured vehicle
Production status	continuing	stopped	continuing	continuing	stopped
Numbers on the grounds	n/a	n/a	n/a	among 70,000 landmines in Cuba	n/a
Mode of attack	track attack	track attack	track attack	belly attack	belly attack
Mode of initiation	first generation	first generation	first generation	first generation	first generation

Mine	PT Mi-Ba-III	PT Mi-D	PT Mi-K	FBM	M/71
Country of origin	Former Czechoslovakia	Former Czechoslovakia	Former Czechoslovakia	Egypt	Egypt
Type	AT blast mine	AT blast mine	AT blast mine	AT blast mine	AT blast mine
Weight (kg)	9.90	9.00	7.20	17.00	9.80
Explosive weight (kg)	7.20	6.20	5.00	13.00	6.25
Explosive type	TNT	TNT	TNT	TNT	TNT
Equivalent TNT (kg)	7.20	6.20	5.00	13.00	6.25
No. of countries used	4	1	6	1	2
Fuze options	pressure fuze, anti-handling device	pressure fuze, anti-handling device	pressure fuze, anti-handling	AP mine, pressure fuze	pressure fuze, tilt-rod fuze
Laying options	manual	manual	manual or mechanical	manual	manual or mechanical
Maximum attack capability	heavy armoured vehicle	heavy armoured vehicle	heavy armoured vehicle	heavy armoured vehicle	heavy armoured vehicle
Production status	stopped	stopped	stopped	continuing	continuing
Numbers on the grounds	n/a	n/a	n/a	n/a	n/a
Mode of attack	track attack	track attack	track attack	belly attack	full-width attack
Mode of initiation	first generation	first generation	first generation	first generation	first generation

Mine	PM-60	Riegel Mine 43	Tellermine 35	Tellermine 42	Tellermine 43
Country of origin	Germany	Germany	Germany	Germany	Germany
Type	AT blast mine	AT blast (bar) mine	AT blast mine	AT blast mine	AT blast mine
Weight (kg)	11.40	9.30	9.10	9.10	8.10
Explosive weight (kg)	7.50	4.00	5.50	5.50	5.50
Explosive type	TNT	TNT	TNT	TNT	TNT
Equivalent TNT (kg)	7.50	4.00	5.50	5.50	5.50
No. of countries used	2	2	3	2	2
Fuze options	pressure fuze (mechanical or chemical), anti-handling	pressure fuze, anti-handling	pressure fuze	pressure fuze, anti-handling	pressure fuze, anti-handling
Laying options	manual or mechanical	manual	manual	manual	manual
Maximum attack capability	heavy armoured vehicle	heavy armoured vehicle	heavy armoured vehicle	heavy armoured vehicle	heavy armoured vehicle
Production status	continuing	continuing	continuing	continuing	continuing
Numbers on the grounds	n/a	n/a	n/a	n/a	n/a
Mode of attack	track attack	belly attack	track attack	track attack	track attack
Mode of initiation	first generation	first generation	first generation	first generation	first generation

Mine	UKA-63 (ATSC)	YM-II	YM-III	No.6	B-2
Country of origin	Hungary	Iran	Iran	Israel	Italy
Type	ATSC using MS warhead	scatterable AT blast mine	AT blast mine	AT blast mine	AT blast (bar) mine
Weight (kg)	9.00	3.20	7.00	8.00	15.00
Explosive weight (kg)	6.00	2.00	5.40	6.00	3.64
Explosive type	TNT	Composite B	Composite B	TNT	TNT
Equivalent TNT (kg)	6.00	2.30	6.20	6.00	3.64
No. of countries used	1	2	4	3	1
Fuze options	pressure fuze, tilt-rod fuze, anti-handling	pressure fuze	pressure fuze	pressure fuze, tilt-rod fuze	pressure fuze
Laying options	manual, mechanical or chute	manual or scattered from helicopters	manual	manual or mechanical	manual
Maximum attack capability	heavy armoured vehicle	light armoured vehicle	heavy armoured vehicle	heavy armoured vehicle	heavy armoured vehicle
Production status	continuing	continuing	continuing	continuing	continuing
Numbers on the grounds	n/a	n/a	n/a	n/a	n/a
Mode of attack	belly attack	track attack	track attack	full-width attack	belly attack
Mode of initiation	first generation	first generation	first generation	first generation	first generation

Mine	SACI	SB-81	SH-55	TC/3.6	TC/6
Country of origin	Italy	Italy	Italy	Italy	Italy
Type	AT blast mine	scatterable AT blast mine	AT blast mine	AT blast mine	AT blast mine
Weight (kg)	8.23	3.30	7.30	6.80	9.60
Explosive weight (kg)	7.00	2.20	5.50	3.60	6.00
Explosive type	TNT	TNT/RDX/HMX	Composite B	Composite B	Composite B
Equivalent TNT (kg)	7.00	2.20	6.31	4.13	6.89
No. of countries used	3	2	1	1	4
Fuze options	pressure fuze, anti-handling	pressure fuze, electronic anti-handling and self-destruct (SB-81/AR-AN)	pressure fuze & electronic anti-handling, remote switch and self-destruct	pressure fuze, electric remote switch (TCE/3.6)	pressure fuze, electric remote switch (TCE/6)
Laying options	manual	manual or scattered from helicopters	manual or mechanical	manual or mechanical	manual or mechanical
Maximum attack capability	heavy armoured vehicle	light armoured vehicle	heavy armoured vehicle	possibly heavy armoured vehicle	heavy armoured vehicle
Production status	continuing	stopped	stopped	stopped	stopped
Numbers on the grounds	n/a	n/a	n/a	n/a	n/a
Mode of attack	track attack	track attack	track attack	track attack	track attack
Mode of initiation	first generation	second generation	second generation	second generation	second generation

Mine	V-3	VS-1.6	VS-2.2	P2 Mk2 and P3 Mk2	MAT-76
Country of origin	Italy	Italy	Italy	Pakistan	Romania
Type	AT blast (bar) mine	AT blast mine	scatterable AT blast mine	AT blast mine	AT blast mine
Weight (kg)	7.70	3.00	3.50	6.50	10.00
Explosive weight (kg)	2.30	1.85	2.20	5.00	9.50
Explosive type	TNT/PETN	Composite B	Composite B	TNT	TNT
Equivalent TNT (kg)	2.60	2.12	2.53	5.00	9.50
No. of countries used	1	4	2	7	5
Fuze options	pressure fuze, possibly anti-handling device	pressure fuze, electronic anti-handling and self-destruct (VS-1.6-EL)	pressure fuze, electronic anti-handling, remote switch and self-neutralisation	AP mine, anti-handling device	pressure fuze
Laying options	manual	manual or scattered from helicopters	manual or scattered from helicopters	manual	manual
Maximum attack capability	possibly heavy armoured vehicle	light armoured vehicle	light armoured vehicle	heavy armoured vehicle	heavy armoured vehicle
Production status	continuing	stopped	stopped	continuing	stopped exporting
Numbers on the grounds	n/a	n/a	n/a	n/a	n/a
Mode of attack	belly attack	track attack	track attack	track attack	track attack
Mode of initiation	first generation	second generation	second generation	first generation	first generation

Mine	MON-90	MON-100	MON-200	OZM-160	PGMDM/PTM-1S
Country of origin	Russian Federation	Russian Federation	Russian Federation	Russian Federation	Russian Federation
Type	Directional fragmentation mine	Directional fragmentation mine	Directional fragmentation mine	bounding fragmentation mine	scatterable AT blast mine
Weight (kg)	12.10	5.00	25.00	85.00	1.5-2
Explosive weight (kg)	6.20	2.00	12.00	4.50	1-1.5
Explosive type	RDX-based plastic PVV-5A	TNT	TNT	TNT	soft plastic PVV-12M
Equivalent TNT (kg)	6.20	2.00	12.00	4.50	1-1.5
No. of countries used	4	12	5	2	1
Fuze options	pressure(mechanical) fuze, electrical fuze, anti-handling	pressure(mechanical) fuze, electrical fuze, anti-handling	pressure(mechanical) fuze, electrical fuze, anti-handling	mechanical fuze, electrical fuze	pressure fuze (hydraulic)
Laying options	manual	manual	manual	manual	Helicopter or fixed-wing aircraft, rockets, portable system (PKM)
Maximum attack capability	light armoured vehicle	light armoured vehicle	light armoured vehicle	light armoured vehicle	light armoured vehicle
Production status	continuing	continuing	continuing	stopped	continuing
Numbers on the grounds	n/a	n/a	n/a	n/a	n/a
Mode of attack	full-width attack	full-width attack	full-width attack	full-width attack	track attack
Mode of initiation	second generation	second generation	second generation	second generation	first generation

Mine	TM-46/TMN-46	TM-57	TM-62B	TM-62M	TM-72 (ATSC)
Country of origin	Russian Federation	Russian Federation	Russian Federation	Russian Federation	Russian Federation
Type	AT blast mine	AT blast mine	AT blast mine	AT blast mine	ATSC using MS warhead
Weight (kg)	8.60	8.47	8.10	9.50	6.00
Explosive weight (kg)	5.70	6.34	7.50	7.50	2.50
Explosive type	TNT	TNT or TGA or MS	TNT	TNT	TNT/RDX
Equivalent TNT (kg)	5.70	6.34	7.50	7.50	2.50
No. of countries used	23	23	2	20	2
Fuze options	pressure fuze, tilt-rod, anti-handling (TMN-46)	pressure fuze, tilt-rod, anti-handling	pressure fuze, magnetic influence fuze	pressure fuze, magnetic influence fuze	pressure fuze, magnetic influence fuze
Laying options	manual or mechanical	manual or mechanical	manual or mechanical (minelayers/ helicopter)	manual or mechanical (minelayers/ helicopter)	manual or mechanical
Maximum attack capability	heavy armoured vehicle	heavy armoured vehicle	heavy armoured vehicle	heavy armoured vehicle	heavy armoured vehicle
Production status	continuing	continuing	continuing	continuing	continuing
Numbers on the grounds	n/a	n/a	n/a	n/a	n/a
Mode of attack	full-width attack	full-width attack	full-width attack	full-width attack	full-width attack
Mode of initiation	first generation	first generation	second generation	second generation	second generation

Mine	TMD-44	TMD-B	TMK-2 (ATSC)	No.8	C-3-A/B
Country of origin	Russian Federation	Russian Federation	Russian Federation	South Africa	Spain
Type	AT blast mine	AT blast mine	ATSC	AT blast mine	AT blast mine
Weight (kg)	9.0 -10.0	9.0-10.0	12.50	7.40	5.70
Explosive weight (kg)	5.0-7.0	5.0-7.0	6 or 6.5	7.00	5.00
Explosive type	TNT or Picric acid	TNT or Picric acid	TNT or TG-50 (RDX/TNT)	Composite B	TNT/RDX/Al
Equivalent TNT (kg)	5.0-7.0	5.0-7.0	6 or 6.5 (TNT)	8.04	5.00
No. of countries used	9	11	6	3	3
Fuze options	pressure fuze	pressure fuze	tilt-rod fuze	pressure fuze, mechanical and electronic anti-handling	pressure fuze
Laying options	manual	manual	manual	manual	manual
Maximum attack capability	heavy armoured vehicle	heavy armoured vehicle	heavy armoured vehicle	heavy armoured vehicle	heavy armoured vehicle
Production status	stopped	stopped	stopped	stopped selling	continuing
Numbers on the grounds	n/a	n/a	n/a	n/a	n/a
Mode of attack	track attack	track attack	full-width attack	full-width attack	track attack
Mode of initiation	first generation	first generation	first generation	second generation	first generation

Mine	FFV 013	Barmine	Mk 5	Mk 7	BLU-91/B (ATSC)
Country of origin	Sweden	United Kingdom	United Kingdom	United Kingdom	United States of America
Type	Directional fragmentation mine	AT blast (bar) mine	AT blast mine	AT blast mine	scatterable ATSC mine (2 MS warhead)
Weight (kg)	20.00	10.40	5.70	13.60	1.95
Explosive weight (kg)	10.00	8.10	3.70	8.89	0.58
Explosive type	n/a	TNT/RDX	TNT	TNT	RDX/Estane
Equivalent TNT (kg)	n/a	9.30	3.70	8.89	0.69
No. of countries used	1	4	6	10	2
Fuze options	electric fuze, mechanical fuze	pressure fuze	pressure fuze	pressure fuze, tilt-rod fuze, and electronic fuze	electronic magnetic influence fuze
Laying options	manual	manual or mechanical	manual	manual or mechanical	aircraft, vehicle-mounted launcher (in M75 form)
Maximum attack capability	light armoured vehicle, helicopter	heavy armoured vehicle	heavy armoured vehicle	heavy armoured vehicle	possibly heavy armoured vehicle
Production status	continuing	stopped	stopped	stopped	continuing
Numbers on the grounds	n/a	n/a	n/a	n/a	n/a
Mode of attack	full-width attack	belly attack	track attack	full-width attack	full-width attack
Mode of initiation	second generation	first generation	first generation	second generation	second generation

Mine	M1A1	M6A2	M7A2	M15	M19
Country of origin	United States of America	United States of America	United States of America	United States of America	United States of America
Type	AT blast mine	AT blast mine	Anti-vehicle blast mine	AT blast mine	AT blast mine
Weight (kg)	5.30	9.10	2.20	14.30	12.56
Explosive weight (kg)	2.75	4.45	1.62	10.30	9.53
Explosive type	TNT	TNT	Tetryl	Composition B	Composition B
Equivalent TNT (kg)	2.75	4.45	1.62	11.82	10.94
No. of countries used	2	5	11	15	12
Fuze options	pressure fuze	pressure fuze, anti-handling device	pressure fuze, anti-handling device	pressure fuze, tilt-rod fuze, and anti-handling device	pressure fuze, anti-handling device
Laying options	manual	manual	manual	manual	manual
Maximum attack capability	possibly heavy armoured vehicle	possibly heavy armoured vehicle	light armoured vehicle	heavy armoured vehicle	heavy armoured vehicle
Production status	withdrawn from the US military	withdrawn from the US military	withdrawn from the US military	continuing	continuing
Numbers on the grounds	n/a	n/a	at least 2.5 million were produced	n/a	n/a
Mode of attack	track attack	track attack	track attack	full-width attack	track attack
Mode of initiation	first generation	first generation	first generation	first generation	first generation

Mine	M24 (HEAT warhead)	TMA-1A	TMA-2	TMA-3	TMA-4
Country of origin	United States of America	Former Yugoslavia	Former Yugoslavia	Former Yugoslavia	Former Yugoslavia
Type	ATSC mine using HEAT warhead	AT blast mine	AT blast mine	AT blast mine	AT blast mine
Weight (kg)	8.20	6.50	7.50	7.00	6.00
Explosive weight (kg)	0.53	5.40	6.50	6.50	5.50
Explosive type	Composition B	TNT	TNT	TNT	TNT
Equivalent TNT (kg)	0.61	5.40	6.50	6.50	5.50
No. of countries used	1	3	5	5	8
Fuze options	n/a	pressure fuze, anti-handling device, electrical command detonated	pressure fuze, anti-handling device, electrical command detonated	pressure fuze, anti-handling device, electrical command detonated	pressure fuze, anti-handling device
Laying options	manual	manual	manual	manual	manual
Maximum attack capability	heavy armoured vehicle	heavy armoured vehicle	heavy armoured vehicle	heavy armoured vehicle	heavy armoured vehicle
Production status	withdrawn from the US military	continuing	continuing	continuing	continuing
Numbers on the grounds	50,000 were initially produced	n/a	n/a	n/a	n/a
Mode of attack	belly attack (side attack)	belly attack	belly attack	belly attack	track attack
Mode of initiation	first generation	first generation	first generation	first generation	first generation

Mine	TMA-5	TMD-1/2	TMM-1	TMRP-6 (ATSC)	MDH-10
Country of origin	Former Yugoslavia	Former Yugoslavia	Former Yugoslavia	Former Yugoslavia	Vietnam
Type	AT blast mine	AT blast mine	AT blast mine	ATSC mine using MS warhead	Directional fragmentation mine
Weight (kg)	6.60	7.50	8.60	7.20	5.00
Explosive weight (kg)	5.50	5.50	5.60	5.10	2.00
Explosive type	TNT	TNT	TNT	TNT	TNT
Equivalent TNT (kg)	5.50	5.50	5.60	5.10	2.00
No. of countries used	8	2	3	5	3
Fuze options	pressure fuze, anti-handling device	pressure fuze	pressure fuze, anti-handling device	pressure fuze, tilt-rod, anti-handling device, electric command detonated	pressure/mechanical fuze, electrical fuze
Laying options	manual	manual	manual or mechanical	manual or mechanical	manual
Maximum attack capability	heavy armoured vehicle	heavy armoured vehicle	heavy armoured vehicle	possibly heavy armoured vehicle	light armoured vehicle
Production status	continuing	continuing	continuing	continuing	continuing
Numbers on the grounds	n/a	n/a	n/a	n/a	n/a
Mode of attack	track attack	track attack	track attack	full-width attack	full-width attack
Mode of initiation	first generation	first generation	first generation	first generation	second generation

Mine	MKTBT	MKT Mod 72	FMK-5	ATM2000E	AVC 100 (AVM 100)
Country of origin	Albania	Albania	Argentina	Austria	Austria
Type	AT blast mine	AT blast mine	AT blast mine	Anti-vehicle shaped-charge mine using MS warhead	Anti-vehicle directed fragmentation mine
Weight (kg)	15.00	8.50	6.13	6.00	10.00
Explosive weight (kg)	12.00	5.50	n/a	1.90	5.40
Explosive type	TNT	TNT	TNT	n/a	n/a
Equivalent TNT (kg)	12.00	5.50	n/a	n/a	n/a
No. of countries used	1	1	n/a	0	0
Fuze options	pressure (mechanical) fuze	pressure (mechanical) fuze	pressure fuze	microprocessor-based sensor system, anti-handling and remote switch	electronic fuze, other fuzing system
Laying options	manual	manual	manual	manual or mechanical using mine layer	manual
Maximum attack capability	heavy armoured vehicle	heavy armoured vehicle	heavy armoured vehicle	possibly heavy armoured vehicle	light armoured vehicle & helicopter
Production status	continuing	continuing	n/a	in production, in service	in production
Numbers on the grounds	n/a	n/a	n/a	n/a	n/a
Mode of attack	track attack	track attack	track attack	full-width attack	full-width attack
Mode of initiation	first generation	first generation	first generation	third generation	third generation

Mine	AVC 195 (AVM 195)	Giant Shotgun	PRB-111	AC NM AE T1	T-AB-1 (AT)
Country of origin	Austria	Austria	Belgium	Brazil	Brazil
Type	Anti-vehicle directed fragmentation mine	Anti-vehicle directed fragmentation mine	AT blast mine	AT blast mine	AT blast mine
Weight (kg)	19.50	8.00	10.50	8.00	5.90
Explosive weight (kg)	10.30	5.00	10.00	7.00	5.20
Explosive type	n/a	composite B	TNT	TNT	TNT
Equivalent TNT (kg)	n/a	5.74	10.00	7.00	5.20
No. of countries used	0	0	0	0	0
Fuze options	electronic fuze, other fuzing system	electronic fuze	pressure fuze, anti-handling	pressure fuze	AP mine (T-AB-1)
Laying options	manual	manual	manual	manual	manual
Maximum attack capability	light armoured vehicle & helicopter	light armoured vehicle & helicopter	heavy armoured vehicle	heavy armoured vehicle	heavy armoured vehicle
Production status	in production	in production	stopped	stopped	stopped
Numbers on the grounds	n/a	n/a	n/a	n/a	n/a
Mode of attack	full-width attack	full-width attack	track attack	track attack	track attack
Mode of initiation	third generation	third generation	first generation	first generation	first generation

Mine	Anti-Transport Mine	PTM-80P	TM-62M PZ	TMD-1	Cadoen Anti-Tank Mine
Country of origin	Bulgaria	Bulgaria	Bulgaria	Bulgaria	Chile
Type	directional fragmentation warhead with MS warhead	AT blast mine	AT blast mine	scatterable AT mine using MS warhead	AT blast mine
Weight (kg)	n/a	8.93	9.00	2.00	14.00
Explosive weight (kg)	n/a	7.60	7.20	0.87	9.50
Explosive type	n/a	TNT	TNT	n/a	Pentolite and Mexal 1500
Equivalent TNT (kg)	n/a	7.60	7.20	n/a	n/a
No. of countries used	0	0	0	0	0
Fuze options	electronic fuze	pressure fuze, magnetic influence fuze	pressure fuze, magnetic influence fuze	pressure, magnetic influence	pressure fuze
Laying options	manual	manual	manual or mechanical using mine layer	cargo rocket	manual
Maximum attack capability	light armoured vehicle & helicopter	heavy armoured vehicle	heavy armoured vehicle	light armoured vehicle	heavy armoured vehicle
Production status	in production	in production	in production	in production	stopped
Numbers on the grounds	n/a	n/a	n/a	n/a	n/a
Mode of attack	full-width attack	full-width attack	full-width attack	full-width attack	track attack
Mode of initiation	third generation	second generation	second generation	second generation	first generation

Mine	MAT.84-F5	MP-APVL 83-F4	SATM	Type 84	PD Mi-PK
Country of origin	Chile	Chile	China	China	Former Czechoslovakia
Type	AT blast mine	dual-purpose mine	scatterable AT mine with MS warhead	scatterable AT mine with MS warhead	off-route mine using MS warhead
Weight (kg)	10.30	6.75	2.20	3.12	10.10
Explosive weight (kg)	9.30	2.00	n/a	n/a	8.50
Explosive type	Pentolite	Pentolite	n/a	n/a	TNT or TNT/RDX
Equivalent TNT (kg)	10.50	2.26	n/a	n/a	8.5 (TNT)
No. of countries used	0	0	0	0	0
Fuze options	pressure fuze	pressure fuze	electronic fuzes (seismic sensor & magnetic influence), electronic safety device	magnetic influence fuze, anti-disturbance,, self-destruct	mechanical fuze (tripwire), electric command detonated
Laying options	manual	manual	mechanical	mechanical	manual
Maximum attack capability	heavy armoured vehicle	light armoured vehicle	heavy armoured vehicle	heavy armoured vehicle	light armoured vehicle
Production status	in service (Chilean Army)	in service (Chilean Army)	in production	in production	in production
Numbers on the grounds	n/a	n/a	n/a	n/a	n/a
Mode of attack	track attack	full-width attack	full-width attack	full-width attack	full-width attack
Mode of initiation	first generation	first generation	third generation	second generation	second generation

Mine	PT Mi-D1M	PT Mi-U	M/80	TC/6	MSM MK2 (PM-87)
Country of origin	Former Czechoslovakia	Former Czechoslovakia	Egypt	Egypt	Finland
Type	scatterable AT mine using MS warhead	universal AT mine using MS warhead	AT blast mine	AT blast mine	AT mine using MS warhead
Weight (kg)	2.65	9.41	3.50	8.40	7.50
Explosive weight (kg)	n/a	7.11	2.40	6.00	4.00
Explosive type	n/a	TNT	TNT/RDX	TNT/RDX	'Hetro' Composite B (50/50)
Equivalent TNT (kg)	n/a	7.11	n/a	n/a	n/a
No. of countries used	0	0	0	0	0
Fuze options	pressure fuze, magnetic influence fuze, self-destruct	pressure fuze, tilt-rod fuze, electronic fuze, self-destruct, self-neutralisation	pressure operated pneumatic transfer fuze	pressure operated pneumatic transfer fuze, electronic remote switch	electronic fuze (seismic & magnetic sensors), self-neutralisation
Laying options	cargo rocket	manual or mechanical	manual or mechanical or scattered	manual or mechanical	manual
Maximum attack capability	heavy armoured vehicle	heavy armoured vehicle	light armoured vehicle	heavy armoured vehicle	heavy armoured vehicle
Production status	in production, in service	in production, in service	in production, in service	in production, in service	in production, in service
Numbers on the grounds	n/a	n/a	n/a	n/a	n/a
Mode of attack	full-width attack	full-width attack	track attack	track attack	full-width attack
Mode of initiation	second generation	third generation	second generation	second generation	third generation

Mine	TM-65/77	ACPR and ACPR-H	ADWAT	HPD-2 series	HPD-3 series
Country of origin	Finland	France	France	France	France
Type	AT blast mine	AT blast mine	AT blast mine	AT mine (MS warhead)	AT mine (MS warhead)
Weight (kg)	10.00	5.00	5.00	7.00	7.00
Explosive weight (kg)	9.50	4.00	n/a	2.80	5.00
Explosive type	TNT	n/a	n/a	Composite B	Composite B
Equivalent TNT (kg)	9.50	n/a	n/a	3.21	5.74
No. of countries used	0	0	0	0	0
Fuze options	pressure fuze	pressure fuze, auxiliary fuze for booby trap	pressure fuze, electronic fuze (self-destruction, self-neutralisation, anti-handling)	magnetic influence sensor, self-neutralisation, anti-handling	magnetic influence sensor, self-neutralisation, anti-handling
Laying options	manual	manual or mechanical	manual or mechanical	manual or mechanical	manual or mechanical
Maximum attack capability	heavy armoured vehicle	heavy armoured vehicle	heavy armoured vehicle	heavy armoured vehicle	heavy armoured vehicle
Production status	in service	in production, in service	in production	in service	in service
Numbers on the grounds	n/a	n/a	n/a	more than 400,000 have been ordered	n/a
Mode of attack	belly attack	track attack	track attack	full-width attack	full-width attack
Mode of initiation	first generation	first generation	second generation	second generation	second generation

Mine	M51 and M 52 MACI	MIACAH F1	MI AC Disp F1	Mitral	AT2
Country of origin	France	France	France	France	Germany
Type	AT blast mine	off-route AT mine (MS warhead)	scatterable AT mine (MS warhead)	scatterable AT mine	scatterable AT mine (MS warhead)
Weight (kg)	7 (M51) or 9 (M52)	12.00	2.25	2.60	2.22
Explosive weight (kg)	6.49	n/a	n/a	n/a	n/a
Explosive type	TNT	n/a	n/a	RDX based	n/a
Equivalent TNT (kg)	6.49	n/a	n/a	n/a	n/a
No. of countries used	1	0	0	0	0
Fuze options	pressure-friction fuze, electronic fuze, tilt-rod fuze	breakwire, programmable igniter	electronic magnetic-influence fuze, self-destruct	n/a, self-destruct	electronic/mechanical fuze, self-destruct, anti-handling
Laying options	manual	manual	vehicle launcher, 155 mm cargo projectile	aircraft, helicopter-mounted munitions dispenser, ground based launcher, or rocket	Light Artillery Rocket System, Multiple Launch Rocket System, Skorpion minelaying system
Maximum attack capability	heavy armoured vehicle	heavy armoured vehicle	possibly heavy armoured vehicle	light armoured vehicle	heavy armoured vehicle
Production status	stopped	stopped	in production, in service	prototype	in service
Numbers on the grounds	n/a	n/a	n/a	n/a	1,304,000 have been produced
Mode of attack	full-width attack	full-width attack	belly attack	track attack	full-width attack
Mode of initiation	2nd generation	2nd generation	3rd generation	3rd generation	3rd generation

Mine	MIFF	MUSPA and MUSA	PARM 1	PARM 2	HAK-1
Country of origin	Germany	Germany	Germany	Germany	Hungary
Type	scatterable AT mine (2 MS warhead)	scatterable fragmentation mine	off-route AT mine (HEAT warhead)	off-route AT mine (HEAT warhead)	AT mine using MS warhead
Weight (kg)	3.40	4.50	10.00	20.00	5.60
Explosive weight (kg)	n/a	n/a	1.40	1.90	2.50
Explosive type	n/a	n/a	n/a	n/a	Composite B3
Equivalent TNT (kg)	n/a	n/a	n/a	n/a	2.87
No. of countries used	0	0	0	0	0
Fuze options	electronic magnetic influence and seismic sensors, self-destruct	electronic fuze (acoustic signal), electromechanical delay fuzes, self-destruct	fiber-optic sensor cable with electronic circuit, remotely command-initiated	Sensor Active Passive Infra-Red sensor system, self-neutralisation, remote command detonation	electronic and magnetic influence sensor (HAKEG fuze)
Laying options	aircraft-mounted dispenser	aircraft-mounted dispenser	manual	manual	manual
Maximum attack capability	heavy armoured vehicle	possibly heavy armoured vehicle	heavy armoured vehicle	heavy armoured vehicle	light armoured vehicle
Production status	in service	in service	stopped	stopped	in production
Numbers on the grounds	n/a	n/a	50,000 have been produced	n/a	n/a
Mode of attack	full-width attack	full-width attack	belly attack (side attack)	full-width attack	belly attack
Mode of initiation	third generation	third generation	second generation	third generation	second generation

Mine	Adrushy	Mine Anti-tank 1A	Mine Anti-tank 3A	ARGES (MACPED)	ATIS
Country of origin	India	India	India	International	International
Type	AT mine using MS warhead	AT blast mine	AT blast (bar) mine	off-route AT mine	AT shape charge mine
Weight (kg)	5.50	7.30	11.00	18 or 22	5.50
Explosive weight (kg)	2.50	6.75	8.00	n/a	n/a
Explosive type	n/a	TNT	n/a	n/a	n/a
Equivalent TNT (kg)	n/a	6.75	n/a	n/a	n/a
No. of countries used	0	0	0	0	0
Fuze options	electronic fuze (seismic and magnetic-influence sensor), self-neutralisation, anti-handling	pressure fuze	pressure-operated (hydraulically single impulse) fuze	acoustic sensor, infra-red detection system and laser, remote command detonation, self-neutralisation, anti-handling	electronic fuze (acoustic sensor), anti-handling, remote control
Laying options	manual	manual	manual or mechanical using minelayer	manual	manual
Maximum attack capability	heavy armoured vehicle	heavy armoured vehicle	heavy armoured vehicle	heavy armoured vehicle	heavy armoured vehicle
Production status	in production, in service	in service	in service	entering production	prototype
Numbers on the grounds	n/a	n/a	n/a	n/a	n/a
Mode of attack	full-width attack	belly attack	full-width attack	belly attack (side attack)	full-width attack
Mode of initiation	second generation	first generation	first generation	third generation	third generation

Mine	BAT/7	MAT/5	MAT/6	MATS/1.4	MATS/2
Country of origin	Italy	Italy	Italy	Italy	Italy
Type	AT mine using MS warhead	AT blast mine	AT blast mine	scatterable AT blast mine	scatterable AT blast mine
Weight (kg)	5.60	7.00	7.10	3.60	4.00
Explosive weight (kg)	3.60	5.00	6.3 (approx.)	1.50	2.60
Explosive type	n/a	Composite B	n/a	n/a	Composite B or T4 (RDX)
Equivalent TNT (kg)	n/a	5.74	n/a	n/a	2.98
No. of countries used	0	0	0	0	0
Fuze options	dual sensor electronic fuze (acoustic and magnetic influence sensor)	pressure operated pneumatic transfer fuze, anti-handling device	pressure operated pneumatic transfer fuze, anti-handling device	pressure operated pneumatic transfer fuze	pressure operated pneumatic transfer fuze
Laying options	manual	manual or mechanical	manual or mechanical	manual or helicopter	manual or mechanical (vehicle or helicopter)
Maximum attack capability	heavy armoured vehicle	heavy armoured vehicle	heavy armoured vehicle	light armoured vehicle	light armoured vehicle
Production status	stopped	stopped	stopped	stopped	in service
Numbers on the grounds	n/a	n/a	n/a	n/a	n/a
Mode of attack	full-width attack	track attack	track attack	track attack	track attack
Mode of initiation	third generation	second generation	second generation	second generation	second generation

Mine	SB-MV/1	SBP-04	SBP-07	TC/2.4	VS-3.6
Country of origin	Italy	Italy	Italy	Italy	Italy
Type	AT mine using MS warhead	AT blast mine	AT blast mine	AT blast mine	AT blast mine
Weight (kg)	5.00	5.00	8.20	3.30	5.00
Explosive weight (kg)	2.40	4.00	7.00	2.40	4.00
Explosive type	Composite B	n/a	n/a	Composite B	Composite B
Equivalent TNT (kg)	2.76	n/a	n/a	2.76	4.59
No. of countries used	0	0	0	0	0
Fuze options	magnetic influence fuze (with seismic transducer), anti-handling, self-neutralisation	pressure fuze	pressure fuze	pneumatic fuze, anti-handling device	pneumatic fuze, electronic fuze
Laying options	manual or mechanical	manual	manual	manual	manual
Maximum attack capability	heavy armoured vehicle	heavy armoured vehicle	heavy armoured vehicle	light armoured vehicle	possibly heavy armoured vehicle
Production status	unknown	unknown	unknown	stopped	stopped
Numbers on the grounds	n/a	n/a	n/a	n/a	n/a
Mode of attack	full-width attack	track attack	belly attack	track attack	track attack
Mode of initiation	second generation	first generation	first generation	second generation	second generation

Mine	VS-AT4 and VS-AT4-EL	VS-DAFM 6 and VS-DAFM 7	VS-HCT	VS-HCT2	VS-HCT4
Country of origin	Italy	Italy	Italy	Italy	Italy
Type	AT blast mine	directional fragmentation mine	AT mine (MS warhead)	AT mine (MS warhead)	AT mine (MS warhead)
Weight (kg)	6.00	18.2 or 10.7	4.00	6.80	5.50
Explosive weight (kg)	4.50	n/a	2.05	2.30	2.30
Explosive type	n/a	n/a	Composite B	Composite B	Composite B
Equivalent TNT (kg)	n/a	n/a	2.35	2.64	2.64
No. of countries used	0	0	0	0	0
Fuze options	pneumatic transfer fuze, electronic fuze, anti-handling, self-neutralisation, self-destruct	command-detonated, tripwire	dual sensor electronic influence fuze (seismic and magnetic influence sensor), self-neutralisation, anti-handling device	dual sensor electronic influence fuze (seismic and magnetic influence sensor), self-neutralisation, self-destructed, anti-handling device	dual sensor electronic influence fuze (seismic and magnetic influence sensor), self-neutralisation, self-destructed, anti-handling device
Laying options	manual or mechanical	manual	manual or mechanical	manual or mechanical	manual or mechanical
Maximum attack capability	possibly heavy armoured vehicle	light armoured vehicle	heavy armoured vehicle	heavy armoured vehicle	heavy armoured vehicle
Production status	stopped	stopped	stopped	stopped	stopped
Numbers on the grounds	n/a	n/a	n/a	n/a	n/a
Mode of attack	track attack	full-width attack	full-width attack	full-width attack	full-width attack
Mode of initiation	second generation	second generation	third generation	third generation	third generation

Mine	VS-SATM1	Type 63 (AT)	ATM-72	K441 and K442	M19 (South Korea)
Country of origin	Italy	Japan	North Korea	South Korea	South Korea
Type	scatterable AT mine (MS warhead)	AT blast mine	AT blast mine	AT mine using MS warhead	AT blast mine
Weight (kg)	2.50	14.50	13.00	7.83	12.56
Explosive weight (kg)	0.80	11.00	9.00	4.90	9.53
Explosive type	Composite B	Composite B	Composite B	Composition H6	Composite B
Equivalent TNT (kg)	0.92	12.63	10.33	n/a	10.94
No. of countries used	0	0	1	1	1
Fuze options	dual sensor electronic influence fuze, self-neutralisation, self-destructed	pressure fuze	pressure fuze	pressure fuze, tilt-rod fuze	pressure fuze, anti-handling device
Laying options	manual, Istric mine scattering system, man-portable launcher, or helicopter system	manual	manual	manual	manual
Maximum attack capability	light armoured vehicle	heavy armoured vehicle	heavy armoured vehicle	heavy armoured vehicle	heavy armoured vehicle
Production status	stopped	n/a	n/a	in production	in service
Numbers on the grounds	n/a	n/a	n/a	n/a	n/a
Mode of attack	full-width attack	belly attack	belly attack	full-width attack	belly attack
Mode of initiation	third generation	first generation	first generation	first generation	first generation

Mine	NR 25	NR 26 and NR26C1	Type 2, T40	MGP-31	Kasia 100 and 170
Country of origin	Netherlands	Netherlands	Netherlands	Peru	Poland
Type	AT blast mine	AT blast mine	AT blast mine	AT blast mine	off-route mine with warhead options
Weight (kg)	12.97	n/a	6.00	n/a	6 or 17.6
Explosive weight (kg)	9.00	9.00	4.08	n/a	n/a
Explosive type	TNT	TNT	TNT	n/a	n/a
Equivalent TNT (kg)	9.00	9.00	4.08	n/a	n/a
No. of countries used	1	0	0	0	0
Fuze options	pressure fuze, anti-handling devices	pressure fuze, anti-handling device	pressure (mechanical) fuze	pressure fuze	electronic fuzes (electro-optic and acoustic sensors), command detonated wire
Laying options	manual	manual	manual	manual	manual
Maximum attack capability	heavy armoured vehicle	heavy armoured vehicle	possibly heavy armoured vehicle	heavy armoured vehicle	heavy armoured vehicle
Production status	in service	in service	in service	in service	in production
Numbers on the grounds	n/a	n/a	n/a	n/a	n/a
Mode of attack	belly attack	belly attack	track attack	track attack	belly attack (side attack)
Mode of initiation	first generation	first generation	first generation	first generation	third generation

Mine	Kaia 2 x 100	MN-111	MN-121	MN-123	MPB
Country of origin	Poland	Poland	Poland	Poland	Poland
Type	off-route mine (warhead options)	scatterable AT mine (MS warhead)	scatterable AT mine (MS warhead)	scatterable AT mine (MS warhead)	off-route mine (MS warhead)
Weight (kg)	10.00	3.50	2.80	3.50	45.00
Explosive weight (kg)	n/a	n/a	0.70	n/a	n/a
Explosive type	n/a	n/a	RDX	n/a	n/a
Equivalent TNT (kg)	n/a	n/a	0.83	n/a	n/a
No. of countries used	0	0	0	0	0
Fuze options	electronic fuzes (electro-optic and acoustic sensors), command detonated wire	electronic fuze, self-destruct	electronic/mechanical fuze, self-destruct, anti-handling	electronic magnetic influence, self destruct, anti-handling	pressure fuze, acoustic sensor, self-destruct, anti-disturbance
Laying options	manual	aircraft or helicopter	aircraft, helicopter pods or artillery rockets	tubes mounted on an armoured vehicle	manual
Maximum attack capability	possibly heavy armoured vehicle	possibly heavy armoured vehicle	possibly heavy armoured vehicle	possibly heavy armoured vehicle	heavy armoured vehicle
Production status	in production	in production	in production	in production	in production
Numbers on the grounds	n/a	n/a	n/a	n/a	n/a
Mode of attack	belly attack (side attack)	full-width attack	full-width attack	full-width attack	belly attack (side attack)
Mode of initiation	third generation	second generation	third generation	second generation	second generation

Mine	MPP-B 'Wierzba'	M453	MAI-GA4	MAT-62B	MC-71
Country of origin	Poland	Portugal	Romania	Romania	Romania
Type	AT blast mine	AT blast mine	directional fragmentation mine	AT blast mine	AT shape charge mine
Weight (kg)	10.8 (max)	3.15	19.00	9.80	8.20
Explosive weight (kg)	8.10	2.00	12.00	7.20	5.10
Explosive type	TNT	Composite B	TNT	TNT	TNT
Equivalent TNT (kg)	8.10	2.30	12.00	7.20	5.10
No. of countries used	0	0	0	0	0
Fuze options	pressure fuze, command detonation, electronic fuze (pressure or magnetic influence)	pressure-actuated fuze	electric remote control	pressure fuze	tilt-rod fuze
Laying options	manual or mechanical	manual	manual	manual	manual
Maximum attack capability	heavy armoured vehicle	light armoured vehicle	light armoured vehicle & helicopter	heavy armoured vehicle	heavy armoured vehicle
Production status	in production, in service	in service	in service	in service	in service
Numbers on the grounds	n/a	n/a	n/a	n/a	n/a
Mode of attack	full-width attack	track attack	full-width attack	belly attack	belly attack
Mode of initiation	second generation	first generation	second generation	first generation	first generation

Mine	M225	MZU	PDM series	PMK-1	PTM-3
Country of origin	Russian Federation	Russian Federation	Russian Federation	Russian Federation	Russian Federation
Type	area attack mine	railways mine	river bottom mines	railways mine	scatterable AT shape charge mine
Weight (kg)	100.00	19.00	47.5 (PDM-6)	8.50	4.90
Explosive weight (kg)	n/a	16.00	28.00	7.10	1.80
Explosive type	n/a	n/a	TNT or PETN	TNT	TG-40 (60% RDX/ 40% TNT)
Equivalent TNT (kg)	n/a	n/a	28.00	7.10	n/a
No. of countries used	0	2	0	0	0
Fuze options	command-detonated, electronic integral impact fuze	anti-handling, magnetic influence, command-detonated	tilt-rod fuze, anti-disturbance	electrical command detonated, pressure fuze	magnetic influence fuze, self-destruct
Laying options	(wide area mine)	manual	manual	manual	man-portable mine dispensing unit, mine scattering system, helicopter mine scattering system
Maximum attack capability	heavy armoured vehicle	heavy armoured vehicle	heavy armoured vehicle & amphibious vehicle	heavy armoured vehicle	heavy armoured vehicle
Production status	in development	in service	in service	in service	in production, in service
Numbers on the grounds	n/a	n/a	n/a	n/a	n/a
Mode of attack	full-width attack	full-width attack	full-width attack	full-width attack	full-width attack
Mode of initiation	third generation	second generation	first generation	second generation	second generation

Mine	TEMP 30	TM-83	TM-89	KRIZNA	Intelligent Horizontal Mine
Country of origin	Russian Federation	Russian Federation	Russian Federation	Former Czechoslovakia	South Africa
Type	off-route mine (2 MS warheads)	off-route mine (MS warhead)	AT mine (MS warhead)	scatterable AT mine (MS warhead)	off-route mine using MS warhead
Weight (kg)	n/a	20.40	11.50	2.75	21.50
Explosive weight (kg)	n/a	9.60	6.70	n/a	11.00
Explosive type	n/a	TG-40 (60%RDX/ 40%TNT)	TG-40 (60%RDX/ 40%TNT)	n/a	RDX/TNT
Equivalent TNT (kg)	n/a	n/a	n/a	n/a	n/a
No. of countries used	0	0	0	0	0
Fuze options	acoustic sensor, seismic sensors, infra-red sensor, self-neutralisation, self-destruct	infra-red sensors, seismic sensor, remotely command-detonated	electronic fuze (2 channel magnetic influence fuze)	magnetic influence, contact sensor mast	infra-red sensor, acoustic sensors, self-destruct, anti-disturbance
Laying options	manual	manual	Manual or mechanical	122 cargo rockets	manual
Maximum attack capability	heavy armoured vehicle	heavy armoured vehicle	heavy armoured vehicle	heavy armoured vehicle	heavy armoured vehicle
Production status	in development	in production, in service	in production	in production, in service	development cancelled
Numbers on the grounds	n/a	n/a	n/a	n/a	n/a
Mode of attack	top attack	belly attack (side attack)	full-width attack	full-width attack	belly attack (side attack)
Mode of initiation	third generation	second generation	second generation	second generation	third generation

Mine	'Non-metallic' anti-tank mine	FFV 016	FFV 028	Model 52 and 52B	M19 (Turkey)
Country of origin	South Africa	Sweden	Sweden	Sweden	Turkey
Type	AT blast mine	off-route mine (MS warhead)	AT mine (MS warhead)	AT blast mine	AT blast mine
Weight (kg)	6.50	2.60	8.40	8.98	12.04
Explosive weight (kg)	5.00	n/a	4.00	7.48	9.53
Explosive type	RDX/TNT	n/a	RDX/TNT	TNT	Composite B
Equivalent TNT (kg)	n/a	n/a	n/a	7.48	10.94
No. of countries used	0	0	0	0	0
Fuze options	pressure (mechanical) fuze	remotely command detonated	mechanical and magnetic influence fuze, self-neutralisation, self-destruct, anti-disturbance	pressure fuze, tilt-rod fuze	pressure fuze, anti-handling devices
Laying options	manual	manual	manual or mechanical using minelayer	manual	manual
Maximum attack capability	heavy armoured vehicle	light armoured vehicle	heavy armoured vehicle	heavy armoured vehicle	heavy armoured vehicle
Production status	stopped	in service	in service	in service	in production
Numbers on the grounds	n/a	n/a	125,200 were ordered by Germany	n/a	n/a
Mode of attack	track attack	belly attack (side attack)	belly attack	full-width attack	belly attack
Mode of initiation	first generation	second generation	second generation	first generation	first generation

Mine	Barmine with add-on fuzes	M21	M75 (GEMSS mine)	M93 'HORNET'	M70 (RAAM)
Country of origin	United Kingdom	United States	United States	United States	United States
Type	AT blast (bar) mine	AT mine (MS warhead)	scatterable AT mine (2 MS warheads)	wide-area munition (WAM) (MS warhead)	scatterable AT mine (MS warhead)
Weight (kg)	11.00	7.83	1.68	n/a	2.27
Explosive weight (kg)	7.20	4.90	n/a	n/a	0.59
Explosive type	RDX/TNT	Composite H6	n/a	n/a	RDX/Estane
Equivalent TNT (kg)	n/a	n/a	n/a	n/a	n/a
No. of countries used	0	0	0	0	0
Fuze options	mechanical fuze, electronic fuze, anti-disturbance	pressure fuze, tilt-rod fuze	magnetic influence fuze	electronic fuzes (seismic and acoustic sensors, infrared sensor), remote control	magnetic influence fuze, self-destruct
Laying options	manual or mechanical using minelayer	manual	Ground Emplaced Mine Scattering System, vehicle-towed mine dispenser, minelaying device, Remote Anti-Armor Mine System	automatic ground launcher, Volcano multiple mine delivery system, Multiple Launch Rocket System, Army Tactical Missile System	modified 155 mm M483 based ejecting cargo projectile
Maximum attack capability	heavy armoured vehicle	heavy armoured vehicle	possibly heavy armoured vehicle	heavy armoured vehicle	possibly heavy armoured vehicle
Production status	in service	in service	withdrawn	in service	in service
Numbers on the grounds	more than 100,000	more than 200,000	more than 344,000	n/a	n/a
Mode of attack	full-width attack	full-width attack	full-width attack	full-width attack	full-width attack
Mode of initiation	second generation	first generation	second generation	third generation	second generation

Mine	SLAM	MPR-M85	TMRP-7
Country of origin	United States	Former Yugoslavia	Former Yugoslavia
Type	lightweight attack munition (MS warhead)	limpet mine	AT mine (MS warhead)
Weight (kg)	1.00	1.60	7.50
Explosive weight (kg)	n/a	0.40	5.10
Explosive type	n/a	plastic Penthrite (PETN based)	TNT
Equivalent TNT (kg)	n/a	n/a	5.10
No. of countries used	0	0	0
Fuze options	magnetic influence fuze, infra-red sensor, command detonated, self-neutralisation, self-destruct	electronic fuze, anti-disturbance	electronic fuze (magnetic influence), anti-disturbance
Laying options	manual	manual	manual
Maximum attack capability	light armoured vehicle	light armoured vehicle	light armoured vehicle
Production status	in service	limited production	prototype
Numbers on the grounds	n/a	n/a	n/a
Mode of attack	full-width attack	track attack	full-width attack
Mode of initiation	second generation	second generation	second generation

APPENDIX B Comparison results between shell and solid elements

This Appendix compares the simulation results between using Belytschko-Lin-Tsay shell and 8-nodes solid elements to represent a RHA single plate (2.5 x 2.5 x 0.020 m) subjected to an exploding charge of 5 kg TNT in hemispherical shape at 400 mm stand off distance. A ¼ symmetric model is developed using AUTODYN 3D remap methods in the same way as used in the thesis. The element sizes between shell and the solid elements are the same except the element height. The solid elements are modelled as 10 mm height so there are 2 layers of solid elements at the plate thickness, while the shell elements is set as having 20 mm thick. The material properties of air, RHA steel, and TNT are also the same as used in the thesis. The results are in table B.1 and figure B.1. It shows that modelling the single plate using shell elements in this configuration gives similar results to the one using solid elements both in terms of the trends and the maximum results. There are only 3% different between the two methods; however, the time taken to run the model using shell elements is 5 hours shorter. It is likely that in a larger or more complex structure such as a vehicle structure, the differences in the time taken to run will be more. Note that the shell elements gave slightly less maximum deformation, velocity, and acceleration, because they assumes that through thickness strain variation is linear, while in the solid elements, the strain variation through thickness can be more complex. Also, in fluid structure interaction the air (fluid) elements should be smaller than the smallest structure elements to prevent leakages. The more layers of solid elements, the smaller element thickness, and hence smaller air elements. If the air elements are too small, which subsequently increases the number of elements in the model significantly; the computational resources may not be enough to run the model.

	Maximum deformation (mm)	Maximum velocity (m/s)	Maximum acceleration (x 10^5 m/s^2)	Time taken to run (hours)
Using solid elements	80.76	74.62	7.56	75
Using shell elements	78.34	73.41	7.52	70
Percentage different from using solid elements (%)	3.0	1.6	0.6	6.7

Table B.1 Maximum deformation, velocity, acceleration and time taken to run the model to 84 ms.

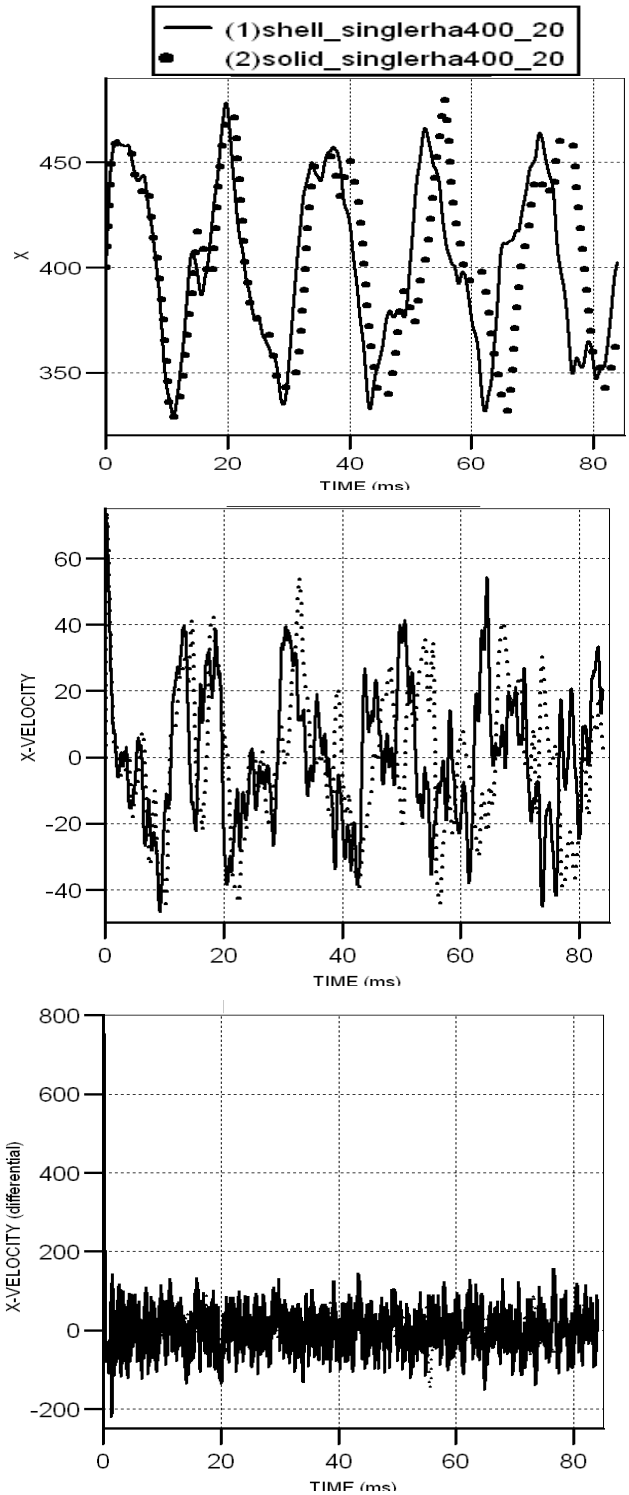

Figure B.1 Maximum deformation, velocity, acceleration plots between modelling the single plate as shell and solid elements.

APPENDIX C Extended results from Chapter 5

This Appendix shows the extended results related to Chapter 5.

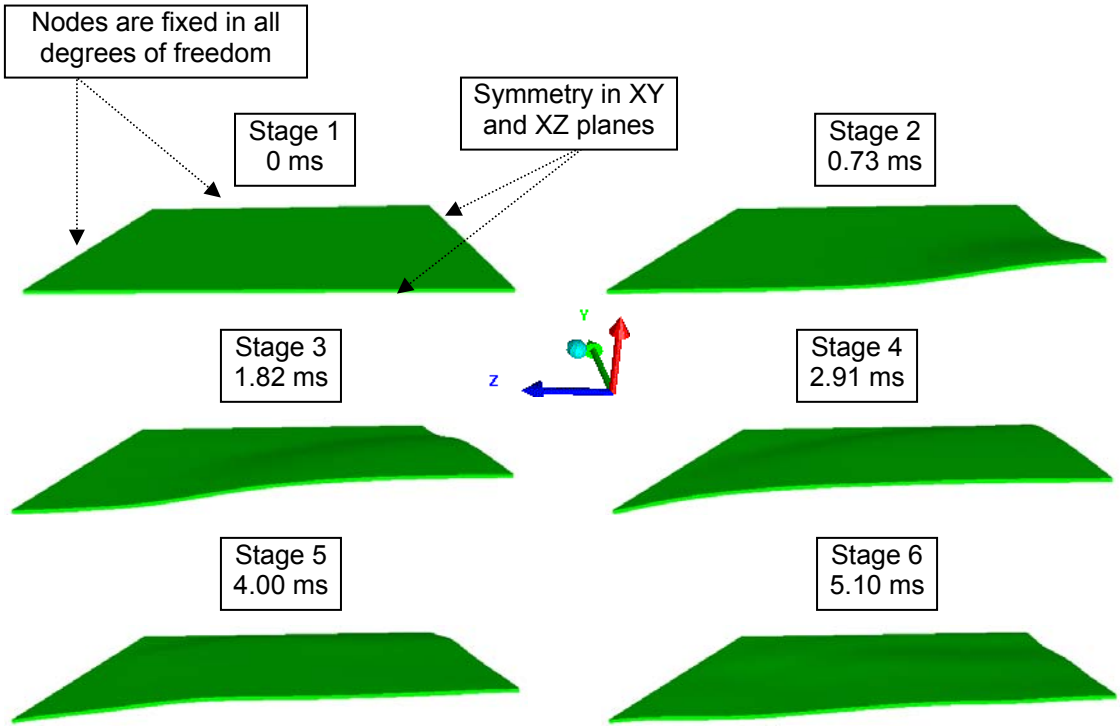

Figure C. 1 Deformation plot of ¼ single plate (10 mm thick) model subjected to 5 kg TNT in an hemispherical shape blast at 400 mm stand-off distance.

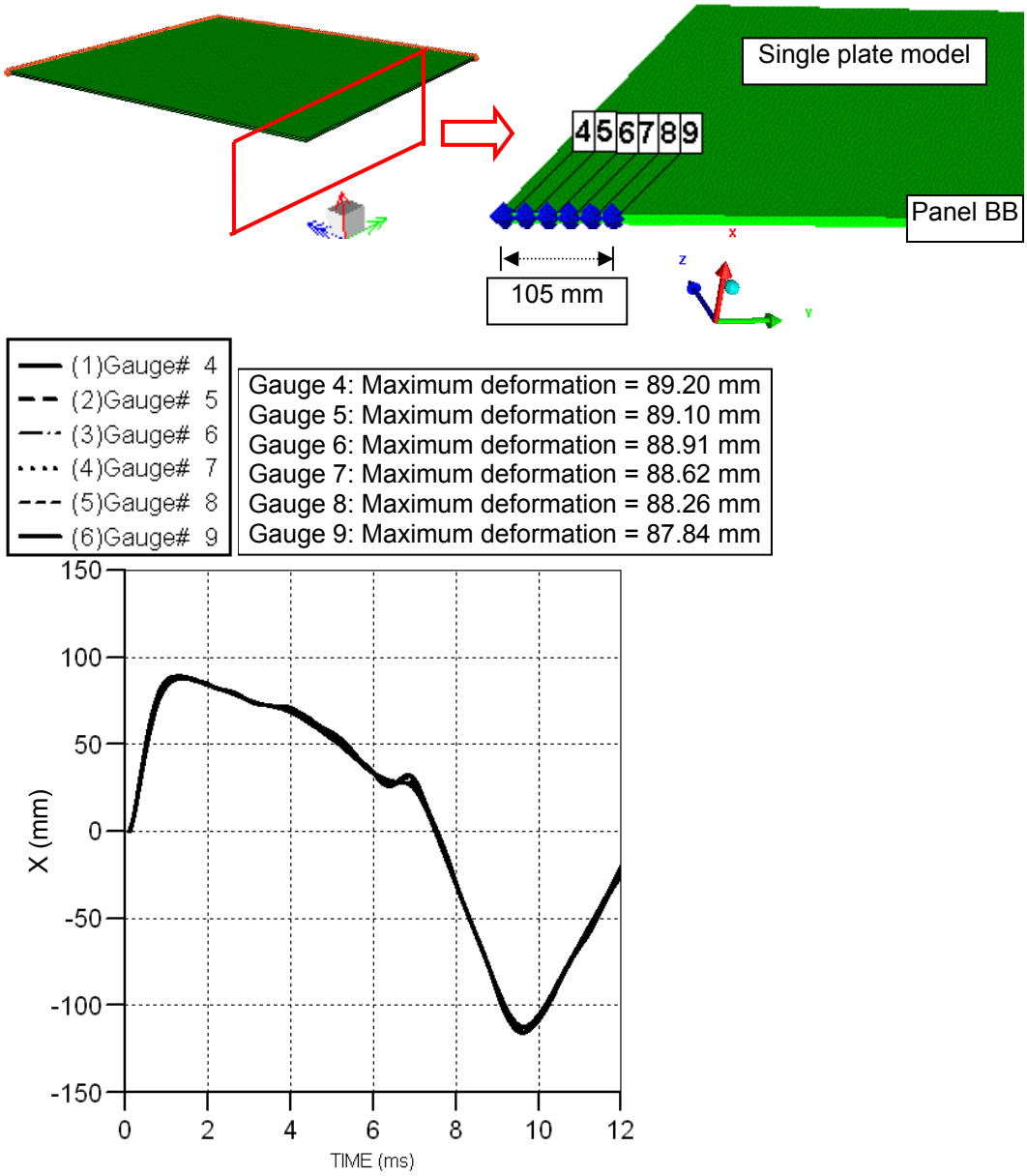

Figure C. 2 Deformation on panel BB (10 mm thick) of single plate model subjected to 5 kg TNT in an hemispherical shape blast at 400 mm stand-off distance using different gauges (deformation curves are based on the net deformation)

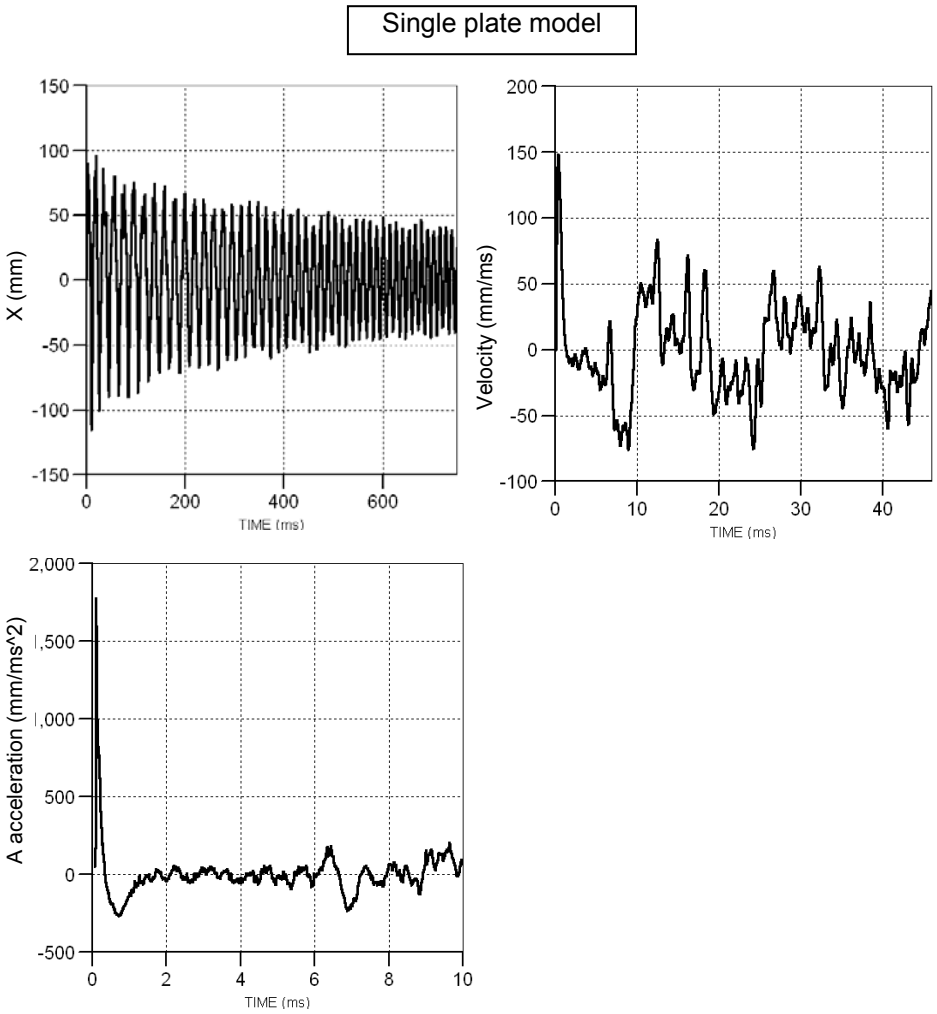

Figure C. 3 Single plate model results having 10 mm thickness subjected to 5 kg TNT in an hemispherical shape on a reflected surface at 400 mm stand-off distance (deformation curve is based on the net deformation)

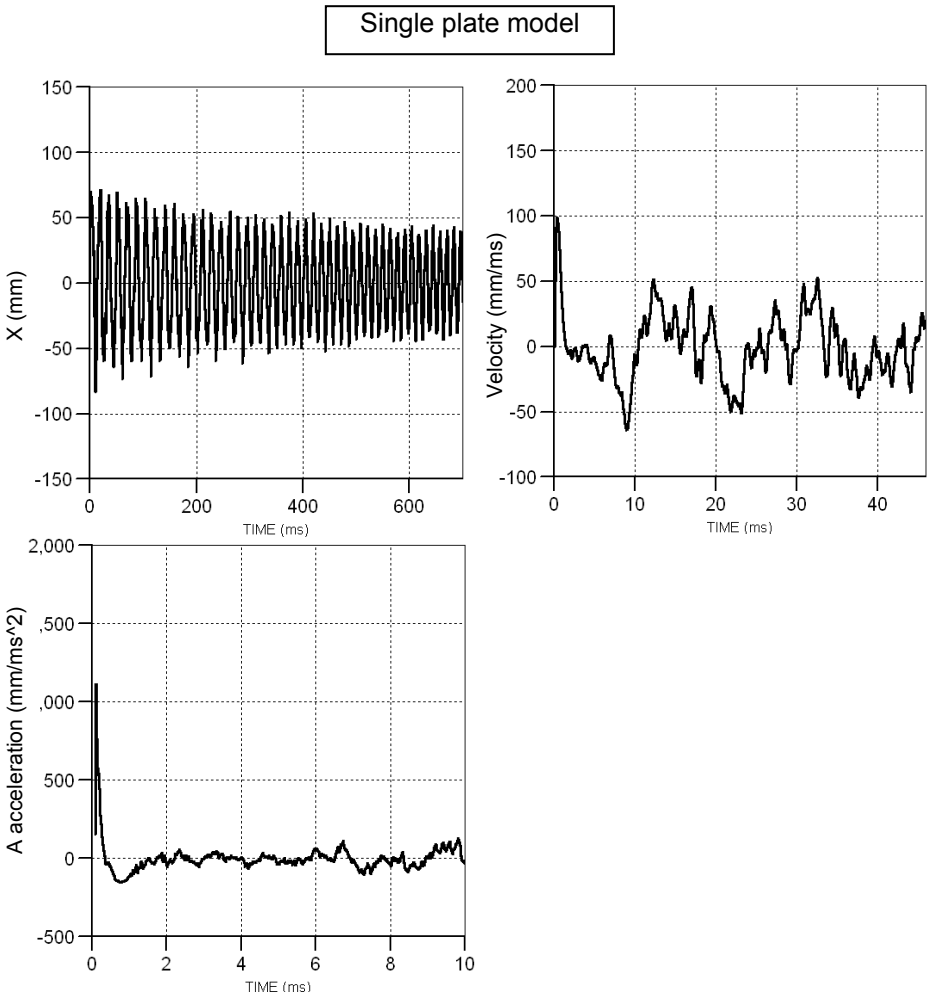

Figure C. 4 Single plate model results having 10 mm thickness subjected to 3.17 kg TNT in an hemispherical shape on a reflected surface at 400 mm stand-off distance (deformation curve is based on the net deformation)

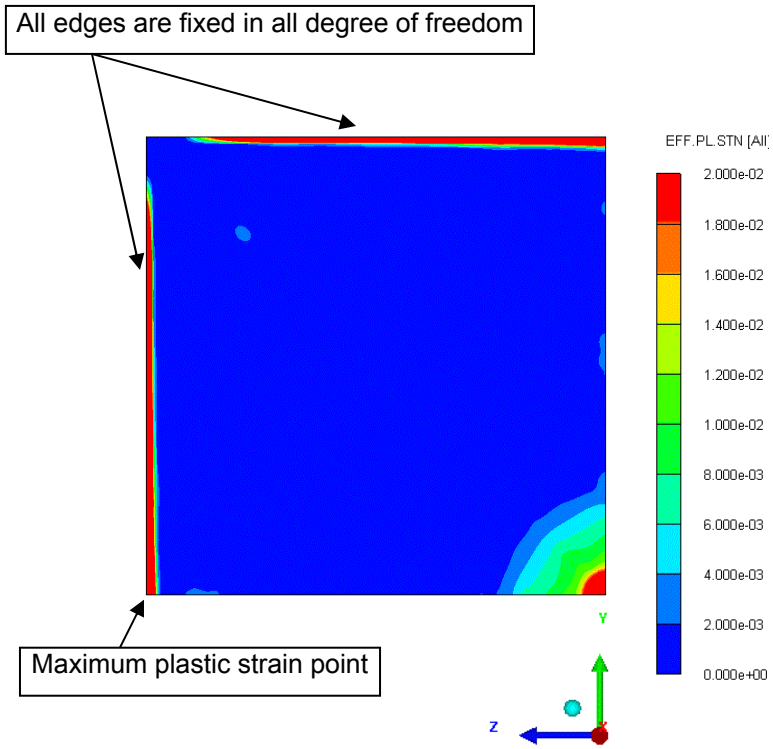

Figure C. 5 Effective plastic strain contour plot of a ¼ single plate model subjected to 5 kg TNT in an hemispherical shape blast at 750 ms.

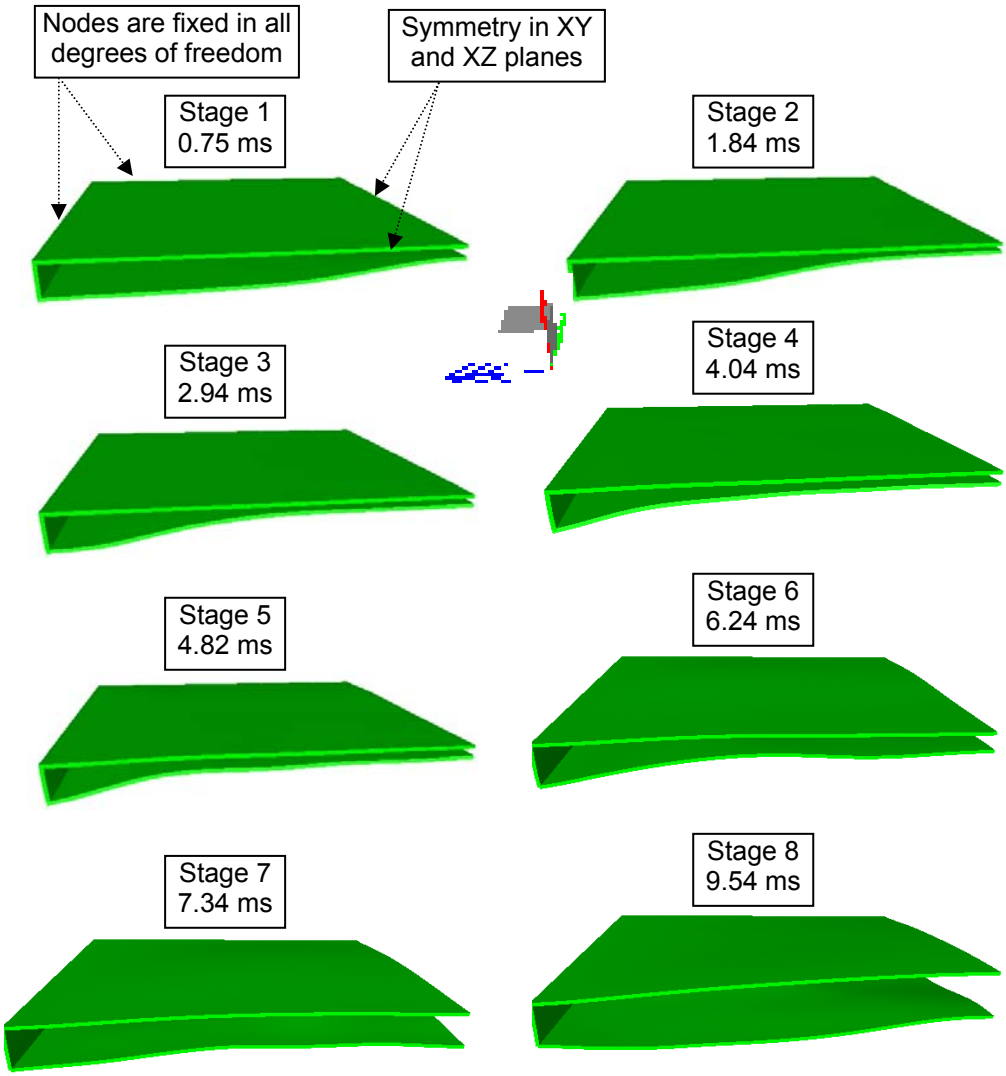

Figure C. 6 Deformation plot of ¼ symmetric 'box' model subjected to 5 kg TNT in an hemispherical shape blast at 400 mm stand-off distance.

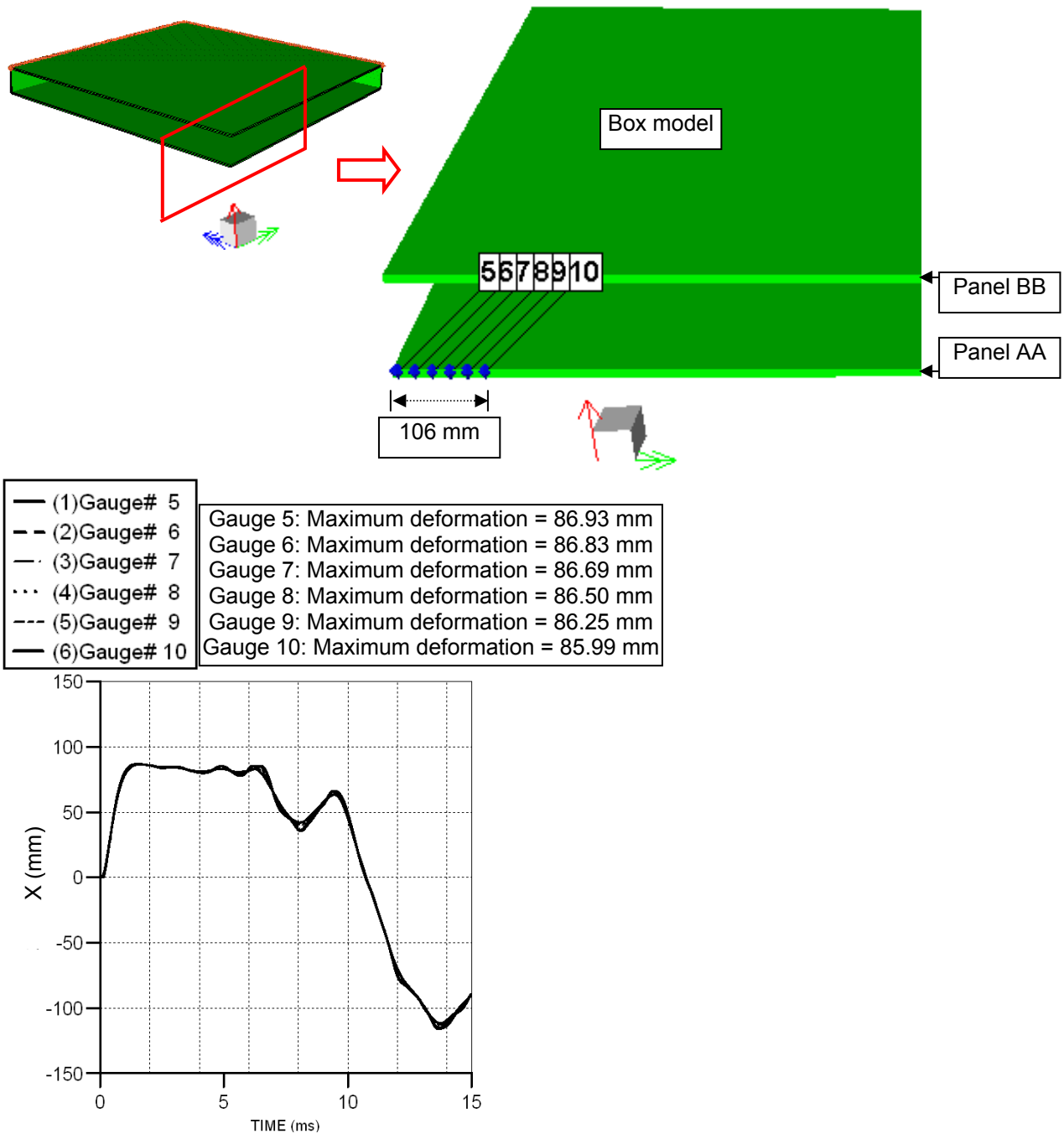

Figure C. 7 Deformation on panel AA of 'box' model subjected to 5 kg TNT in an hemispherical shape blast at 400 mm stand-off distance using different gauges (deformation curves are based on the net deformation)

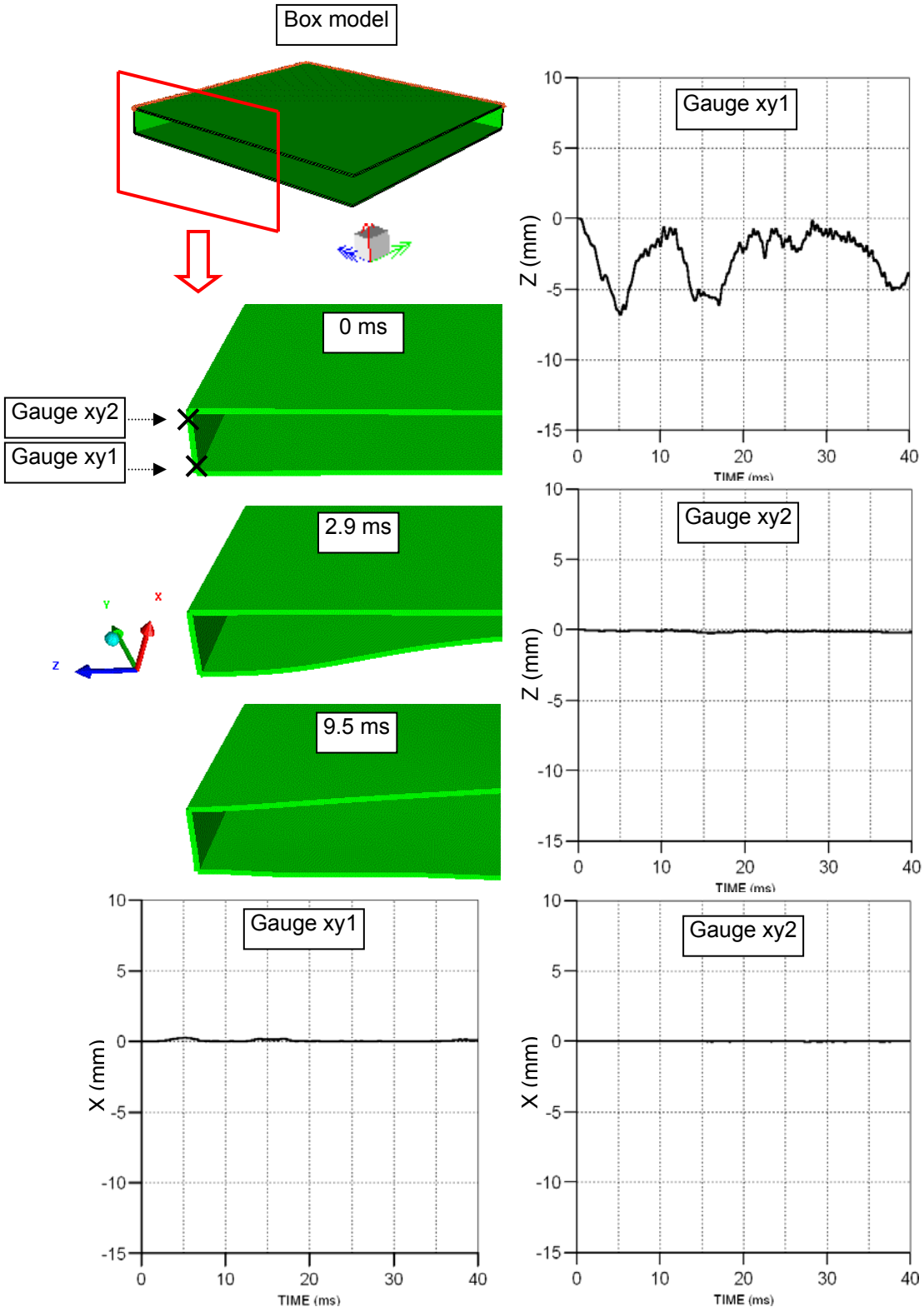

Figure C. 8 Deformation on side panels of 'box' model subjected to 5 kg TNT in an hemispherical shape blast at 400 mm stand-off distance (deformation curves are based on the net deformation)

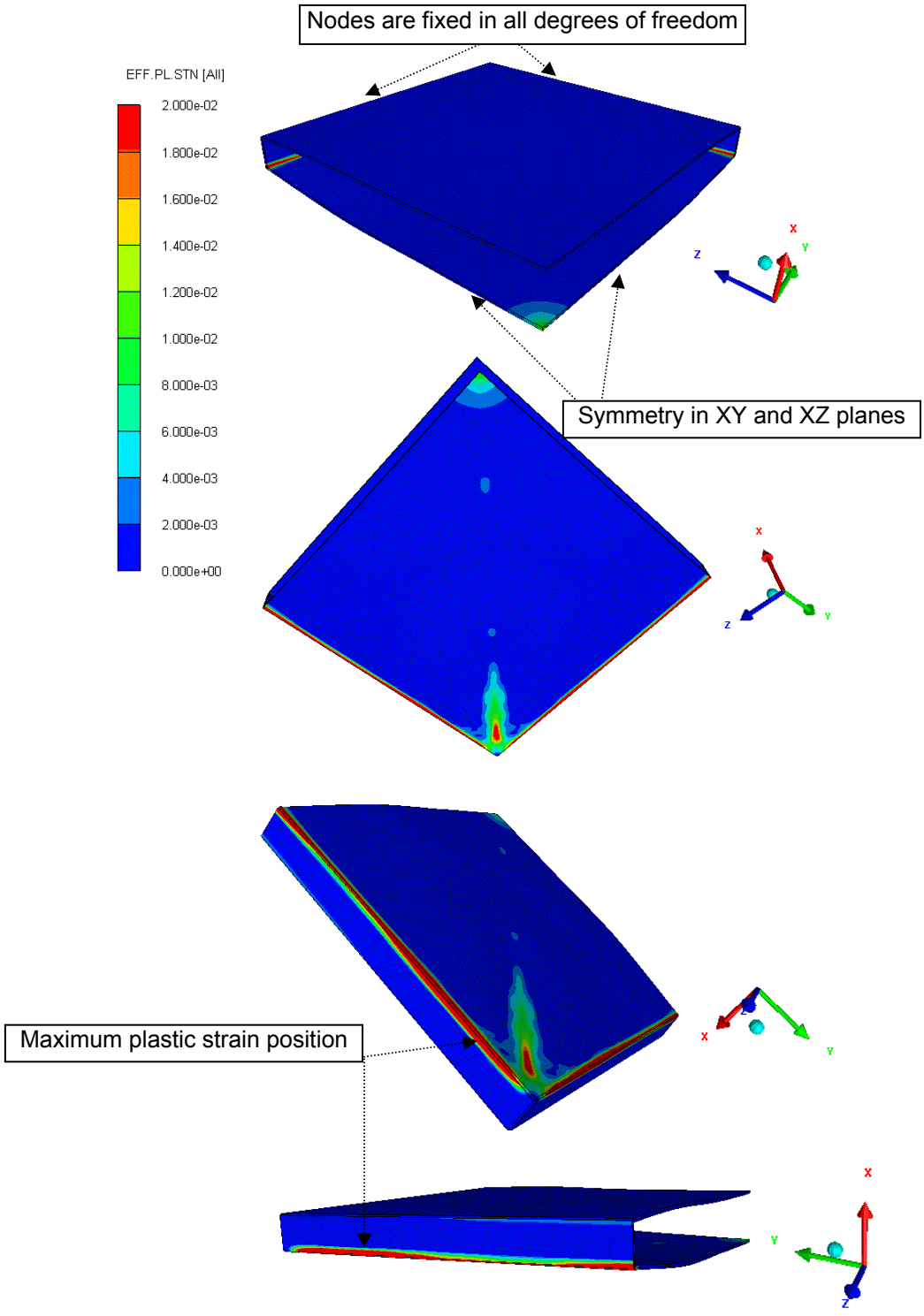

Figure C. 9 Effective plastic strain contour plot of a ¼ symmetric 'box' model subjected 5 kg TNT in an hemispherical shape blast at 40 ms.

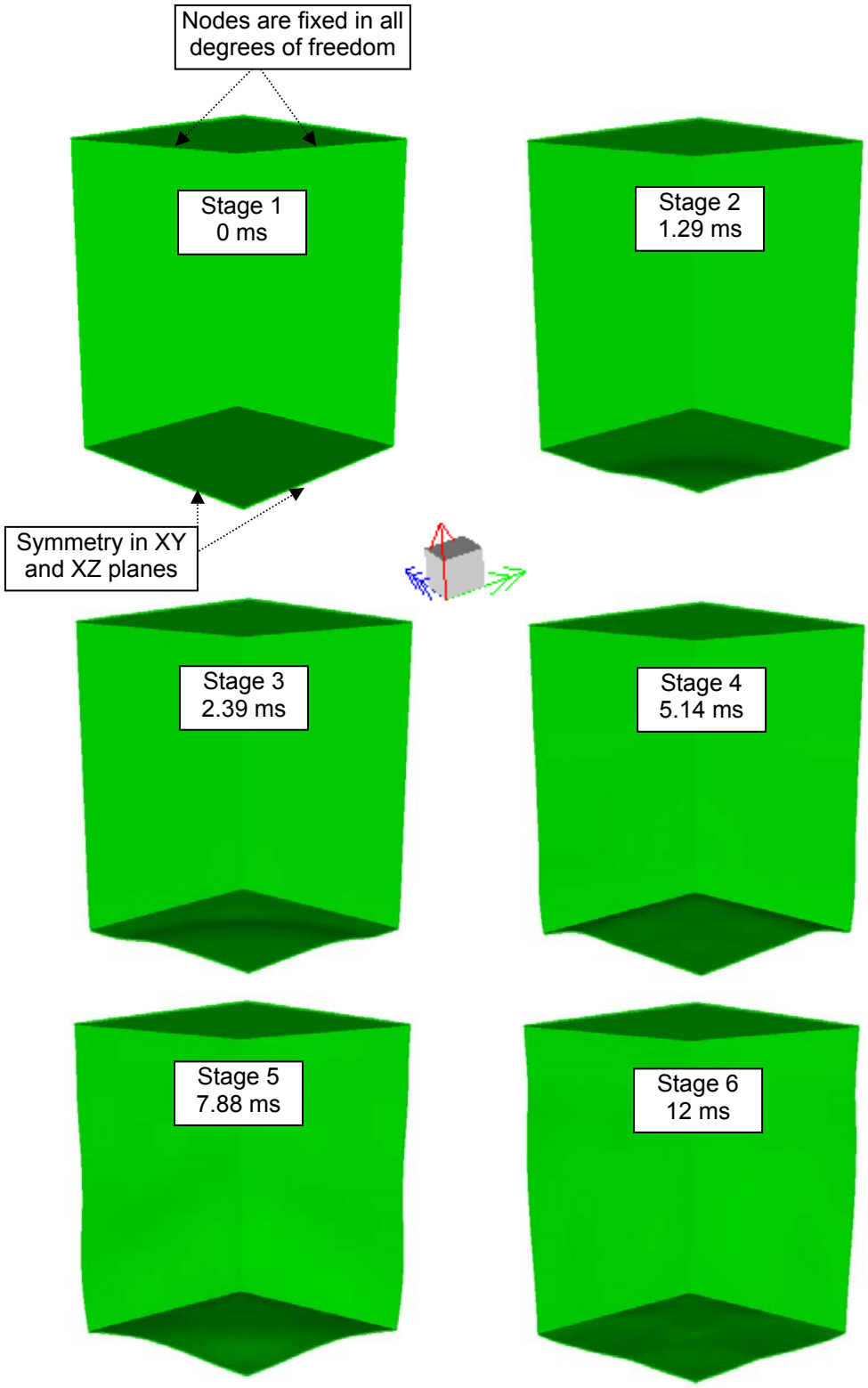

Figure C. 10 Deformation plot of ¼ symmetric 'single-floor hull' model subjected to 5 kg TNT in an hemispherical shape blast at 400 mm stand-off distance.

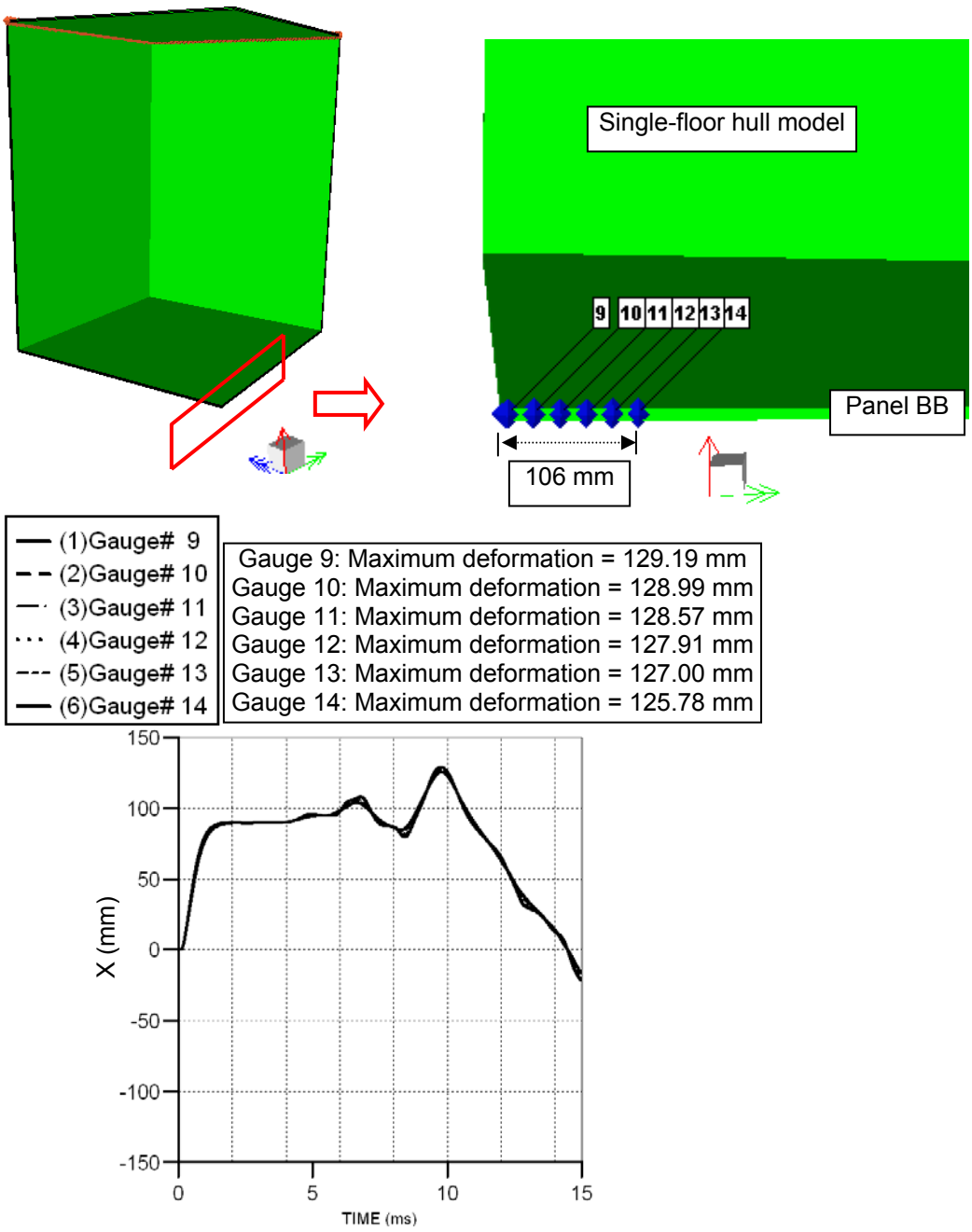

Figure C. 11 Deformation on panel BB of 'single-floor hull' model subjected to 5 kg TNT in an hemispherical shape blast at 400 mm stand-off distance using different gauges (deformation curves are based on the net deformation)

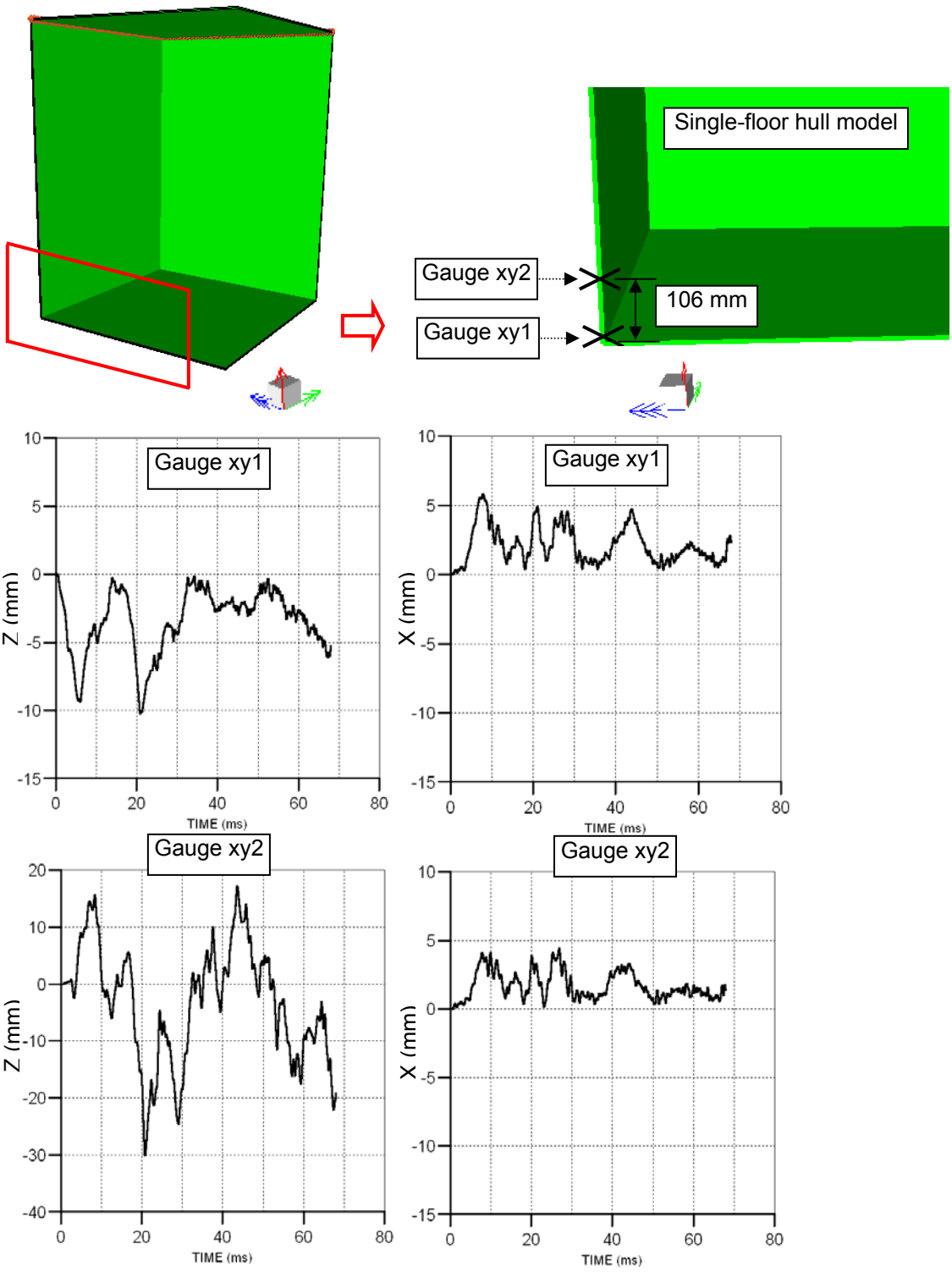

Figure C. 12 Deformation on a side panel of 'single-floor hull' model subjected to 5 kg TNT in an hemispherical shape blast at 400 mm stand-off distance (deformation curves are based on the net deformation)

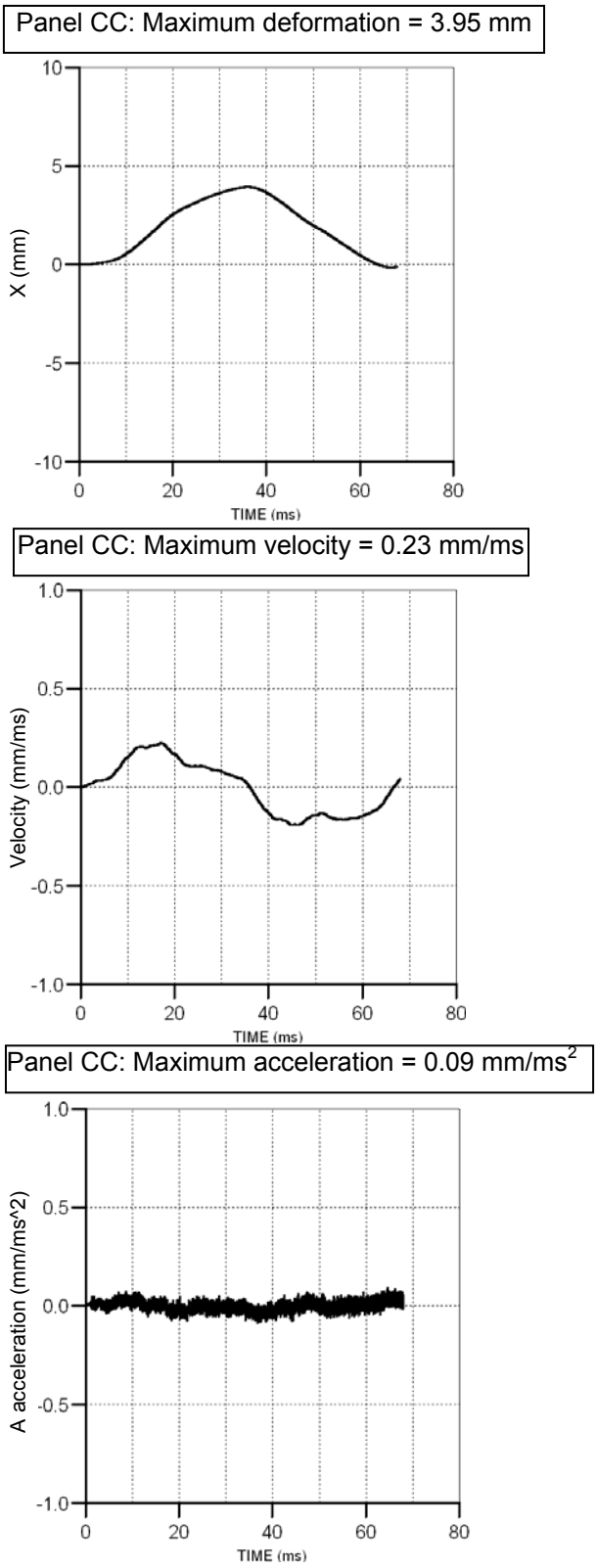

Figure C. 13 Deformation, velocity, and acceleration on panel CC of 'single-floor hull' model subjected to 5 kg TNT in an hemispherical shape blast at 400 mm stand-off distance (deformation curve is based on the net deformation)

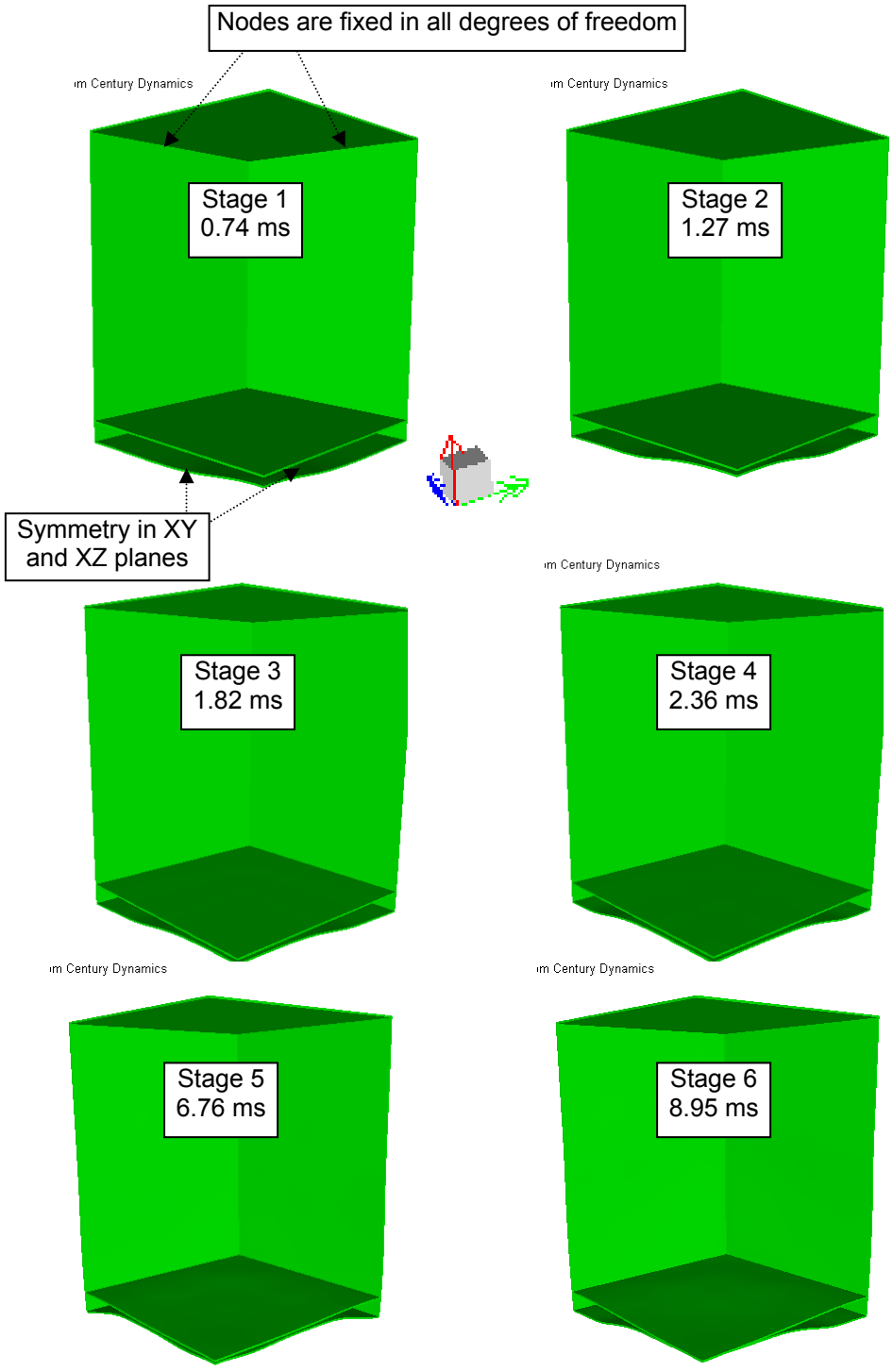

Figure C. 14 Deformation plot of ¼ symmetric 'double-floor hull' model subjected to 5 kg TNT in an hemispherical shape blast at 400 mm stand-off distance.

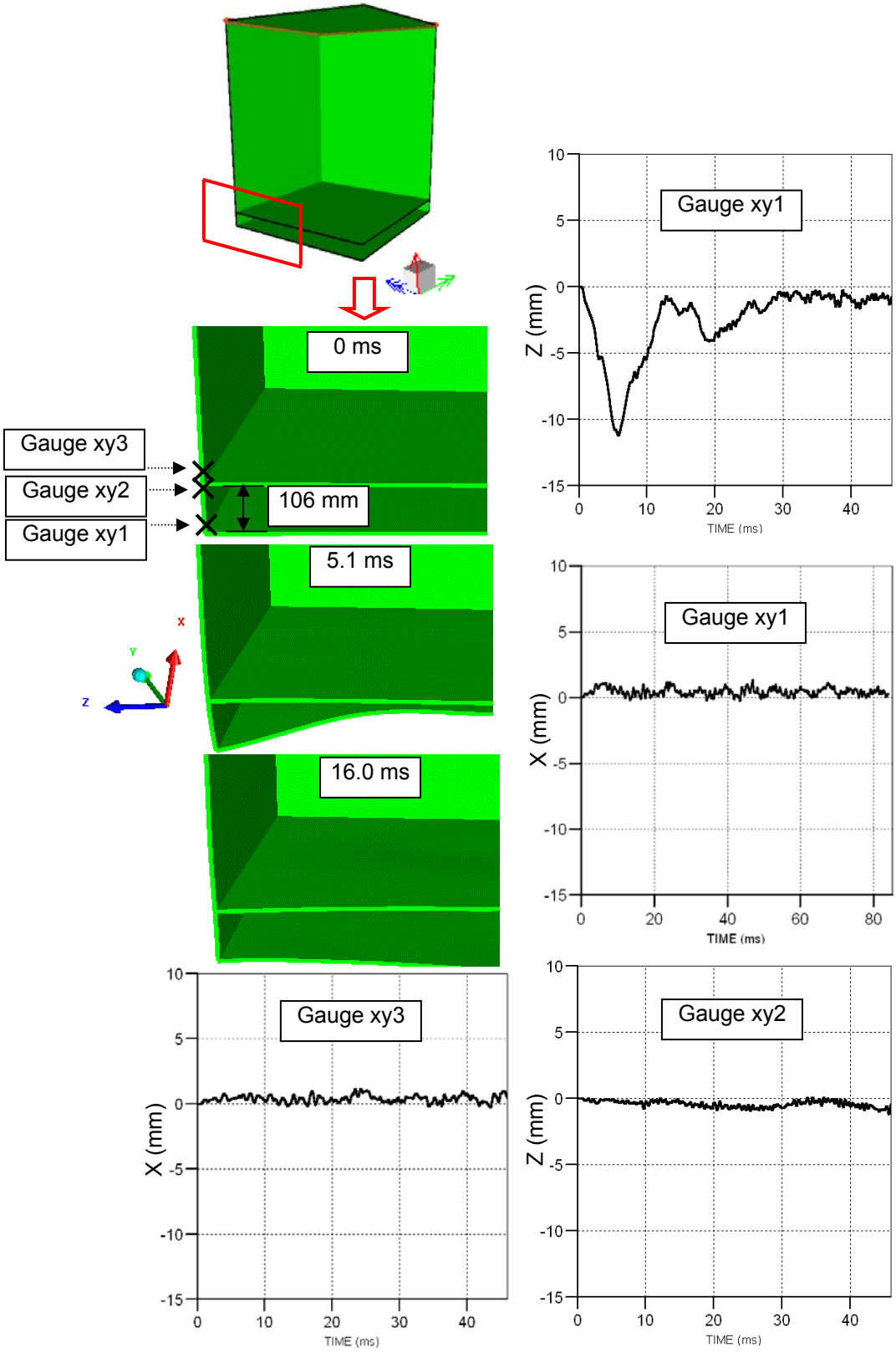

Figure C. 15 Deformation on a side panel of 'double-floor hull' model subjected to 5 kg TNT in an hemispherical shape blast at 400 mm stand-off distance (deformation curves are based on the net deformation)

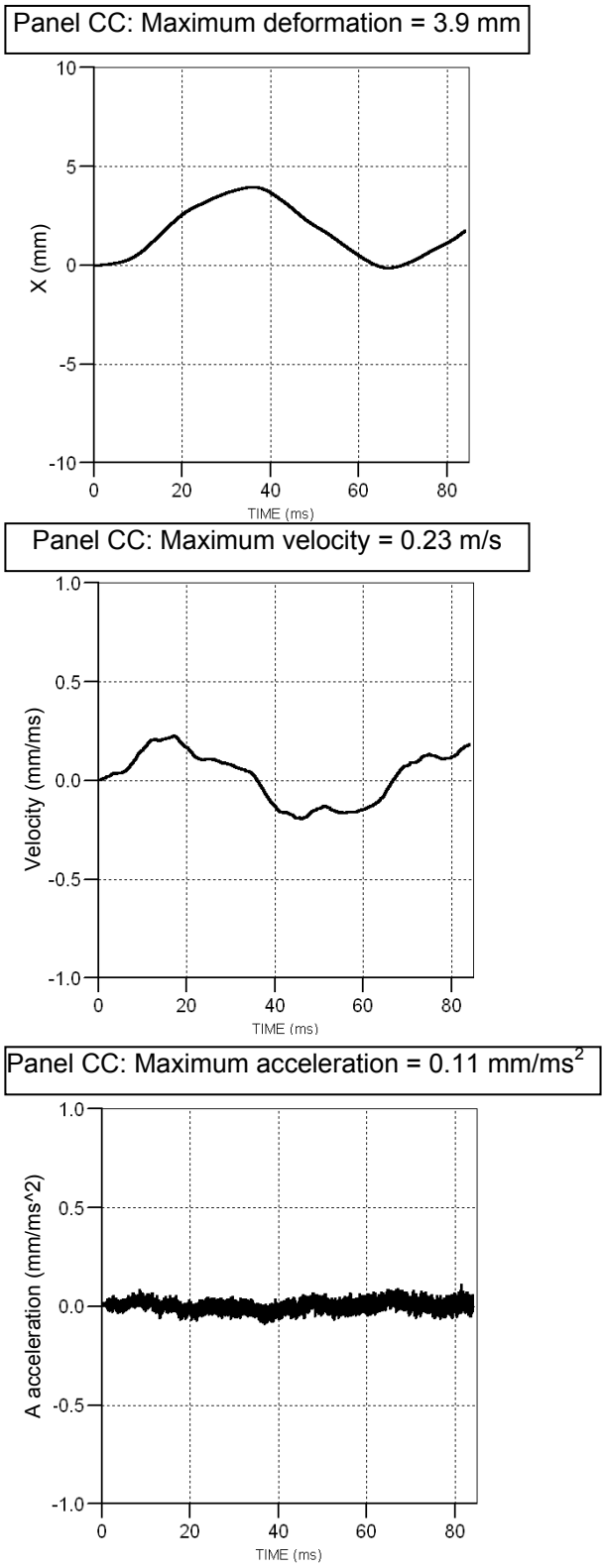

Figure C. 16 Deformation, velocity, and acceleration on panel CC of 'double-floor hull' model subjected to 5 kg TNT in an hemispherical shape blast at 400 mm stand-off distance (deformation curve is based on the net deformation)

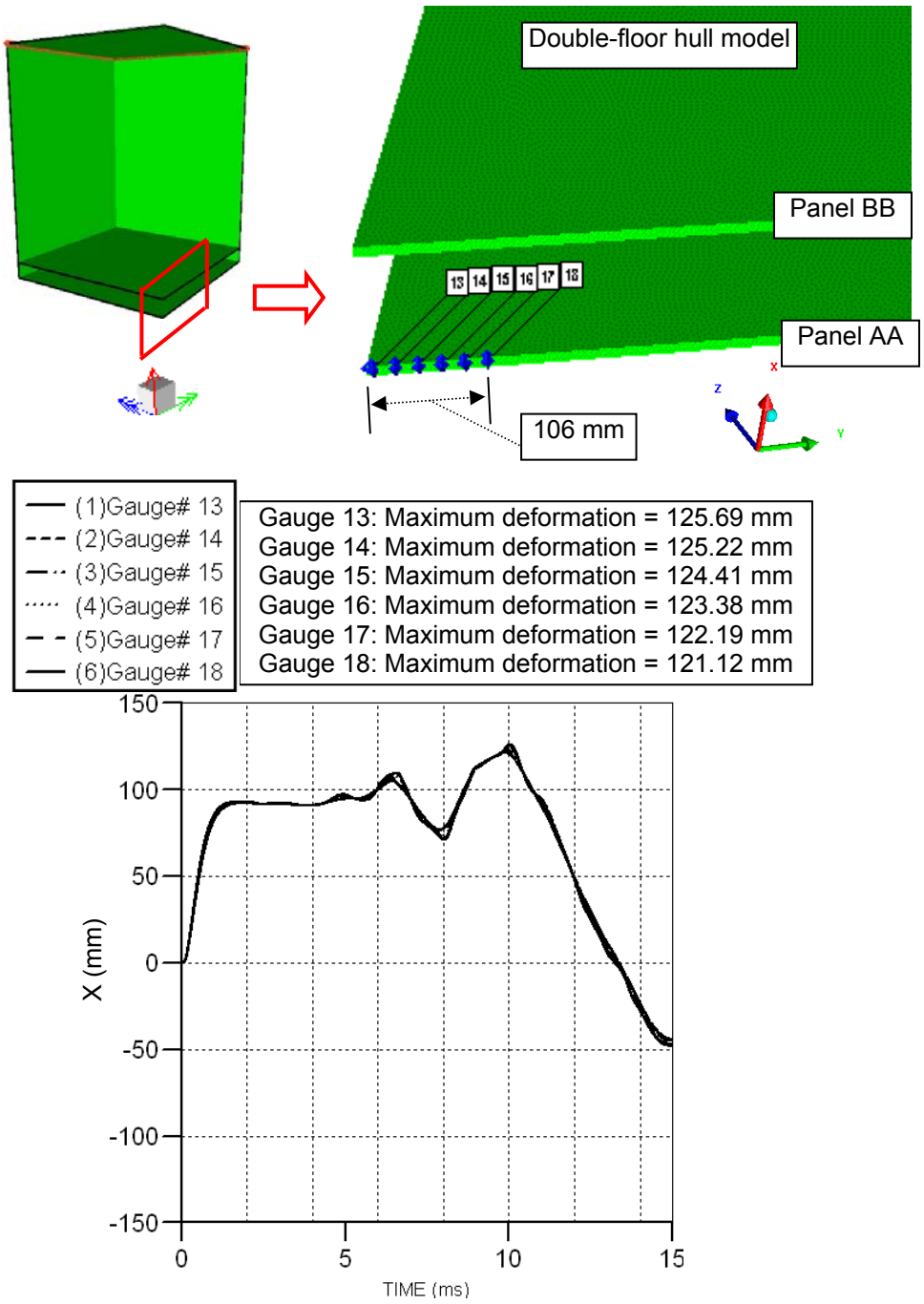

Figure C. 17 Deformation on panel AA of 'double-floor hull' model subjected to 5 kg TNT in an hemispherical shape blast at 400 mm stand-off distance using different gauges (deformation curves are based on the net deformation)

APPENDIX D Extended results from Chapter 6

This Appendix shows the extended results related to Chapter 6.

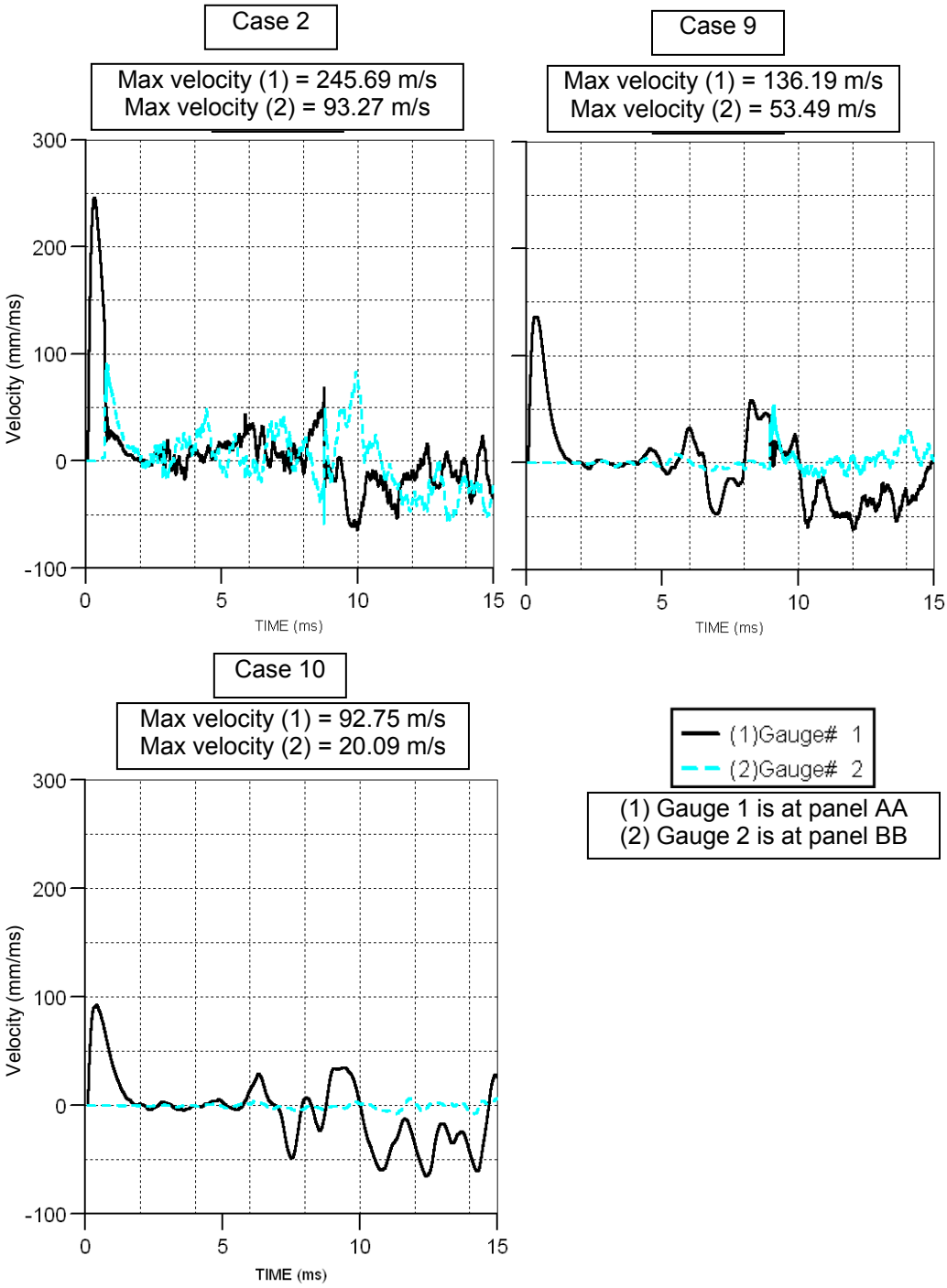

Figure D. 1 Velocity results of cases 2, 9, and 10. Note that all cases contain the same scales.

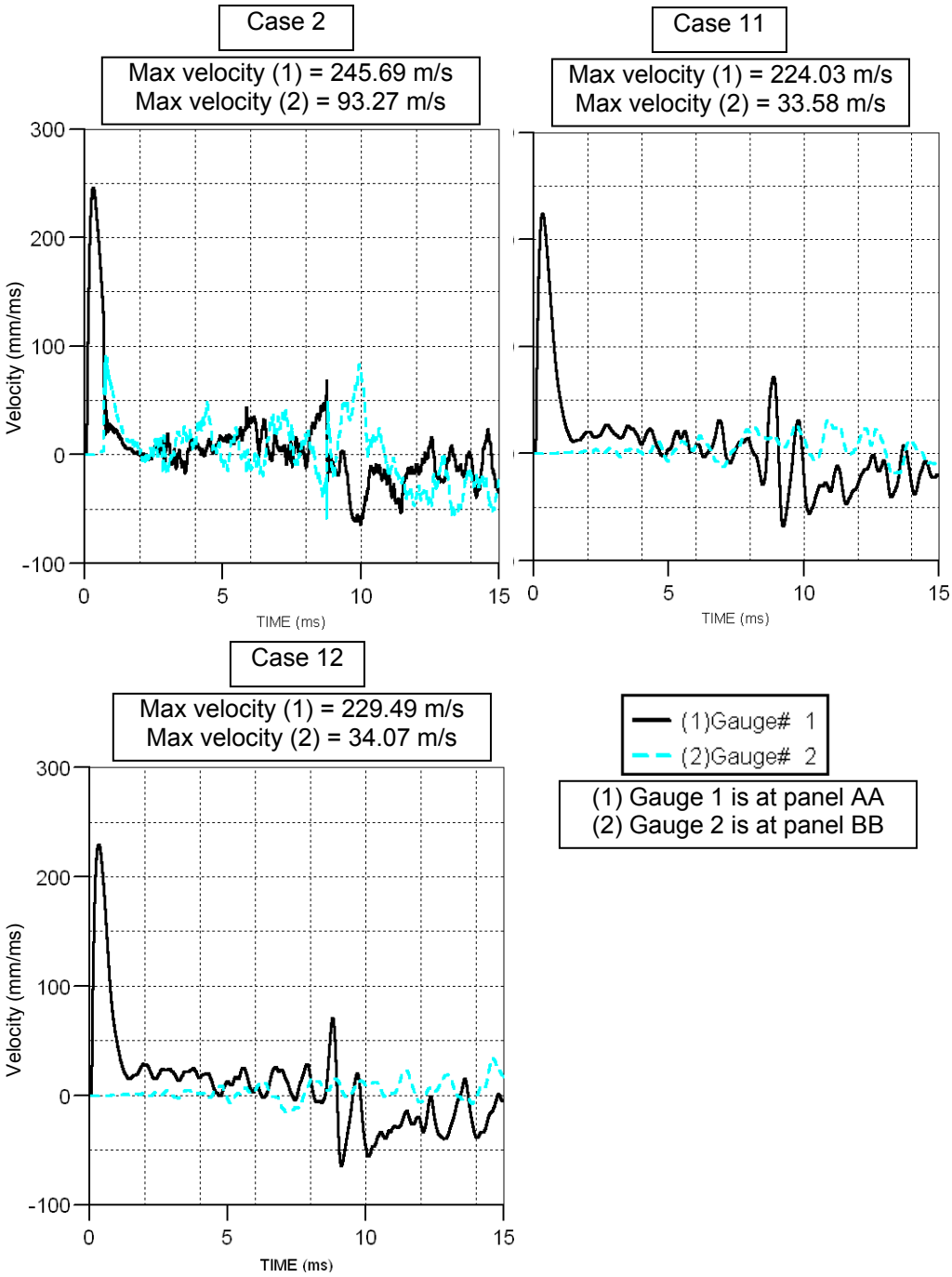

Figure D. 2 Velocity results of cases 2, 11, and 12. Note that all cases contain the same scales.

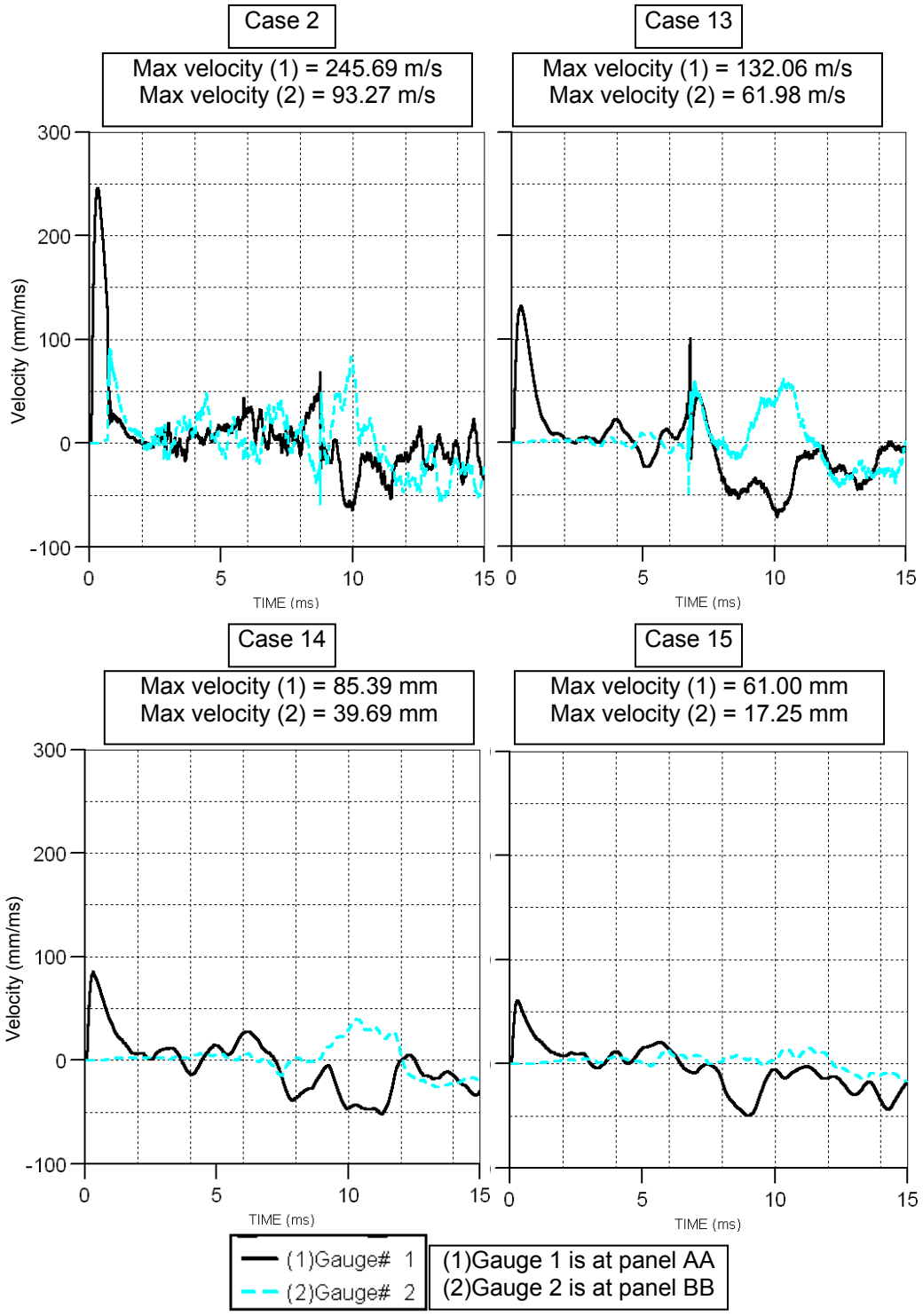

Figure D. 3 Velocity results of cases 2, 13, 14, and 15.

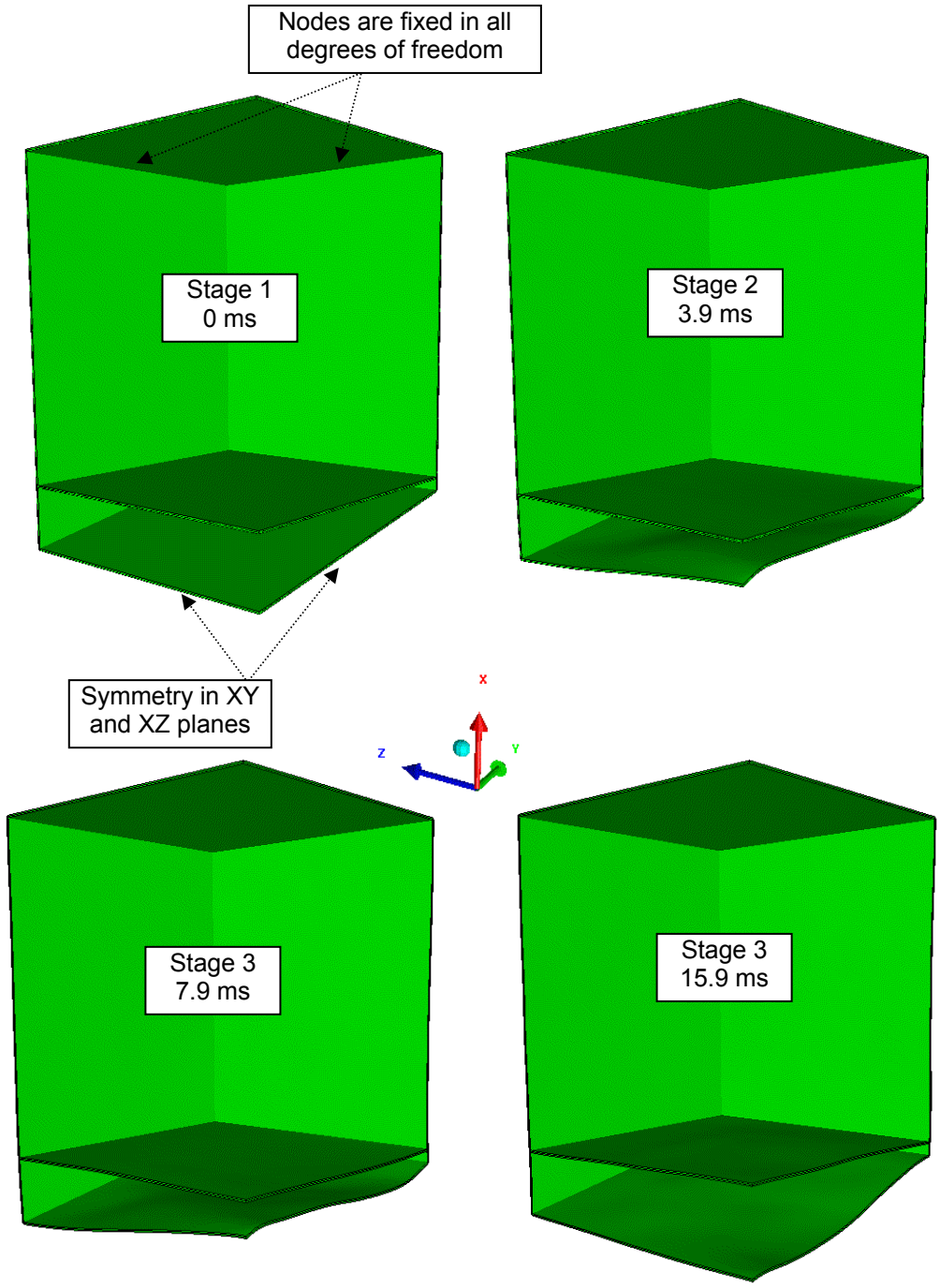

Figure D. 4 ¼ 'V' bottom hull model deformation plot in ¼ model's view

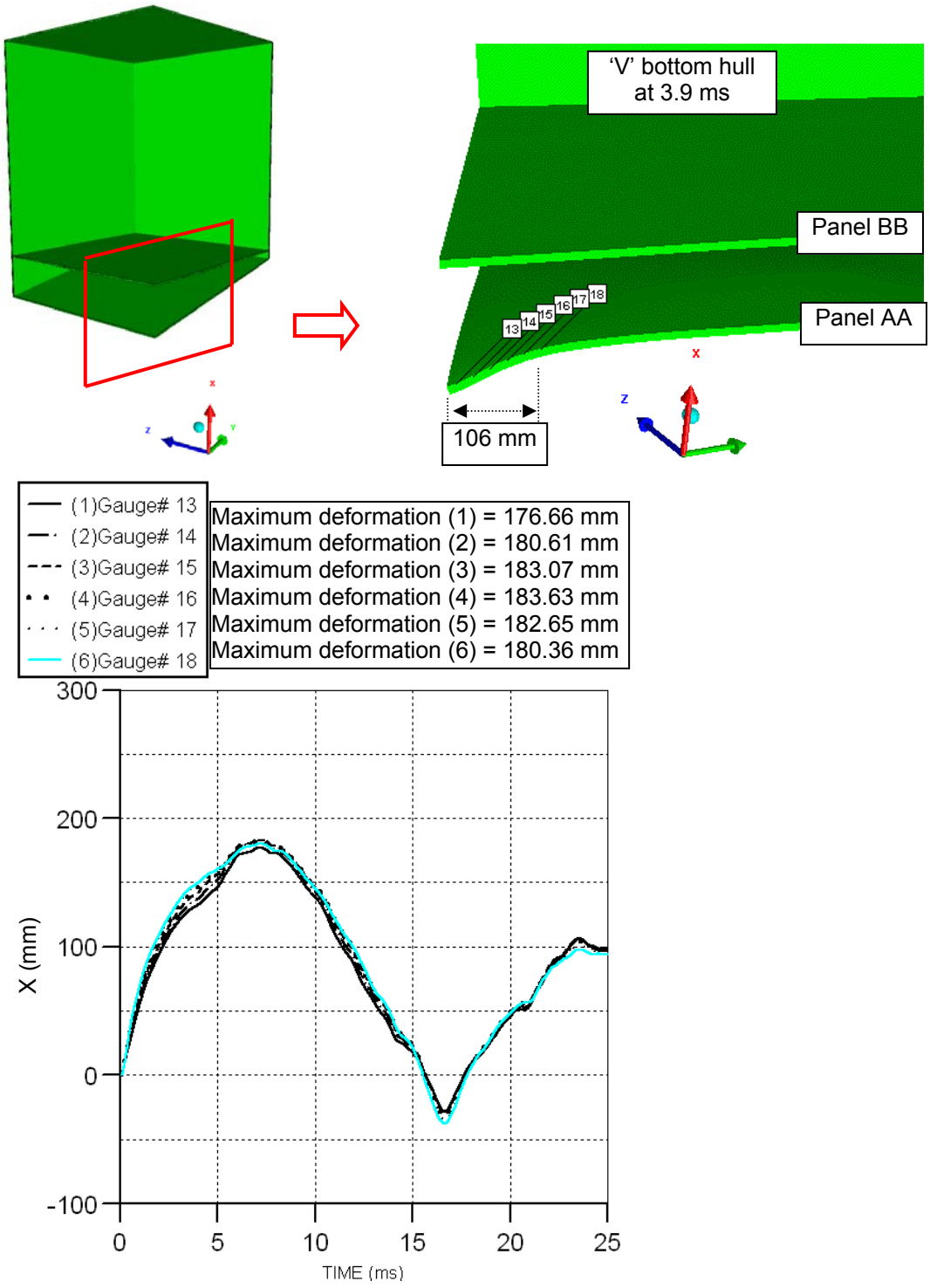

Figure D. 5 Deformation profile of panel BB on 'V' bottom hull model (deformation curves are based on the net deformation)

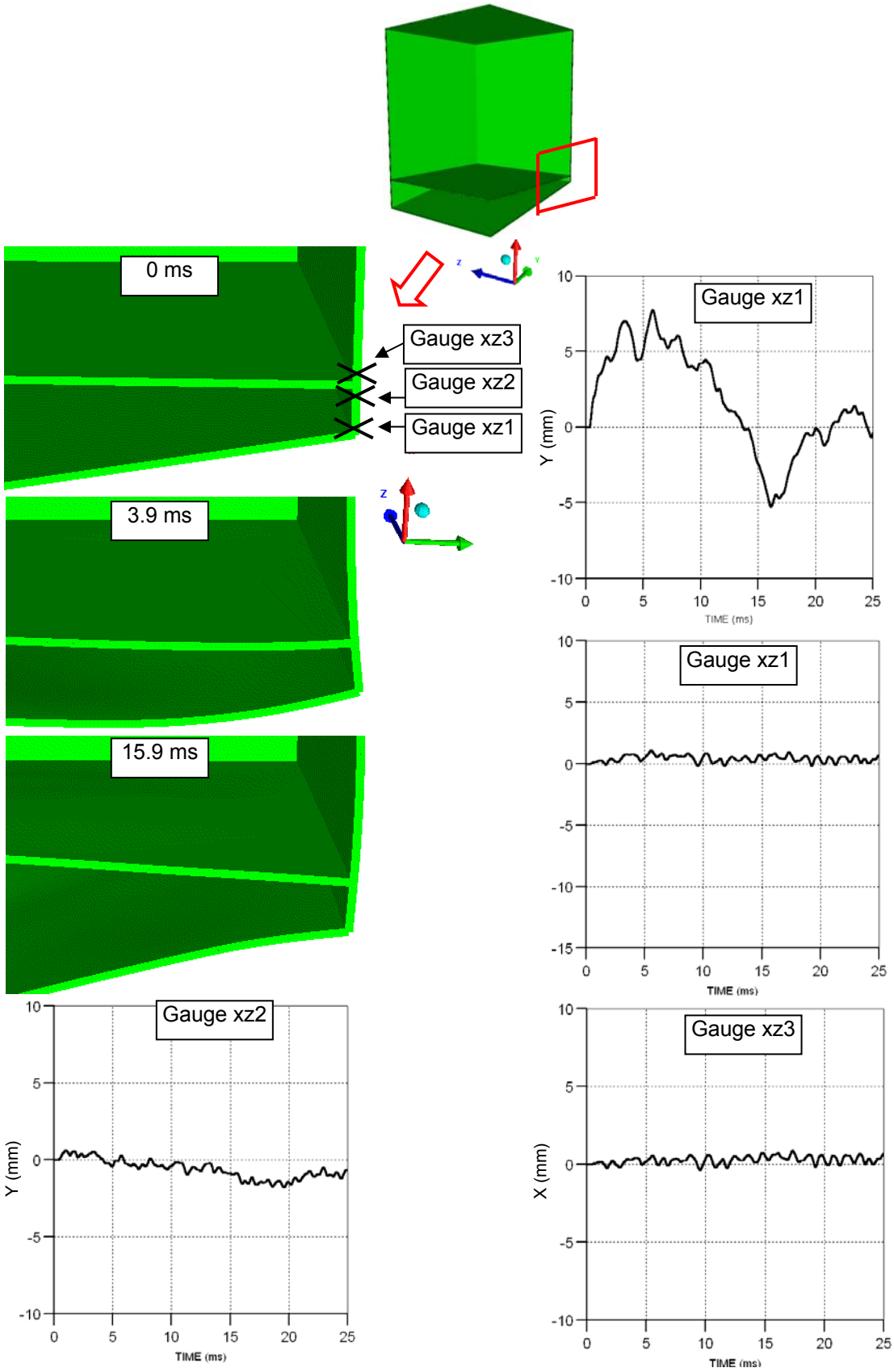

Figure D. 6 XZ panel deformation on 'V' bottom hull model (deformation curves are based on the net deformation)

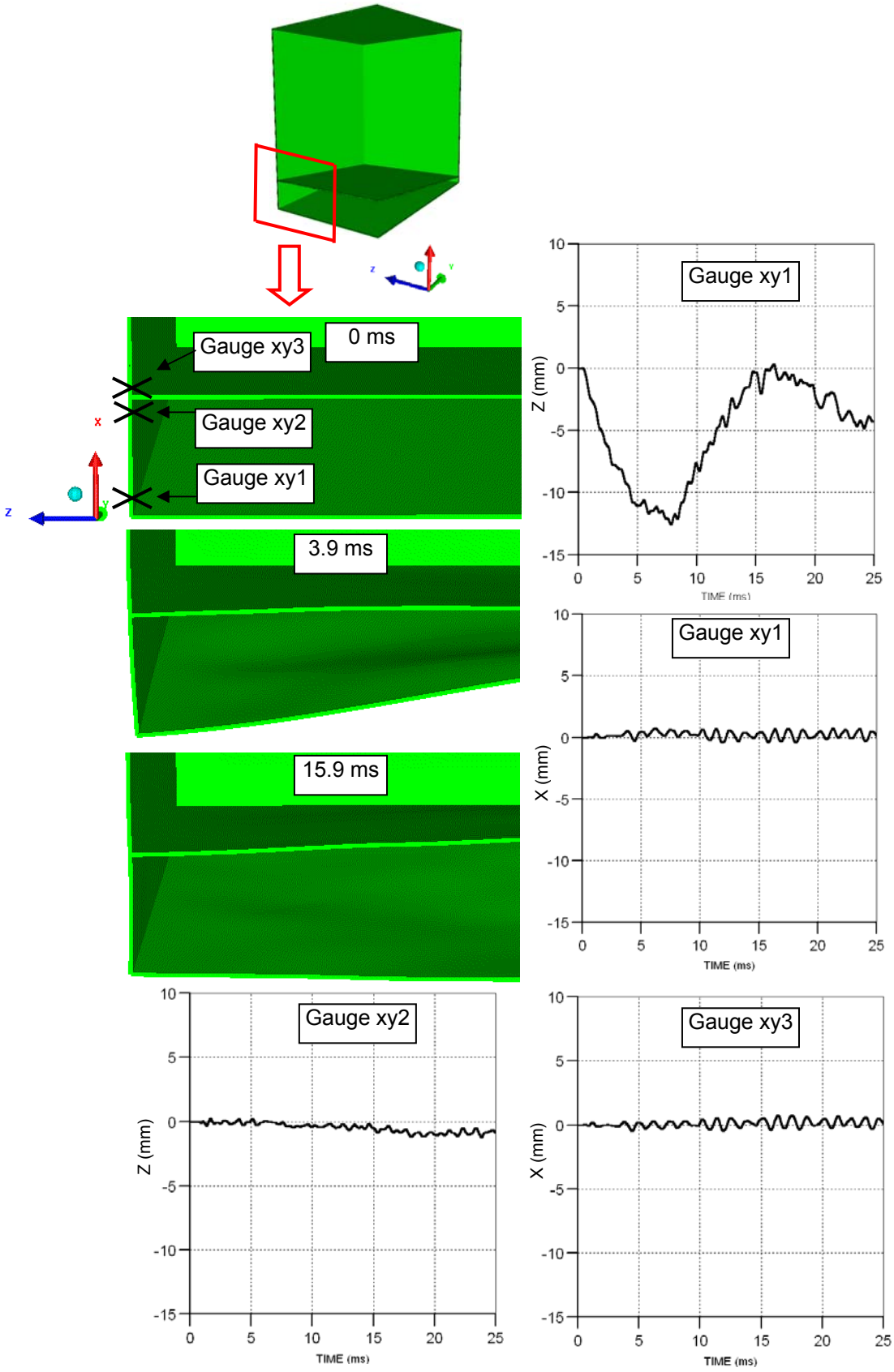

Figure D. 7 XY panel deformation on 'V' bottom hull model (deformation curves are based on the net deformation)

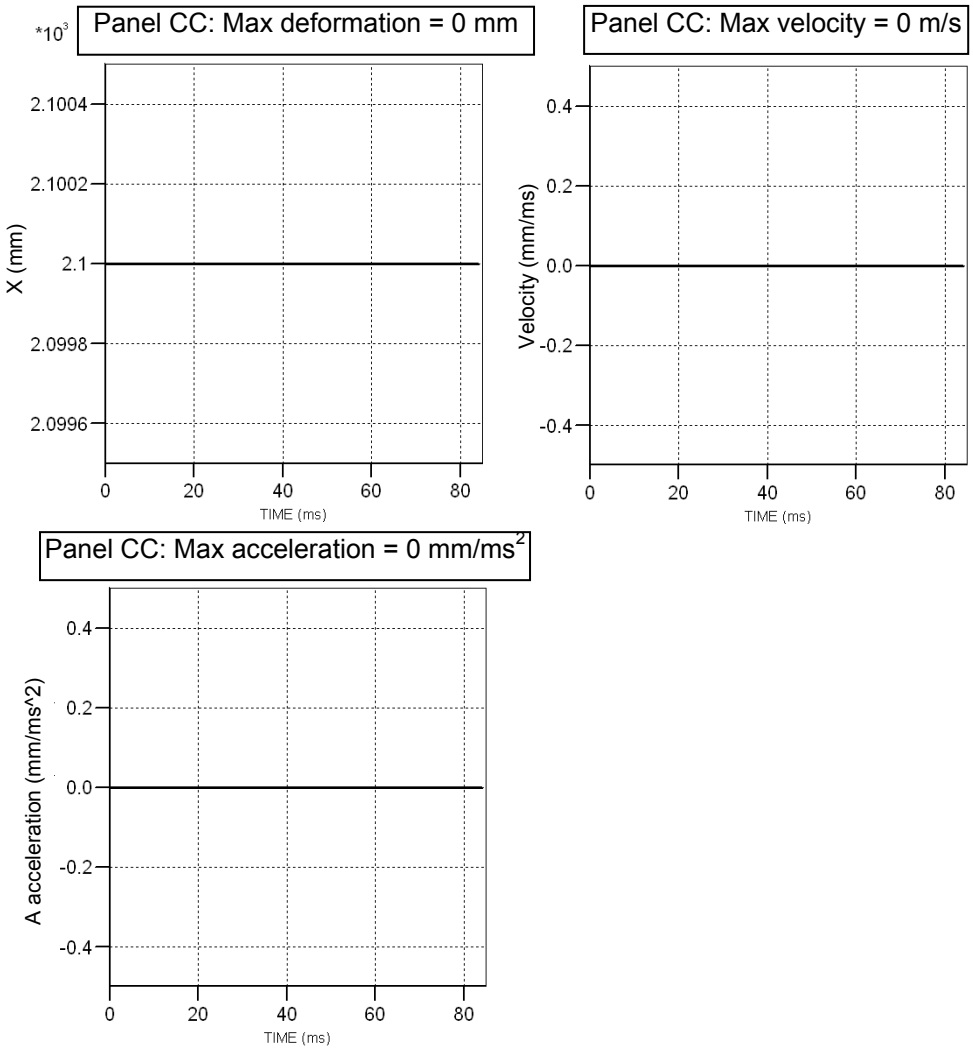

Figure D. 8 Deformation, velocity, and acceleration on panel CC of 'V' bottom hull model (deformation curve is based on the actual gauge position)

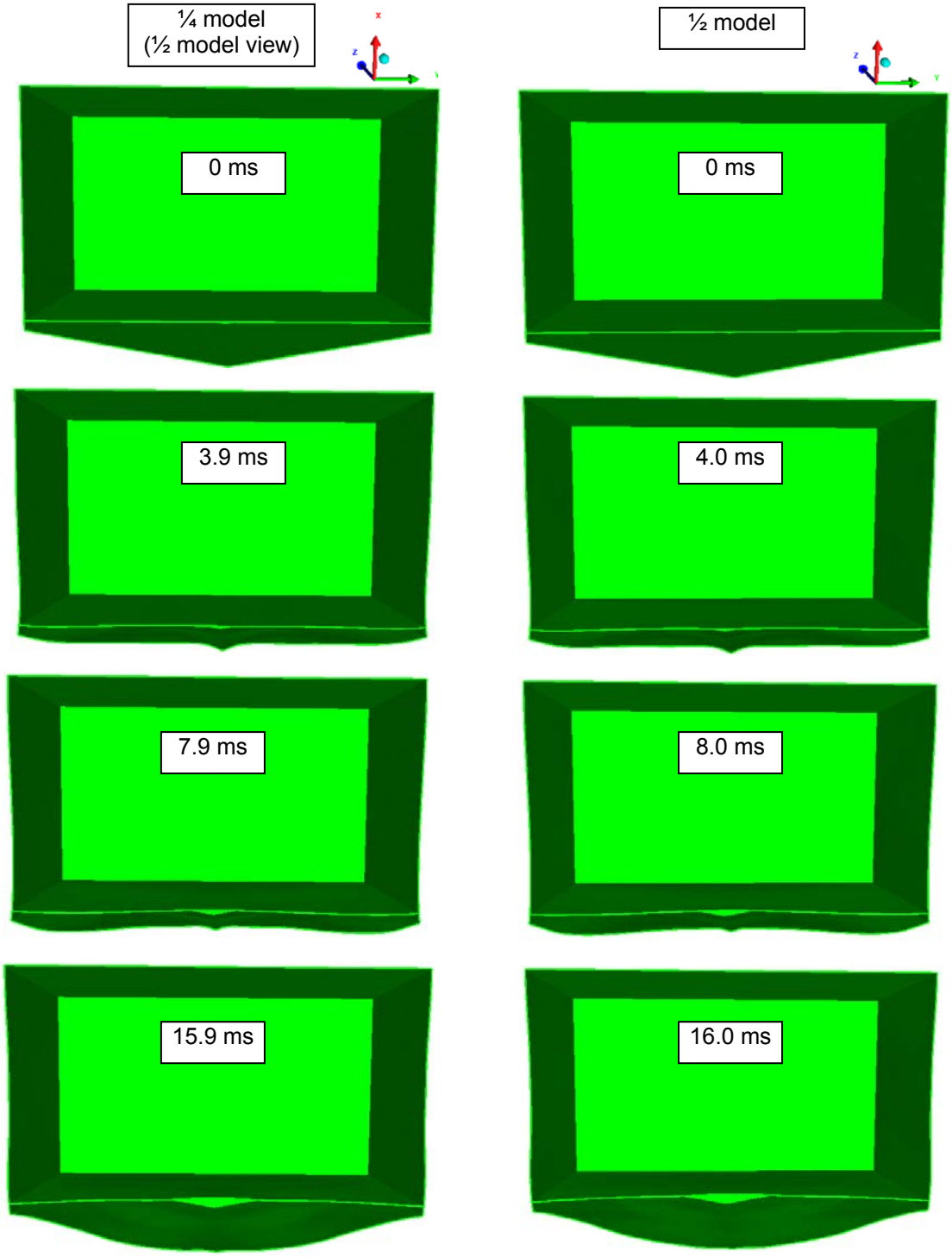

Figure D. 9 ½ and ¼ 'V' bottom hull model deformation plot in ½ model's view

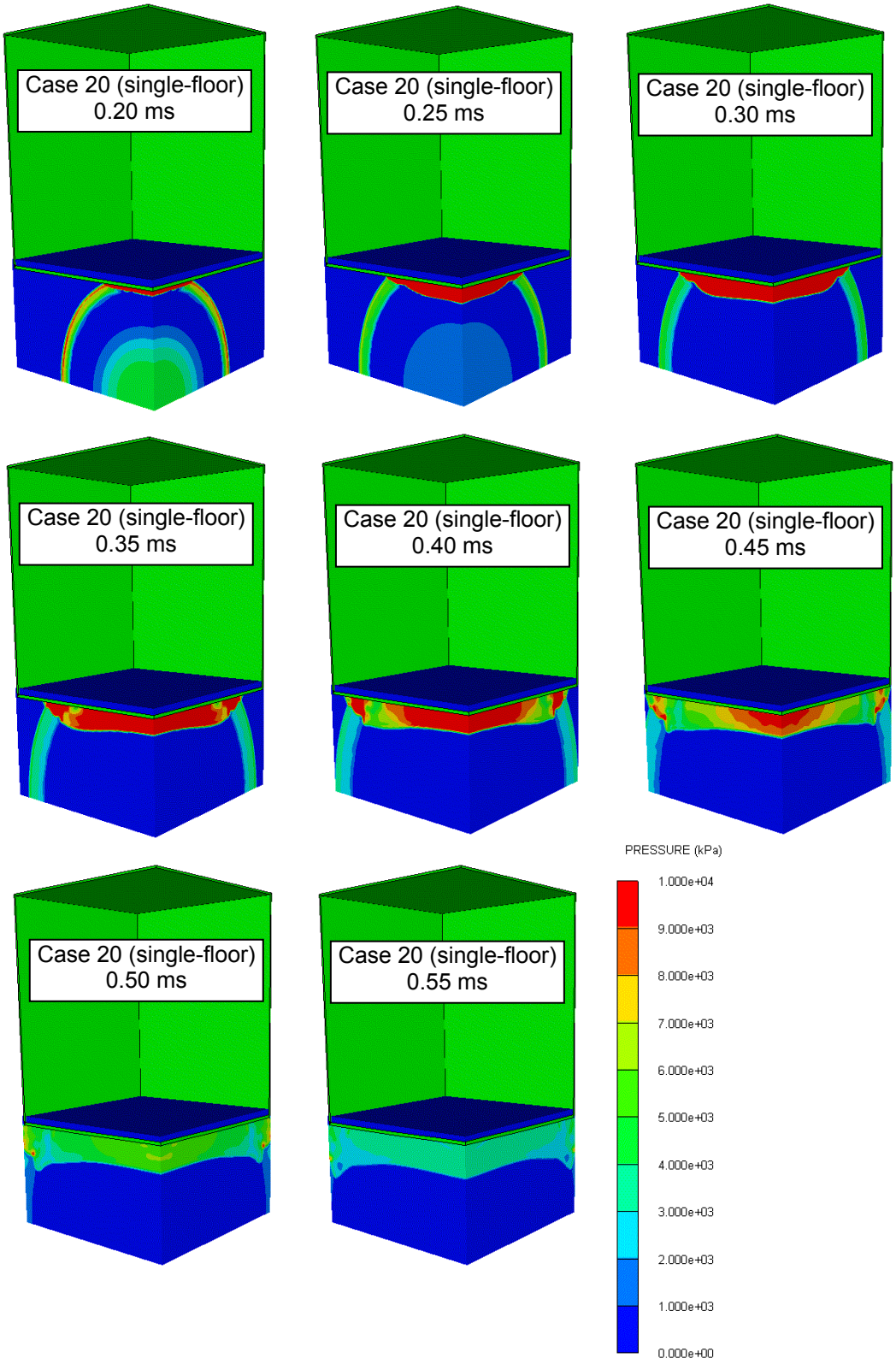

Figure D. 10 Pressure contour plot in case 20 (1)

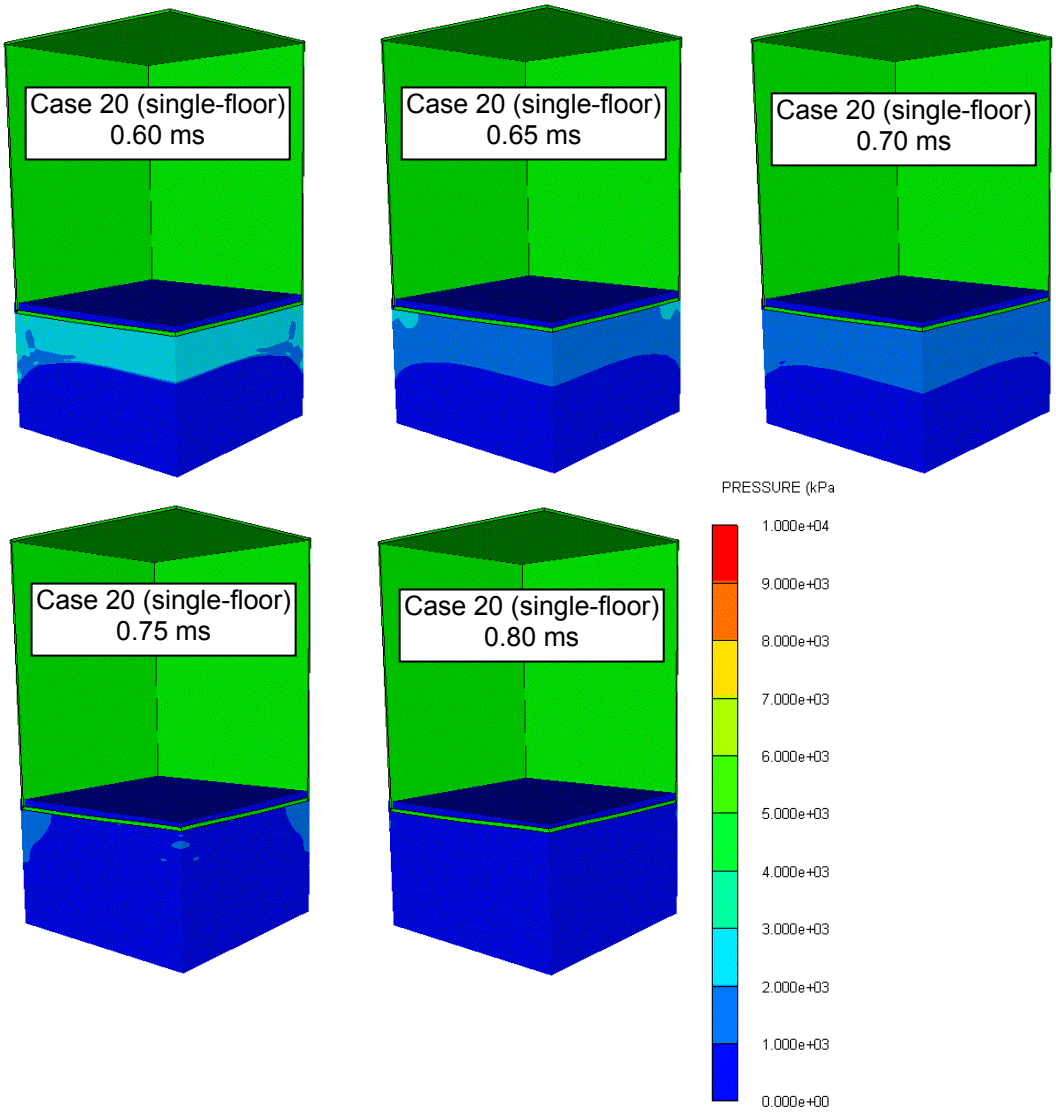

Figure D. 11 Pressure contour plot in case 20 (2)

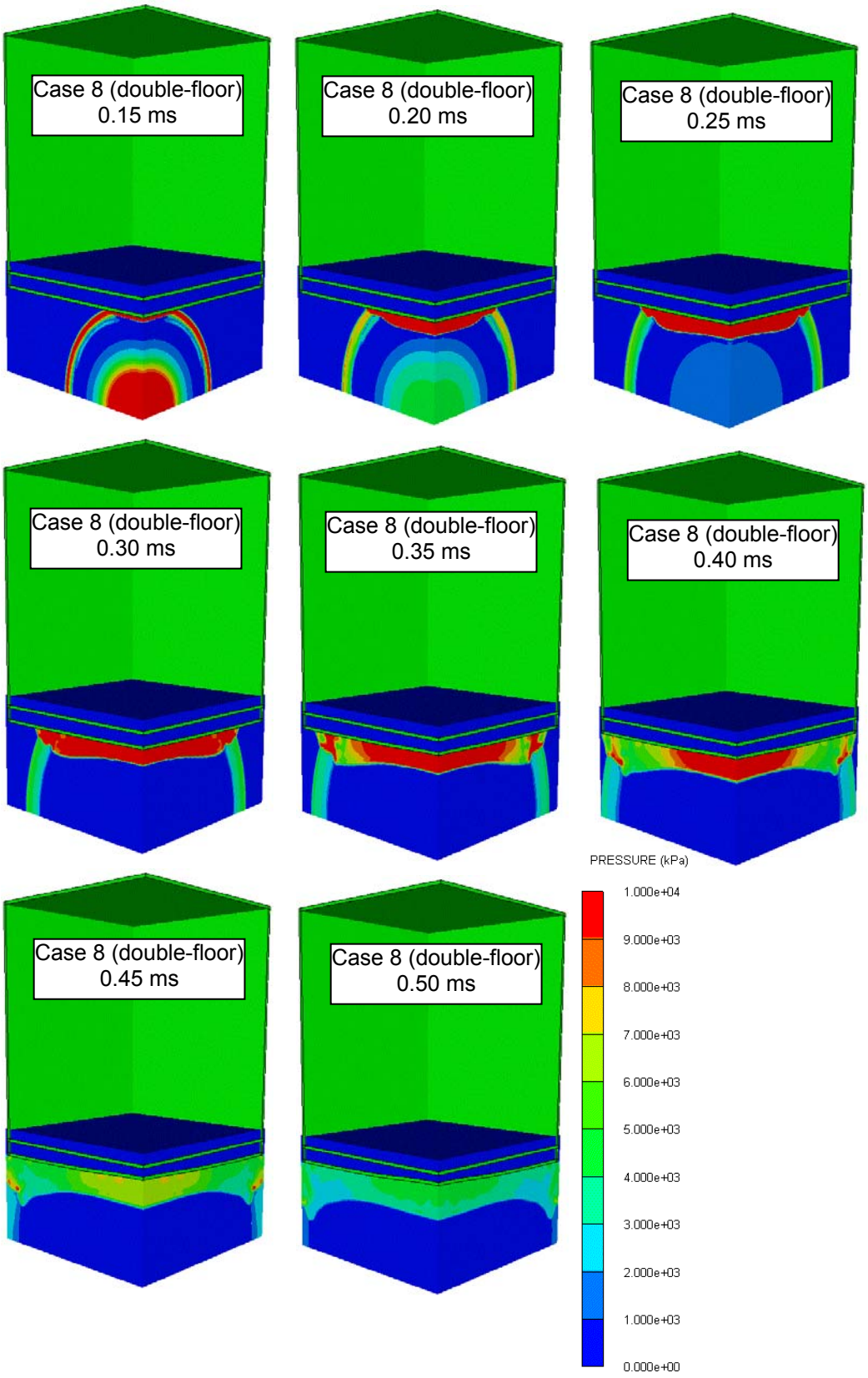

Figure D. 12 Pressure contour plot in case 8 (1)

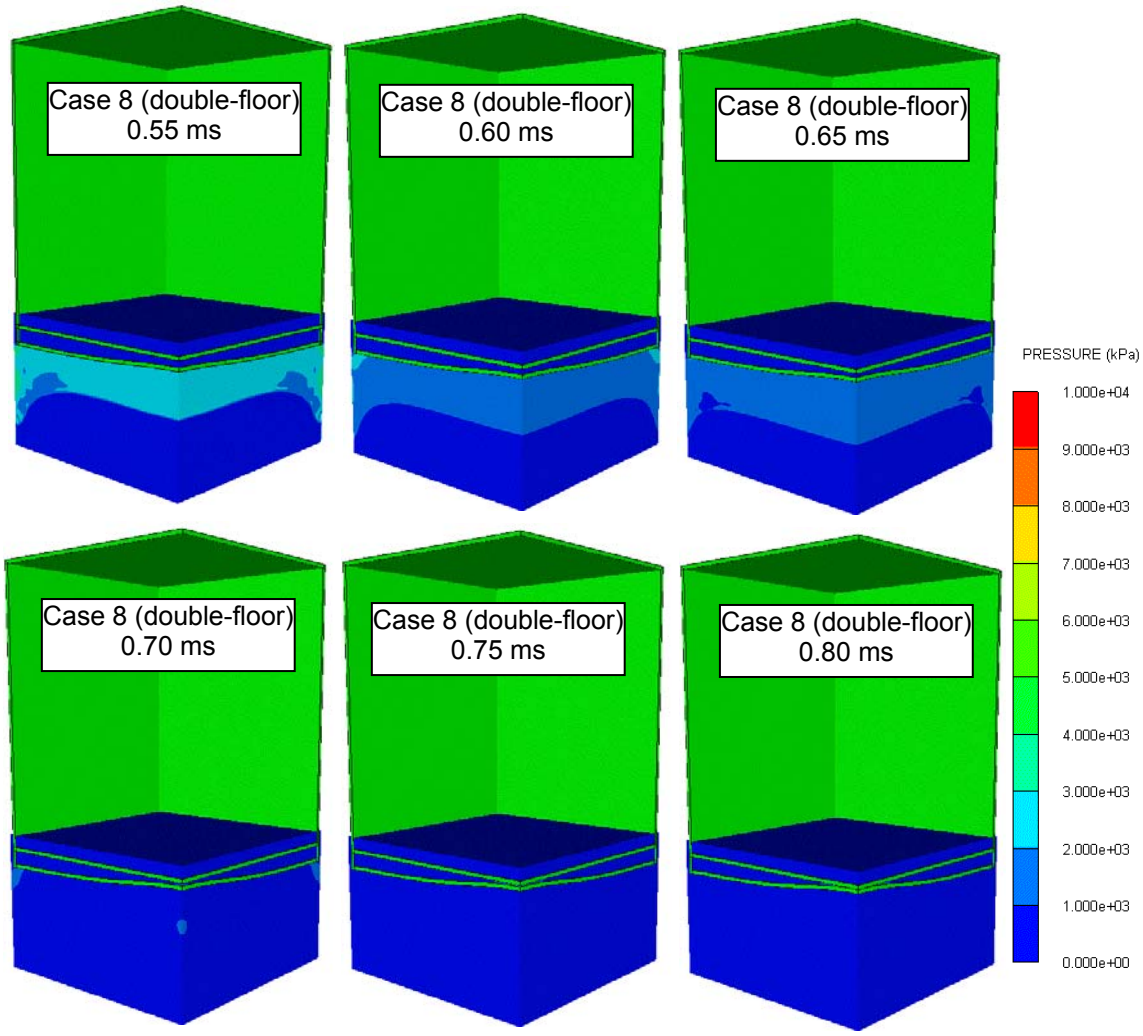

Figure D. 13 Pressure contour plot in case 8 (2)

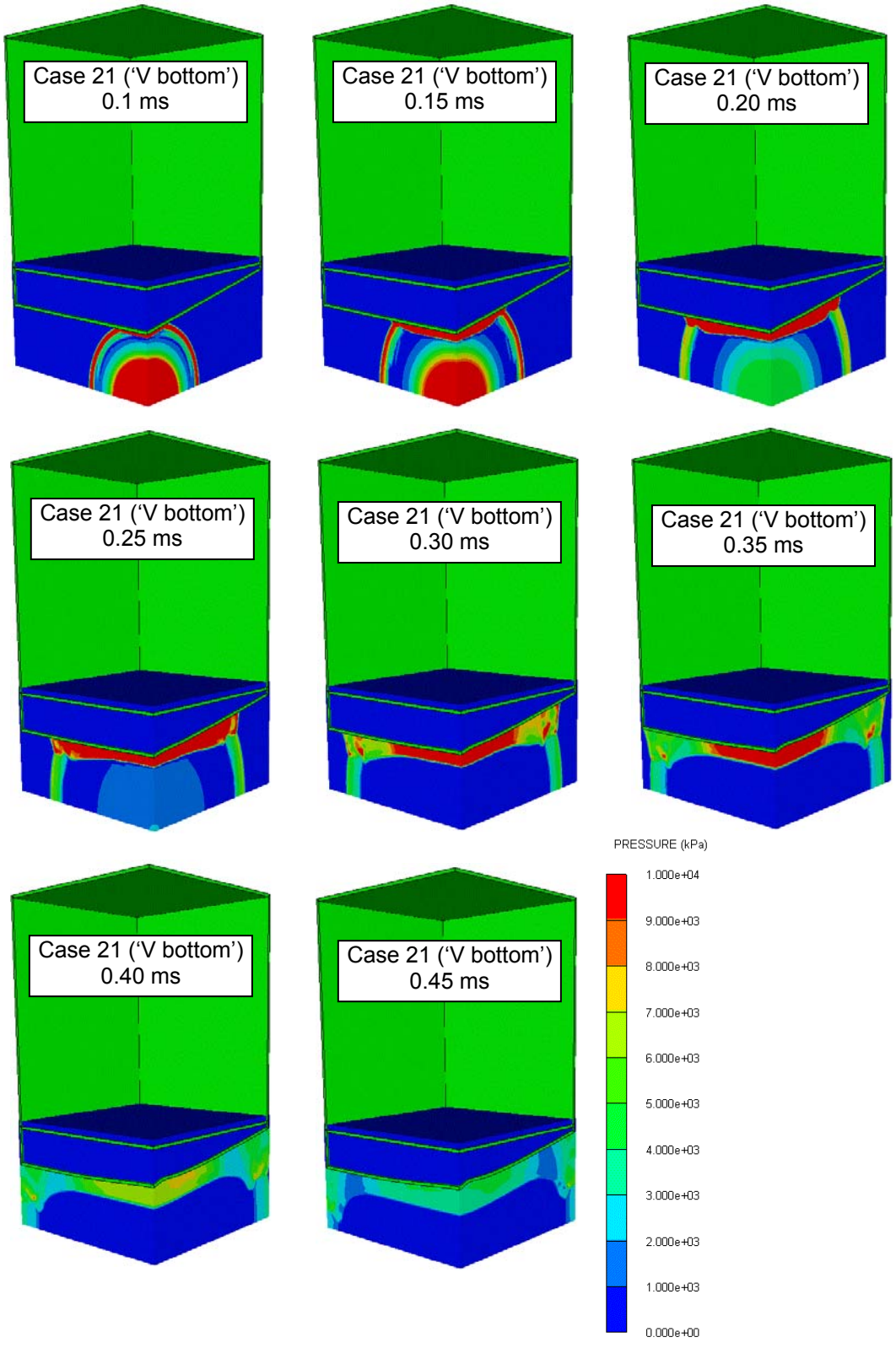

Figure D. 14 Pressure contour plot in case 21 (1)

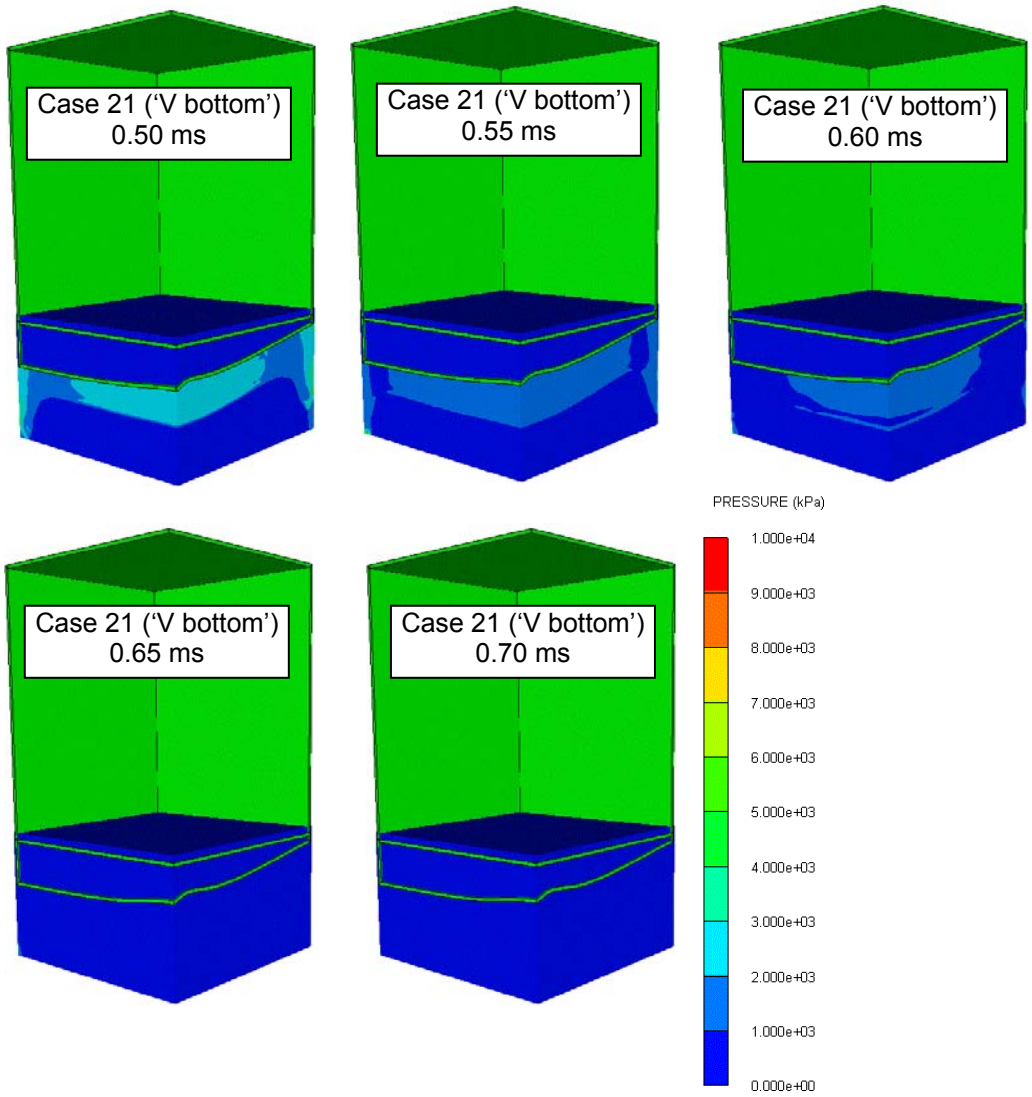

Figure D. 15 Pressure contour plot in case 21 (2)